EFFECTS OF INTERFACES AND PREFERRED ORIENTATION ON THE ELECTRICAL RESPONSE OF COMPOSITES OF ALUMINA AND SILICON CARBIDE WHISKERS

A Dissertation
Presented to
The Academic Faculty

by

Brian D. Bertram

In Partial Fulfillment
Of the Requirements for the Degree
Doctor of Philosophy in Materials Science and Engineering

Georgia Institute of Technology

December 2011

EFFECTS OF INTERFACES AND PREFERRED ORIENTATION ON THE ELECTRICAL RESPONSE OF COMPOSITES OF ALUMINA AND SILICON CARBIDE WHISKERS

Approved by:

Prof. Rosario A. Gerhardt, Advisor
School of Materials Science and Engineering
Georgia Institute of Technology

Dr. Tom Quantrille
Advanced Composite Materials LLC

Prof. Arun M. Gokhale
School of Materials Science and Engineering
Georgia Institute of Technology

Dr. John W. Schultz
Signature Technology Lab
Georgia Tech Research Institute

Prof. W. Steve Johnson
School of Materials Science and Engineering
Georgia Institute of Technology

Date Approved: November 3, 2011

ACKNOWLEDGEMENTS

I am sincerely grateful for all of the support I have received throughout this undertaking. My family, especially my parents and my brother John, were pillars of moral support. My advisor, Professor Rosario Gerhardt, provided thoughtful guidance throughout and financial support via NSF DMR# 0604211. Without her foresightful direction to study electrode effects at the onset of this project, it may not have turned out as well as it did. The insights gained during these studies, and those derived from working in her research group−which has a long history with insulator-conductor and ceramic-matrix composites−were very useful. I would also like to thank the rest of my committee for their service and for specific useful provisions. I am grateful to Profs. Gokhale and Johnson for teaching me about stereology and composites, respectively. I am also thankful to Dr. Schultz for pointing me in the right direction on matters of connectivity and contributing the financial support needed to finish strong. The support of Dr. Quantrille and Advanced Composite Materials (ACM) LLC was also critical for the undertaking of this project, as they provided the materials, facilities, and expertise for the composite fabrication. Moreover, I am very grateful to Bill Rogers, a long-time veteran of whisker composites who taught me how to do and assisted with the ceramics processing, and who I hope will continue to enjoy his retirement for a long time. The carbon-analysis and hot-pressing contributions to this project from Lew Short are also appreciated. At Georgia Tech Research Institute, I am thankful to Mark Scott for showing me how to do coaxial measurements, and to Kathleen Silver for assistance with the Agilent and Novocontrol units. Justin Brandt was very helpful with the machining of the samples. Furthermore, I am glad to acknowledge useful discussions and general help in

the lab from Charles Capozzi, Chunqing Peng, Salil Joshi, and David Reid. I also was grateful to have the support of a Georgia Tech President's Fellowship, a Georgia Tech Research Institute Shackelford Fellowship, and Susan Bowman and Prof. Thomas H. Sanders of the Materials Science and Engineering Department.

TABLE OF CONTENTS

LIST OF TABLES

LIST OF FIGURES

LIST OF COMMONLY-USED SYMBOLS AND ABBREVIATIONS

SiC_w	Silicon Carbide Whisker
V	Voltage or Volume Fraction
DC or dc	Direct-Current
V_{dc}	Direct-Current Bias
f	Frequency
ω	Radial Frequency
E	Elastic Modulus or Electric Field
T	Temperature
z	Sample Dimension Along Applied Field
A_{cs}	Cross-Sectional Area
σ_{dc}	Direct-Current Conductivity
G	Conductance
R^2	Coefficient of Linear Regression
R	Resistance
R_b	DC Resistance of Bulk Composite
R_c	DC Resistance of Electrode Contacts
R_0	Resistance at the Zero-Bias Limit
ρ	Direct-Current Bulk Resistivity
ρ_s	Specific Resistivity of Electrode Contacts
C_s	Specific Capacitance
C_0	Specific Capacitance at Zero-Bias Limit
Φ	Symmetrical Schottky Barrier Height

κ	Bias-Partitioning Factor
p	Filler concentration or Whisker loading
p_c	Percolation Threshold
t	Conductivity Divergence Exponent (Above Percolation)
D	Relative Density
P	Relative Porosity
Δ_o	Denotes an Orientation-based Difference
d_{avg}	Average Distance Between SiC Inclusions Along a Direction
Z^*	Complex impedance
Z'	Real Impedance
Z''	Imaginary Impedance
ε^*	Complex Permittivity
ε_r^*	Complex Relative Permittivity
ε_r'	Dielectric Constant
ε_r''	Dielectric Loss
ε_s'	Static Limit of the Dielectric Constant
ε_∞'	High-Frequency Limit of the Dielectric Constant
$\Delta\varepsilon$	Relaxation Strength in Permittivity Units
τ	Relaxation Time
α_τ	Relaxation-Time Non-Ideality Factor
α_b	Exponential Non-Linearity Strength of Composite Bulk
α_c	Exponential Non-Linearity Strength of Electrode Contacts
α_i	Exponential Non-Linearity Strength of Interwhisker Interfaces
α_V	Varistor Coefficient for Non-Linearity Strength

SUMMARY

Ceramic-matrix composites of alumina and silicon carbide whiskers have recently found novel commercial application as electromagnetic absorbers. However, a detailed understanding of how materials issues influence the composite electrical response which underpins this application has been absent until now. In this project, such composites were electrically measured over a wide range of conditions and modeled in terms of various aspects of the microstructure in order to understand how they work. For this purpose, three types of composites were made by different methods from the same set of ceramic powder blends loaded with different volume fractions of whiskers. In doing so, the interfaces between whiskers, the preferred orientations of whiskers, and the structure of electrically-connected whisker clusters were varied.

In Chapter 3, it shown that Schottky energy barriers form at the junctions of the wide-bandgap semiconductor whiskers when metal electrodes are applied for measurements. These barriers were characterized on the microscopic and macroscopic level, and the gap between these different scales was bridged. Also, a modeling approach was developed for the loading dependence of the composite non-linear response which results from the barriers. In Chapter 4, the effects of significantly different types of preferred orientation are elucidated and a strong structure-property correlation is established. The effects of other structural issues on the electrical response are uncovered as well, such as those pertaining to porosity in the ceramic and the interfaces between electrically-connected SiC_w. In Chapter 5, the non-linear response model of Chapter 3 is adapted in the development of a new model for electrically-percolated clusters. This model demonstrates how loading and interfacial issues influence the cluster topology and

may result in the cluster having a non-linear electrical response. In Chapter 6, the effects of various factors on the broadband frequency dependence of the electrical response are explained and then contextualized for the electromagnetic absorber application. Such factors include whisker orientation, percolation, cluster structure, and interfaces. Finally, in Chapter 7, it is demonstrated that the interwhisker interfacial conduction mechanism differs from those which have been previously reported for other disordered mixtures of relatively conductive particles dispersed inside insulating polymer hosts. A new model for the interfacial conduction mechanism is then developed, which connects the temperature dependencies of the static- and radio-frequency electrical response and helps explain the aforementioned structure-property correlation.

CHAPTER 1

INTRODUCTION

Ceramic composites of alumina (Al_2O_3) and SiC whiskers (SiC_w) were invented in the 1980s and the initial applications of the material exploited their mechanical and thermal behavior. It is only with the recent commercial application of these composites as electromagnetic absorbers that the science underlying their phenomenal electrical response has become of great practical interest. They may be regarded as disordered insulator-conductor composites, and the literature is rich with models which describe or pertain to various facets of the electrical response of such materials. Models include those for conduction mechanisms, frequency dependencies, random and/or multi-component networks, filler anisotropy, conductor percolation, and effective medium approximations. Although the latter two types of theories have been widely applied with considerable success, they are typically plagued by a deficiency concerning a lack of attention paid to the interfaces between the conductor particles.

In this dissertation, the above concepts are applied, adapted, and unified to the extent that it was fitting and possible for the Al_2O_3-SiC_w system, which exhibits significant similarities and differences to other typical insulator-conductor systems. Also, the effects of interfaces are considered in depth in order to form a self-consistent description of the complicated electrical response of the Al_2O_3-SiC_w system. To this end, the present work thoroughly explores but does not provide complete cross-coverage of a wide multi-parameter space. The space includes whisker loading, orientation, and interface type, as well as frequency, direct-current (dc) bias, temperature, and electrode

material. A number of different models are applied and/or developed in order to explain various trends in the data in terms of different aspects of the material structure, and this resulted in a good deal of interconnectivity between the above-described parameters. The various modeling approaches are guided by theory, firmly grounded in empirical correlations, and varied in qualitative-quantitative character. In Chapters 3-5, the focus is on the direct-current and low-frequency impedance response, whereas in Chapter 6, the focus is on the permittivity response and includes high frequencies. In Chapter 7, these perspectives converge.

In this Chapter, the background needed to understand the content of this thesis and its context in the literature is given. It includes information about SiC whiskers (the key components of the composites), the history of the Al_2O_3-SiC_w system, how it relates to other composite materials, its applications, and how such composites are typically made. Then, pertinent results, concepts, and models of others which are leveraged in the in the subsequent Chapters are briefly introduced. A significant portion of the mathematics pertaining to the foundational concepts are described in the subsequent Chapters prior to being applied to the composites at hand.

1.1. SiC Whiskers

The term ‘whisker‘ is commonly used in materials science to describe a small single-crystalline rod. The novel properties of the composites investigated in this project are mainly derived from the embedded silicon carbide whiskers. Therefore, it is fitting to discuss general aspects of how such whiskers may be produced.

1.1.1. SiC Whisker Fabrication

SiC whiskers may be synthesized by various methods, such as sol-gel, plasma deposition, chemical vapor deposition, and pyrolysis of agricultural waste. The latter method seems to be preferred for industrial-scale production of SiC whiskers. Generally, agricultural waste containing both silica (SiO_2) and carbon is used. Waste sources include rice hulls, coconut shells, bean-curd refuse, sugarcane leaf, and rice straw. Silicon carbide whiskers can also be fabricated from mixtures of silica and carbon powders, carbon and silicon halides, polymer precursors, or other materials like silicon nitride. In addition to SiC whiskers, the synthesis process also usually produces some amount of (usually unwanted) non-whisker SiC particles which varies depending on processing details. After synthesis, whiskers are often cleaned by ultrasonication[28] and/or acid washing[28,29] to remove contamination of particulates[30] and trace amounts of amorphous silica which often remain on the whiskers.[28]

Synthesis from rice hulls may be conducted in the 1000-1500°C range in an inert gas ambient,[28] e.g. N_2. In another work, a 700-800°C carbonization pretreatment of the organic waste was performed to increase carbon surface area before conducting the 1400°C pyrolysis in argon.[31] Reaction occurs when silica (SiO_2) undergoes a carbothermic reduction to SiC. The overall reaction is given by Reaction 1.1 and the related sub-reactions (1.2-1.5) are:

$$SiO_2 + 3C \rightarrow SiC + 2CO_{(g)} \quad (1.1)$$

$$SiO_2 + C \rightarrow SiO_{(g)} + CO_{(g)}) \quad (1.2)$$

$$SiO_{(g)} + 2C \rightarrow SiC + CO_{(g)} \quad (1.3)$$

(1.3)$SiO_{(g)} + C \rightarrow Si + CO_{(g)}$ (1.4)

$Si + C \rightarrow SiC$ (1.5)

It is believed that silica is first reduced to gaseous SiO (Reaction 1.2) and then forms SiC either by a replacement reaction (1.3) or through the continued reduction to Si (1.4) and subsequent addition reaction (1.5).[28] The initial reaction between carbon and the silica (or silica derivative) depends upon the physical contact between the two. Ideally, the silica should be intimately mixed with the cellulose. As the reduction reaction proceeds, the intimate contact between silica and carbon is lost and further reduction of silica depends mainly on the gas-phase carbon source. Certain waste, such as coconut shells, are believed to produce more carbonaceous vapors (e.g. CO) for more efficient carbothermal reduction and higher yield. It is believed that the porous cellular structure of rice hulls facilitates vapor-phase transport. To achieve high-yield, it seems important to achieve a certain balance of silica:carbon in the starting materials.[28,31]

A small amount of metal catalyst may be mixed in with the source materials for SiC whisker synthesis. This can be done by soaking the raw ingredients in an appropriate metal-salt solution. Examples of metals include iron, Pd, Ni, or Co. Catalysts generally promote whisker growth by the vapor-liquid-solid (VLS) mechanism, which is fairly well-established in the growth of "1-dimensional" materials such as nanowires and nanotubes.[32] For SiC whiskers, the theory implies that Si- and C-containing vapors dissolve into the molten metal catalyst balls and SiC precipitates when the solution becomes sufficiently supersaturated. This is then followed by unidirectional growth in the energetically-favored crystallographic direction. However, it should be noted that it is possible to grow SiC whiskers without such catalysts and these are believed to grow by a

vapor-solid mechanism.[31] Such whiskers tend to exhibit pointed tips at the ends and are not capped with catalyst balls, unlike VLS-grown whiskers.

1.1.2. SiC Whisker Structure

Figure 1.1a shows an image of as-grown SiC whiskers. Typically, SiC whiskers have lengths and diameters on the order 5-50 μm and 0.2-1.0 μm, respectively. The crystal structure of SiC may be described by a polytype. Broadly, the SiC polytypes may be categorized as β (cubic, i.e. zinc blende) or α (non-cubic, e.g. hexagonal). However, there are many other SiC_w structural characteristics to consider. Generally, the whisker morphology and structure of the SiC particles results from the growth process.[1,2,33]

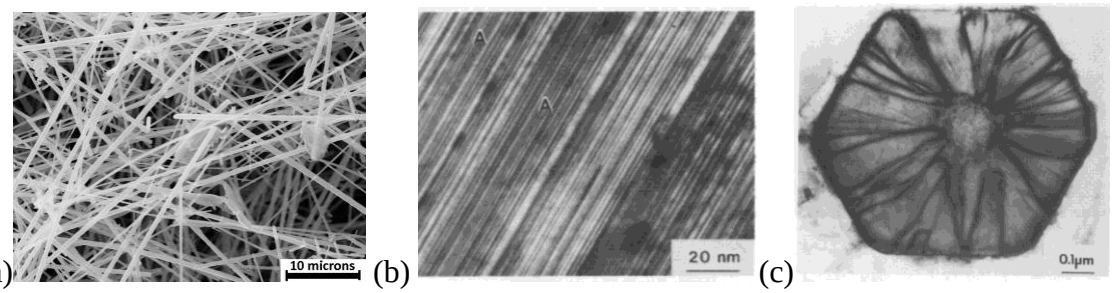

Figure 1.1. Electron micrographs of (a) loose as-grown SiC whiskers, [34] (b) planar defects perpendicular to the length of a single SiC whisker, and (c) a whisker cross-section showing partial dislocations and core cavities.[1,2]

The structure and defects of silicon carbide whiskers made from rice hulls have been studied by transmission electron microscopy and this provided insight into their atomic- and nano-structure.[1] The whiskers were found to have grown in the <111> direction and exhibited a high density of planar defects such as stacking faults and twins on the {111} planes. As shown in Figure 1.1b, the spacings between planar faults in SiC_w may be as small as a few nm. The presence of these planar defects means that the whisker

structure may be described as a complex mixture of α and β polytypes arranged in thin lamellae perpendicular to the growth axes. However, it is common for whiskers to be reported as being of a single polytype[9,21,35] based on x-ray diffraction phase identifications and reports from the manufacturer.

Other common SiC_w defects include core cavities and partial dislocations,[1] as shown in Figure 1.1c. The size range for core-cavities and voids was 2-20 nm. Whiskers were found to have hexagonal faceting, likely traceable to anisotropy in the surface energy during SiC crystal formation. Other studies indicate that as-fabricated whiskers may contain small pockets of silicon oxycarbide glass.[36] Generally speaking, whisker structure and arrangement can have significant effects on composite properties. Rice provides a more general review of ceramic (and metal) whisker growth and points out that for general growth of inorganic crystals, the morphology and growth habits are affected by impurities in the growth environment.[5]

1.1.3. Health Risk of Loose SiC Whiskers

Finally, it should be noted that the loose whisker morphology (i.e. when the whiskers are not incorporated in solid composites) gives rise to a serious respiratory health risk and inhalation of loose SiC whiskers can lead to deadly lung diseases.[37,38] Generally, the elongated shapes (high aspect ratio), small sizes (micron level), and the facts that they are chemically inert and cannot be readily removed by natural human-body processes make SiC whiskers behave similarly to asbestos when in the lungs. Therefore it is of utmost importance to take care when working with loose whiskers or whisker-laden powders and to avoid stirring them up into the air. Also, one should always employ engineering controls (e.g. filtered respirators, specialized hoods) to minimize human

inhalation and exposure during handling. That said, current safety technology appears to be sufficient for managing the risk if one works carefully.

1.2. Composite Materials

Before specifically focusing on a specific type of composite, it is useful to obtain a sense of how the ceramic-matrix composites (CMCs) of the present work fit into the broader context of composite materials. These include polymer-matrix and metal-matrix composites (PMCs and MMCs, respectively), where the term 'matrix' denotes the majority phase in the composite mixture. For MMCs, hard inclusions such as SiC_w may be incorporated into the metal matrix in order to improve its strength and stiffness[39]; electrical conductivity is likely sacrificed. In polymer matrices, continuous fibers are often layed up in an organized fashion to improve strength and stiffness[40] and discontinuous fibers or particulates may be added to improve both mechanical[41] and electrical properties.[7,42] For CMCs, the purpose of including second phases has commonly been aimed at improving the fracture toughness of the brittle matrix.[43]

In all cases, the processing method used to create the composites as well as the models which have been developed to describe structure-property relationships thereof depend on the (desired) distribution of the different phases in the final microstructure. Common types of phase distributions are shown[3] in Figure 1.2. When phases are arranged as continuous layers (laminates) or as continuous fibers in a matrix, rules of mixtures are often used to describe the properties. Alternatively, when the second phase is a discontinuous and dispersed throughout the matrix in a disordered fashion, it may be called 'filler' or 'reinforcement', depending on whether one is interest in electrical or mechanical properties, respectively. For such materials, effective medium theory[10]

(EMT) or micromechanics models[39,44] are commonly used to predict the electrical and mechanical responses of the mixture, respectively. Both EMT and rules of mixtures are described in Chapter 6 prior to being invoked.

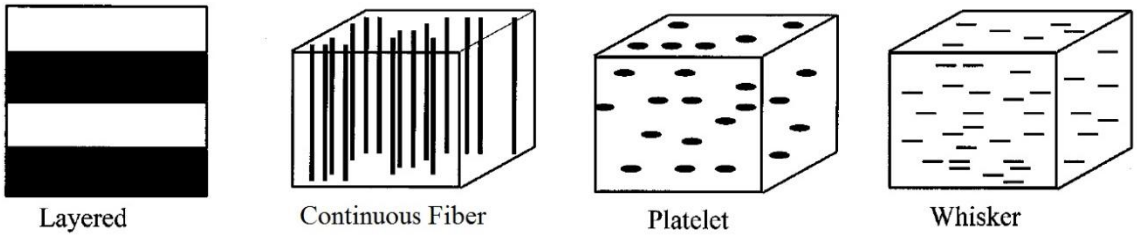

Figure 1.2. Common types of composite structures. Modified from Ref. 3.

1.3. Ceramic Processing Methods

The fabrication of ceramic composites which take advantage of property enhancements from dispersed fillers (e.g., SiC_w) typically has a great deal in common with conventional ceramic processing methods. Those methods which are relevant to the work of the present thesis are now described. Additional information and other approaches to ceramic fabrication may be found elsewhere.[4,5,45]

1.3.1. Powder Processing

The sizes, shapes, and surfaces of the discrete ceramic particles forming a powder significantly impact one's ability to process and densify the powder into a useful solid ceramic part. Due to space-filling limitations for fixed size spheres (which isotropic particles may be approximated as), it is generally desirable to have a distribution of particle sizes. Finer particles are sometimes preferred for processability, e.g., for extrusion,[5] and larger agglomerates can be detrimental. Mesh screens may be used to

control the maximum particle size and separate larger particles or agglomerates for removal or division into smaller particles via pulverization.

Ball milling is a commonly-used process in material processing which reduces the average particle size, results in a size distribution, and mixes multi-component powders. It involves deformation and fracture of particles of a powder via impact of milling media (e.g., ceramic spheres) moving at significant velocities (energies) within a closed container holding the powder sample. Milling may also be used to mix multi-component powders and break up anisotropic phases such as whiskers. In previous studies of SiC_w loaded composites, including one considering samples examined in this dissertation, the ball-milling process resulted in a lognormal distribution of whisker lengths which peaked around ~10 μm.[6,46]

A simple tumbling ball mill consists of a capped and sealed vessel loaded with the sample powder and the milling media which is placed on rotating pins and whose axis remain stationary such that the vessel rotates. The spherical media often has diameters on the order of ~1 cm and is chosen based on the material to be milled. The speed of the vessel rotation is tuned in order to stimulate a continuous cascade of the milling balls onto the sample powder resulting from them "climbing" the wall of the container and then falling onto the powder below. If the rotation speed is too slow, gravity will hold the balls at the bottom of the jug and they will not strike the powder with significant force. If the speed is too fast, the centrifugal force results in the balls sticking to the side of the container and the milling action is similarly reduced. Although it is fairly easy to execute as a user, ball milling is a complicated process from a scientific standpoint and depends on several parameters besides the rotation speed. These include the size, shape surface,

and material properties of the vessel, the degree to which the jug is filled, the number of media, the material properties of the sample powder and media, the temperature and time, and the (liquid or gaseous) ambient inside the vessel.[47]

1.3.2. Dry Pressing

Dry pressing may be used to consolidate loose powders into green bodies having simple shapes. It involves filling the die with the powder and compacting the powder inside the die via uniaxial pressure from the top and bottom punches. During compaction, the densification occurs via particle flow, which eliminates formerly-empty space. Dry-pressing pressures may be as high[4] as 300 MPa and vary depending on the material being compressed, the desired level of porosity in the final part, and subsequent processing. After dry pressing, the compacted (and fragile) green body is then carefully ejected from the die for pressureless sintering or, alternatively, sintered during subsequent hot pressing. A simple diagram demonstrating the basic steps of the dry-pressing process is shown in Figure 1.3.

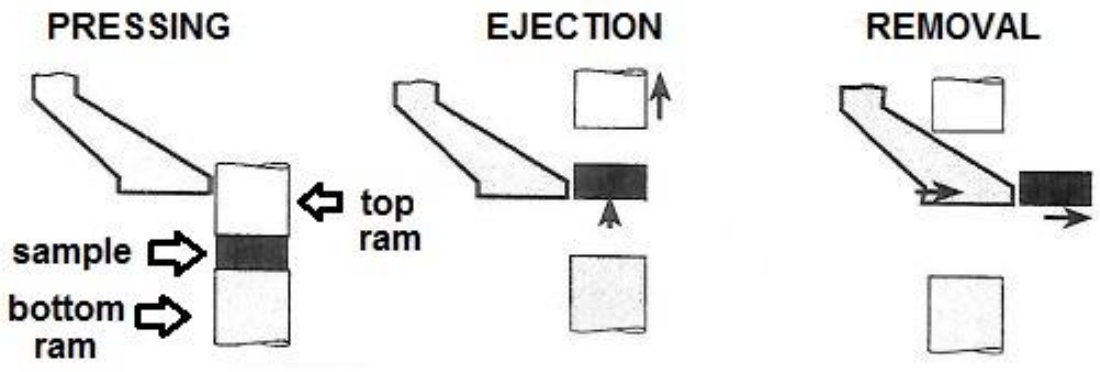

Figure 1.3. Dry-pressing processing. After filling the die, the sample is then pressed, ejected, and removed. Modified from Ref. 4.

1.3.3. Extrusion Processing

For the extrusion of technical ceramics, binders are uniformly mixed with the dry ceramic powder in order to provide plasticity similar to that of natural clays.[5] Binders must also provide sufficient strength for the handling of otherwise-fragile green bodies. Binder systems often include water, a flocculant (e.g., methylcellulose or polyvinyl alcohol), a coagulant (e.g., $CaCl_2$), and a lubricant (e.g., stearates or oils). After degassing the ceramic-binder mixture, extruders commonly use a hydraulically-powered ram to push the mixture through the enclosing metal-barrel and the die at the other end at typical pressures of a few to 15 MPa. The basic concept of extrusion is demonstrated in Figure 1.4.

The presence of submicron ceramic particles tends to facilitate the process. Also, the extrudate tends to be anisotropic, e.g., the ceramic grains and the binder tend to exhibit preferred orientation and tubular structure aligned with the extrusion direction, respectively. The degree of preferred orientation depends on the anisotropy of the particles and the extrusion lateral dimensions and pressures.[5]

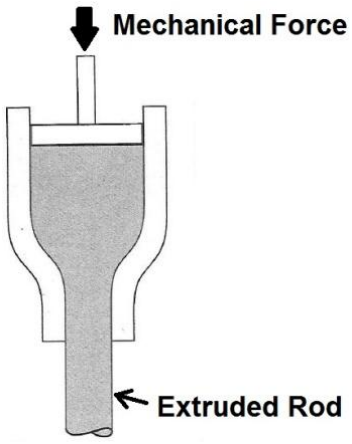

Figure 1.4. The basic concept of extrusion. Modified from Ref. 4.

After extrusion, the binders must be removed prior to sintering. Water and mineral oil may be slowly evaporated from the extrudate over long times at low temperatures, but other more stable organics of the binder system must be removed by a burnout process. This is typically conducted in an oxidizing ambient at temperatures on the order of 500°C. Notably, binder constituents which may be removed at lower temperature allow for the enhanced removal of the remaining binders by facilitating the ingress of the burnout atmosphere and the outward flow of the burnout products in the green-body pore structure. Care must be taken during binder removal to avoid or minimize cracking and pore generation from shrinkage, constrained outgassing, and differential thermal expansion in the ceramic-binder mixture.[5]

1.3.4. Sintering

Sintering is an ancient process in which adjacent discrete particles of a material become fused together at an elevated temperature beneath the melting point of the material. It is commonly used for ceramics due to their high melting points. The driving force for sintering is the reduction of surface energy, and the process may take place by a variety of kinetic pathways, depending on availability. These include surface diffusion, evaporation and condensation, viscous flow, and plastic deformation.[45] The latter can be expected to be more significant when pressure is applied during sintering. Densification begins with necking between discrete particles, and its rate depends on the particle size, viscosity, surface energy, and temperature.[45] Oxides tend to be easier to sinter than non-oxides, and oxides sintering additives are commonly added into the sample[5] in amounts varying from a tenth of to a few percent of the sample composition to improve densification. The additives function by inducing the presence of a liquid phase which

serves to facilitate mass transport, and thus, densification. Sintering tends to be inhibited by the presence of anisotropic phases such as whiskers, fibers, or platelets.[5]

1.3.5. Hot Pressing

In hot-pressing, a green body which has already been formed at room temperature from a loose powder is subsequently sintered at elevated temperature during the simultaneous application of a pressure. Unless designated otherwise, the term usually means that pressure is applied uniaxially. This process allows for the easier and faster achievement of theoretical or near-theoretical density at temperatures 100-200°C lower than those typically used for pressureless sintering.[5] The elevated temperature provides for the usual sintering mechanisms and also facilitates plastic flow in the powder under pressure, which aids densification.[4] A hot press is made of a press frame and a ram which is used to compress powder in a die, which is surrounded by a furnace. Figure 1.5a diagrams a typical hot-pressing setup.[4]

Die material selection is important and dies of graphite are often used (in non-oxidizing ambients) since it is compatible with many other materials and offers ~3000°C temperature capability.[5] Spacers may be used within the die to make multiple samples at the same time, as shown in Figure 1.5b. Furnaces commonly operate by resistive heating with graphite or refractory-metal elements. Pressure is often applied gradually in order to allow outgassing of the powder. Accurate temperature measurement of the part being pressed with a thermocouple of pyrometer is difficult since it is fully encased within the die. Ceramic composites with dispersed whiskers (e.g., SiC_w) are commonly densified by hot-pressing[9,17,48,49] because these phases tend to inhibit densification during pressureless sintering.[5,50]

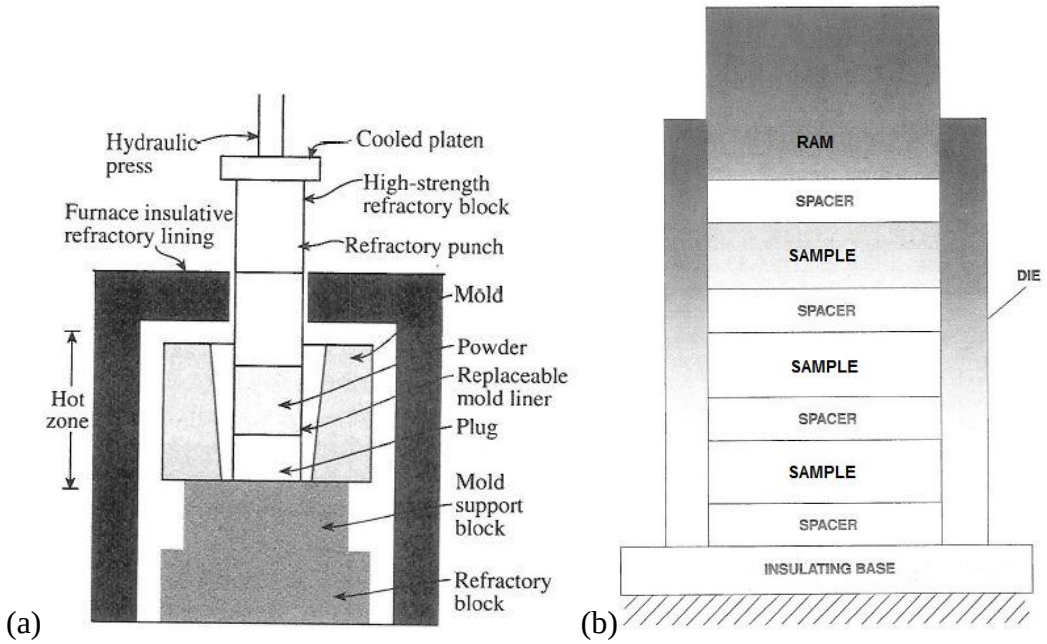

Figure 1.5. (a) Typical hot-pressing configuration, from Ref. 4. The frame is not shown. (b) Diagram showing how multiple parts may be made simultaneously by using spacers within the die.[5]

1.4. Historical Background of the Alumina-SiC_w Composite System

In the early 1980s, researchers at Oak Ridge National Laboratory developed the first ceramic composites reinforced with dispersed silicon carbide (SiC) whiskers.[43] The inclusion of a relatively small volume fraction of SiC_w in the aluminum oxide (Al_2O_3) matrix had a large impact on the properties and eventually allowed for interesting applications which otherwise would not have been possible with Al_2O_3 alone. For example, the whisker form of SiC made the composites exceptionally non-brittle compared to conventional monolithic ceramics due to advantageous effects on mechanical stress distributions within the composites. The invention of the composites roughly coincided with the U.S. Department of Energy's development of the 1983 "Ceramic Technology Program for Advanced Heat Engines."[51] A few years earlier,

President Carter pushed for the development of more fuel-efficient automobiles to mitigate the energy problems of the United States[52] which were earlier noted by President Ford.[53] Ceramic engines operating at high temperatures have the potential for high energy efficiency due to the thermodynamics of engine operation[54] and the whisker-reinforced composites were candidate materials for this purpose. However, subsequent research found that significant degradation of the whisker-laden composites occurred during extended exposure to stress and air at high temperatures due to reaction of the SiC whiskers, leading to extensive deformation by creep phenomena.[55-67] Such structural degradation was correlated to worsening of mechanical properties and the development of Al_2O_3-SiC_w composites for engines apparently stalled. However, Al_2O_3-SiC_w composites have been found to be useful and commercially viable in other applications.

1.5. Modern Applications of the Al_2O_3-SiC_w Composite System

The incorporation of SiC_w into an alumina host matrix has generally provided significant increases in fracture toughness, thermal conductivity, and electrical conductivity compared to single-phase Al_2O_3. In modern times, the main commercialized applications of these materials are as inserts in cutting tools and as substrates for microwave-heating and cooking. The more well-established application of the composites in cutting tools, which is discussed first, relies on the enhancement of the former two properties, whose enhancement is discussed elsewhere. The application of Al_2O_3-SiC_w as an electromagnetic absorber in microwave heating and cooking is of greater interest in the context of this thesis, which focuses on the electrical behavior.

1.5.1. Cutting Tools

Images of Al_2O_3-SiC_w cutting-tool inserts are shown in Figure 1.6a. Cutting tools usually must be hot-pressed to achieve full density and the necessary thermal-mechanical properties. Such tools are cost-effective for shaping difficult-to-machine metals such as steel (Figure 1.6b) and Ni-based superalloys for turbines in aerospace applications. For the cutting tool application, one is generally interested in the following properties of the composite: fracture toughness, thermal conductivity, abrasive wear resistance, chemical inertness, and thermal shock resistance (which depends on fracture toughness and thermal conductivity). Compared to conventional ceramics, Al_2O_3-SiC_w composites provide improvements (increases) in all the above properties except chemical inertness. During cutting with tools of Al_2O_3-SiC_w, damage is accompanied by whisker toughening mechanisms and reaction may occur between SiC and Fe. This generally limits cutting of ferrous materials to lower speeds.[68,69]

Notably, the general cutting process is complicated and depends on many factors,[70,71] including the defect distribution in the tool, tool shape, and the properties of the piece being cut. Also, there are different types of tool degradation which depend on the location on the tool. For SiC_w-reinforced tools, literature suggests that the residual stresses in the microstructure are rather important in determining mechanical and wear response, e.g. at the sample surface and at whisker-matrix interfaces.[69,72] It has also been found that wear performance relates to sample orientation relative to the processing direction and fracture toughness at the microstructural level, not the fracture toughness of the bulk sample.[73] Moreover, one may use a lamination process to increase control of the

Al_2O_3-SiC_w microstructure and thus improve cutting tool performance.[74] Also, tools employing specially-coated whiskers can provide increased toughness, tool life, and cutting speed, e.g., those from Greenleaf Corporation.

(a) 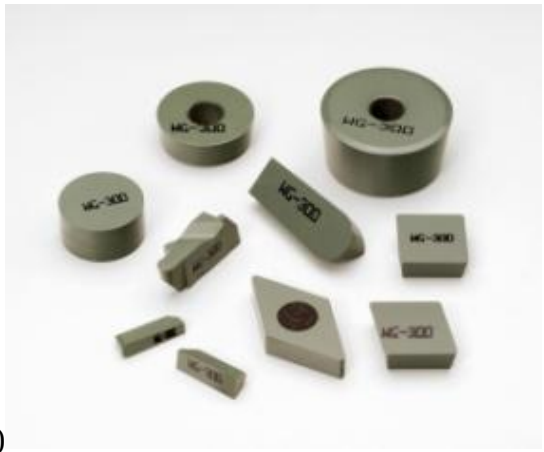 (b) 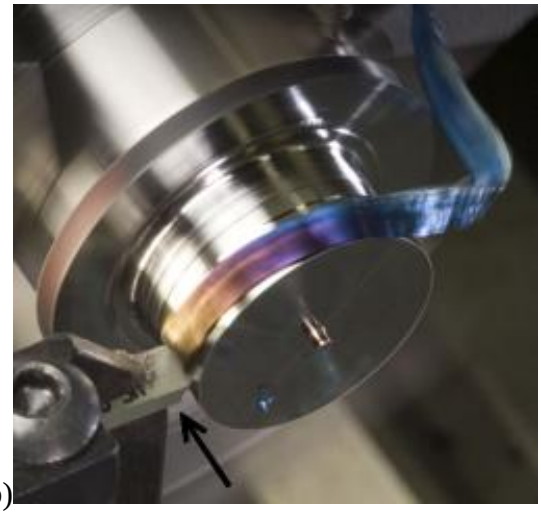

(c)  (d) 

Figure 1.6. Applications of Al_2O_3-SiC_w composites: (a) cutting-tool inserts, (b) insert (marked with arrow) machining hardened tool steel, (c) microwave flatstone, (d) panini sandwich speed-grilled with Silar© technology. Images provided by Greenleaf Corporation in Saegertown, PA (a,b) and Advanced Composite Materials LLC in Greer, SC (c,d).

1.5.2. Electromagnetic Absorbers for Microwave Heating and Cooking

The role of these composites as electromagnetic absorbers is the motivating application for this thesis, and is currently being led by Advanced Composite Materials LLC in Greer, SC.[35] Their Silar© whisker-embedded composites are useful substrates for cooking food and have been NSF-51 approved for food contact.[75] For this application, density and mechanical properties are not as critical and composite rods or bars ~1 foot long and ~½ inch wide are made by extrusion and pressureless sintering. Several rods are then arranged with a metal clip to form a grill or flatstone like that shown in Figure 1.6c which is then placed in a microwave oven having a clip-compatible design. Food products such as fresh dough pizza and panini sandwiches can then be cooked faster than with conventional cooking while still yielding high quality results (e.g. crispy crust, grill marks, etc.) via application of microwave radiation in the cavity. An example is shown in Figure 1.6d. The microwaves are believed to preferentially heat the ceramic composite compared to the food due to the latter having a reduced dielectric loss compared to the former at the frequencies of interest, i.e., 915 or 2450 MHz for common microwave ovens. The dielectric loss is generally proportional to the microwave heating rate.[76]

For solid food, the dielectric loss can be expected to follow mainly from moisture and oil content.[76-78] Regarding the composites, one study[77] found that loss values are ~180 times greater for SiC compared to Al_2O_3. The literature suggests that substrate thermal conductivity, thermal runaway, and thermal shock response might influence food heating during cooking and the lifetime of the parts, respectively.[77-82]

Quantrille has analyzed the heat transfer into the food during cooking and reported results of various microwave heating tests.[78,82] The ceramics heat quickly, e.g. at ~2.3-4.6

°C/s from 900 W incident on powders blends of 7.5-15 wt% SiC_w in Al_2O_3. Food heating results from three processes: (1) dielectric loss in the food itself (2) air convection from the ceramic and (3) thermal conduction across the thermal gradient at the ceramic-food interface. Due to (3) and the fact that food moisture content declines as cooking proceeds, it is possible to sear the food with grill marks at the end of cooking. It was found that pizzas and paninis could be "grilled, toasted, and cooked to perfection" in ~80 and ~90 seconds, respectively.[78]

1.6. Microstructural Considerations: Percolation and Anisotropy

For dispersed conductive fillers in any type of insulating matrix (e.g., polymer or ceramic) and the electromagnetic absorber application, the phenomenon of percolation is highly relevant. In addition to other natural phenomena, percolation describes how a sample-spanning cluster of interconnected fillers develops from the continued addition of discrete fillers to an insulating matrix. This occurs when the volume fraction of fillers p reaches or exceeds the (critical) percolation threshold, p_c. Solutions for p_c are available for models in which the problem is recast in the form of site or bond percolation on various geometrical lattices. For example, $p_c = 0.5$ for bond percolation on a square lattice or site percolation on a triangular lattice.[83] Generally, the values of site and bond percolation are different for each type of lattice, e.g., $p_c \approx 0.593$ for site percolation on a square lattice,[83] e.g., Figure 1.7a. The above values of the percolation threshold for site percolation are when connections are defined by adjacent sites; when more distant connections are allowed (e.g., second or third nearest neighbors), the percolation threshold decreases.[83]

Regarding Figure 1.7a, it is easy to imagine that percolation of white pixels along a particular direction could be achieved with the lowest possible ratio of white-to-black in the overall grid if the white pixels were arranged in a straight line along the direction of interest. This fact relates to the percolation of stick-like fillers, e.g., Figure 1.7b.

(a) 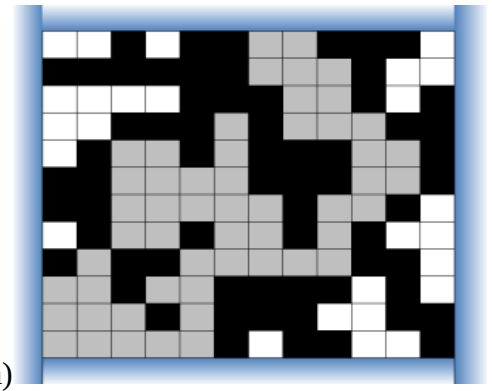 (b) 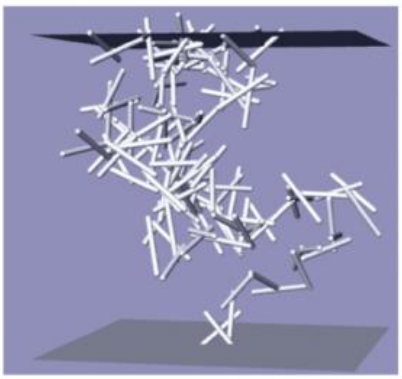

Figure 1.7. Top-to-bottom percolation pathways in models of greatly-differing complexity: (a) Binary black-and-white composite on a square grid, where white-site percolation is darkened to gray.[84] (b) Three-dimensional percolation of whiskers based on structural measurements in a real composite.[6]

Whiskers can be considered a subset of 'sticks,' a general term for an anisotropic structure elongated along one direction with no implications for crystallinity. For sticks having lengths 2*A* and diameters 2*B*, the stick aspect ratio[7] is *A*/*B* and is inversely related to the percolation threshold p_c, i.e.,

$$p_c \propto B/A \tag{1.6}$$

Figure 1.8a demonstrates this with experimental data from chopped-fiber composites.[7,85] This relation has been concluded by several investigators and can be proven with an excluded volume concept.[6,86] For ensembles of sticks in three-dimensional space, simulations indicate that increasing alignment along a given direction increases the

percolation threshold, as shown by simulation results in Figure 1.8b. This figure also shows that the effect is stronger for sticks of lower aspect ratio.

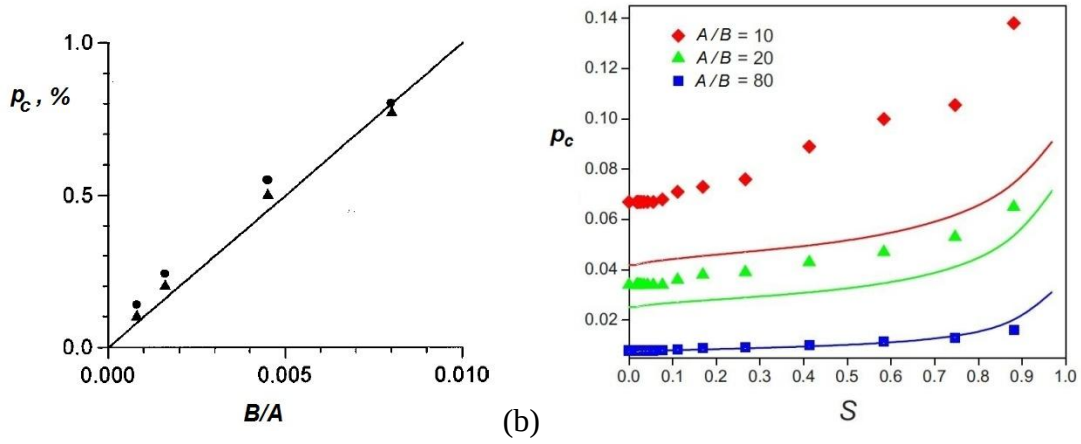

Figure 1.8. (a) Linear dependence of percolation threshold (p_c) on inverse aspect ratio (*B*/*A*). Modified from Ref. 7. (b) Dependence of the percolation threshold on the uniaxial alignment factor (*S*) of ensembles of sticks, which varies from 0 (random alignment) to 1 (perfect alignment), for different values of aspect ratio. Modified from Ref. 8.

The dependence of percolation on alignment highlights the relevance of the unidirectional nature of the above-described ceramic forming methods, which tend to result in anisotropic structures.[5] Hot-pressing induces preferred orientation of SiC_w such that the microstructural texture may be described by a symmetry axis along the pressing direction.[87,88] Conversely, percolation of SiC_w is also known to affect the results of the processing and tends to inhibit the densification of composites due to the formation of a rigid interlocking network.[50]

The orientation distribution of SiC_w may be determined by x-ray diffraction,[9] as shown in Figure 1.9. However, it is not clear how to quantitatively relate such distributions to the measured electrical response when the orientations are not incrementally varied in a controlled fashion. Perhaps the most straightforward to do this

is during extrusion. In one study, the length/diameter ratio of the extrusion needle was linearly proportional to a unitless orientation factor determined by a stereological method.[46]

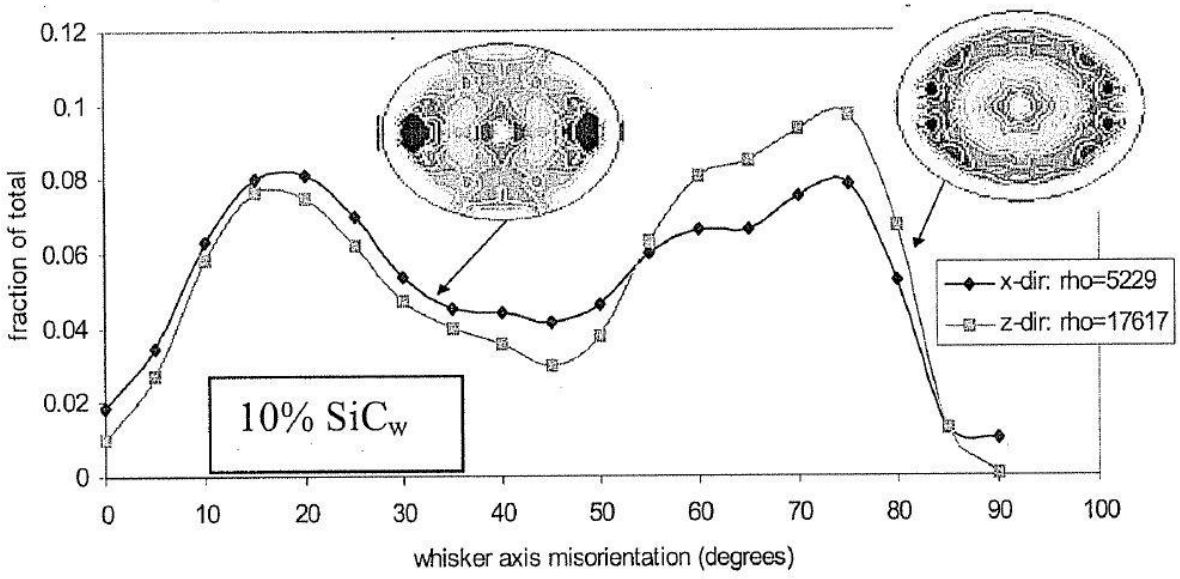

Figure 1.9. Orientation distribution of SiC_w and pole figures from x-ray diffraction analysis on surfaces of hot-pressed Al_2O_3-SiC_w composites.[9]

Finally, it is worth noting that information about length-orientation coupling is lost in such isolated characterizations of the orientations. This was established via characterization of the trivariate length-radii-orientation distribution with a comprehensive stereological method and may be explained by a given force translating into a larger torque for longer whiskers.[6,89]

1.7. Electrical and Electronic Considerations

1.7.1. Electrical Formalisms

When a voltage $V(\omega)=V_{amp}\sin(\omega)$ which varies sinusoidally with radial frequency ω is applied to a sample, the current generally lags the voltage by a phase shift (θ), i.e., $I(\omega)=I_{amp}\sin(\omega)$. Here, subscript '*amp*' denotes the amplitude of the sinusoidal signals. The impedance (Z^*) of the sample is a complex number defined by

$$Z^* = V(\omega) / I(\omega) \equiv Z' - j\,Z'' \qquad (1.7)$$

where $j = (-1)^{1/2}$, Z' and Z'' are the real and imaginary parts of the impedance, respectively, and the sign of Z'' is a matter of convention. At the low-frequency limit $\omega\rightarrow 0$, Z'' tends to zero and the real impedance (Z') is equal to the dc resistance, which may be converted to a materials property by normalizing over the geometry of the sample. For example, at this limit the dc resistivity and dc conductivity are equal to ($Z' A_{cs} / z$) and ($z / Z' A_{cs}$), respectively, where A_{cs} is the sample cross-sectional area and z is the sample dimension in the direction of the applied electric field, i.e., the thickness or length. The complex admittance is the inverse of the impedance and also has a real and imaginary part,

$$Y^* = 1 / Z^* = Y' + jY'' \qquad (1.8)$$

and the ac conductivity follows from geometrical normalization of the admittance. The complex permittivity (ε^*) is also inversely related to the impedance and has a real and imaginary part,

$$\varepsilon^* = z / j\omega Z^* A_{cs} = \varepsilon' - j\varepsilon''. \qquad (1.9)$$

1.7.2. Conductivity Percolation

The percolation of a conductive filler having conductivity (σ_0) in an insulating matrix of conductivity (σ_1) results in a large increase in the effective conductivity (σ_e) of the composite. This may be called an insulator-conductor transition. When the conductivity of the filler (σ_0) is finite, σ_e diverges at the percolation threshold and increases via a power law as p is further increased above p_c. Assuming that the conductive fillers have resistance-free connections,

$$\sigma_e \propto \sigma_0 (p - p_c)^t \qquad (1.10)$$

where t is an exponent[10] which may be theoretically related to other aspects of the transition.[83] From this assumption, it follows that the strength of the percolation transition depends on the filler/matrix conductivity ratio (σ_0/σ_1), as shown in Figure 1.10b.

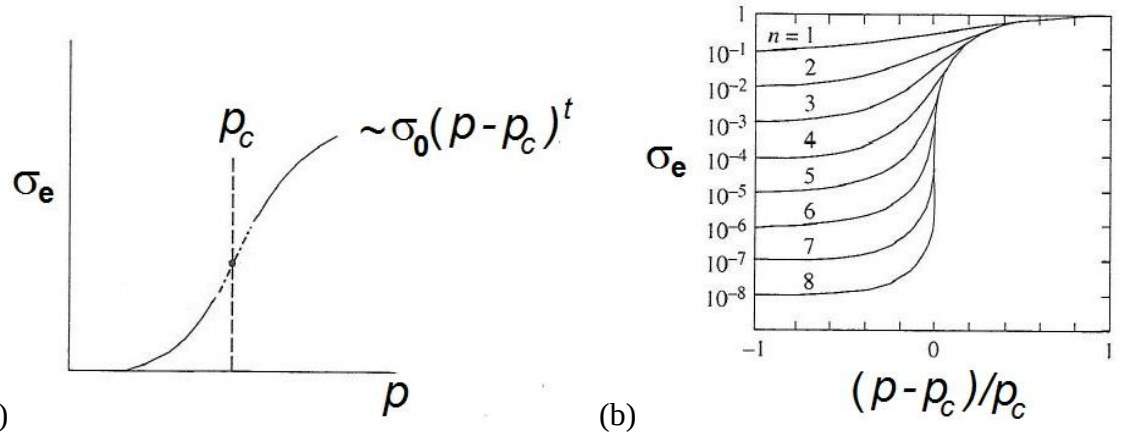

Figure 1.10. (a) Divergence of the conductivity at the percolation threshold (plotted on linear scales). (b) Effect of the logarithm of the filler/matrix conductivity ratio $n = \log(\sigma_0/\sigma_1)$ on the strength of percolation transition. Modified from Ref. 10.

Notably, many real insulator-conductor composites are well-described by Relation 1.10 with *t* as a largely-empirical fitting parameter which varies widely among different systems and has been observed to depend on microstructural orientation.[3]

1.7.3. Conductivity Anisotropy in Percolated-Stick Composites

Since anisotropy influences percolation and percolation strongly affects electrical response, it is not surprising that the electrical response of conductive-stick loaded systems are often anisotropic. Figure 1.11 shows the complex impedance response geometrically normalized to resistivity for hot-pressed alumina composites loaded with 20% SiC_w measured parallel and perpendicular ("perp") to the hot-pressing direction (HPD). For these samples, the whiskers axes tended to be aligned perpendicularly to the HPD in order to accommodate compaction. It can be seen that the resistivities are smaller for the perpendicular direction compared to the HPD.[9] Figure 1.12 shows that the logarithm of the difference in dc resistivity measured along the different directions decreased approximately linearly with the volume fraction of SiC_w, thereby indicating increasing isotropy.

The effects of preferred orientation have also been explored via simulation. In one study,[8] the effective conductivity of percolated networks of sticks in three-dimensional space was simulated assuming that the resistances of the sticks, matrix, and stick-interfaces were zero, infinite, and 1 Ω, respectively. The crux of the study was the incremental variation of the preferred alignment of the sticks (as quantified by a unitless alignment parameter, S) from randomly aligned (S=0) to perfect uniaxial alignment (S=1). It was found that the conductivity increased slightly with the degree of preferred alignment up to a maximum, and then decreased with increasing alignment after that until

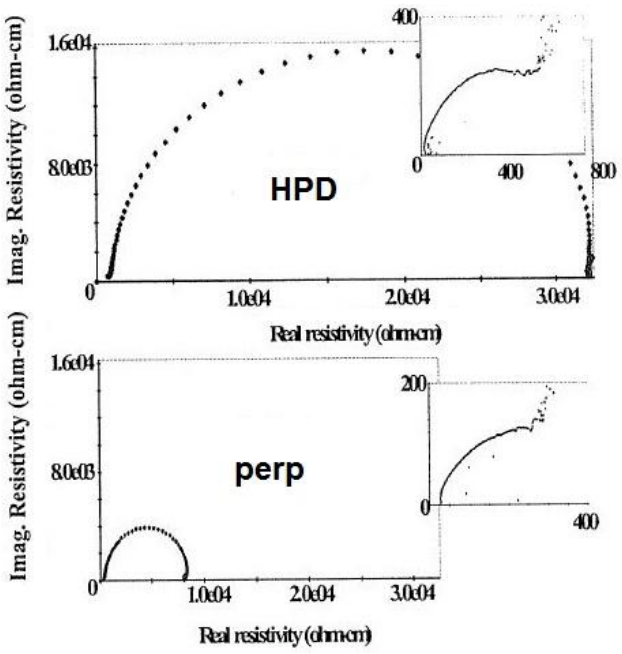

Figure 1.11. Complex impedance data normalized to resistivity for hot-pressed Al_2O_3 composites with 20% SiC_w. The field was applied parallel (top) and perpendicular to (bottom) the HPD and the insets show an expanded view of the high-frequency data. Modified from Ref. 9.

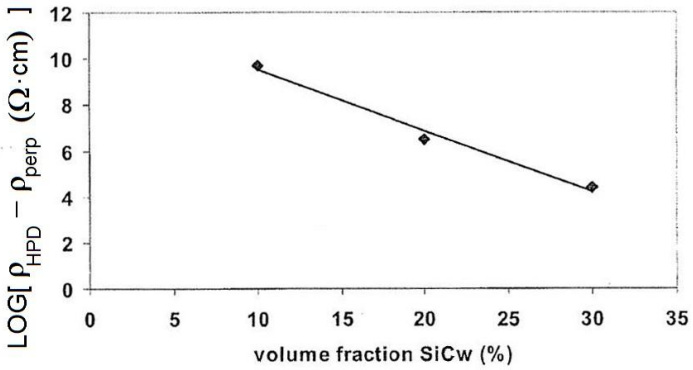

Figure 1.12. The logarithm of the difference in dc resistivity measured along the HPD and the perpendicular (perp) direction for Al_2O_3-SiC_w composites as a function of SiC_w loading. Modified from Ref. 9.

connectivity was completely destroyed. Figures 1.13a and 1.13b show this for different values of the stick aspect ratio, i.e., 10 and 20, respectively. Notably, these simulation

results are contradictory to experimental results on SiC_w-loaded Si_3N_4 composites,[90] for which the conductivity monotonically increased with a similarly-defined alignment parameter from ~0.46 to ~0.87.

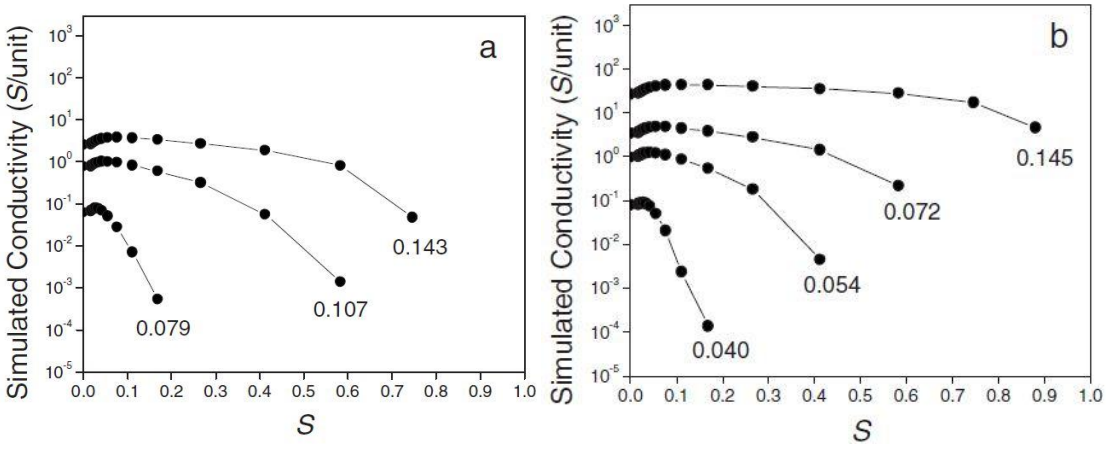

Figure 1.13. Simulated conductivity of three-dimensional conductive-stick networks as a function of the degree of preferred uniaxial alignment[8] for aspect ratios of (a) 10 and (b) 20.

It can also be seen that the sensitivity to alignment is stronger when the volume fraction of sticks (marked next to each curve) is lower. This result may help explain the trend of Figure 1.12 Furthermore, the effective conductivity at a given volume fraction was larger for sticks of higher aspect ratio, as can be seen by comparing Figures 1.13a and 1.13b, e.g., at the 0.079 and 0.072 volume fractions.

1.7.4. Effects of Interfaces on the Simulated Conductivity of Percolated-Stick Networks

The result of the conductivity exhibiting a maximum as a function of preferred alignment was reproduced in a simulation of conductive sticks in a two-dimensional insulating matrix.[11] In this work, it was also found that the strength of the divergence of conductivity with composition above percolation was significantly increased when the

network conductivity was limited by the interstick interfaces rather than the intrastick conductivity. This is shown in Figure 1.14 for the case of randomly aligned sticks; for the case of sticks preferentially aligned along an axis, similar results were obtained for the conductivity both parallel and perpendicular to the axis.[11]

In another work,[6] different volume fractions of conductive sticks described by the stereologically-measured trivariate length-radius-orientation distribution[89] of a 20 vol% SiC_w Al_2O_3-composite sample were placed in three-dimensional simulation space. Resistor networks were generated by assuming a constant shorting distance through which SiCw were electrically connected through the matrix such that the simulation matched the experimental percolation threshold of 9 vol% SiC_w. The interfacial resistance between the whiskers was assumed to be independent of SiC_w loading and was effectively determined by matching the effective conductivity of the simulated network to the experimentally measured conductivity at 10 vol% SiC_w. This was then input into simulations for higher SiC_w loadings and it was found that the simulated conductivities significantly exceeded the experimental values (Figure 1.15). This discrepancy suggests that the conductivity was limited by a factor which was not accounted for in the model, which gives precedence to geometrical connectivity. As noted by the authors of the study, it is possible that an improved treatment of the interwhisker interfaces might help reconcile the differences between the model and the data. Furthermore, it is suggested here that frequency-based shorting of capacitive regions — which is the foundation of the shorting-distance assumption and is considered further in Chapter 6 — is inappropriate for the treatment of dc response.

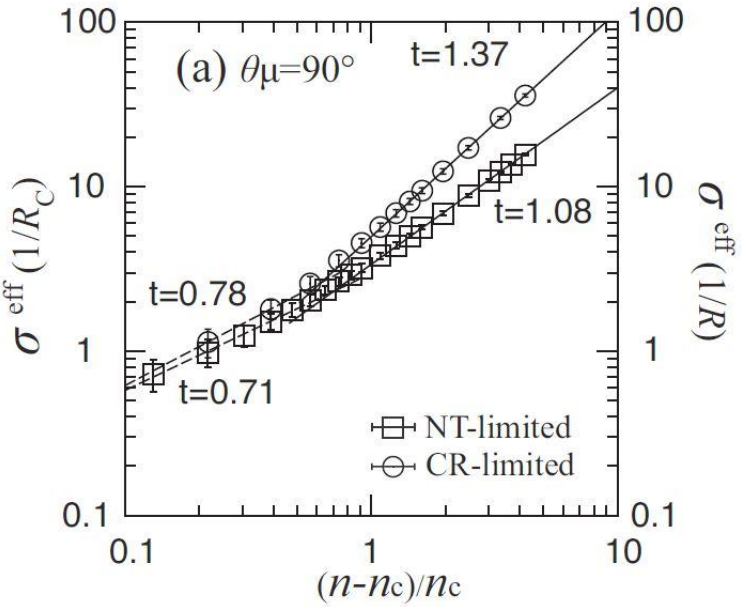

Figure 1.14. Composition dependence of effective conductivity of networks of conductive sticks randomly aligned in two dimensions in an insulating matrix for the cases where this conductivity is limited by the stick-interface (circles) or intrastick (squares) resistances.[11] The conductivity magnitudes for the different cases are plotted on different but similarly-scaled axes and are not comparable.

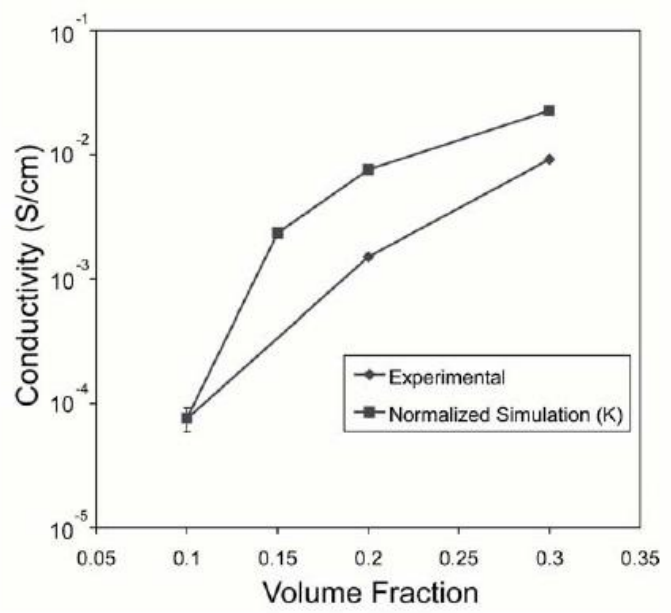

Figure 1.15. Comparison of the dependence of conductivity on SiC_w volume fraction determined by experimental measurements to that predicted by a microstructural simulation in which interwhisker conduction was modeled via an electrical-shorting concept.[6]

1.7.5. Discussion of Electrical Interfaces in Real Stick-Percolated Composites

The latter two simulations highlight the importance of interfaces on the behavior of the composites.[6,11] The simulation of percolated Al_2O_3-SiC_w, in particular, highlights difficulties associated with bridging the gap between experimental measurements of composite conductivity and resistor networks constructed via the abstract translation of a dispersion of discrete particles having zero connectivity into a network possessing finite connectivity. An incomplete understanding of the interfaces, which play an integral role in the topology construction, is the main source of these difficulties.

The fillers undoubtedly participate in and determine the pathway of the percolating current (which is enormously influenced by geometrical connectivity), but the upper-bound limit on the magnitude of that current is likely determined by interfacial behavior, not intrafiller conductivity. In real composites, the conductive fillers are separated by an interface which is composed of the matrix and has a finite width.

How close is close enough for "connections" to be made and networks to be formed? How do these connections behave, i.e., to what extent is their character resistive, capacitive, and/or (non)linear? These issues are depicted in Figure 1.16. Another question which arises concerns how to model the variability in the nature of the connections which may be inferred to exist by examining the microstructures of such disordered composites. The electrical behavior of the interfaces between sticks may depend on the intimacy of their contact, their proximity and relative orientation, and the details of the local electronic structures. Figure 1.16c demonstrates the orientation and proximity issues, and Figure 1.17 demonstrates contrast in intimacy between indirect vs. direct contact.[6] Before proceeding to discuss electronic structure, we look to models of

random electrical networks to gain a sense of how such randomness could be manifested in composite electrical response.

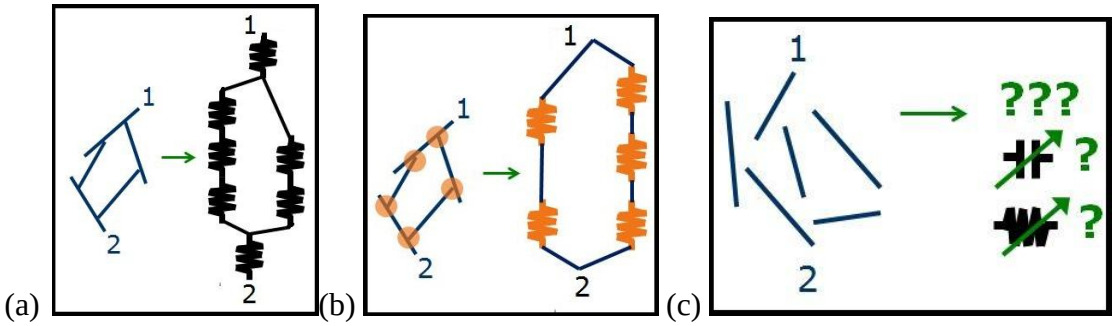

Figure 1.16. Translations of stick ensembles into resistor networks which consider only intrastick (a) and interstick (b) resistances. In part (c), the constituent electrical components and the structure of the equivalent-network model for the sticks are unclear due to the spatial disconnects between the sticks.

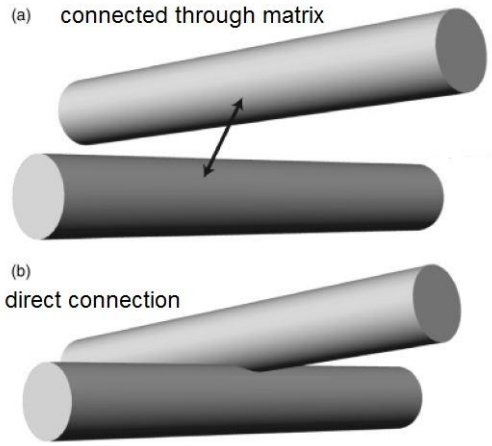

Figure 1.17. Interfacial connections between three-dimensionally rendered sticks. (a) indirect, (b) direct. Modified from Ref. 6.

1.7.6. Randomly-Configured Multi-Component Electrical Networks

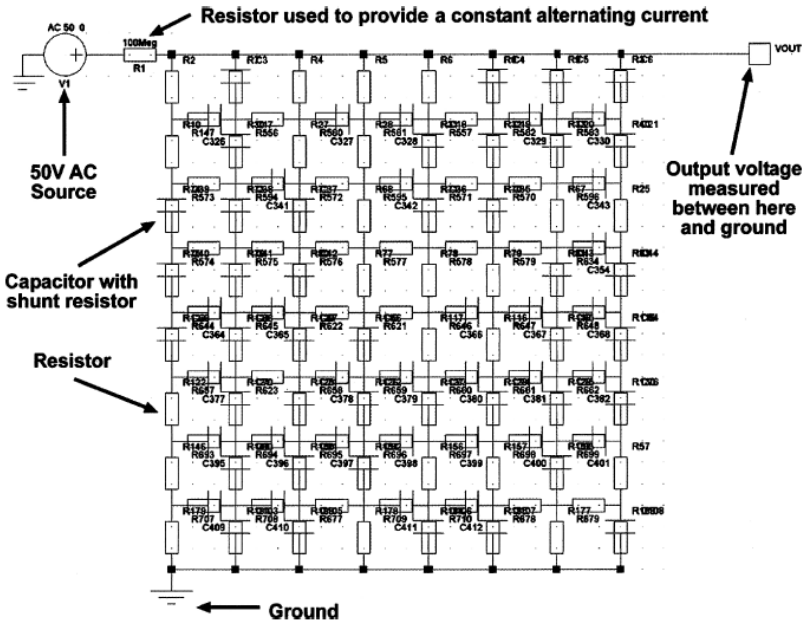

Figure 1.18. Randomly-configured eight-by-eight network of resistors and capacitors containing 64 components.[12]

Randomly configured square networks of comparable quantities of resistors and capacitors (Figure 1.18) give rise to power-law behavior for the frequency dependence of conductivity (Figure 1.19a) and permittivity (Figure 1.19b).[12,91] It can be seen that the responses on the low-frequency and high-frequency sides of the power laws were relatively sensitive to the percolation of resistors and capacitors, respectively. Furthermore, these sensitivities were most clearly manifested in the conductivity and real part of the permittivity, respectively.

In another work,[13] randomly-configured networks on a two-dimensional square lattice which consisted of purely linear resistors and non-linear resistors having a weak non-linear component were considered. It was found that the effective strength of the non-linear response of the network depends on the fraction of non-linear components and the linear conductances of the components.

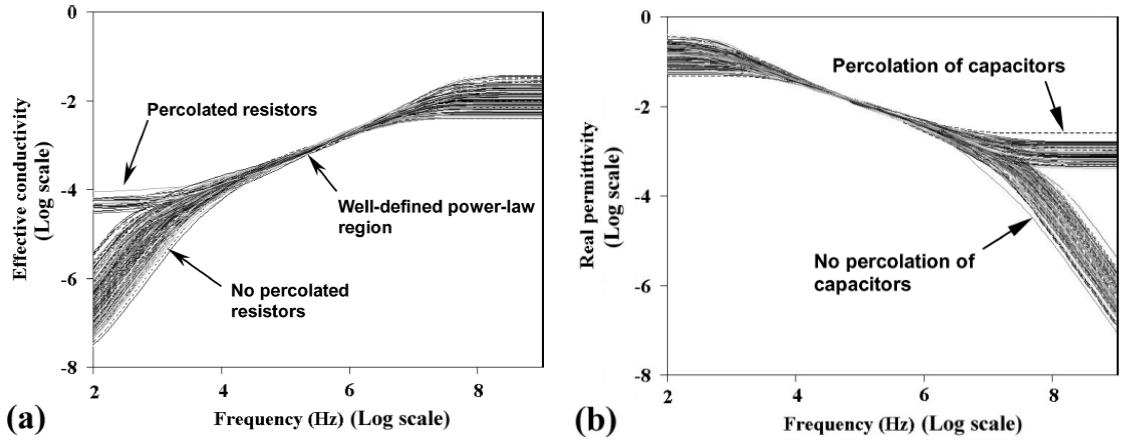

Figure 1.19. Frequency dispersions from randomly-configured resistor-capacitor networks like that shown in Figure 1.18. (a) conductivity (b) real permittivity.[12]

This is shown in Figure 1.20, in which the strength of the network non-linearity is normalized to that of the individual non-linear resistors. It can be seen from the progression through the Figure parts that increasing the linear conductance of the linear component relative to that of the non-linear component magnifies the network non-linearity arising from the latter component type in a composition-dependent fashion.

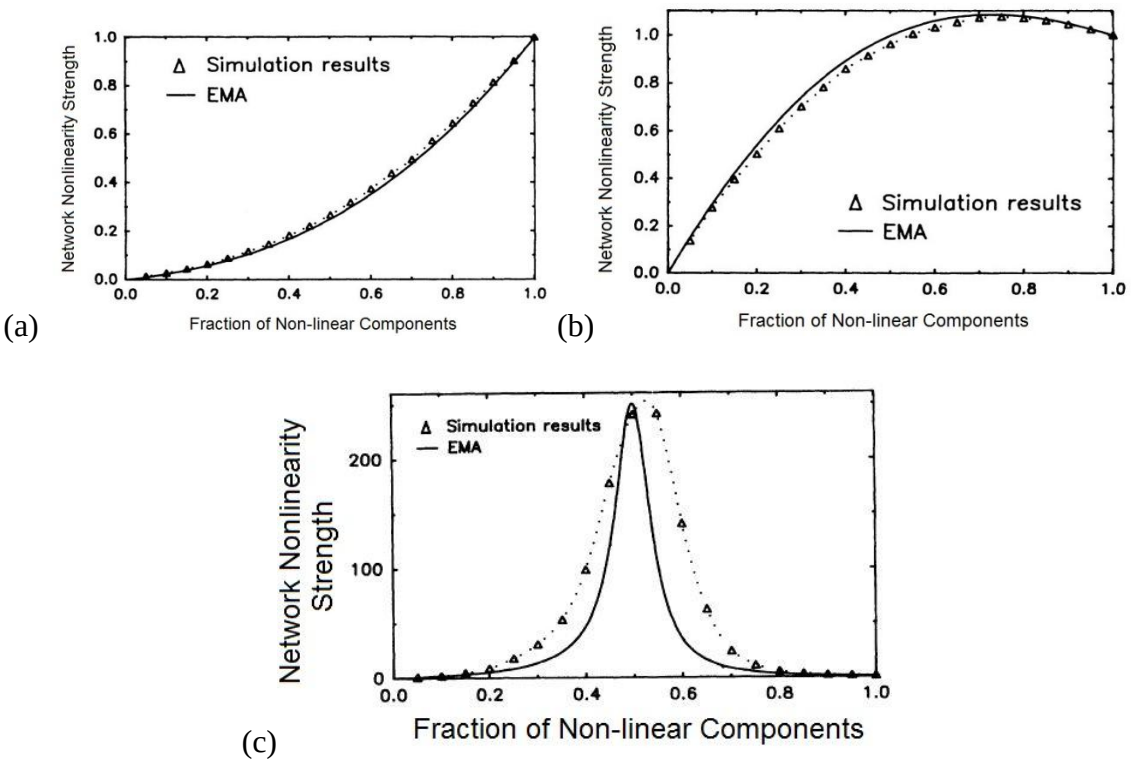

Figure 1.20. Effective non-linearity strength of randomly configured networks of linear and non-linear resistors given in units of the non-linear-component non-linearity and as a function of the fraction of the latter component. The linear/non-linear component conductance ratios were (a) 1:2, (b) 2:1, (c) 500:1. The solid black curves give the result of an effective medium approximation (EMA). The figures were modified from Ref. 13.

1.7.7. Electronic-Structure Considerations for SiC Whiskers and Alumina

The electronic structures of Al_2O_3 and SiC are significantly different from those of many other insulator-conductor composites. These are often composed of an insulating polymer matrix and metal-like filler particles.[92-94] The valence electrons of the former are confined within localized covalent bonds in polymer chains, and the delocalized valence electrons of the latter may sometimes leak outside the surface[95,96] in a manner analogous to quantum mechanical particles in finite potential wells. For both of these structures,

there is no bandgap to speak of. In contrast, Al_2O_3 and SiC are wide-bandgap insulators and semiconductors, respectively.

The bandgap of alumina[97] is 9.9 eV and is much greater than that of SiC, which is 2.4, 3.0, and 3.3 eV for the 3C, 6H, and 4H polytypes, respectively.[98] The reported activation energies for the low-field conductivity of alumina have varied widely between 2.97 and 4.26 eV in the 1000-1600°C temperature range and the results of an additional investigation at these temperatures suggested that the alumina conductivity was not significantly larger than that of the surrounding air.[99] Conduction through single-phase alumina may occur via tunneling or dielectric breakdown if it is sufficiently thin or the electric field is sufficiently high, respectively.[100,101]

The latter process depends on the activity of traps, i.e., localized electronic states associated with atoms which significantly disrupt the periodic potential associated with the formation of valence and conduction energy bands in perfect semiconductor and insulator crystals.[102] In such crystals, intrinsic conductivity is derived from carriers associated with electron excitation across the bandgap, i.e., from the valence to the conduction band. The term 'trap' implies that the state exists within the bandgap far away from the band edges. Examples of traps include highly dissimilar chemical impurities and surface states, which correspond to the termination of the crystal. For semiconductors, the replacement of a small amount of atoms in the host lattice by foreign atoms which are chemically similar tends to produce states within the gap near the band edges. This proximity means that the ionization of these foreign atoms—which are commonly known as dopants—requires a relatively small amount of energy. Dopant ionization results in the

existence of extrinsic electrons or holes in the conduction or valence band, respectively, depending on which band the associated states were near.

Due to lack of purification involved in typical (semiconductor) SiC_w fabrication, intrawhisker conductivity is likely to be determined by extrinsic rather than intrinsic conductivity, and thus, its chemical impurities. However, as already mentioned, the limiting factor for the conductivity of composites is more likely to be conduction at the interfaces of SiC_w rather than intrawhisker conductivity. Interfaces between semiconductor particles have sometimes been modeled as a back-to-back Schottky barrier. Figure 1.21a is a classic depiction of this for an n-type material;[14] similar diagrams are available elsewhere.[15,19,103] The barrier has a height Φ_B which result from a density n_t of filled trap states, which correspond to defects. The filling of these states constitutes a sheet of negative charge at the interface which results in depletion regions on both sides containing positively charged donor ions. These regions correspond to the bending of the conduction-band minimum (E_C) farther above the Fermi level (E_F).

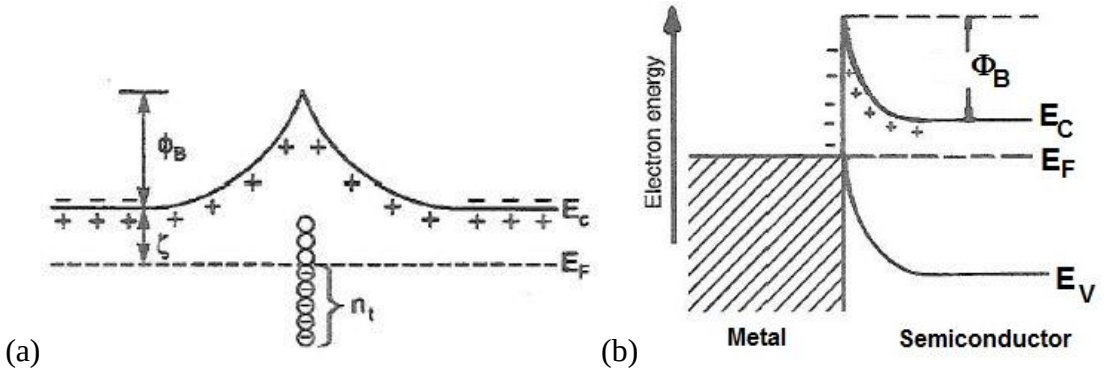

Figure 1.21. (a) Back-to-back Schottky barrier at the interface of semiconductor grains.[14] (b) Ideal single Schottky barrier for an n-type semiconductor/metal junction. Modified from Ref. 15.

Single Schottky barriers commonly result at the interfaces between semiconductors and metals. Figure 1.21b shows an example of an ideal single barrier to an n-type semiconductor in order to demonstrate correspondence to the symmetrical barrier in Figure 1.21a. It may similarly be characterized by a depletion space charge and band bending in the semiconductor near the interface. In this figure, the top of the valence band is denoted as E_V and the depiction of the charge displacement at the interface is somewhat clearer. Experimentally, pinning of the Fermi level by interface trap states often affects metal-semiconductor barrier structure[104] and it has been found that ultra-thin layers of aluminum oxide can sometimes alleviate such pinning.[100]

1.7.8. Charge Displacement and Dielectric Response

Space charges at interfaces also result when carriers move in response to an applied field until they are stopped at electrostatic potential barriers, e.g., at grain or phase boundaries.[15] This is a type of dielectric polarization and charge displacement (between the centers of positive and negative charge); it and other types are shown schematically in Figure 1.22 in relation to the associated neutral configurations of the charges which result when the field has been removed and enough time has passed. When the field is applied, the moments of the electrical dipoles associated with the various displacement types points in the opposite direction compared to the applied field. The charges which define the structure of atoms and ionic solids behave as if bound to their equilibrium positions by springs such that the restoring force is proportional to the displacement; this gives rise to resonances.[15] For space charge and dipolar polarizations, the amount of time needed to return to the unpolarized from the polarized state is known

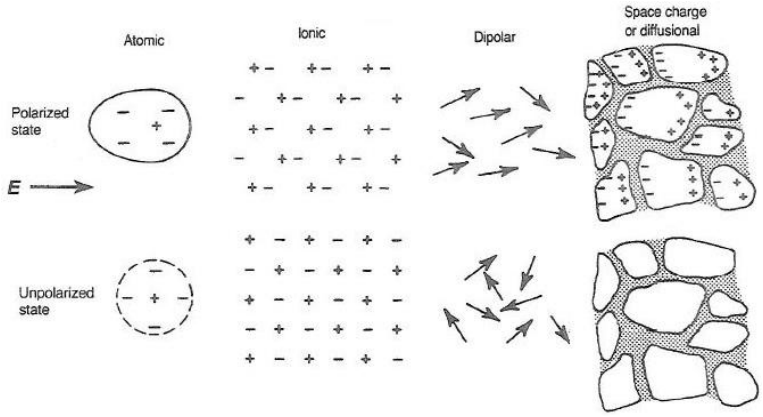

Figure 1.22. Diagram of various charge displacement processes. The applied electric field *E* points along the arrow. Modified from Ref. 15.

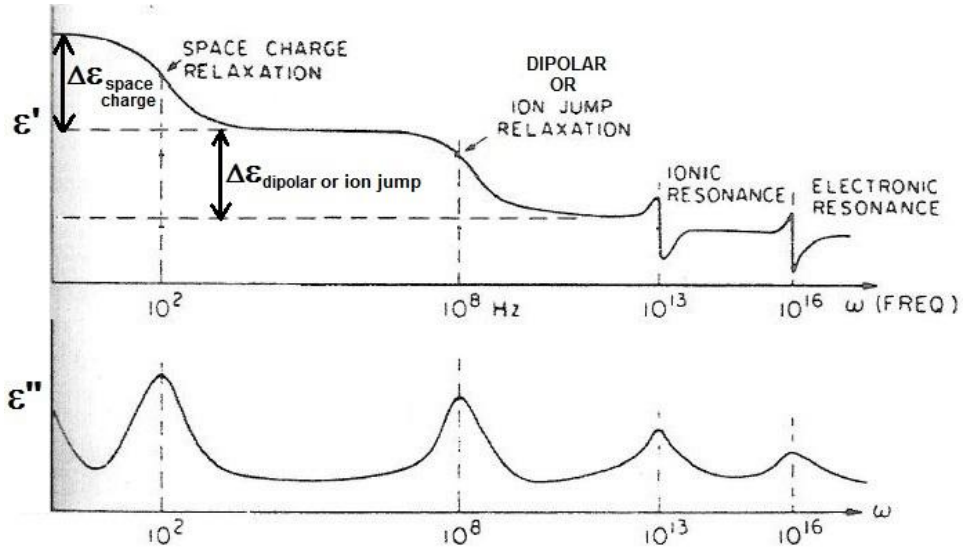

Figure 1.23. Real and imaginary permittivity spectra showing order-of-magnitude expectations for the frequency regime of the various types of polarization processes drawn in Figure 1.22. The dotted lines demonstrate correspondence between the real and imaginary functions and that real-permittivity contributions from fast processes add to the total permittivity measured at lower frequencies. Modified from Ref. 16.

as the relaxation time (τ), which scales inversely with position of the associated features in the permittivity spectra, e.g., Figure 1.23. Space charge relaxations are commonly regarded as the slowest type of relaxation. It has been proposed that the underlying mechanisms of dielectric loss in SiC are polarizations of the dipolar or ion-jump[105] kind

specifically involving vacancy (V_C -V_{Si}) and antisite (Si_C-C_{Si}) defect pairs.[106] The electrical measurements upon which this proposition was based were conducted after mixing SiC powders into a paraffin-wax matrix to make 67 vol% SiC composite samples,[106] which were likely percolated.

The classic model of dielectric relaxation was developed by Debye for the relaxation of non-interacting dipoles.[107] It predicts:

$$\varepsilon' = \varepsilon_\infty + \Delta\varepsilon / (1 + \omega^2\tau^2) \tag{1.11a}$$

$$\varepsilon'' = \omega\tau\Delta\varepsilon / (1 + \omega^2\tau^2) \tag{1.11b}$$

where $\Delta\varepsilon$ is the relaxation strength. This quantity is marked on Figure 1.23 for dipolar and space charge relaxations and may be described as the additional real permittivity which the polarization mechanism provides above that which exists on the high-frequency side of a given relaxation, ε_∞. The Debye form was subsequently modified by Cole and Cole[108] with a parameter α_τ to account for a distribution of relaxation times:

$$\varepsilon' = \varepsilon_\infty + C_1 / C_2 \tag{1.12a}$$

$$\varepsilon'' = C_3 / C_2 \tag{1.12b}$$

where

$$C_1 = \Delta\varepsilon \left[1 + \sin(\pi\alpha_\tau / 2) \cdot (\omega\tau)^{1-\alpha\tau} \right] \tag{1.12c}$$

$$C_2 = 1 + 2(\omega\tau)^{1-\alpha\tau} \sin(\pi\alpha_\tau / 2) + (\omega\tau)^{2(1-\alpha\tau)} \tag{1.12d}$$

$$C_3 = \Delta\varepsilon \cdot \cos(\pi\alpha_\tau / 2) \cdot (\omega\tau)^{1-\alpha\tau} \qquad (1.12e)$$

This form collapses into Equation 1.11 when $\alpha_\tau = 0$ and has been generally found to be more agreeable with experimental data compared to that Equation. The classic Maxwell-Wagner model[109] for interfacial space-charge polarization is also similar to the Debye form and is introduced in Chapter 6.

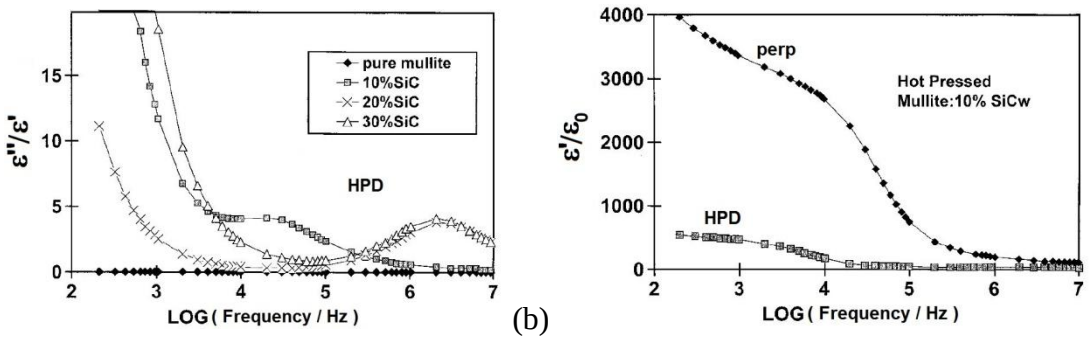

Figure 1.24. (a) Data measured along the HPD of mullite composites with variable SiCw loading showing frequency dispersions of the loss tangent ($\varepsilon''/\varepsilon'$) in which peaks in the imaginary permittivity are manifested. (b) Frequency dispersion of the real permittivity normalized to the permittivity of free space ε_0 from measurements parallel and perpendicular ("perp") to the hot-pressing direction of a mullite composite with 10% SiC_w. Modified from Ref. 17.

In Figure 1.23, it can be seen that space-charge polarizations are classically expected to occur at rather low frequencies, e.g., 100 Hz. For SiC_w-loaded mullite-matrix composites, imaginary-permittivity peaks attributed to interfacial space-charge polarization at mullite/SiC interfaces were observed.[17] They are manifested in Figure 1.24a, in which the ratio of the imaginary to the real permittivity was plotted. This type of plot changes the imaginary-peak shape somewhat, but typically does not change its central position in the frequency spectrum by very much. It can be seen that the peak

frequencies are higher by orders of magnitude compared to the order-of-magnitude expectation for space charge polarization in Figure 1.23.

In the same samples, the real permittivity was found to be consistently lower when the applied field was applied parallel rather than perpendicular to the hot-pressing direction, e.g., in Figure 1.24b for a 10% SiC_w sample. It was proposed that this difference was the result of there being fewer interfaces for the former case. Notably, this orientation difference is present even at high-frequencies, e.g., 10^6 Hz.

1.7.9. Early Work on the Electrodes of Al_2O_3-SiC_w Composites

After the interwhisker interfaces were considered in that work, it was found that the interfaces of the electrodes with Al_2O_3-SiC_w composites significantly affected their measured response. Specifically, it was shown that the geometric normalization of the impedance spectra from samples which had the same SiC_w loading but different thicknesses and contact areas brought one of the two semicircles in the complex impedance plane into approximate coincidence, but not the other (see Figure 1.25). Therefore, the latter was attributed to the electrodes. In this dissertation, the effects of the interfaces of the whiskers (with each other and with the electrodes) on the composite electrical response are studied in greater detail.

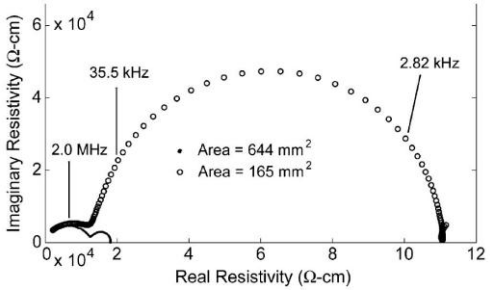

Figure 1.25. Effect of electrode area on the normalized impedance of 10% SiC_w-Al_2O_3.[6]

CHAPTER 2

EXPERIMENTAL PROCEDURES

This chapter gives information about the fabrication of the composites from the raw materials and the widely- but not universally-applied methods of preparing and characterizing the samples. Additional experimental details and methods, as well as conformity with the methods presented here, are noted in the relevant chapters.

2.1 Composite Fabrication

Two batches of composites of alumina and silicon carbide whiskers were studied. The first batch was made by Advanced Composite Materials (ACM) LLC in Greer, SC before the present author began work on this research project. These samples were characterized by a previous student[110] and used by the present author to study electrode effects. The second batch was fabricated by way of a collaboration between the present author and ACM LLC; this batch is the subject of Chapters 4-7.

2.1.1. Batch #1

The composites of the first batch are described first. These were disc-shaped with ~8 mm thicknesses, ~28 mm diameters, and contained different volume fractions of SiC_w (V_w = 0.06, 0.08, 0.09, 0.10, 0.20, 0.30) in an aluminum oxide matrix. The SiC whiskers were synthesized by ACM and are nominally of the β polytype of SiC. The composite samples were made by hot-pressing (HP) typically conducted at ~1800°C for 60 minutes in an inert gas environment with ~30 MPa pressure.[75] The length-radius-orientation distribution of the whiskers in these composite samples was previously reported.[6,89,110]

2.1.2. Batch #2

The samples of the second batch were solidified from a single set of new powder blends by three different methods: hot pressing, extrusion and pressureless sintering, and dry pressing and pressureless sintering.

2.1.2.1. Powder Processing

To make the new powder blends, dry powders of Al_2O_3 with varying volume fractions of SiC_w were mixed in an attempt to achieve the target compositions given in Table 2.1. The alumina appeared as a fine white powder, and the starting SiC whiskers had an interesting powder morphology shown in Figure 2.1a. After ultrasonically dispersing a small amount of whiskers in methanol and placing droplets on a metal-coated glass slide, they were imaged by SEM. The results (Figures 2.1b through 2.1f) show that the unmilled whiskers varied a great deal in size and morphology. The SiC_w polytype was determined as 4H by x-ray diffraction of whiskers dispersed on an uncoated glass slide (as in Ref. 9).

Table 2.1. Compositions of Fabricated Al_2O_3-SiC_w Composites of Batch #2 by SiC_w Volume Percent and Related Data

Target (vol%)	**0**	2.5	5.0	7.5	10.0	12.5	15.0	17.5	20.0	25.0	30.0
Extra SiC_w (vol%)	0	0.25	0.25	0.25	0.25	0.25	0.25	0.25	0.25	0.75	0.5
Measurement (vol% = 100p)	1.09	**3.52**	**5.81**	**7.68**	**9.96**	**12.2**	**14.5**	**17.0**	**19.1**	**24.0**	**28.2**
Error (vol%)	0.04	0.04	10^{-7}	0.07	0.04	0.1	0.1	0.2	0.1	0.4	0.2
Hot-Pressing Temperature (°C)	1525	1550	1600	1625	1625	1625	1650	1650	1675	1700	1750

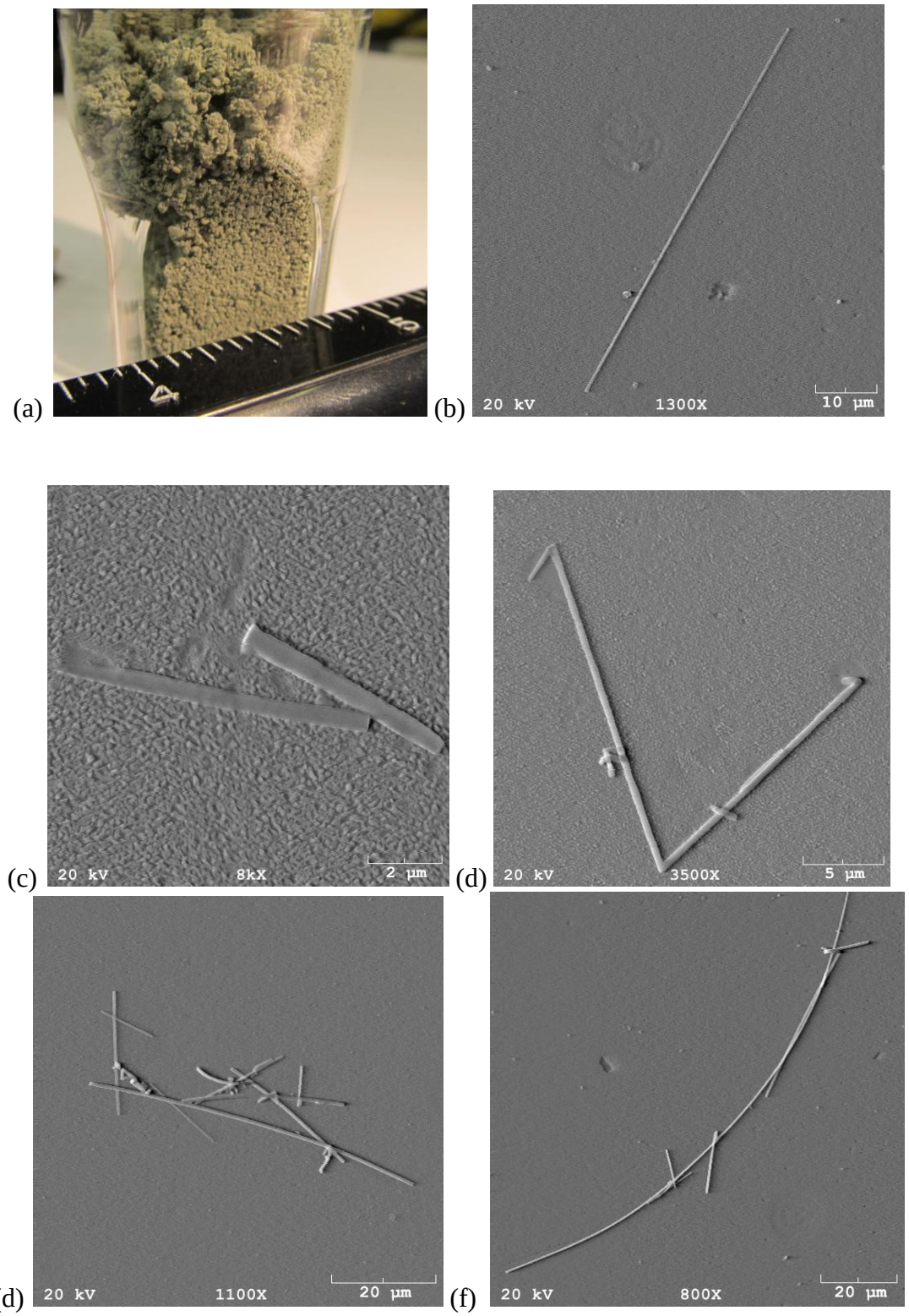

Figure 2.1. Silicon carbide whiskers. Part (a) shows them in a small plastic container next to the 4-inch mark of a common ruler and parts (b)-(e) are SEM views of dispersed whiskers on a metal-coated glass slide.

Each powder blend in the set had a total mass of approximately 5 kg. Oxide sintering additives (1.0 wt% total), including a rare-earth metal oxide, were also incorporated in each composition but cannot be identified due to their proprietary nature. The same ball mills and alumina media were used for all compositions and for both the wet and dry milling phases, which lasted 8 and 6 hours, respectively. In between, the mills and media were dried for several hours. To expedite production, the mills and media were not cleaned between compositions. Presumably, this diluted the whisker content of blends due to carryover from previous compositions. To compensate for such dilution, extra SiC_w were added such that the volume percentage of whiskers in the weighed-out powder was increased by a small amount (see Table 2.1). The actual whisker content in each milled blend was measured experimentally with a LECO carbon analyzer which tracked the oxidized carbon products of SiC decomposition. The results are reported in Table 2.1. These measured composition values are used throughout this thesis for all SiC_w-containing samples. The measurement of 1.09 ± 0.04 vol% carbon in the mills where no whiskers were added is suggestive of non-SiC carbon contamination such as that which might arise from the plastic walls of the milling jars. Powder blends were screened to 20 mesh and this involved manually pulverizing agglomerates via mortar and pestle. After milling, typical whisker lengths and diameters were found to be ~10 μm and ~0.5 μm, respectively, by examination of the blended powders with an optical microscope.

2.1.2.2. Hot and Dry Pressing

For each composition, 6 (or more) discs were made by two (or more) hot-pressing runs at ~25-30 MPa for 20 minutes each in flowing N_2 at peak temperatures reported in Table 2.1. In each run, two thin discs and one thick disc were made via separation with boron nitride spacers in the load train (see Figure 1.5). The die was graphite and the powder was separated from the die and spacers by graphite foil to facilitate post-pressing sample removal. A few discs of each composition were also uniaxially dry-pressed into green bodies from the same dry powder blends with ~100 MPa of pressure at room temperature.

2.1.2.3. Preparation of Extrudable Dough

For the extrusion of each composition, 4.540 kg of dry powder was mixed with liquid and organic components with a Lancaster mixer (Figure 2.2) using a wheel and plows to produce mixtures suitable for extrusion. The other components were polyvinyl alcohol (60 g), methocel (35 g), mineral oil (130 g), crystallizer C (110 g), and water (768 g). The water included fugilite colored tints supplied by Chemurgy Products, Inc. (Greenville, SC) which were useful for monitoring mixing progress, contamination, and separating the different compositions during extrusion. Sometimes a small amount of extra water (e.g., ~20 g) was necessary in addition to the base level of 768 g in order to achieve the proper morphology for extrusion, i.e., a soft and clumpy granular texture with a viscosity similar to natural clay. Figures 2.3a and 2.3b show the large metal bowl containing the 24.0% SiC_w powder before and after the addition of extra water, which also changed the appearance of the mixture.

Figure 2.2. The Lancaster mixer used to mix the liquids and organics with dry powder blends.

(a)  (b) 

Figure 2.3. The 24.0 % SiC_w mixture before (a) and after (b) adding an additional 20 g of water. The ungloved hand is shown for scale purposes and did not touch the mixture, unlike the gloved hand, which was used to test/verify the granular texture.

2.1.2.4. Extrusion

The mixtures were added to an industrial extruder (Figure 2.4a) in order of ascending SiC_w composition and were pushed through with ~240 kN force. The extruder used a 15.2 cm diameter cylindrical ram, a truncated cone of height ~19 cm, and a circular die of 1.788 cm diameter. The extrudate was placed on wooden boards (Figure 2.4b), and transition periods between different compositions were identified by multi-colored extrudate which was discarded. Sometimes the extrudate emerged from the die in spurts and this is believed to result from imperfect mixing of the liquids and organics into the dry powder blends. Extrusion attempts with narrower dies were unsuccessful; the extrudate would not come out. The non-uniform extrusion rate may have resulted in some structural inhomogeneity (e.g., variation in whisker alignment) along the rod lengths. The as-extruded rods were cut to ~11 inch (27.9 cm) lengths and allowed to dry for several days by water evaporation at room temperature and 60°C.

(a)  (b) 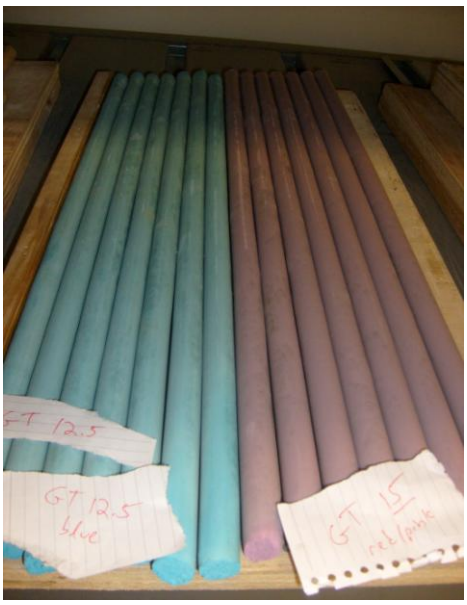

Figure 2.4. (a) Industrial extruder. (b) Extrudate containing colored dyes, prior to cutting and binder burnout.

2.1.2.5. Binder Burnout and Sintering

The organic components were then burned out in air at 550°C. Finally, the rod green bodies were pressureless sintered at a peak temperature of 1725°C in a flowing N_2 ambient with an ACM-proprietary ramp/hold schedule. The dry-pressed discs were sintered under the same conditions. The N_2 ambient was used in order to maintain similarity with the commercial ACM microwave product and the hot-pressed discs.[21] The composition-invariant peak temperature was used to minimize the number of variables. Higher temperature does not always yield higher density composites[111,112] and a separate sintering trial of a few rods which spanned the compositional range and peaked at 1660°C did not provide significantly different densities. Results from this trial are otherwise not reported in this dissertation. After sintering, the dry-pressed discs were ~7 mm thick and ~25 mm in diameter. The final lengths and diameters of the as-sintered extruded rods were 23-26.5 cm and 14-15 mm, respectively.

2.2. Sample Preparation

A general description of the preparation methods are given in this section. Additional details are given in the experimental sections of the relevant chapters.

2.2.1. Sectioning

A saw with a diamond-edged blade was used to section the as-fabricated composites into samples of appropriate size for electrical measurements. Hot-pressed discs of Batch #1 were sectioned along the HP direction with a diamond saw into half- and quarter-cylinder shapes. The thick hot-pressed samples of Batch #2 were sectioned parallel to the hot-pressing direction (HPD) to form ~1-2 mm thick rectangular slices for

measurements in which the electric field would be applied perpendicular to the HPD. These cuts also produced half- and quarter-cylinder shapes. The dry-pressed discs were typically not sectioned. Slices having typical thickness ~ 2 mm were cut from the ends of the as-sintered extruded rods and discarded in order to remove the visible surface reaction layer and minimize its influence on electrical measurements. The plane of slicing was perpendicular to the extrusion direction. Additional slices (z ~ 1-2 mm thickness) were then taken and these, along with the long-rod remainders which had the ends removed (z~22-26 cm length) were used for electrical measurements. Due to porosity, extruded slices were necessarily dried at ~120°C to remove moisture from the water-based machining coolant before electrode application.

2.2.2. Grinding and Polishing

For the sintered dry-pressed discs, diamond grinding with coarser particle size (250, 125 μm) was done to remove the reaction layer from pressurelesss sintering. On hot-pressed and dry-pressed samples, the faces on which electrodes were subsequently applied were first ground to ~6 μm roughness with a sequence of embedded-diamond grinding wheels having progressively finer diamond-particle size, i.e., 70, 45, 15, 6 μm. All samples which were examined by microscopy were additionally polished to a mirror-like finish via a sequence of diamond pastes (i.e., 3, 1, and 0.25 μm) a final 0.05 μm colloidal-silica step. These procedures are very similar to those developed in Ref. 110.

2.2.3. Surface Cleaning

Prior to electrode deposition, the hot-pressed composite samples underwent a rinsing sequence of acetone, isopropyl alcohol (IPA), distilled water, and IPA (again) to

clean the sample surface. For the pressureless-sintered samples which were more porous, a similar sequence was used, but the distilled-water step was skipped to prevent moisture uptake. After rinsing, samples were dried by spraying with compressed air.

2.2.4. Electrode Deposition

Electrodes were deposited on samples to yield a parallel-plate configuration either by applying SPI conductive silver paint or sputtering Ag or Pt with an argon plasma in a Denton Vacuum Desk II Turbo Sputter Coater. On a given sample, both electrodes were made by the same method. Any residual organic solvent leftover from rinsing is presumed to have evaporated during chamber evacuation prior to sputtering. During sputtering, shadow masking was employed to prevent metal deposition on the sidewalls of samples. Sputtering was used to create thick-film electrodes and a secondary layer of Ag was applied on top of Pt electrodes to reduce spreading resistance, allow for consistent reproduction of the high-frequency bulk feature in impedance spectra, and conserve expensive Pt. The Ag and Pt sputtering targets had nominal purities of 99.9% and 99.99%, respectively. Silver paint was given 24-48 hours to dry and confirmed with a multimeter to have ~1 ohm resistance prior to ac measurements.

Due to the size constraints of the sputter coater chamber, long extruded rods always had painted electrodes applied on the circular faces of the rod ends. For electrodes of almost-all other samples, the metal at the metal-composite interface was sputtered. Details are given in the experimental sections of the respective chapters.

2.3. Electrical Characterization

A general description of the various electrical characterization methods is given in this section. Additional details are given in the experimental sections of the chapters.

2.3.1. Alternating-Current Spectroscopy

The bulk of the electrical characterization employed alternating-current (ac) spectroscopy, which is also known as impedance spectroscopy or dielectric spectroscopy. In this, three different impedance analyzers were used to measure the response to a small (0.1-1 V) ac voltage: a Solartron 1260 with a 1296 dielectric interface, an Agilent 4291B, and a Hewlett Packard 4192A (HP) LF Impedance Analyzer. These had frequency ranges of 1 mHz-32 MHz, 1 MHz – 1.8 GHz, and 5 Hz – 13 MHz, and are shown in Figures 2.5, 2.6, and 2.7, respectively. The different instruments were useful for verifying the accuracy of measurements via cross-checking of results and needed to characterize the widely-varying responses of the samples over a wide range of frequencies.

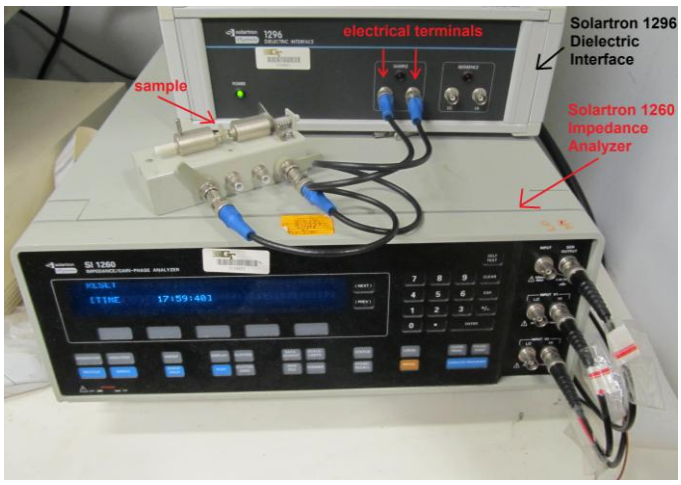

Figure 2.5. Solartron 1260 impedance analyzer with Solartron 1296 Dielectric Interface. A sample is loaded into the attached Agilent 16034E Test Fixture, which is connected to the electrical terminals of the 1296 via coaxial cables.

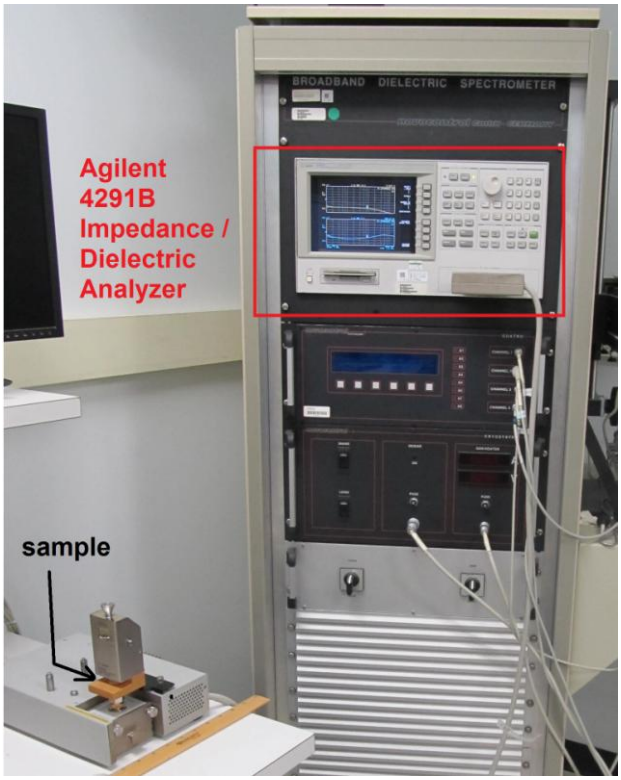

Figure 2.6. Agilent 4291B impedance analyzer connected to the Agilent 16453A test fixture with a loaded sample.

Figure 2.7. Hewlett Packard 4192A (HP) LF Impedance Analyzer.

2.3.2. Measurement of the Response to Static Electrical Bias

The direct-current (dc) response was measured in the -40 to +40V range with a Keithley 2612A Sourcemeter. In many ac-spectroscopy measurements, additional dc biases were applied in ranges of 0 to 40 V and 0 to 4 V with built-in DC sources in the Solartron and HP analyzers, respectively. This allowed discrimination of the effects of the dc bias on the bulk and electrode impedance contributions to the total response. Furthermore, it sometimes allowed for the calculation of static capacitances in addition to dc conductivity, as discussed in Section 2.3.6.

2.3.3. Measurement Direction Relative to Microstructure

For hot-pressed samples, the measurement direction (i.e. the direction of the applied electric field) was either parallel to the hot-pressing direction (HPD) or perpendicular to the hot-pressing direction (perp). For dry-pressed discs, extruded rods, and slices of rods, the field was always applied parallel to the processing direction, i.e., the pressing or extrusion direction.

2.3.4. Electrical Test Fixtures

For electrical measurements, the samples were electrically-connected and mechanically-clamped in a fixture which depended on the analyzer, the sample geometry, and the measurement type. At *room-temperature*, measurements with the Agilent analyzer employed an Agilent 16453A fixture (Figure 2.8).

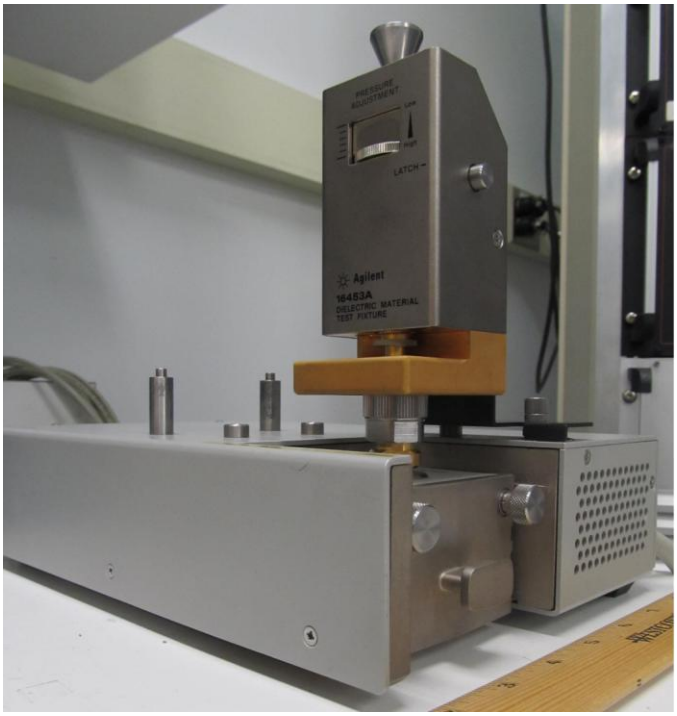

Figure 2.8. The Agilent 16453A dielectric test fixture holding a sample.

For *room-temperature* measurements with the Solartron and HP analyzers, the fixture choice was aimed at minimizing stray capacitance and constrained by incompatibilities between the geometries of the samples and fixtures. Thin slices of the rods, thin hot-pressed discs, and perpendicular slices of the thick hot-pressed discs were always measured with the Agilent 16034E Test Fixture (Figure 2.9a). Thicker hot-pressed and dry-pressed discs which could not fit in this fixture were measured in a homemade fixture using a gripping device, two epoxy pucks with protruding SEM-like stubs for electrodes, and connections made with alligator clips (Figure 2.9b). A separate, similar custom-built fixture using a larger gripping device was used to measure the long extruded rods (Figure 2.9c).

(a) 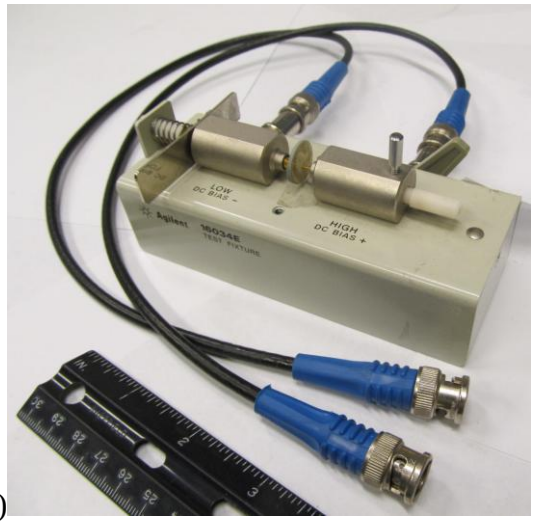

(b) 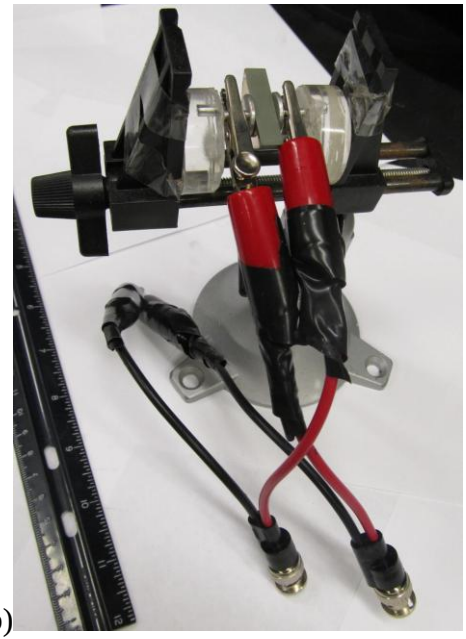

(c) 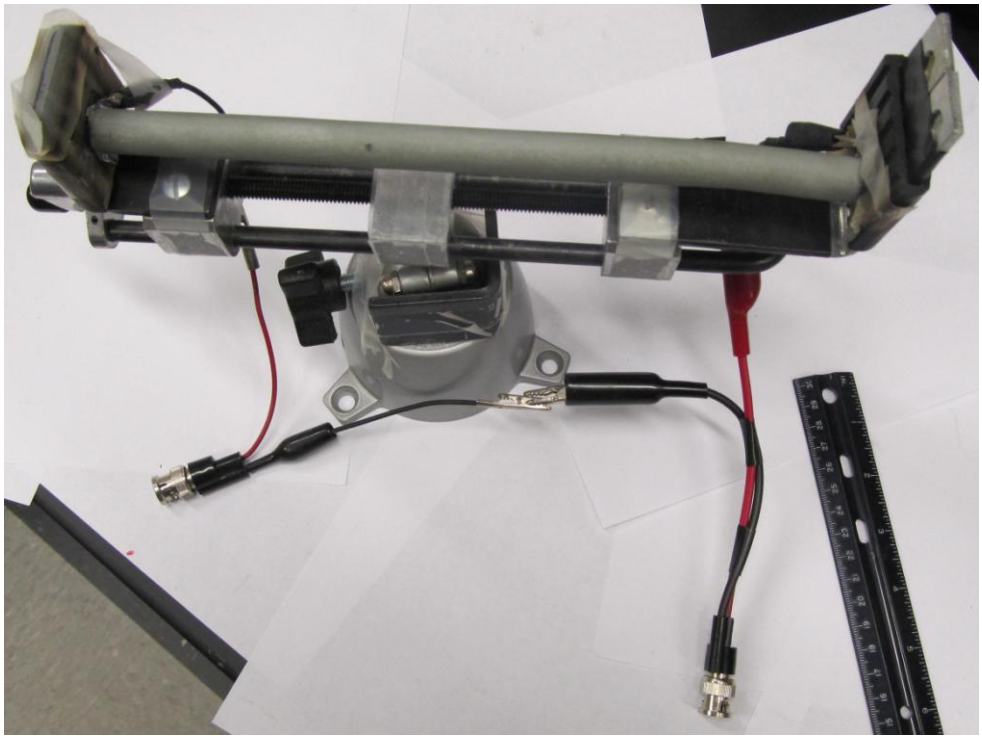

Figure 2.9. Fixtures used with the Solartron and Hewlett Packard analyzers to measure samples (shown) having different geometries, including coaxial connectors (a) Agilent 16034E Test Fixture for thin samples (b) Homemade fixture for thick samples (c) Custom-built fixture used for measuring long extruded rods.

2.3.5. Variable-Temperature Measurements

Variable-temperature measurements required specialized setups and different fixtures; these are described in detail in Chapter 7. Measurements at low-frequency were made with the Solartron between room temperature (~20°C) and 700°C. Measurements at high frequency with the Agilent analyzer were made between -160°C and 300°C.

2.3.6. Extraction of Static Resistances, Capacitances, and Conductivities

DC conductivity (σ_{dc}) was calculated from $\sigma_{dc} = z/(A_{cs} \cdot R_{b0})$, where A_{cs} is the area of one of the opposing electrodes, z is the sample dimension along the direction of the applied electric field, and R_{b0} is the low-frequency limit of the real impedance of the impedance semicircle relating to the composite bulk. The value of R_{b0} was determined from plots of the complex impedance at zero dc bias. Extrapolations based on fits of impedance arcs (i.e., portions of presumably-full semicircles) with Zview software by Scribner Associates were used to determine R_{b0} when deemed appropriate, e.g., for samples which were highly-insulating or which had separable electrode impedance. The logic underlying this approach is elucidated in Chapter 3. Similar fits using the same software function (which relies on a parallel resistor-capacitor circuit model) were sometimes used to determine effective static capacitances when the maximum in the imaginary impedance (i.e., the top of the semicircle) was observed.

2.4. Other Characterization Methods

The characterizations of porosity, sintering-induced shrinkage, dynamic elastic modulus, structural anisotropy, and secondary-phase formation by x-ray diffraction are described in Chapter 4. Atomic-force microscopy is described in Chapter 3.

2.4.1. Scanning-electron microscopy (SEM)

A few different scanning-electron microscopes were used to examine the distribution of the whiskers in the relatively conductive composites: a LEO 1530 (Carl Zeiss Industrial Metrology, Maple Grove, MN), a Hitachi 800S, and a Hitachi S4100 (Tokyo, Japan). Prior to microscopy, the samples were mounted on metal SEM stubs with conductive carbon tape and/or silver paint. It was found that sputter-coating the samples with a thin layer of silver prevented observation of the embedded whiskers and thus all of the presented images show uncoated portions of composite surfaces.

2.4.2. Stereological Measurement of the Distances between SiC Inclusions

Instead of the previously developed stereological method[6,89] for quantifying the microstructure in terms of the trivariate length-radius-orientation distribution of the whiskers, a new method was used to estimate the distances between the SiC inclusions (whiskers, whisker clusters, and any particulate contamination) along the two principal directions of the axisymmetric material. This method acquires the distributions of interparticle distances between the SiC phase strictly in the directions parallel and perpendicular to the symmetry axis (i.e. the hot-pressing direction, HPD). For the former measurement, sets of equally-spaced test lines aligned parallel to the HPD were randomly placed on LEO-SEM images of planes parallel to the HPD. For the latter measurement, equally-spaced test lines with arbitrary alignment were placed on images showing planes perpendicular to the HPD. The distances were then measured manually with ImageJ software to zoom-in on SiC intersections with digital test lines (1-pixel wide). Charging effects (particularly for the more insulating samples) partially obscured the whiskers such that image binarization was inappropriate and human measurement of distances was

required. The number of images and test-lines-per-image analyzed for a given composition-orientation combination was increased until the percent variation observed in as-so-far acquired data seemed sufficiently small. For a given combination, this involved 3-7 images with 4-10 test lines on each image. More images and test lines per image were generally needed for samples with lower SiC_w loading. An example of an SEM image on which stereological test lines were applied is shown in Figure 2.10.

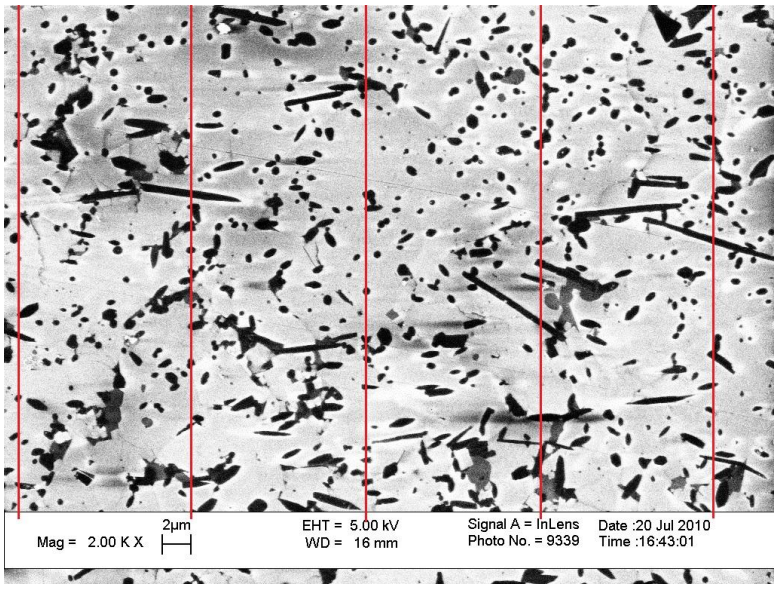

Figure 2.10. Set of five stereological test lines on an SEM image from a hot-pressed 14.5 vol% SiC_w sample. The lines are aligned along the hot-pressing direction, are colored red, and have been thickened by three times for clarity.

2.5. Scope of Characterizations

There was in-depth exploration of the parameter space, but not complete cross-coverage. The various characterization methods were not applied to all types of samples. Table 2.2 shows how the parameter space was explored and which of the various sample types were characterized by the key methods.

Table 2.2. Map showing the key electrical and structural characterization types, electrode types, which samples they were applied to, and how the multi-parameter space was explored. Abbreviations are defined below.

Sample Type	**Porosity**	**Stereology**	**Electrodes**	**Variable DC Bias**	**Coaxial Airline 2-18 GHz**	**Broadband ε* $0.01 \leq f \leq 1.8 \times 10^9$ Hz T=20°C**	**-160 ≤ T ≤ 300°C High-Freq ε* $1 \leq f \leq 1800$ MHz**	**20 ≤ T ≤ 700°C σ_{dc} via Z* $0.1 \leq f \leq 32 \times 10^6$ Hz**	**σ_{dc} via Z* T = 20°C V_{dc} = 0**
DP //	✓ ch4 wp,np,m	x	Ag Pt wp np	ch5-WVR-LC-wp	x	x	x	LC-NS-wp	✓ ch4 wp np
HP // B1	x	Refs. [6,89,110,113] wp	✓AFM, wp Ag,Pt, Paint, ch3, Ref. [110]-LC	✓ch3 LVR wp	x	x	x	x	Ref. [6,9,110] wp np m
HP // B2	✓ ch4 wp,np,m	✓ ch4 ch7 wp	Ag-wp-np-m, Pt-LC-wp	ch5-WVR-LC-wp, LVR-NS	x	✓ ch6 wp np m	✓ ch7-wp-m, np-NS	✓ ch7-wp, np-LC-NS	✓ ch4 wp np m
HP ⊥ B2	X	✓ ch4 wp	Ag wp np	LC-NS-wp	✓ ch6 wp np m	✓ ch6 wp np	x	LC-NS-wp	✓ ch4 wp np
EX // Rod	✓ ch4 wp,np,m	x	Paint ch5 wp np m	✓ ch5-WVR-wp	x	x	x	x	✓ ch4, ch5 wp np m
EX // Slice	LC-NS	x	Ag-wp-np, Pt-LC-wp, Paint-NS, ch5	✓ ch5-WVR-wp	x	✓ ch6 wp np m	x	ch7-LC-WVR-wp	✓ ch5 wp np m

Abbreviations: Batch number (B#), Hot-Pressed (HP), Extruded (EX), Dry Pressed (DP), measurement parallel to processing direction (//), measurement perpendicular to processing direction (⊥), samples which were SiC_w-percolated (wp) non-percolated (np) or whisker-free matrix (m), Temperature (T), Frequency (f), ε* (complex permittivity), Z* (complex impedance), V_{dc} (direct-current bias), Sputtered Silver (Ag) or Platinum (Pt) electrodes, Silver-Painted Electrodes (Paint), Atomic Force Microscopy (AFM), Limited V_{dc} Range associated with electrodes (LVR), Wide V_{dc} Range associated with bulk (WVR), Characterized relatively thoroughly (✓), Limited Characterization (LC), not characterized (x), Chapter with reported results (ch#), Results Not Shown (NS), Reference to a work of another investigator listed in the reference list (Ref #).

CHAPTER 3

ELECTRODE RESPONSE OF HOT-PRESSED COMPOSITES

3.1. Introduction

Impedance spectroscopy studies on percolated Al_2O_3-SiC_w composites made by hot-pressing have shown evidence of two distinguishable semicircles in the complex impedance plane.[110] Interpretations of the semicircles and the underlying physical processes have evolved over time in the literature. In early work, the two semicircles were assigned to the two different phases, Al_2O_3 and SiC_w.[114] Investigators of a similar composite, where the matrix was mullite, proposed a different explanation. The high- and low-frequency semicircles were ascribed to bulk conductivity and space-charge polarization at SiC_w-matrix interfaces, respectively.[17] In the most recent studies of SiC_w-Al_2O_3 composites, the low-frequency semicircle was proposed to be related to polarization at the electrodes and the interpretation of the bulk semicircle was broadened to include interfacial relaxation processes inside the bulk.[6,9]

In this work, the latter explanation is considered because the samples used are from the earlier percolation phenomena studies.[6,9] For these samples, the steady-state conductivity associated with the bulk semicircle was modeled through the connectivity of the whisker distribution via computer simulation.[6] The percolation threshold associated with conductivity parallel to the hot-pressed direction is ~9 vol% SiC_w.[6]

The low frequency semicircle has not been extensively characterized until now. However, previous researchers noted that this feature had a capacitance suggestive of interfacial phenomena[9] and a size which scaled inversely with electrode area and was

independent of sample thickness.[6] These observations were reasonably attributed to Schottky blocking to the SiC whiskers at the electrodes. However, one might also reasonably expect a contribution from interfacial polarization[17] at back-to-back Schottky barriers[19,103] of whisker-whisker interfaces in the bulk (see Figure 1.21). The objective of the present study is to obtain an improved understanding of this feature because it commonly accounts for the majority of the total sample impedance measured.[6,9]

Studies of vapor-deposited metal electrodes on high quality SiC fabricated by chemical vapor deposition are plentiful in the literature.[115-117] Most such metals, including Ag and Pt, form Schottky barriers on the order of ~1 eV.[33] The Schottky barrier height is affected by the SiC polytype, dopant type (p- or n-), dopant concentration,[118] metal work function, measurement method,[119] and interface issues such as the character of the SiC crystal face and surface state pinning of the Fermi level.[104] The reader is referred to a comprehensive review by Porter and Davis.[33] By contrast, there are no other known studies focusing on electrical contacts to SiC whiskers or host composites.

Both of these forms present additional complications. Composite surfaces offer a distribution of SiC_w contact areas and SiC crystal-face types. The SiC_w themselves are created from sand and agricultural waste (possibly rice hulls) in a pyrolysis process.[28,31] The resulting whiskers grow along <111> directions and contain a high density of partial dislocations and stacking faults.[1] Such SiC_w are nominally of the β polytype but the persistence of the latter defect results in a complex mixture of thin β and α lamellae normal to the grow axis.[1] The doping of the SiC_w is also unknown. In the energy dispersive x-ray analysis of Zhang *et al.* there is evidence of Al^{3+} from alumina doping whiskers to ~1-2 atomic % after hot-pressing at 1600°C for 40 min.[120] In as-fabricated

whiskers, a much lower impurity concentration of 300 ppm was reported for Al which was the only Column III-V impurity.[28] Additional results by Ou *et al.* have indicated that the electrical conductivity of polycrystalline SiC within SiC-AlN composites increases with increasing AlN content.[121]

It would be difficult to account for all of the issues mentioned above in Schottky blocking to SiC_w composites. Fortunately, the identity of the contact metal is easy to control. The experiments described in this chapter employed contacts of the same type on both sides of samples to simplify the problem through symmetry. This approach ideally results in two Schottky barriers of the same height. Moreover, the electrical response of a semiconductor sandwiched between two similar metal electrodes is like that for back-to-back Schottky barriers[15] and some theoretical groundwork[19] has been developed and tested for analyzing the latter situation. Adams and coworkers[103] considered the electrical properties of polycrystalline ceramics in terms of symmetrical back-to-back Schottky barriers at the interfaces of semiconducting grains. They invoked the model[19] developed by Mukae *et al*. in which the conductive intergranular interphases are approximated as metals and the measured specific capacitance C_s accounts for both the forward biased and reverse biased depletion regions.[19] This capacitance can be described by

$$(1/ C_s - 1/2C_0)^2 = 2 (\Phi_B + V)(\varepsilon_s q N_d)^{-1} \qquad (3.1)$$

where V is the dc bias across the symmetrical back-to-back barrier, C_0 is the specific capacitance with no applied bias, Φ_B is the Schottky barrier height, q is the elemental charge, and N_d is the charge carrier concentration in the semiconductor. If the squared term is plotted as a function of V, a straight line is produced and the values of Φ_B and N_d can be derived from manipulations of the slope and intercept.

The capacitance-bias data for the above analysis can be obtained from impedance spectroscopy. In the complex impedance plane, Schottky blocking is often manifested as a semicircle that can be modeled by an equivalent circuit of a resistor and capacitor in parallel.[103,122-124] The associated resistance R and capacitance C are associated with space-charge polarization in the depletion region(s) and are related by

$$\omega RC = 1 \tag{3.2}$$

where ω is the characteristic frequency of the relaxation process. Such a model has been used for blocking from both single[122-124] and symmetrical[103] Schottky barriers. The dependence of R on bias can be understood from the Schottky diode equation.

The electrical current I through a single Schottky barrier ideally obeys

$$I = A_j B_R T^2 \exp(-q\Phi_B/kT)\exp(qV/nkT) \tag{3.3}$$

where A_j is the junction area, B_R is the Richardson constant, T is the absolute temperature, k is the Boltzmann constant, n is an ideality factor, and V is the forward bias applied across the barrier.[118] Recasting this non-linear direct current-voltage response into $V=IR$ form implies that an expression for the dc resistance R includes an inverse exponential dependence on applied voltage. The data of Adams *et al.*[103] shows that the dc resistance arising from symmetrical Schottky barriers is controlled by such an exponential and can be fitted to

$$R = R_0 \exp(\alpha V_{dc}) \tag{3.4}$$

where V_{dc} is total dc bias applied to the sample, subscript '*0*' designates the value at zero dc bias, and α determines the strength of the exponential dependence and is negative.[103]

These authors proposed that the strength of the R-V_{dc} dependence is determined by the division of V_{dc} among the interfacial barriers and the results of the present thesis support this view.

3.2 Experimental Methods

Hot-pressed composite discs of Batch #1 containing different volume fractions (V_w) of SiC_w in an alumina matrix were studied. In particular, electrically-percolated samples with V_w = 0.10, 0.20, 0.30 were focused on, were sectioned along the hot-pressing direction with a diamond saw into half- and quarter-cylinder shapes, and were ground and polished with diamond media. Samples for atomic force microscopy (AFM) characterization underwent additional polishing with 0.25 μm diamond paste. AFM studies were conducted on V_w = 0.20 samples and were adhesively mounted on metal chucks with conductive silver paint which simultaneously provided a backside electrical contact of macroscopic area. A Veeco Dimension V Scanning Probe Microscope was used with a NSC36 Cr/Au tip.[18] The dc bias was applied to the tip and the chuck was grounded. Current and topography information were acquired in parallel. The conductive AFM experiments were carried out at the Center for Nanophase Materials Sciences at Oak Ridge National Labs, a facility which is funded by the Scientific User Facilities Division, Office of Basic Energy Sciences, U.S. Department of Energy.

Three different electrode types were studied: Ag paint, sputtered Ag, and sputtered Pt. These were applied to sample surfaces after cleaning, as described in Sections 2.2.3 and 2.2.4. Samples with and without electrodes are shown in Figure 3.1.

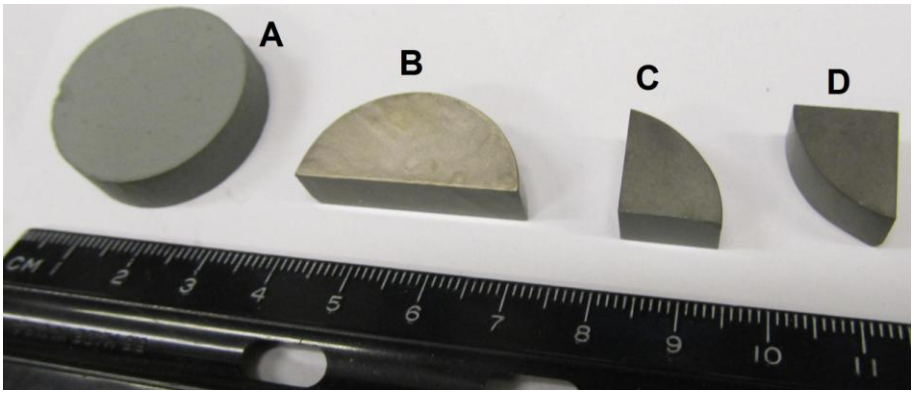

Figure 3.1. Hot-pressed Al_2O_3-SiC_w samples of Batch #1. (A) As-pressed disc. (B) Half of a disc with silver-paint electrodes. (C, D) Quarters of discs with sputtered electrodes.

AC electrical measurements were conducted with the electric field applied parallel to the hot-pressing direction. These measurements were performed primarily with the Solartron 1260 Impedance Analyzer, and the Solartron 1296 Dielectric Interface was additionally used for samples with low whisker content (≤10 vol%). For samples with high whisker content (≥20 vol%), the HP 4192A LF Impedance Analyzer was also used. All of the measurements reported used an ac amplitude 0.1 V_{rms}.

In the complex impedance plane, the low-frequency semicircle was modeled in accordance with Equation 3.2, which was used to calculate its capacitance C_c. The resistance R_c was derived from the semicircle width on the real axis. The characteristic frequency was calculated from $\omega_c = 2\pi f_c$ where f_c was the measurement frequency producing the largest magnitude of imaginary impedance. All necessary fitting, extrapolation, and interpolation employed ZView2 software (Scribner Associates, Inc.). Extrapolation and interpolation were sometimes needed to determine R_c and ω_c, respectively. In some cases, equipment limitations prevented measurement of ω_c. These

situations most often occurred at higher values of dc bias or very low small values of R_c. Extrapolation was never used to determine ω_c, as such would be unreliable.

Due to ageing effects, samples were measured as soon as possible after electrode deposition. All electrode properties that are reported in this paper, except for those related to ageing, were derived from measurements conducted within an hour after electrode fabrication. For ageing experiments, samples having 10-30 vol% SiC_w were simply set out and exposed to open air in a laboratory having normal room temperature, pressure, and humidity. Samples were set on their sides to avoid physical damage to the electrodes on their faces.

3.3. Results and Discussion

3.3.1. Macroscopic Electrical Properties

Figure 3.2a shows a complex impedance spectrum for a sample with $V_w = 0.10$ and how it was modeled with an equivalent circuit. The two semicircles are modeled through a series of two parallel resistor-capacitor circuits. As in previous works[6,9] the higher frequency semicircle is severely depressed and is attributed to conduction processes occurring in the bulk. The low frequency semicircle always had positive capacitance and is assigned to the contact/electrode material. Similar to the contact resistance R_c, the bulk resistance R_b was obtained from the semicircle width along the abscissa. In samples with $V_w \leq 0.09$, only one semicircle could be detected because the electrode response could not be distinguished from the large bulk impedance. Experimentation on such samples was relatively limited.

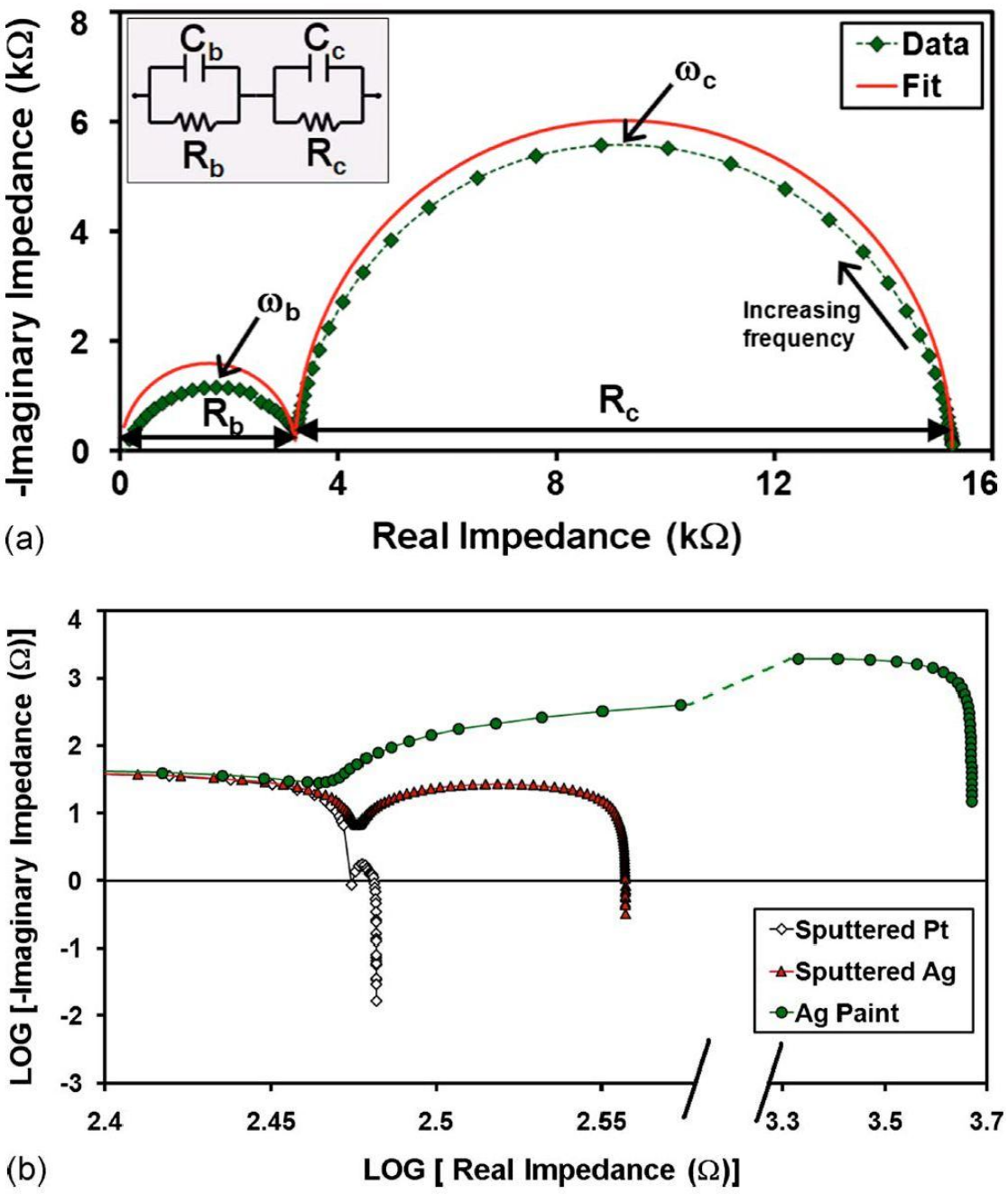

Figure 3.2. (a) Complex impedance spectrum and fit to equivalent circuit model (inset) for a representative sample having 10 vol% whiskers and Ag paint electrodes. The labeling shows how information was extracted from experimental data. Fitting parameters were R_c = 12.055 kΩ, R_b = 3.21 kΩ, C_c=10.128 nF, and C_b = 10.69 pF. (b) Complex impedance data for a typical sample with 20 vol% whiskers and different electrodes. The plot employs log scales and a change in scale on the abscissa for clearer comparison. Although Ag paint data falling within the change in scale are not shown, they did smoothly connect the broken curve.[18]

Figure 3.2b shows the typical effect of the electrode material on a sample containing 20 vol% whiskers. The high frequency semicircle and R_b are relatively unaffected, confirming their association with the bulk. However, the size of the low frequency semicircle varies drastically with the different electrode materials. The use of log scales[125] and the change of scale along the abscissa emphasize the order-of-magnitude differences. These differences suggest that the low frequency feature depends primarily on the electrodes and that both the work function and the morphology of the contact metal strongly influence the blocking behavior. Since the work function[33,119] of Pt (5.65 eV) is much higher than that of Ag (4.3 eV), Pt contacts are expected to result in smaller Schottky barriers to p-type semiconductors.[118] Therefore it is suspected that the majority of the whiskers have p-type conductivity, perhaps arising from Al^{3+} doping from alumina during hot-pressing.[120]

The observed behavior of all samples having $V_w \geq 0.10$ was consistent with the electrode dependences shown in Figure 3.2b. Sputtered Pt contacts provided much lower contact resistance compared to sputtered Ag, and sputtered Ag electrodes acted as superior contacts compared to Ag paint. By using multiple samples to quantify average properties for each composition-electrode combination, Table 3.1 was produced. Two cells are left empty because the low frequency feature from freshly sputtered electrodes could not be distinguished from the much-larger bulk impedance when $V_w = 0.10$. The table shows that the order-of-magnitude differences in R_c caused by the differing electrode materials are maintained in area-normalized specific contact resistance ρ_s values, despite large degrees of scatter. Such variation is expected to arise due to the differences in the whisker distribution and contact area on the composite surface. These

parameters can be expected to vary somewhat because of the grinding process (which may be slightly different for different electrodes on the same sample) and also depend on the actual whisker distribution in the composite bulk (which can vary between samples).

Table 3.1. Average characteristics of the low-frequency semicircle observed in the complex impedance plane for different combinations of whisker loading and electrode material. All values are from measurements with freshly applied electrodes and zero dc bias. Error values refer to standard deviations from averaging over several samples measured for each combination. Units for the specific contact resistance (ρ_s), specific capacitance (C_s), and characteristic frequency (ω_c) are $\Omega \cdot cm^2$, F/cm^2, and rad/s, respectively. Values of ρ_s were calculated by multiplying R_c by the area of the electrodes. Values of C_s were calculated by dividing C_c by this area. Reprinted with permission from Ref. 18 (Copyright 1998, American Institute of Physics).

V_w (%)	**Conductive Ag Paint**	**Sputtered Ag**	**Sputtered Pt**
10	$\rho_s = (4.5 \pm 1.6) \times 10^4$ $C_s = (1.47 \pm 0.20) \times 10^{-9}$ $\omega_c = (1.68 \pm 0.93) \times 10^4$	Not Applicable	Not Applicable
20	$\rho_s = (1.07 \pm 0.57) \times 10^4$ $C_s = (2.18 \pm 0.56) \times 10^{-9}$ $\omega_c = (5.4 \pm 2.8) \times 10^4$	$\rho_s = 165 \pm 51$ $C_s = (4.14 \pm 0.90) \times 10^{-8}$ $\omega_c = (1.69 \pm 0.29) \times 10^5$	$\rho_s = 31.0 \pm 7.3$ $C_s = (2.95 \pm 0.56) \times 10^{-8}$ $\omega_c = (1.16 \pm 0.30) \times 10^6$
30	$\rho_s = (8.54 \pm 0.28) \times 10^3$ $C_s = (4.8 \pm 1.3) \times 10^{-9}$ $\omega_c = (3.1 \pm 1.7) \times 10^4$	$\rho_s = 30.2 \pm 17.6$ $C_s = (1.66 \pm 0.54) \times 10^{-7}$ $\omega_c = (2.07 \pm 0.28) \times 10^5$	$\rho_s = 1.4 \pm 1.3$ $C_s = (2.5 \pm 1.0) \times 10^{-7}$ $\omega_c = (1.33 \pm 0.49) \times 10^6$

The trends in the data of Table 3.1 also provide additional insight. The characteristic frequency ω_c of the relaxation process, reflected by the low frequency feature, is subject to order-of-magnitude differences depending on the electrode material and has no clear dependence on whisker loading fraction. This suggests that the low frequency process occurs at the electrodes and not in the bulk. For Ag paint electrodes, the specific capacitance C_s is much lower than for the sputtered electrodes. Such decreased capacitance is partially attributed to interfacial layers of polymer between whiskers and Ag particles of the paint. The reduced C_s also suggests diminished metal-whisker contact area. One can imagine that the amount of interfacial area between whiskers on the composite surface and metal particles in the paint is subject to variation and is less than that from sputtered metal films. In Table 3.1, the importance of metal contact area to surface whiskers is also supported by dependences on whisker loading. As loading increases for a given electrode material, C_s increases and ρ_s decreases. In Section B, it is shown that the strengths of these relationships are consistent with the interpretation of the AFM results.

The dependence of representative complex impedance spectra on total applied dc bias V_{dc} is shown in Figures 3.3a and 3.3b for samples with Ag paint and sputtered Ag electrodes for the 10% and 20 vol% SiC_w specimens respectively. As V_{dc} increases, the bulk semicircle is unaffected and therefore the conduction processes occurring in the bulk are ohmic. In contrast, the size of the low frequency semicircle and its associated conduction process are strongly affected by dc bias. This result was generally observed for samples having distinguishable electrode semicircles and was insensitive to bias polarity.

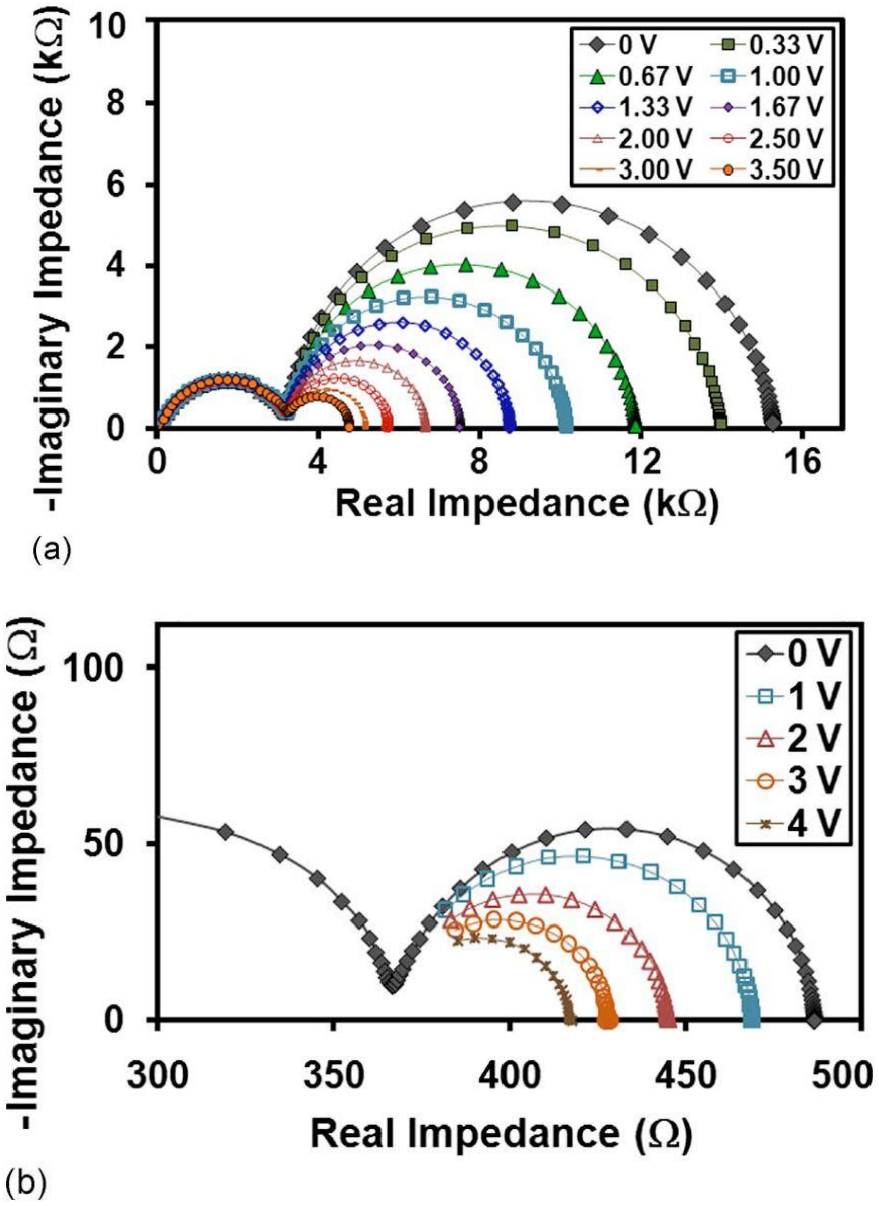

Figure 3.3. (a) Effect of dc bias on the complex impedance spectrum of a sample having 10 vol% whiskers and Ag paint electrodes. The bulk feature is unaffected but the electrodes semicircle shrinks with increasing DC bias. This general behavior was observed for 10-30 vol% loading and all electrode types. (b) Similar data from a sample having 20 vol% whiskers and sputtered Ag electrodes. An equipment effect prevented the full contact semicircle from being captured.[18]

In Figure 3.3b, portions of some contact semicircles could not be obtained due to equipment limitations. However, since the tops of the semicircles were captured, it was

possible to estimate ω_c and thus C_c and C_s for these partial semicircles. Unfortunately, this was usually not the case for samples having very low R_c or those subjected to larger V_{dc}. This effect limited the range of V_{dc} that could be applied and affected several samples having Pt electrodes.

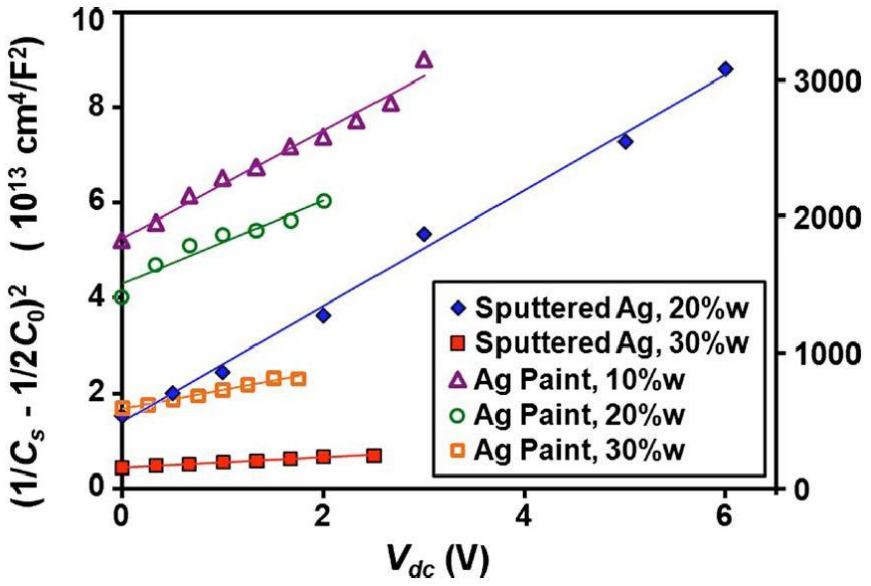

Figure 3.4. Fits of C_s-V_{dc} data for five representative samples to the model of symmetrical Schottky blocking proposed by Mukae *et al.*[19] The left-hand y-axis scale applies to the filled data points for sputtered Ag. The right-hand y-axis scale applies to the hollow data points for Ag paint.[18]

The V_{dc}-induced shrinkage of the low-frequency semicircle shown in Figures 3.3a and 3.3b was accompanied by increasing ω_c, decreasing R_c, and decreasing C_c. In Figure 3.4, the C_s data for samples representative of different electrode-loading combinations are fit to Equation 3.1, which models the capacitance arising from the depletion regions of two oppositely biased Schottky barriers of equal height. The correlation coefficients for the fitting lines ranged from 0.93 to 0.995 and four out of five were ≥0.98. Such good fitting establishes the fundamental source of the low frequency feature as blocking from

symmetrical Schottky barriers. This result is not surprising because the physical situation underlying Equation 3.3.1 is expected to be similar[27] to that for samples in the present study, in terms of the two electrode-composite interfaces of each sample. These interfaces are oppositely polarized from the applied dc bias and therefore one is expected to encompass forward-biased metal-whisker Schottky junctions and the other reverse-biased metal-whisker Schottky junctions. The strong dependences on electrode material established in Figure 3.2 and Table 3.1 affirm that this blocking occurs at the electrodes and not at whisker-whisker interfaces in the bulk. Figure 3.5 shows an equilibrium band-diagram model of the situation at the electrodes which is based on principles of semiconductor physics.[118] In this model, it is assumed that the SiC phase in the composite bulk is continuous (i.e., the effects of SiC_w/SiC_w interfaces are neglected) and p-type such that its work function exceeds that of the metal electrodes.

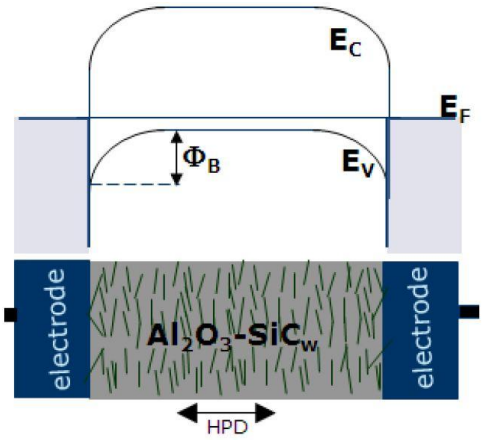

Figure 3.5. Band model of a hot-pressed composite based on assumptions discussed above.[84] The electron energy levels in the SiC corresponding to the top of the valence band (E_V), the bottom of the conduction band (E_C), and the system-wide equilibrium Fermi Level (E_F) are labeled.

Figure 3.6a shows how R_c decreased exponentially with V_{dc} for all electrode materials and loading fractions. As discussed earlier, such dependences are expected for symmetrical Schottky blocking and follow from Equation 3.4. However, the slopes (α_c) of the fitting lines in Figure 3.6a are very shallow for sputtered electrodes thus indicating that these exponential dependences are relatively weak and unaffected by the filler content. In fact, some plots of R_c as a function of V_{dc} for sputtered samples could be fitted linearly with minimal decreases in the goodness of fit. By contrast, R_c-V_{dc} data for samples having Ag paint electrodes exhibited strong exponential dependences which could not be ignored and which are strengthened by increasing whisker content.

The different dependences of R_c on V_{dc} for painted and sputtered electrodes can be understood in terms of the magnitudes of the voltage drops existing across the electrode-composite interfaces. By applying Kirchoff's Voltage Law to the equivalent circuit model of Figure 3.2a, the key parameter to consider is

$$\kappa_c = R_c / (R_c + R_b) \qquad (3.5)$$

which estimates the fraction of the total V_{dc} voltage drop that occurs at the electrode-composite interfaces, i.e., the contacts. The leftover dc bias is $V_{dc}(1-\kappa_c)$ and drops across the composite bulk. It is clear in Figures 3.3a and 3.3b that κ_c is not constant and decreases with increasing V_{dc}. When $V_{dc} = 0$, $R_c = R_{c0}$, and $\kappa_c = \kappa_{c0}$; since the bulk semicircle was independent of bias over the entire measured range, it is generally true for hot-pressed samples that $R_b = R_{b0}$. To facilitate comparisons, κ_{c0} is used as a benchmark value in the following examples and analysis of this Chapter.

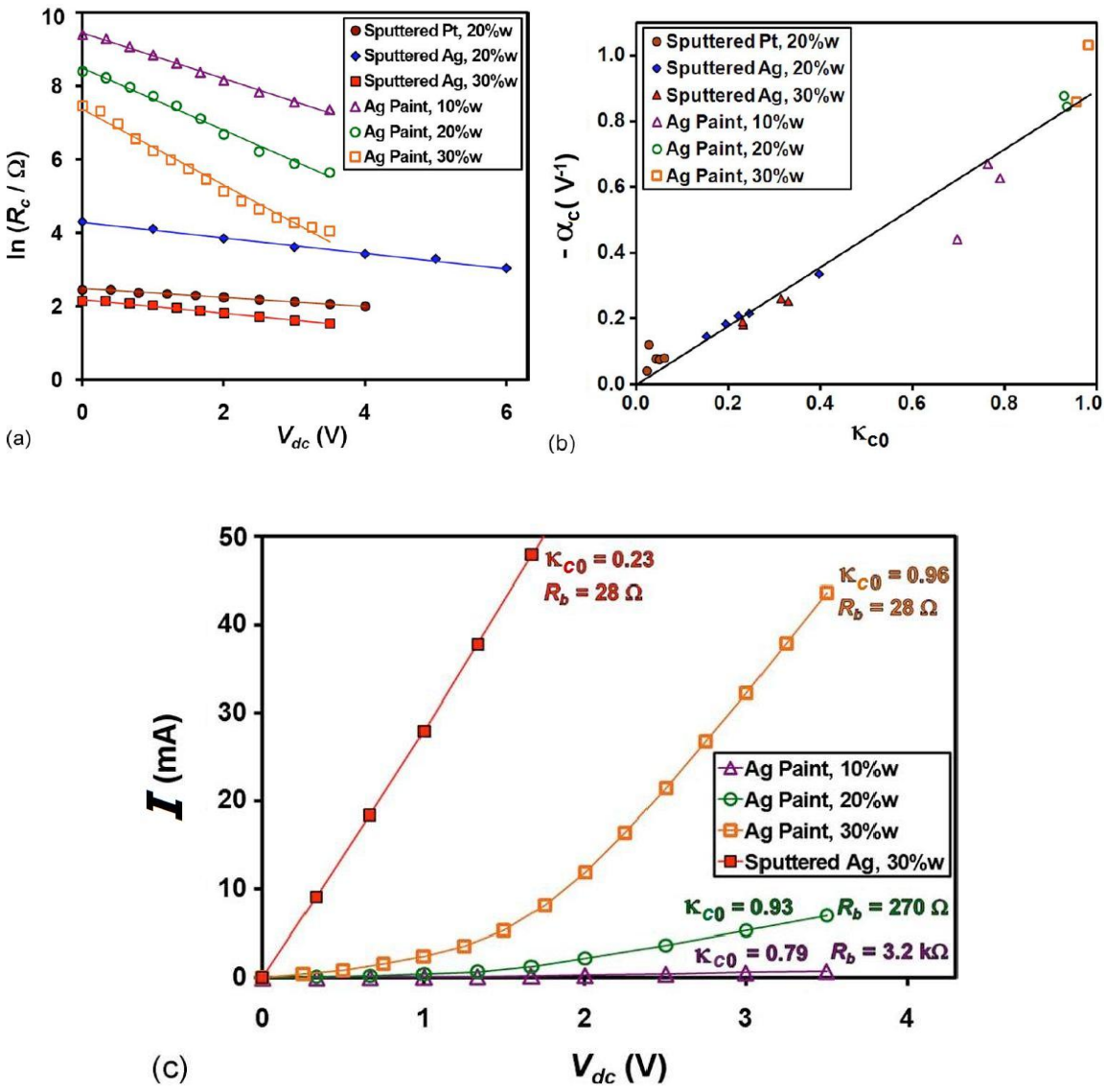

Figure 3.6. (a) The dependence of contact resistance R_c on V_{dc} for five representative samples. (b) Plot of $-\alpha_c$ as a function of the voltage correction factor κ_{c0} for different combinations of electrode material and whisker content. Each data marker represents a different sample. (c) The dependence of current on dc bias for three typical samples. The two datasets with square data markers refer to different electrode types on the same 30 vol% SiC_w sample. The bias-partitioning factor, κ_{c0}, and bulk resistance, R_b, are also listed for each dataset.[18]

For a sample having 30 vol% whiskers and Ag paint electrodes, R_b and R_{c0} are on the order of ~50 Ω and ~2 kΩ, respectively. Thus, $\kappa_{c0} \sim 0.98$ and the vast majority of the V_{dc} drops at the electrode-composite interfaces. Thus it is not surprising that the exponential dependence of R_c on V_{dc} is strong and $|\alpha_c|$ is large. If the electrode is changed to sputtered Ag, R_{c0} and κ_{c0} become ~15 Ω and ~ 0.23, respectively. Thus, when $R_b > R_{c0}$ only a small fraction of V_{dc} drops at the electrode-composite interfaces and $|\alpha_c|$ is small.

In Figure 3.6b, the trend of $\kappa_{c0} \propto |\alpha_c|$ suggested by the above examples is established with data from various samples having different combinations of electrode material and whisker content. The correlation coefficient of the fitting line is 0.96. Based on these results, κ_{c0} acts as a correction factor which can be used to estimate the bias dependence of R_c via

$$\alpha_c = (-0.89\ V^{-1})\ \kappa_{c0} \tag{3.6}$$

for 10-30 vol% SiC_w-Al_2O_3 composites of Batch #1. The -0.89 V^{-1} constant seems to apply to this composite system but α_c and κ_{c0} are not true materials properties. In Equation 3.5, substituting simple resistance equations $R_b = \rho_b z/A_{cs}$ for the bulk and $R_{c0} = \rho_s/A_{cs}$ for the contacts reveals that κ_{c0} and thus α_c are independent of contact area A_{cs} but not sample thickness z when samples have simple shapes. The bulk resistivity ρ_b in general composite systems is sensitive to the filler loading and distribution, especially around the percolation threshold where it may change by many orders of magnitude.[126,127] Thus, when an insulator-semiconductor composite experiences Schottky barrier blocking at the electrodes, the response of the electrode blocking to bias will be affected by the composite bulk in terms of ρ_b, z, and ρ_s due to Equations 3.4-3.6.

In Figure 3.6b, the data may be viewed as having significant scatter or as being better-fitted by two separate lines (not shown), one for the sputtered electrodes and the other for painted electrodes. This might be explained by the bias dependence of κ_c, which is not accounted for in κ_{c0}. For Ag painted electrodes, the denominator in Equation 3.5 changes significantly with V_{dc} because $R_{c0} > R_b$ for 10 vol% samples, $R_{c0} >> R_b$ for 20-30 vol% samples, and R_c has a strong exponential dependence on V_{dc}. By contrast, the effect of R_c on the same denominator is comparably weak for sputtered electrodes because $R_b > R_{c0}$ and the dependence of R_c on V_{dc} is weaker.

Figures 3.6a and 3.6b can also be considered in terms of the electric field E across an average Ag/SiC_w interface that follows from the partitioning of V_{dc} between the bulk and contacts. If one assumes a thin interfacial layer with constant thickness t_{ic}, then $E = \kappa_{0c}V_{dc}/t_{ic}$ and $dE/dV_{dc} = \kappa_0/t_{ic}$. It is then apparent from Figure 3.6a that $|\alpha_c| \propto dE/dV_{dc}$. Such thin interfacial layers (~ 1 nm) could form by partial oxidation of the SiC_w on the sample surfaces after grinding in air. The presence of such oxide layers implies metal-insulator-semiconductor structures which require carrier tunneling across the oxides[128] in addition to Schottky-modified thermionic emission for interfacial conduction. Field emission could also be expected to take on a larger role or supersede Schottky emission at higher electric fields.[129] The larger κ_{c0} values for painted compared to sputtered electrodes suggests higher E and that such a changeover to field emission might contribute to the apparently steeper slope for the data points of painted samples in Figure 3.6b. However, results in Chapter 5 suggest that the bias-dependence of κ_c is the better explanation.

Figure 3.6c shows current-voltage (I-V_{dc}) characteristics for three representative samples. The I values were calculated using total sample dc resistances, i.e., from $V_{dc}/(R_b + R_c)$ with data like that shown in Figures 3.3a and 3.3b. In Figure 3.6c, the two datasets assigned to 30 vol% are for the same composite sample but with different electrodes. The behavior of the sample with sputtered Ag contacts appears to be ohmic. This deceptive result was seen for all samples with sputtered electrodes and can be explained by the relatively low value of κ_{c0}. For samples with painted electrodes, κ_{c0} is larger and non-ohmic I-V_{dc} behavior similar to that expected[15] for symmetrical Schottky barriers results. The non-linearity is barely detectable for 10 vol% SiC_w samples but becomes more dramatic as κ_{c0} increases. Such distinctly non-ohmic behavior and its dependence on contact material affirm the presence of Schottky energy barriers at the electrode-SiC_w interfaces. Current constriction at SiC_w contact points to Ag particles in the paint may serve to magnify the non-linearity caused by the energy barriers but by itself would only add an ohmic series resistance.

Figure 3.7a shows how ω_c increased with V_{dc} for both sputtered and painted Ag contacts of various loading fractions. For the sputtered Ag electrodes, the dependence of ω_c on V_{dc} showed slight positive curvature for some samples, but the relationship was usually best fit by linear regression. The resulting slopes were 46.5 ± 7.9 ms^{-1} and 49.2 ± 6.9 ms^{-1} for groups of 20 and 30 vol%, respectively, and thus statistically independent of filler content. For samples having Ag paint electrodes, the dependence of ω_c on V_{dc} is excellently modeled with exponential dependences, which increase in strength as whisker content increases. Such fits have correlation coefficients ≥ 0.98.

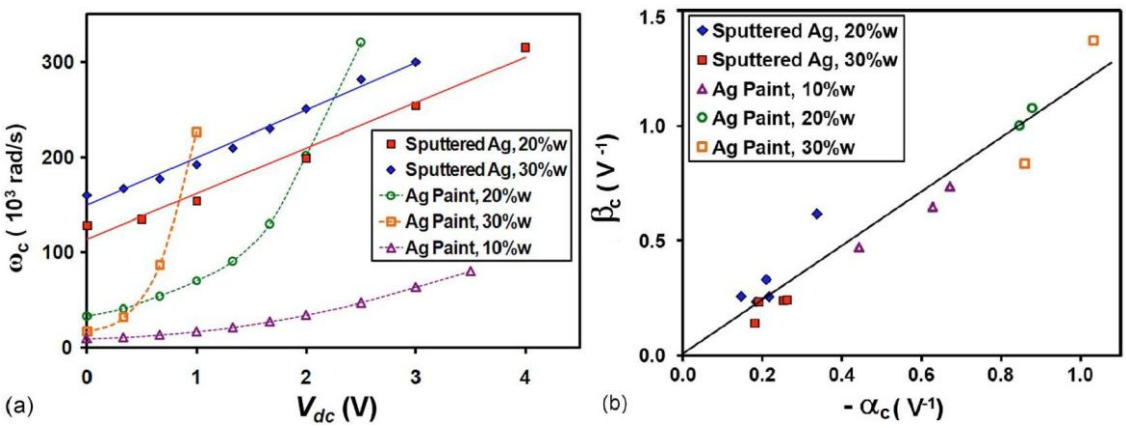

Figure 3.7. (a) The dependence of relaxation frequency, ω_c, on V_{dc} for five representative samples. Regression lines are shown for the sputtered samples. (b) Plot of β as a function of $-\alpha_c$ for various combinations of electrode material and whisker content. Each data marker represents a different sample.[18]

The respectively exponential and linear dependences of ω_c on V_{dc} for painted and sputtered electrodes follow directly from Equations 3.2 and 3.4. If one substitutes the former equation into the latter and approximates C as a constant, ω is expected to depend on applied bias V_{dc} in the form

$$\omega = \omega_0 \exp(\beta V_{dc}) \qquad (3.7)$$

where $\omega_0 = (R_0 C)^{-1}$ and $\beta = -\alpha$. This result was applied to data from the (contact) electrode semicircle, and in Figure 3.7b, the experimentally determined value of β_c is plotted as a function of $-\alpha_c$ for various samples having different combinations of electrode material and whisker content. The resulting slope of the regression line is 1.18, which is reasonably close to the ideal value of unity, and the correlation coefficient is 0.93. These good results affirm the validity of the equivalent circuit model and the dominating effect of the exponential dependence of R_c on V_{dc} in determining the ω_c-V_{dc} relationship. The $C_s \propto V_{dc}^{-1/2}$ relationship implied by Equation 3.3.1 is insignificant

compared to the exponential dependence but may be responsible for some of the scatter and the non-ideal slope in Figure 3.7b.

Based on the above understanding of the voltage drop, it seemed reasonable to modify C_s-V_{dc} data like that plotted in Figure 3.4 to estimate values for the Schottky barrier height and carrier concentration. The V_{dc} axis was corrected with a multiplied factor of κ_{c0} and the capacitance function was modified with a multiplied factor of V_w to account for the limited amount of composite surface area that was SiC. These corrections were necessary in order to obtain reasonable values for Φ_B. Without such corrections, an unreasonable range of values for the Schottky barrier height, Φ_B, would be obtained (1 to 7 eV) for sputtered Ag electrodes. After correction, Φ_B values obtained ranged from 0.2-1.6 eV for sputtered Ag electrodes and 3.3-4.6 eV for Ag paint electrodes. The former range of corrected values compares well to the 0.8-1.2 eV range reported for Ag deposited onto SiC by thermal evaporation in vacuum.[119] This agreement suggests that the C_s-V_{dc} analysis is reasonable and could be applied to other composites systems with semiconducting fillers within insulating matrices. Using a relative dielectric constant of 9.7 for β-SiC,[130] N_d was estimated for surface whiskers at ~10^{18}-10^{19} cm^{-3} for sputtered Ag samples and ~10^{17} cm^{-3} for Ag painted samples.

The above estimations of N_d and Φ_B can be regarded as average values relating to a vast number of whisker-metal interfaces. It is reasonable to imagine that particular SiC_w contacts with the largest contact areas and smallest Φ_B values have disproportionate influence on the averages. All of the N_d values imply relatively high dopant concentrations in the whiskers. Such doping could result from Al diffusion during hot-pressing[120] or impurities in the as-fabricated whiskers, [28] as discussed earlier. The

different values of N_d and Φ_B found for painted compared to sputtered Ag electrodes might be due to effects of the paint microstructure. For example, paint usage may result in an interfacial layer due to the organic polymeric binder[131] of the paint wetting the metal and ceramic because both have relatively high surface energy.[132] Moreover, the flake morphology[131] of the Ag in the paint likely reduces the Ag/SiC_w interface area and this would translate into an inadvertent decrease in specific capacitance, C_0, since the normalization uses the larger nominal total-electrode area. This could inflate Φ_B values for the paint because the intercept in Figure 3.4 is $1/4C_0^2$ (since $C_s = C_0$ when $V_{dc} = 0$) and is proportional to Φ_B via Equation 3.1. By creating an appearance of reduced charge density, an underestimated C_0 could also result in unduly deflated N_d values for the Ag paint case.

3.3.2. Microlevel Electrical Behavior

Figure 3.8 shows an SEM image of a typical distribution of whiskers on the composite surfaces of interest. Atomic force microscopy was used to help understand how current is distributed as it passes through such surfaces from a metal contact. Figure 3.9a-c compares current-mode images of a single region on a $V_w = 0.20$ sample with three different values of dc bias applied to the tip. For all cases, it is clear that no significant current flows through the interfaces between alumina and the metal tip. The whiskers are demonstrated as the conductive phase in Figure 3.9a where they are brightly highlighted by a strong current signal compared to the matrix. This image was acquired with an applied dc bias of +10 V. Figure 3.9b was acquired with 0 V dc bias and shows that the same whiskers did not carry any significant current or show significant contrast with the

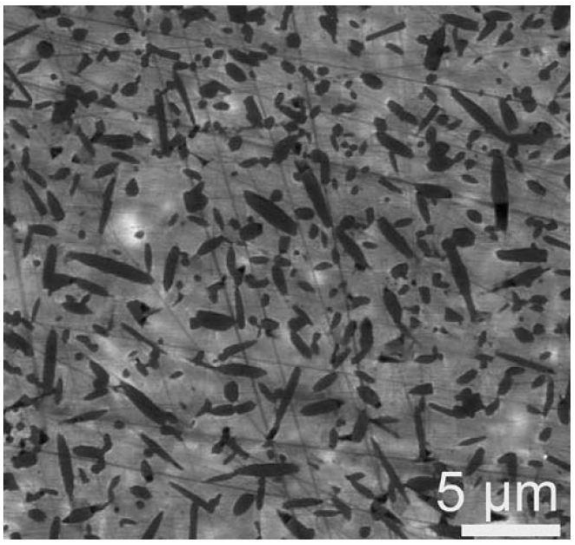

Figure 3.8. Scanning electron microscopy image of whisker morphology on the plane perpendicular to the hot-pressing direction in a sample having 30 vol% whiskers.[18]

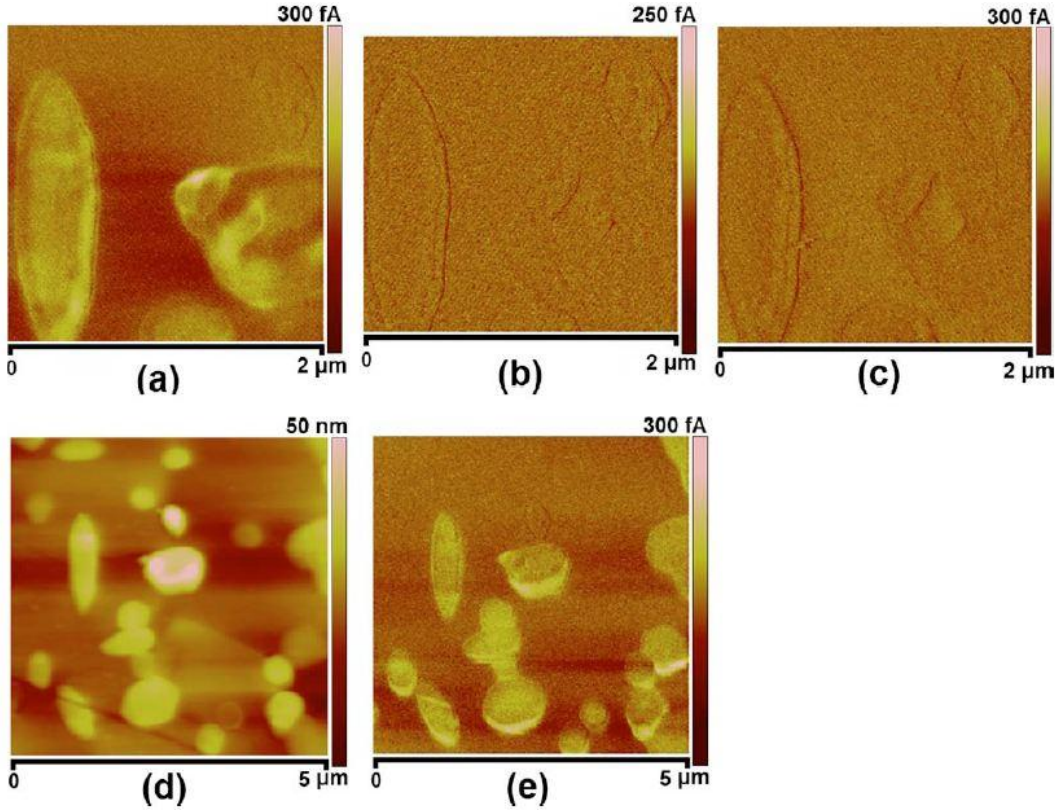

Figure 3.9. Parts a-c show current images of a single region on the surface of a sample containing 20 vol% whiskers. The dc bias on the tip is different for each: (a) +10 V (b) 0 V (c) -10 V. Topographic and current images of a larger region taken with +10 V bias are shown in parts d-e, respectively.[18]

matrix. This different response suggests that the positive bias functioned in overcoming some barrier for the otherwise conductive whiskers. In Figure 3.9c, the dc bias on the metal tip was -10 V and again there was no significant current through the whiskers. Such polarity in the bias response is expected from Schottky diodes and cannot be attributed to symmetrical back-to-back barriers in the bulk. The absence of such bias polarity in macroscopic experiments is attributed to the associated samples having symmetrically-applied large-scale electrodes. Taken together, Figures 3.9a-c confirm that Schottky blocking occurs at metal-whisker junctions on the composite surface and provide evidence that such blocking is the microscopic source of the low frequency semicircle observed in impedance spectra and the associated dependences on V_{dc}.

In Figures 3.9d-e, two AFM images of the same region on a 20 vol% sample are shown. The former and the latter show the topographic and current information, respectively. It is useful to compare the two images: since certain whiskers appearing in the topography do not appear in the current image, it is inferred that those whiskers do not conduct significant current through the sample because they are not involved in percolating linkages of whiskers. This refines the interpretation confirmed above: the low-frequency semicircle in the complex impedance plane is caused by Schottky blocking at metal-whisker junctions, but only those of whiskers connected to percolating linkages. With macroscopic electrodes, through-thickness current is concentrated in such linkages because they provide paths of drastically lower resistance and therefore any blocking contribution from non-percolated whiskers is negligible. This conclusion gains additional support from data in Table 3.1 which is inconsistent with the theory that all surface whiskers contribute to the semicircle.

If one assumes that all SiC_w contact areas on the composite surface contribute equally, the bulk whisker volume fraction V_w must equal the fraction of the composite surface area accounted for by the contributing whiskers A_{cw}, because of the stereological equivalence of area and volume fractions.[133] It follows that $dA_{cw}/dV_w = 1$ and the values of ρ_s and C_s for a given electrode material in Table 3.1 would be expected to scale linearly with nominal V_w to adjacent cells. The ideal scaling factor is usually 1.5, and in one case, it is 2. However, examination of Table 3.1 reveals that the experimental scaling factor is usually much larger and has a mean of 6.2. This implies whisker content has a stronger effect and that $dA_{cw}/dV_w > 1$.

Such a result is consistent with the explanation of Figure 3.9d-e. If the only contributing whiskers are those involved in percolating linkages, $A_{cw} \neq V_w$ must be true in general because at the percolation threshold $V_w \sim 0.09$ and A_{cw} is smaller and very close to zero. Moreover, at the limit of $V_w = 1$, $A_{cw} = 1$. Therefore, $dA_{cw}/dV_w > 1$ on average between the percolation threshold and $V_w = 1$.

3.3.3. Electrode Ageing Behavior

Figure 3.10a shows the time dependence of the complex impedance spectra of a 30 vol% SiC_w sample with Pt electrodes. The times listed are those which passed under normal room conditions of temperature, pressure, and humidity and are referenced to when the sample was brought back to atmosphere from the vacuum of the sputtering chamber. It can be seen in Figure 3.10a that the bulk feature, which appears at the highest frequencies, was unaffected by the passage of time. The bulk semicircle always appeared in the fourth quadrant for 30 vol% samples and in the first quadrant for all other

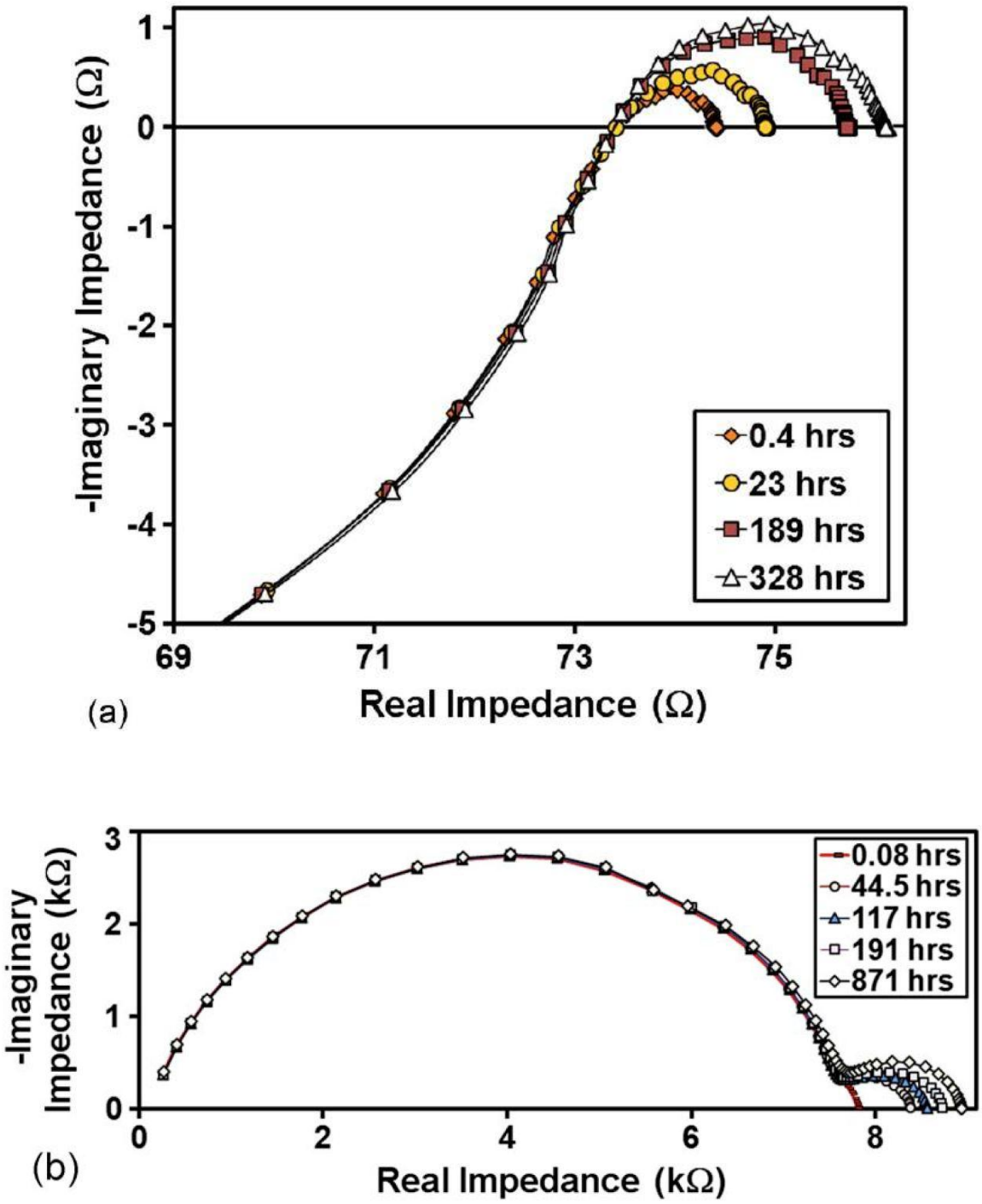

Figure 3.10. (a) Nyquist plot showing the growth of the contact semicircle with time (under normal room conditions) after electrode deposition for a typical 30 vol% SiC_w sample with sputtered Pt contacts. The bulk feature appears as an upside-down partial semicircle which could be reasonably extrapolated to the origin, but not all of it is shown. (b) Similar plot for a sample with 10 vol% SiC_w and sputtered Ag contacts. The presence of a low-frequency semicircle is revealed after sufficient time.[18]

samples. Although this suggests inductive behavior for the 30 vol% samples, fits with the equivalent circuit model of Figure 3.2a using $C_b < 0$ were better than similar fits which used an inductor in place of C_b. This apparent negative capacitance may be an instrumental artifact resulting from the large sample conductance or may be related to the dynamics of charge exchange through trap states at $SiC_w/Al_2O_3/SiC_w$ interfaces in the composite bulk. The latter notion is based on the results presented in Chapter 7 and various works[134-136] reporting on negative capacitance.

In Figure 3.10a, the low frequency semicircle, related to the electrode contact, grew with time. This growth is accompanied by increasing R_c, decreasing ω_c, and no systematic change for C_c. Such ageing behavior was observed for all tested combinations of SiC_w loading (10-30 vol%) and electrode type (sputtered Ag, sputtered Pt and Ag paint). It was also seen for sparsely used electrode types not mentioned in the experimental section, such as sputtered Pt coatings with Ag paint overcoats and sputtered Pt coatings with no overcoat.

Ageing also occurred for $V_w = 0.10$ samples which did not show a low frequency semicircle in measurements conducted immediately after sputtering the electrodes. An example is shown in Figure 3.10b for a sample having sputtered Ag electrodes. When the electrodes are fresh (~0.4 hrs old), the only trace of the low-frequency feature is a small tail. This tail is presumably part of a low-frequency semicircle that is initially too small to be distinguished from the much-larger high-frequency bulk semicircle which conceals it via superposition. A distinguishable semicircle becomes apparent after sufficient growth through ageing time. There was some evidence suggesting that the ageing rate decreased

with time such that R_c approached a plateau value. However, not enough experiments were performed to firmly establish this due to the prohibitively long times required.

Although a singular physical reason underlying the changing electrical properties is unclear, it likely relates to the deactivation of metal-SiC_w contacts. Ageing was often detectable without any changes in physical appearance. However, the electrode faces of several sputtered samples showed bare composite around the edges after very long times (e.g., hundreds of hours), suggestive of film delamination. This could be attributed to weak bonding at the metal-ceramic interfaces[137] and stress-concentrating action of the edges. After thousands of hours, several sputtered electrodes showed blue-greenish or whitish discoloration near the edges or brownish discoloration across the entire surface, suggestive of reaction or Ag tarnishing. For others, regions of the electrodes were dulled white, suggestive of Ag oxidation. An example of ageing induced discoloration is shown in Figure 3.11. For samples having Ag paint electrodes, the growth of the electrode semicircle was accompanied by smaller but still distinct fractional changes to R_c but no changes to paint appearance or multimeter-determined paint resistance.

Figure 3.11. Sputtered Ag electrode showing ageing-induced discoloration (right). The bright white color on the upper-right portion of this sample is a reflection from the light source. A sputtered Ag electrode exhibiting minimal discoloration is shown (left) for comparison.

3.4. Conclusions

Electrical contacts to Al_2O_3-SiC_w composites are manifested in the complex impedance plane by a semicircle that is well-modeled by a parallel R_cC_c circuit. This semicircle shrinks with total applied dc bias V_{dc}, appears at a lower frequency than the ohmic bulk response. The C_s-V_{dc} data evidenced that the underlying physical process is blocking by symmetrical Schottky barriers. Atomic force microscopy results showed that this Schottky blocking occurs at metal contacts to whiskers on the composite surface and showed that it is not relevant for all such whiskers, only those participating in percolating linkages.

Compared to sputtered electrodes, the behavior of Ag painted contacts was inferior. These exhibited a higher ρ_s and Φ_B values and lower values of C_s and ω_c. These inferior properties are attributed to limited interfacing between metal particles and whiskers on the composite surface. Sputtered contacts of Pt were superior to those of Ag, suggesting a dependence on metal work function and that the estimated carrier concentrations of ~10^{17}-10^{19} cm^{-3} in the whiskers are related to p-type dopants.

For all types of electrodes, the electrode semicircle is unstable at room temperature and grows with time. Decreasing V_w in the composite decreases C_s and increases ρ_s by factors that are agreeable with the percolation-network sensitivity proposed above. Also, the dependences of both R_c and ω_c on V_{dc} are exponential and are related through the equivalent circuit model. However, for sputtered electrodes these exponential dependences are often so weak that they appear linear. This is because sputtered contacts contribute little to the total resistance and thus only a small fraction of

V_{dc} is applicable. As the fraction κ_{c0} of the bias partitioned to the electrodes relative to the bulk increased, the exponential strength was found to increase approximately linearly and the non-linearity of the current-voltage response strengthened. Corrections using this factor and V_w were needed to obtain reasonable estimates of Φ_B as 0.2-1.6 eV for sputtered Ag from the capacitance-voltage response.

CHAPTER 4

EFFECTS OF PROCESSING ON COMPOSITE STRUCTURE AND PROPERTIES

4.1. Introduction

The microwave application is one of the contexts of this study, for which one of the goals is to achieve an increased understanding of how the processing and structural characteristics of the composites affect their performance. Unlike the cutting-tool application of Al_2O_3-SiC_w composites, the microwave-heating application places demands on both the electrical and mechanical behavior of the composite material. Since the microwave application is relatively new, exact requirements for electrical and mechanical properties have not yet been established but desirable traits have been identified.

For example, rapid heating and heating-cooling cycling requires the ceramic to be resilient against thermal shock. Mechanical durability is also needed for handling by kitchen workers and could be evaluated by measurements of fracture toughness or strength by bending- or indentation-based methods. However, these destructive techniques preclude subsequent electrical measurements and rely on brittle fracture, a stochastic process dominated by a minority of local flaws. In contrast, the sonic resonance measurement[138,139] of elastic modulus is an effective means to non-destructively characterize large samples and is believed[81] to be sensitive to the entire distribution of flaws throughout bulk samples. In this method, the dynamic elastic modulus (E) depends on the sonic resonance frequency (f_{sr}) via

$$E = C_{s\nu} M f_{sr}^{2} \quad (4.1)$$

where M is the sample mass and $C_{s\nu}$ is a constant dependent on the sample size, shape, and Poisson ratio.[140]

The electrical behavior of the composites provides the basis for the microwave application, is of academic interest, and depends on the connectivity of the more conductive phase, SiC_w. Connectivity depends on structural aspects of the whisker distribution, e.g., the lengths, orientations, and spatial dispersion. Connection quality is also important and refers to the character of the interfaces between discrete SiC_w, i.e., the 'connections.' Electrical percolation is observed when connectivity becomes great enough such that a continuous interconnected cluster of SiC_w exists between the electrodes *and* the connection quality is sufficiently high such that the effective conductance of this percolating cluster is much greater than that of the matrix. The dc conductivity (σ_{dc}) of percolated samples is believed to generally increase with the connectivity of the SiC_w phase,[6] and the lowest volume fraction of SiC_w for which percolation exists is the percolation threshold, which is known to scale inversely with the whisker aspect ratio[7] (see Figure 1.8). From these, it is inferred that connectivity generally increases with whisker aspect ratio. Since the hot-pressed and pressureless-sintered samples were all made from the same ball-milled powder blends, the distribution of whisker aspect ratios should be the same for a given composition, regardless of processing method. This provides a basis for comparing the electrical behavior of samples fabricated by the three different methods.

Unlike the hot-pressed composites, the composites made by extrusion are used in the microwave application, but all previous studies on the electrical response of such

composites have been on the hot-pressed type. In this study, composites were made by both hot-pressing and extrusion from the same powder blends to allow for the possible application of lessons learned from the former to the latter; the dry-pressed samples act as an intermediary for comparison. Also, it is of interest to find out the extent to which the hot-pressing and characterization of a small sample could be used to predict the behavior of rods made by extrusion and pressureless sintering, i.e., processes which generally require greater investments of time and resources.

The electrical and dielectric properties of hot-pressed composites containing SiC_w have been found to depend on the orientation of the electrical measurement relative to the preferred orientation of the whiskers.[9,17,90] The texture results from pressing and effectively makes the microstructure axisymmetric.[87-89] In such structures, the orientation of a typical whisker tends to be perpendicular to the hot-pressing direction (HPD) and random within planes which are perpendicular to the HPD. Conductivity is reduced along the HPD compared to the perpendicular direction.

4.2. Experimental Methods

As described previously, composites of Al_2O_3 and SiC_w were made by hot-pressing, extrusion and pressureless sintering, and dry-pressing and pressureless sintering. The thicknesses of the thick and thin hot-pressed disc samples were ~7.2 and ~2.6 mm for all compositions and did not affect the dc conductivity. The diameters were ~29 mm. After sintering, the dry-pressed discs were ~7 mm thick and ~25 mm in diameter. The final lengths (z_{as}) and diameters (d_{as}) of the as-sintered extruded rods were 23-26.5 cm and 14-15 mm, respectively, and are reported in Table 4.1. Radial and

longitudinal shrinkages (S_R and S_L) were calculated based on the die size and green-rod length, i.e. via S_R= (1.788 cm - d_{as})/1.788cm and S_L=(27.9 cm - z_{as})/27.9 cm.

Table 4.1. Theoretical Densities and As-Sintered Dimensions of Extruded Rods (modified from Ref. 20, Copyright 2011 by The American Ceramic Society).

Powder Composition (SiC_w vol%)	*Theoretical Density (g/cm^3)*	*As-sintered Rod Length (cm)*	*Rod Diameter (mm)*
0	3.972	23.44 ± 0.32	14.72 ± 0.01
3.52	3.951	24.02 ± 0.14	14.49 ± 0.03
5.81	3.932	24.25 ± 0.13	14.34 ± 0.01
7.68	3.913	25.45 ± 0.28	14.16 ± 0.05
9.96	3.895	25.81 ± 0.07	14.31 ± 0.07
12.2	3.876	26.19 ± 0.06	14.45 ± 0.07
14.5	3.857	26.21 ± 0.10	14.49 ± 0.11
17.0	3.838	26.30 ± 0.09	14.65 ± 0.03
19.1	3.819	26.43 ± 0.13	14.93 ± 0.11
24.0	3.778	26.50 ± 0.08	15.13 ± 0.14
28.2	3.746	N/A	N/A

The ±error defines one standard deviation.

Density measurements were performed geometrically for all samples. The theoretical density of fully dense composites was calculated for each composition based on the starting materials, e.g. 3.97 g/cm^3 and 3.216 g/cm^3 for Al_2O_3 and SiC_w, respectively. The results are given in Table 4.1 and neglect the effect of secondary-phase formation during sintering. However, two reaction phases were detected in 0 vol% hot-pressed samples via very-small x-ray diffraction peaks and traced to reactions of alumina with the proprietary additives. The theoretical densities were used to calculate the relative density (D) of the sintered ceramics, i.e. the fraction of theoretical density obtained. Values may be given as percentages, e.g., D=1=100% for a fully dense sample. Porosity (P) was calculated by P=1-D and was determined to be open and connected based on

water intake of samples during immersion. The previously-described stereological measurement of the distances between SiC inclusions was also applied to the hot-pressed discs.

The longitudinal dynamic elastic moduli of the as-sintered rods were measured by a sonic resonance technique prior to machining to prevent machining-induced cracks and damage from affecting the results. For this, a Dynamic Elastic Properties Analyzer (DEPA, Matrix Enterprises, Waterville, OH) was used with an assumed Poisson ratio of $\nu = 0.20$. It was found that varying the Poisson ratio over a range of reasonable values ($0.15 < \nu < 0.30$) had minimal effect on the resulting modulus values, e.g. differences were typically ~0.2 GPa or less. During the measurement, the rods were marked at the center- and quarter-points with a black marker, which was also used to label the rods. Then, the rods were supported at the quarter points by balsa wood and tapped at the center point with a mallet, as prescribed by the DEPA method. The discs were too small for DEPA measurements.

Samples were prepared for electrical measurement in accordance with the procedures described in Chapter 2; examples of electrodes on samples of the new batch are shown in Figure 4.1. AC spectroscopy measurements were conducted with the Solartron on all samples. Extrapolations were used to determine R_{b0} when deemed appropriate, i.e. for samples which were relatively insulating or had clearly-separable electrode impedance.

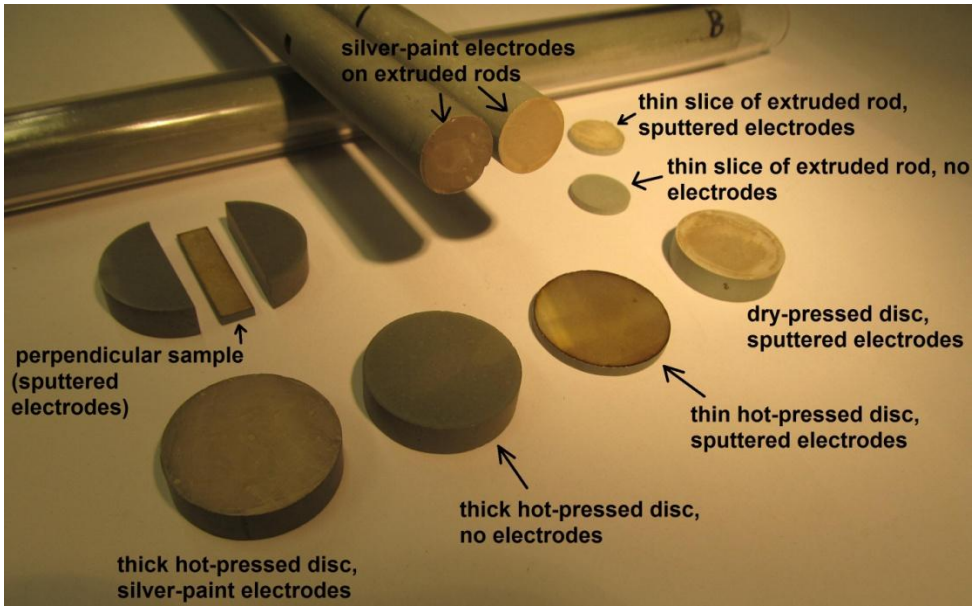

Figure 4.1. Samples showing the different electrode schemes for the different sample types. Samples with no electrodes are shown for comparison.

4.3. Results and Discussion

4.3.1. Composite Microstructures

Discs resulted from hot-pressing and dry-pressing and pressureless sintering, whereas rods resulted from extrusion and pressureless sintering (Figure 4.2a). The different processing methodologies affected the preferred orientation of the SiC whiskers and the densification of the ceramic composites. In the discs which were hot-pressed or dry-pressed and sintered without pressure, whisker long axes were preferentially aligned perpendicular to the pressing direction (PD). In the extruded material, the whisker long axes were preferentially aligned with the extrusion direction (EXD). These different preferred orientations are shown in the schematic of Figure 4.2b, which provides perspectives both parallel and perpendicular to the processing directions, i.e. the EXD and PD. For all samples, the processing direction may be regarded as an axis of symmetry and the microstructures may be regarded as being axisymmetric with two

principal directions, i.e., the directions parallel and perpendicular to the processing direction.

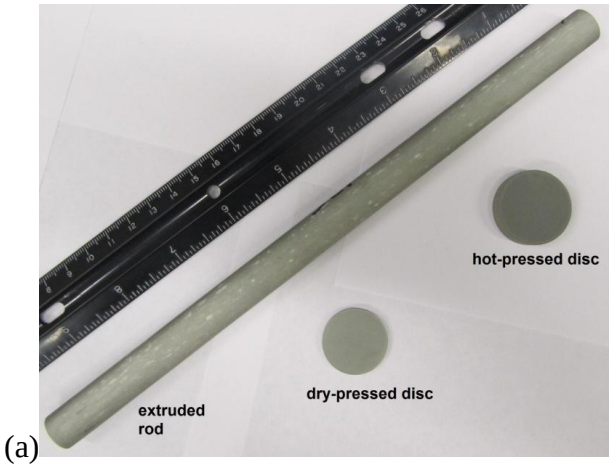

(a)

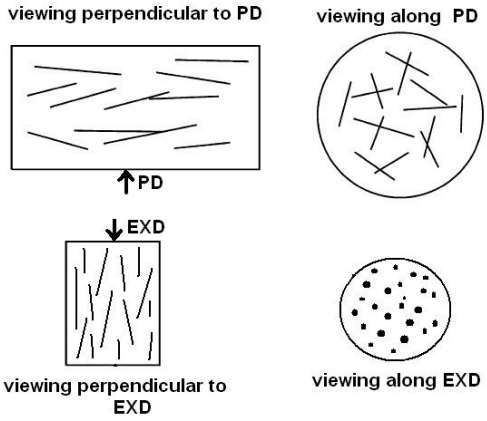

(b)

Figure 4.2. (a) Different sample types made from the 17.0% SiC_w powder blend. (b) Depictions of preferred whisker alignment relative to the pressing direction (PD) and extrusion direction (EXD) for pressed microstructures (top[6]) and extruded microstructures (bottom).[20]

4.3.1.1. Morphology Observations

Figure 4.3a and 4.3b are SEM images of typical sample microstructures of hot-pressed 14.5 vol% SiC_w samples. These images show the planes which are parallel and perpendicular to the hot-pressing direction, respectively. The dispersions of whiskers

appear similar to those in previous investigations.[6,18] Charging was found to affect imaging of the sample surface during electron microscopy. It was generally increased for samples having lower dc conductivity, and was very prominent for dry-pressed samples. Charging negatively impacted observation of the whiskers in a dry-pressed 24.0% SiC_w sample, as shown in Figure 4.4.

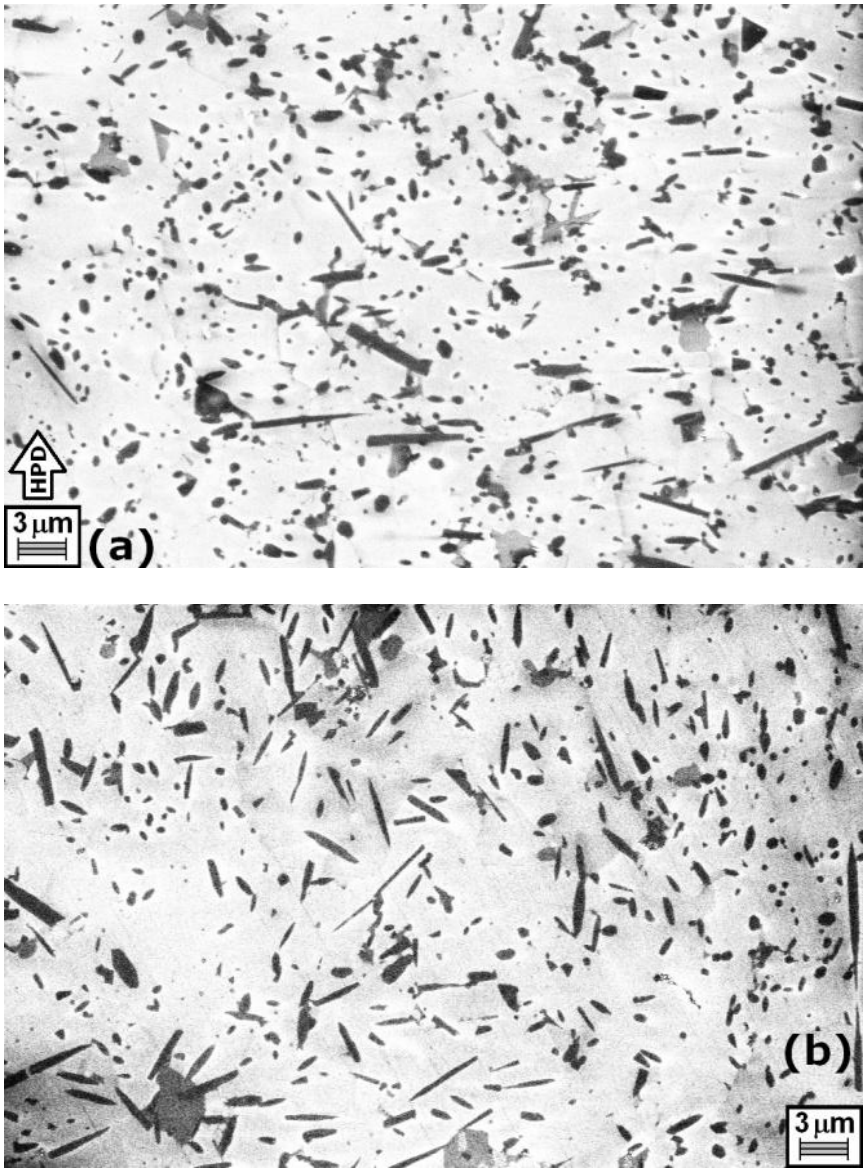

Figure 4.3. SEM images[21] of the *planes* parallel (a) and perpendicular (b) to the HPD for an Al_2O_3-SiC_w sample containing 14.5 vol% SiC_w taken at 5 kV. The white arrow in (a) points along the HPD. The microstructure is viewed along the HPD in (b).

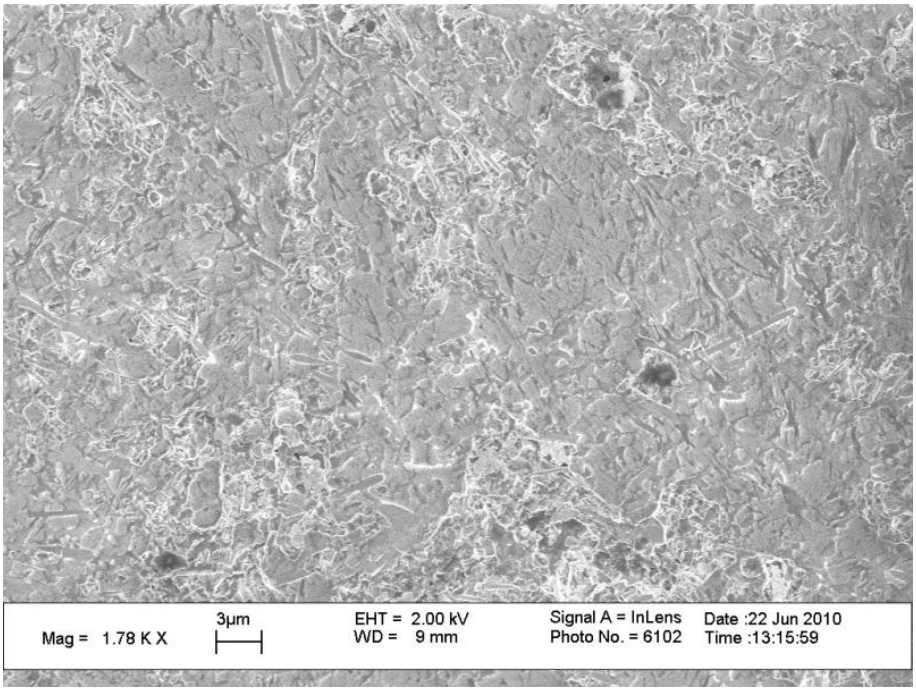

Figure 4.4. Scanning electron micrograph of a dry-pressed and pressureless sintered 24.0% SiC_w sample. Substantial charging is evident.

Figures 4.5a, 4.5b, and 4.5c are SEM images of polished sections of the 24.0 % SiC_w composition, which was chosen for imaging to minimize charging. The former shows a pore in the whisker surface; porosity was a characteristic trait of the pressureless-sintered samples. In Figure 4.5b, the microstructure is viewed along the EXD and the ends of several SiC_w aligned with the extrusion direction (black spots) demonstrate the preferred orientation. The image also shows the rough morphology of the polished sample surface which appeared mirror-like to the naked eye. This morphology is believed to be associated with the porosity. Figure 4.5c shows a microstructural plane parallel to the EXD, the preferred alignment of the SiC_w parallel to the EXD, and pores. Some SiC_w are partially obscured due to effects of charging and the pore in the top-middle portion of the image contains a cluster of SiC_w.

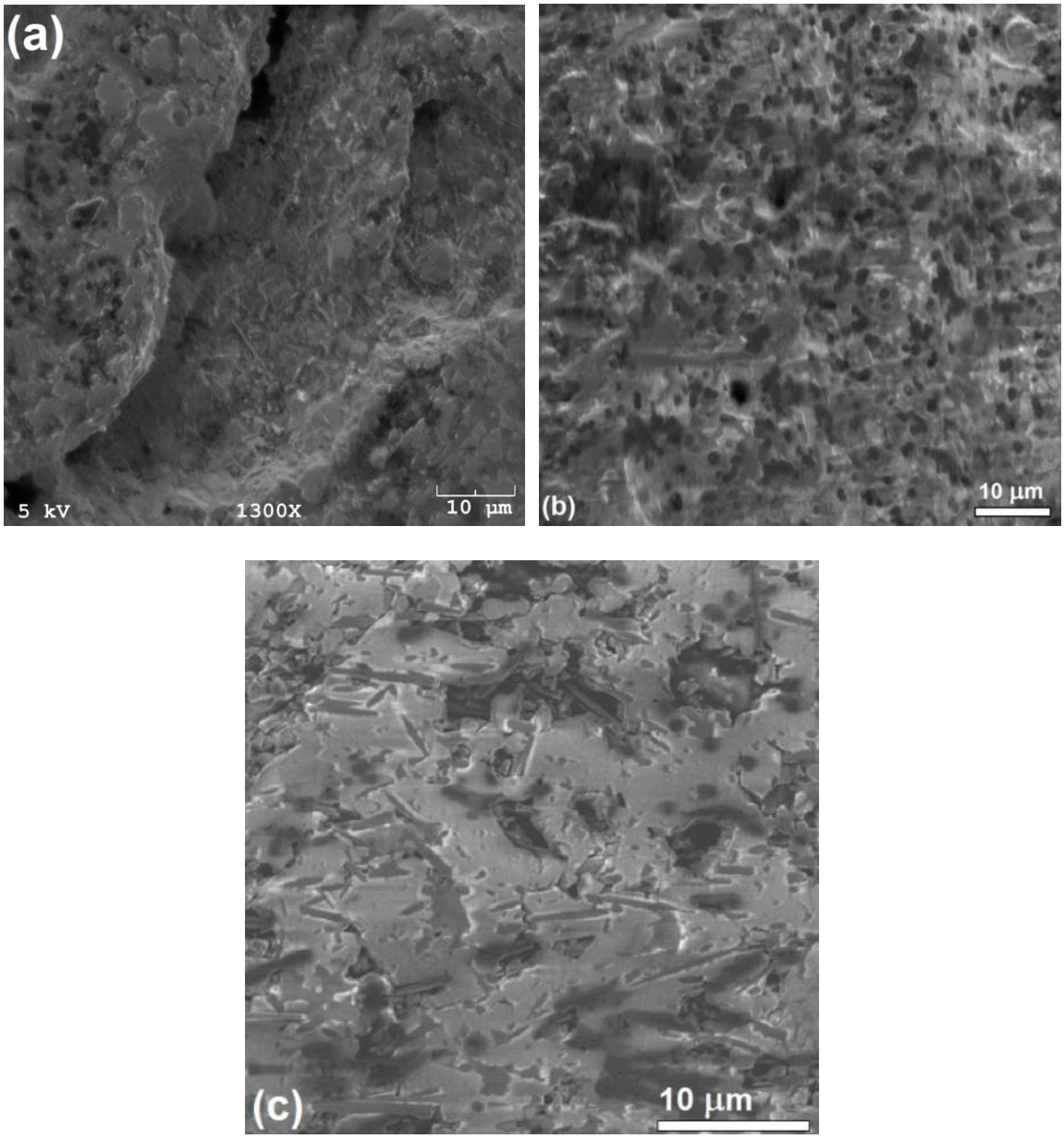

Figure 4.5. Scanning electron micrographs of 24.0% SiC_w extruded and sintered samples. In part (a), a large pore is shown. In part (b), the microstructure is viewed along the EXD.[20] In part (c), microstructure is viewed along a direction which is perpendicular to the EXD. The scale bar is parallel to the EXD in part (c).[20]

Some of the pores in the extruded samples were apparent to the naked eye and were aligned with the EXD, as shown in Figures 4.6a and 4.6b. In Figure 4.7, no large pores

are visible for the hot-pressed sample and only a few large pores are visible at the bottom of the dry-pressed sample surface, which suggests samples made by these methods had different pore-size distributions.

(a)  (b) 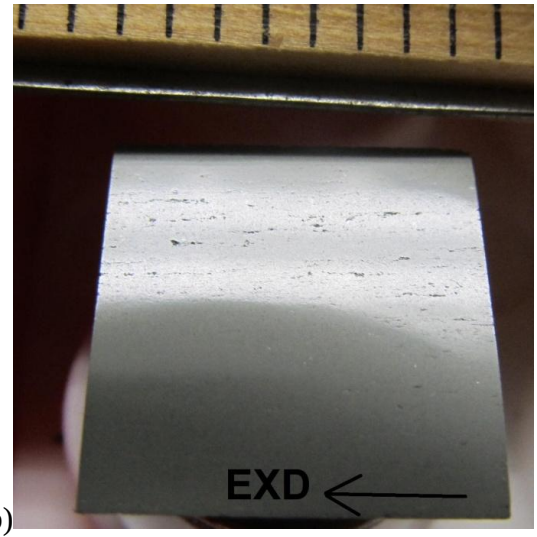

Figure 4.6. Polished slices of a 24.0 % SiCw extruded rod showing porosity when viewed at a suitable angle. The bright-white and darker portions of the surfaces correspond to the reflection and shadowing of the light source, respectively. The sample surfaces in (a) and (b) show planes which are perpendicular and parallel to the extrusion direction (EXD), respectively. The marks on the adjacent rulers are spaced by 1/16 inch.

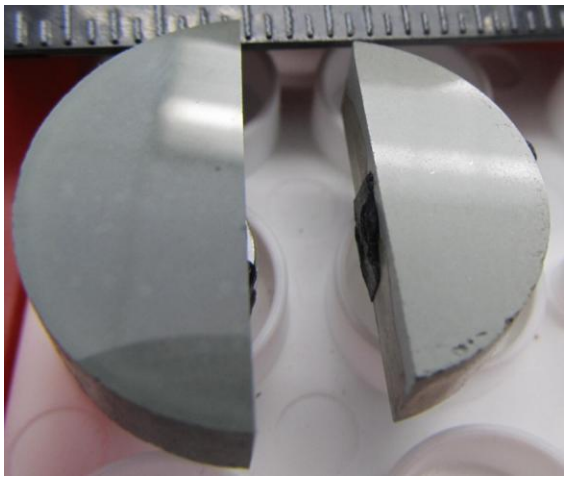

Figure 4.7. Polished half-disc samples made by hot-pressing (left) and dry-pressing (right) from the 24.0% SiC_w powder blend. The bright-white portions of the surfaces are reflections from the light source. The dark portion of the hot-pressed sample is shadowed from the light source. The marks on the adjacent ruler are spaced by 1/16 inch.

4.3.1.2. Quantitative Characterizations

4.3.1.2.1. Densification and Shrinkage from Sintering

For the pressureless-sintered rods and discs, the volume fraction of porosity increased with increasing whisker content in the starting powder blends. This is evident in Figure 4.8a, which shows that the relative bulk density of the samples decreased with increasing whisker content for both sample types. It is believed that clustering and alignment of the SiC_w inhibit densification during sintering and that the extent of clustering increased as whisker content increased towards and beyond percolation. Percolation is defined by the formation of a sample-spanning cluster/network of SiC_w and the presence of such a network is expected to significantly impede densification of whisker composites.[50] However, since the trend applies for all compositions, it is inferred that interlocking whisker clusters need not be sample-spanning to inhibit densification.

Figure 4.8a also shows that the final relative densities of the dry-pressed discs were similar to those of the extruded rods. For all compositions, these densities are much lower than those for hot-pressed samples made from the same powder blends. This can be attributed to plastic-flow enhanced sintering resulting from applied mechanical pressure during hot-pressing. The hot-pressed samples were fully (100%) dense to within experimental error except for the 24.0% and 28.2% compositions, which were 99.8% and 99.1% dense, respectively.

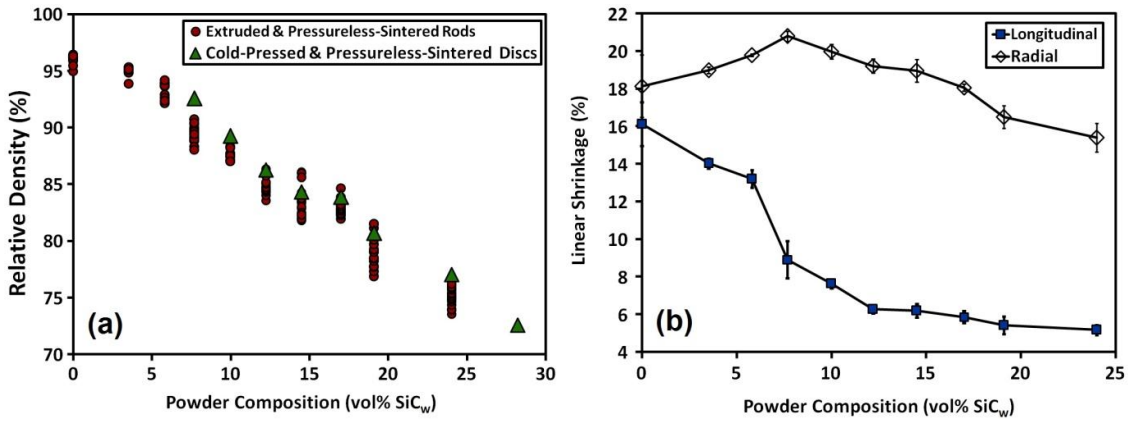

Figure 4.8. (a) Densities of pressureless-sintered rods and dry-pressed discs as a function of SiC_w content in the starting powder blends. Densities are expressed in terms of percent of the theoretical values given in Table 4.1. (b) Sintering-induced shrinkage of extruded rods compared to the pre-burnout green state for the radial and longitudinal (EXD) directions.[20]

Figure 4.8b shows the shrinkage from the green state induced by sintering for the longitudinal (EXD) direction and the radial direction, i.e. the set of equivalent directions perpendicular to the EXD. The plot shows that the longitudinal shrinkage decreased monotonically with increasing SiC_w content in a manner suggestive of a broad percolation transition spanning the 5.8-12.2 $\%SiC_w$ range and is attributed to SiC_w clustering. The radial shrinkage was greater than the longitudinal shrinkage for all compositions because the whiskers were aligned along the rod lengths. The decreased shrinkage along the whisker alignment direction suggests that porosity might scale with the degree of preferred alignment for a given composition.

With increasing SiC_w content, the radial shrinkage increased to a maximum at 7.7% SiC_w and then declined with further increase of SiC_w content. To explain this interesting behavior, it is proposed that samples having 0 - 7.7 % SiC_w were devoid of well-formed percolating SiC_w networks and increasing SiC_w content within this range

increasingly inhibited the action of the driving force for sintering (i.e., the reduction of powder surface energy) in the longitudinal direction due to the preferred alignment of the whiskers. As a result, the driving force for sintering acted preferentially in the radial direction and the radial shrinkage increased. Furthermore, clustering of SiC_w increased with increasing SiC_w content and well-formed percolating SiC_w clusters/networks existed for samples having SiC_w content ≥ 10.0%. For such samples, further addition of SiC_w increasingly constrained sintering in the radial direction because this process was coupled to sintering in the longitudinal direction by the percolating SiC_w networks.

4.3.1.2.2. Anisotropic Distances Between SiC Inclusions

The stereological method of measuring the whisker distance was applied to the hot-pressed composites of various compositions for the two principal directions. The results are shown in Figure 4.9 and the average distance (d_{avg}) is consistently smaller along the hot-pressing direction. For both measurement directions, the average interparticle distance decreases with increasing whisker content. If the powder composition is defined as p, the data may be replotted in the form $1/d_{avg} \propto p^{1/3}$ with an average R^2 regression coefficient of 0.991 (not shown), a trend which is consistent with expectations for randomly distributed particles in a unit volume.[94,141] Alternatively, the data may also be replotted in the form $\exp(-d_{avg}) \propto p$ with an average R^2 of 0.979 (not shown). The difference in average R^2 values suggests that the former relation is a more precise description of the physical reality. The latter relation, like other exponential fits described in Section 4.3.2.2, uses micron-valued numbers for distances inside the exponential function.

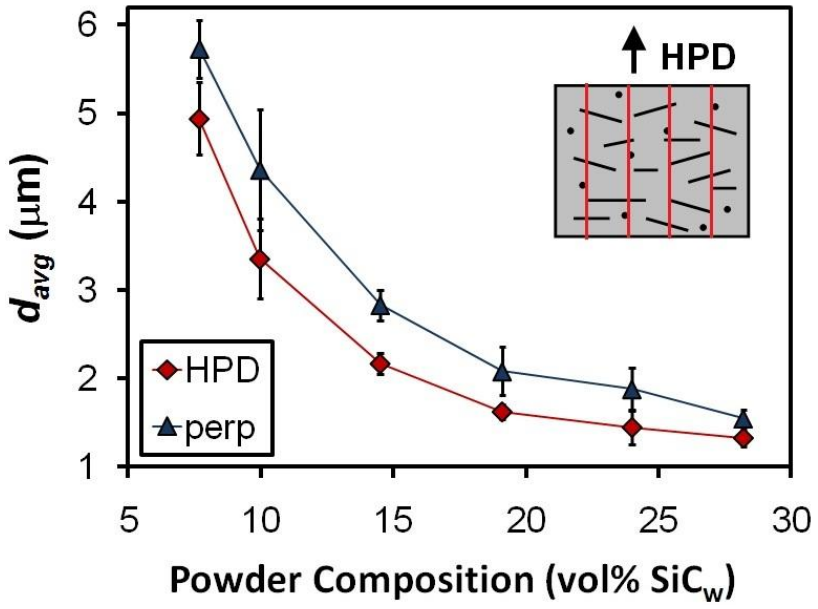

Figure 4.9. The average distance between SiC inclusions along the HPD and perpendicular direction as a function of whisker loading in the hot-pressed samples. In the inset schematic, the principle of the stereological measurement of the distances along the HPD is demonstrated.[21]

4.3.2. Direct-Current Conductivity

4.3.2.1. Effect of Processing Method on Percolation

Figure 4.10a shows the dc conductivity associated with the composite bulk as a function of whisker loading in the powder blends for the long (22-26 cm) extruded rods, the dry-pressed discs, and the hot-pressed discs. For all data, dc bias was not applied and the ac electric field was applied along the processing direction, i.e. the direction of extrusion or pressing. Compared to slices, long rods reduce the influence of the electrodes on the measurements and provide better statistical sampling of the conductivity of the extruded material due to the larger volumes.

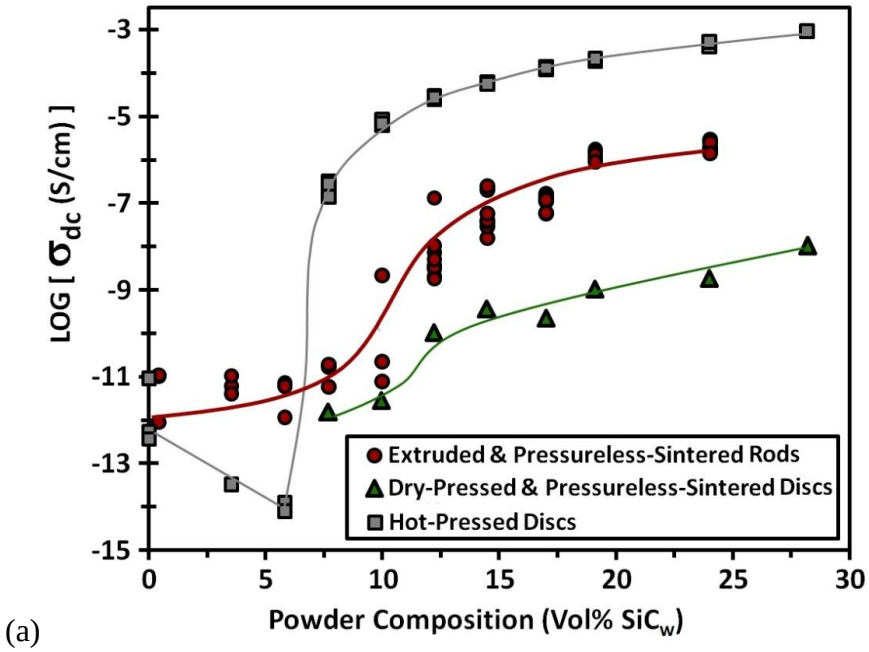

(a)

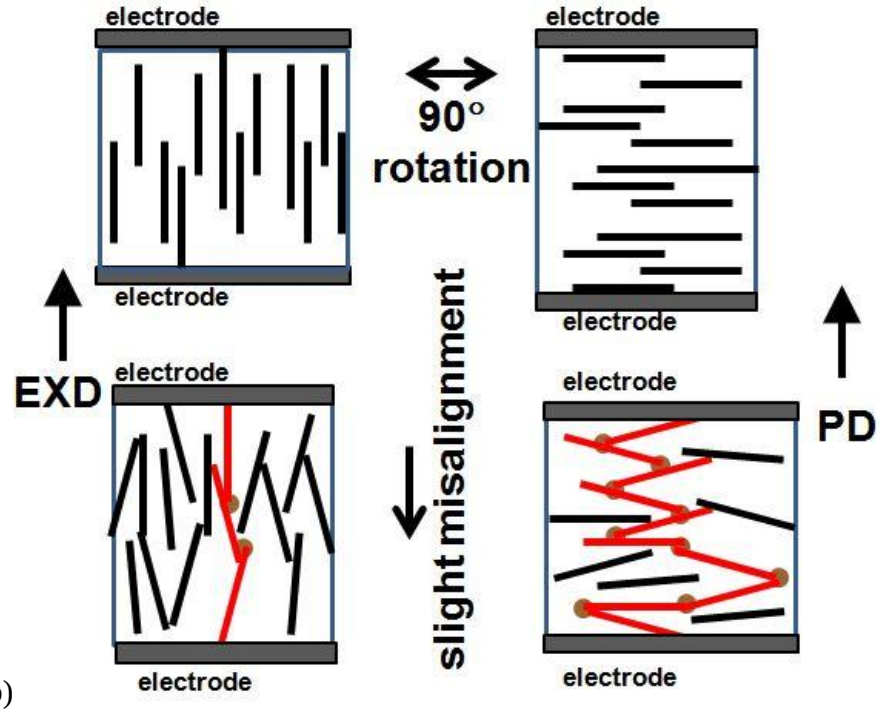

(b)

Figure 4.10. (a) Comparison of dc-conductivity percolation of Al_2O_3-SiC_w composites made from the same powders by hot-pressing, dry-pressing, or extrusion. The latter two were sintered without pressure.[20] (b) Schematic diagram showing the effect of preferred whisker orientation relative to the processing direction, as applicable to the pressureless-sintered composites. Red whiskers and brown interfaces are involved in the direct-current pathway.

The data for hot-pressed material shows that SiC_w percolation occurred between 5.8 and 7.7 vol% SiC_w. Percolation in the extruded material required a greater SiC_w volume fraction in the composite and spanned a significantly broader compositional range, i.e. ~7.7 to 12.2 vol% SiC_w in the starting powder. Furthermore, for given percolated compositions, the extruded dc conductivity values were significantly smaller (i.e. by about two orders of magnitude). These differences in percolation threshold and conductivity magnitudes cannot be accounted for with linear density-based normalizations of the data from the porous rods, i.e. accounting for true filler volume fraction and solid cross-sectional area (for conductivity calculation) in the porous microstructures.

Insight into this matter can be garnered by separately comparing the hot-pressed and extruded material data to the dry-pressed material data. Ideally, data for hot-pressed and dry-pressed samples may be compared more directly to determine the effect of porosity because both types exhibit the same general preferred orientation of SiC whiskers. Similarly, data for extruded and dry-pressed samples may be compared to determine the effect of parallel vs. perpendicular preferred whisker orientation because both types possess similar levels of overall porosity.

For dry-pressed material, percolation appeared to occur between 10.0-12.2 % SiC_w and was associated with conductivity increasing by about two orders of magnitude. This transition is weak and suggests minimal conductance contrast between the percolated cluster and the matrix. The percolation of the hot-pressed material resulted in a conductivity increase of approximately eight orders of magnitude. For a given percolated composition, the conductivity of cold-pressed material was less than that of hot-pressed

material by approximately five orders of magnitude. Since hot- and cold-pressed material have similar preferred alignment of SiC_w (i.e., perpendicular to the pressing direction), it is inferred that the large difference in relative density is associated with the conductivity difference.

It may be that pores directly cause disruptions in connectivity and/or that porosity is non-causally associated with lower-quality SiC_w-SiC_w connections which result from the absence of applied pressure during sintering. The stress from the applied mechanical load during hot pressing was probably more concentrated in the percolated network of the harder whiskers compared to the softer matrix particles,[142] and this could result in SiC_w-SiC_w connections having more intimate contact and more conductive interfaces.

Pressureless-sintered extruded and dry-pressed samples should have SiC_w-SiC_w connections of similar quality and may be compared to determine the effect of preferred whisker orientation because the relative densities were similar. Dry-pressed material had significantly lower conductivity and a weaker percolation transition compared to extruded material. This may be attributed to the extruded material having greater SiC_w-SiC_w connectivity and/or conduction pathways across the percolated networks involving fewer high-resistance SiC_w-SiC_w connections per unit distance between electrodes. The preferred alignment of whiskers relative to the applied electric field implies relatively direct and circuitous conduction pathways for the extruded and dry-pressed materials, respectively. This concept is shown in the bottom half of Figure 4.10b. Simulations indicate that a modest degree of uniaxial alignment results in increased conductivity compared to completely random orientation (Figure 1.13).[8] Stricter uniaxial alignment is expected to reduce connectivity and conductivity along that axis,[8] and strict alignment

perpendicular to the axis can be imagined to similarly reduce conductivity along the axis. This concept, and the fact that the two-dimensional projections associated with such alignments are related by a 90° rotation, is demonstrated in the top half of Figure 4.10b.

4.3.2.2. Effect of Structural Anisotropy

Figure 4.11a shows data from hot-pressed samples plotted in terms of dc resistivity from measurements where the electric field was applied parallel and perpendicular to the hot-pressing direction. Percolation for both directions occurs between 5.81 and 7.68 vol% SiC_w. The data is in good agreement with the scaling law $\sigma_{dc} \propto (p - p_c)^t$, where $p_c = 0.06745$ and $t = 2.612$ and 2.216 with R^2=0.9991 and 0.994 for the HPD and the perpendicular direction, respectively. Also, it can be seen that the resistivity is higher along the hot-pressing direction for all of the percolated compositions. This result is consistent with previous work on similar composites (Figure 1.11, Refs. [9,17,90]), has been attributed to the preferential orienting of whiskers[11,12] during pressing,[87,88] and is conceptually explained in Figure 4.11b.

Conduction perpendicular to the HPD corresponds to conduction within planes which are perpendicular to the HPD; within such planes, the random orientation of the whiskers suggests high network connectivity.[8] In Figure 4.11b, the whisker network has multiple parallel conduction paths (involving green whiskers) in addition to the most direct conduction path, which has the fewest number of (orange) whisker-whisker interfaces and involves (maroon) whiskers. By comparison, the preferred whisker alignment perpendicular to the HPD is associated with reduced whisker connectivity and the most direct path for conduction along the HPD has a circuitous character and the

same color-coding as in Figure 4.10b. The colors used in Figures 4.10b and 4.11b were chosen to be agreeable with the depictions of the topology in Chapter 5.

In Figure 4.11a, as whisker content increases on the insulating side of the percolation curve, dc resistivity increases for measurements along the HPD and decreases for the perpendicular direction. An explanation for this, based on additional information, is proposed in Chapter 7.

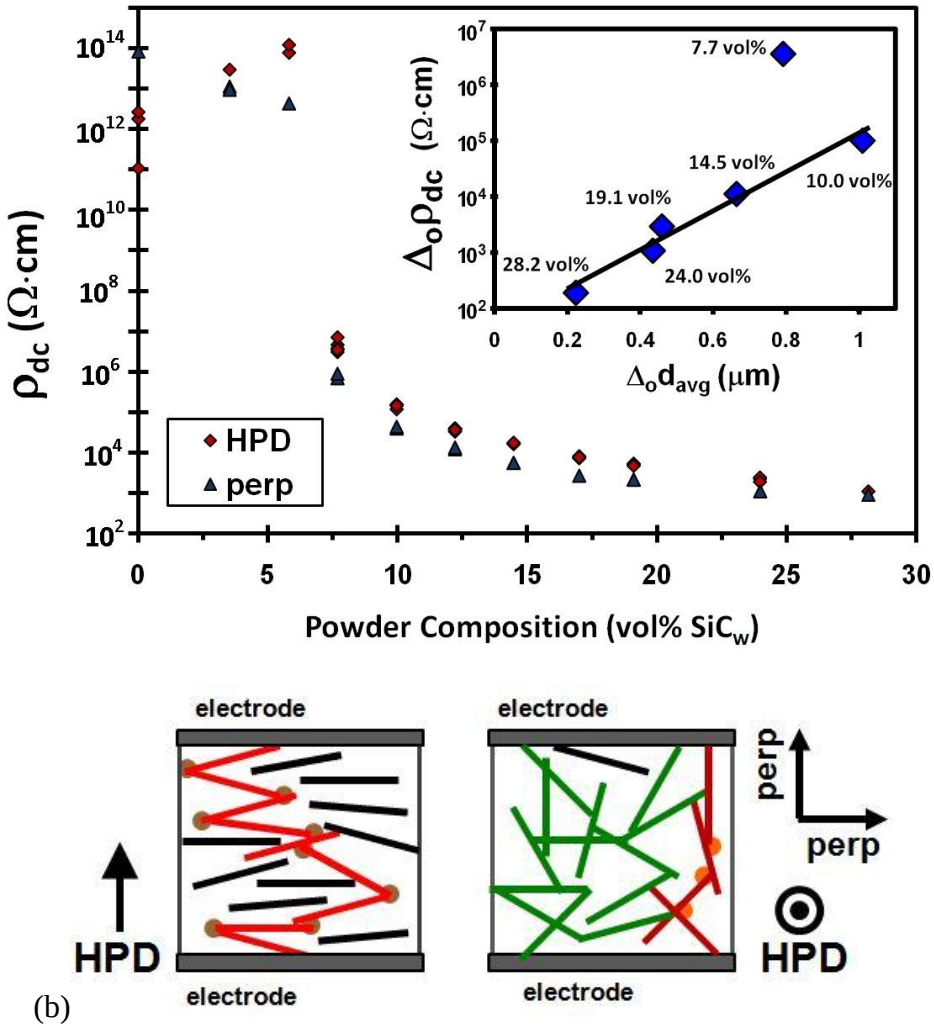

(b)

Figure 4.11. (a) Percolation curves of the dc resistivity of the hot-pressed Al_2O_3-SiC_w composites measured along the HPD and the perpendicular direction. The inset shows the relation between the orientation-based differences in resistivity and average interwhisker distance.[21] (b) Schematic diagram showing conduction parallel to (left) vs. perpendicular to (right) the HPD.

The inset of Figure 4.11a shows the relation between the sample-orientation-based differences in dc-conductivity $\Delta_o\rho_{dc} \propto \exp(\Delta_o d_{avg})$, and sample-orientation-based differences in interwhisker distance $\Delta_o d_{avg}$. These are defined as $\Delta_o d_{avg} = d_{perp} - d_{HPD}$ and $\Delta_o\rho_{dc} = \rho_{HPD} - \rho_{perp}$, where d_{perp} and d_{HPD} refer to the plotted values of Figure 4.9 and ρ_{HPD} and ρ_{perp} relate to Figure 4.11a. From the inset, it might be inferred that $\Delta_o\sigma_{dc} \propto \exp(-\Delta_o d_{avg})$. The deviation of the 7.7 vol% data point may be attributed to (1) microstructural variation around the percolation threshold and (2) limitations of the stereological measurement for larger distances. Fitting to $\Delta_o\sigma_{dc} \propto \exp(-\Delta_o d_{avg})$ yielded a R^2 of 0.97 if the 7.7 vol% data point is ignored. A similar fit which used the 7.7 vol% point and ignored the 28.2 vol% data point yielded R^2= 0.83. Similar fits to the cubic relations $(\Delta_o d_{avg})^3 \propto \Delta_o\rho_{dc}$ and $(\Delta_o d_{avg})^3 \propto 1/(\Delta_o\sigma_{dc})$ yielded an average R^2 of 0.970.

Regardless of which relations (cubic or exponential) more precisely describe the behavior, it is clear that $\Delta_o d_{avg}$ values are related to the sample-orientation-based differences in dc conductivity. Thus, the trend of the inset is a structure-property correlation. If structural and electrical anisotropy are defined by $\Delta_o d_{avg}$ and $\Delta_o\rho_{dc}$, respectively, the trend indicates increasing isotropy as SiC_w content increases (consistent with the result of Figure 1.12). In this vein, the experimental data may also be replotted as another power law: $\Delta_o\rho_{dc} \propto p^{-5.69}$ (with R^2=0.98, excluding the 7.7 vol% point).

4.3.2.3. Determination from Complex-Impedance Response

For the percolated hot-pressed samples, the dependence of the complex impedance on electrode material and dc bias was the same as in Chapter 3. For samples having ≥7.7 vol% SiC_w, the impedance of the bulk could be separated from the contacts

due to the presence of two separable semicircles in the complex impedance plane; only the low-frequency semicircle depended on electrode material and bias. Therefore, the dc conductivity was extracted from the high-frequency semicircle. For hot-pressed discs with ≤ 5.8 vol% SiC_w , dry-pressed discs, and long extruded rods, there was usually only one semicircle and σ_{dc} calculation was straightforward. This is further elucidated in the next section (4.3.2.4) and the next Chapter (5).

4.3.2.4. Effect of Small Variations in Density

The effects of large differences in density on the electrical response of Al_2O_3-SiC_w microstructures have already been presented and discussed. Smaller, natural variations in density within the populations of the porous (D < 90%) extruded rods are apparent in Figure 4.8a and allowed for additional investigation into the relationships between density and electrical response of extruded-type microstructures. Figure 4.12a shows Nyquist plots of the complex impedance ($Z^* = Z' - jZ''$) data geometrically normalized to resistivity units for long-rod samples of the 14.5 % SiC_w composition having differing values of relative density. From the intercepts on the real axis, it can be seen that the dc resistivity of the rods increases as density decreases. The inset shows that the application of a large dc bias to the 81.85% dense rod had a minimal impact on the impedance. This was a typical result for the long rods, i.e. the electrical behavior was ohmic or nearly ohmic.

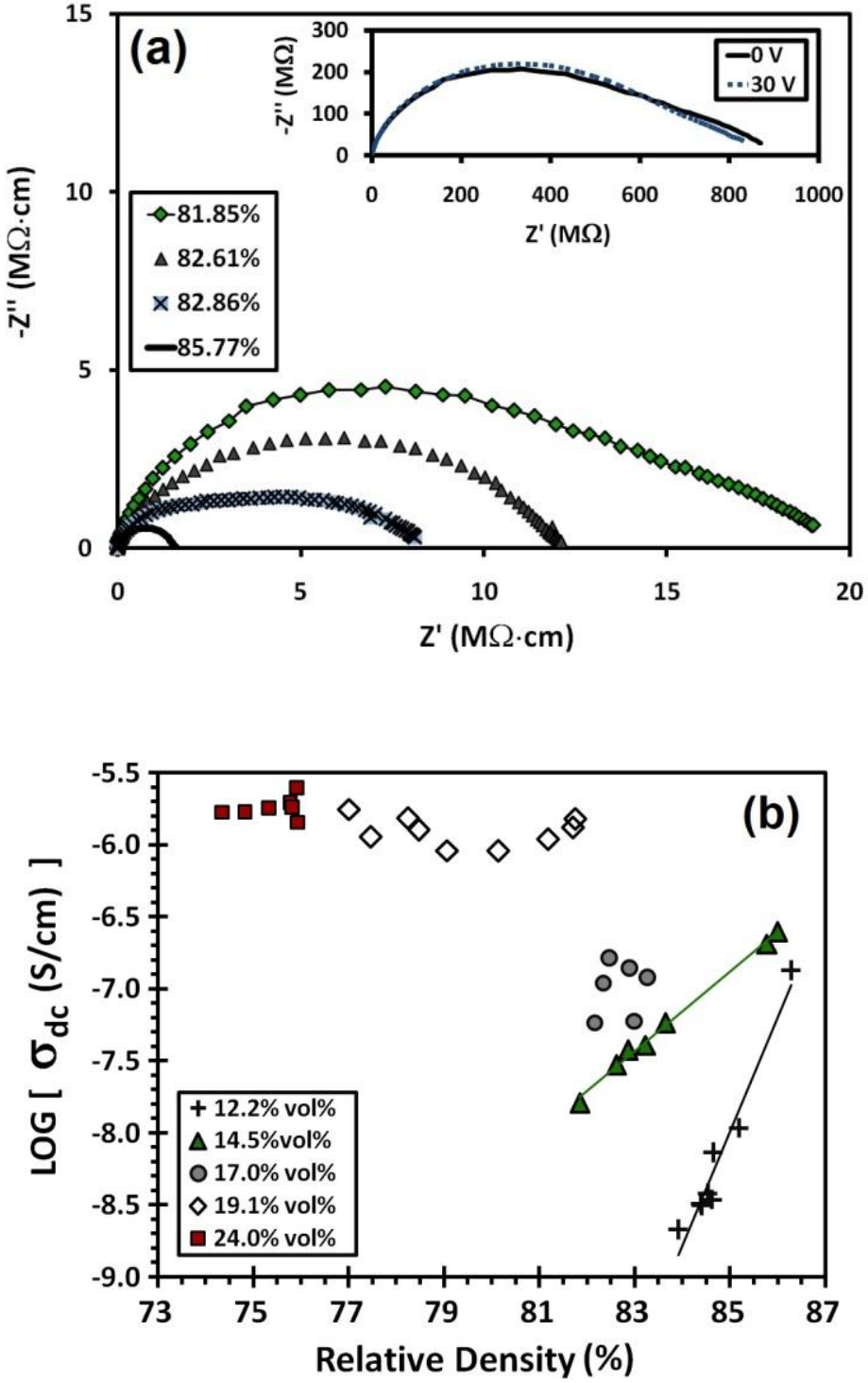

Figure 4.12. (a) Geometrically-normalized complex-impedance data from long (z ~ 25 cm) rods of the 14.5% SiC_w composition having silver-paint electrodes and different sintered densities (D), which are given in the legend. The inset shows the (weak) effect of dc bias on rod having D=81.85%. (b) Effect of sintered density on the dc-conductivity of long extruded rods of various compositions.[20]

Figure 4.12b shows the effect of relative density on the dc conductivities of the long rods for the various well-percolated compositions. In Figure 4.12b, the qualitative relation suggested by Figure 4.12a for the 14.5% SiC_w composition appears to be a power-law or exponential dependence of dc conductivity on relative density based on the good straight-line fit on the log scale. For the 12.2% SiC_w composition, a similar but stronger relationship between the two variables is evidenced by the steeper slope of the fitting line. These trends indicate a strong correlation between relative density and SiC_w-SiC_w connectivity and show that small changes to the former can strongly affect the latter when composition is near the percolation threshold, even when D is much less than unity. For the 17.0-24.0% SiC_w compositions, the correlation is absent for the $0.74< D<0.84$ range shown in Figure 4.12b but is inferred to exist somewhere in the $0.84<D<1.00$ range based on the previously-discussed relation of density to the conductivity differences shown in Figure 4.10a.

These density-conductivity relations can be interpreted in terms of the slope of the log σ_{dc} vs. filler content percolation curve, i.e. Figure 4.10a. When composition is near to the percolation threshold, the dependence of conductivity on the filler volume fraction is strong, and the actual volume fraction of SiC_w in the porous rods is equal to the product of the relative density and the volume fraction of SiC_w in the powder blend. By comparison, the dependence of dc conductivity on filler volume fraction is relatively weak for compositions far from the percolation threshold. Alternatively, one may consider the correlation in terms of the percolated network or a possible coupling between porosity and SiC_w alignment. Percolated filler networks associated with compositions near to the percolation threshold can be expected to have a relatively

tenuous connectivity that is more sensitive to disruptions (e.g., those caused by porosity) compared to networks associated with higher filler concentrations. The idea of a porosity-alignment coupling follows from the facts that the increased alignment of SiC_w along an axis is associated with decreased shrinkage along that axis (Figure 4.8b) and sometimes with reduced connectivity.[8]

4.3.3. Dynamic Elastic Modulus of Extruded & Sintered Rods

4.3.3.1. Effect of Porosity

Figure 4.13 shows the relation between porosity (P) and the elastic modulus (E) of all the full-length extruded and sintered rods. All compositions of rods fall on the same linear trend line having R^2=0.991, i.e.

$$E\ (\text{GPa}) = -910.0\ P + 385.0 \qquad (2)$$

which indicates that porosity determined the composite elastic modulus. These results are consistent with expectations for aligned tubular pores from extrusion processing and the associated linear decrease of the elastic modulus with increasing pore volume fraction.[143] The similarity of the quantified trend to that from an ultrasound-based study of porosity in monolithic alumina[144], i.e., E (GPa) = -933.58 P + 396.1, further indicates that the whisker inclusions reduced the elastic modulus by inducing porosity during sintering. The shallower slope of Equation 2 compared to Ref. 144 might indicate a mitigation of the stiffness loss from porosity related to the increased stiffness of SiC (480 GPa) compared to Al_2O_3.(410 GPa).[145] The reduced constant of Equation 2 (385.0 GPa) might be associated with the sintering additives.

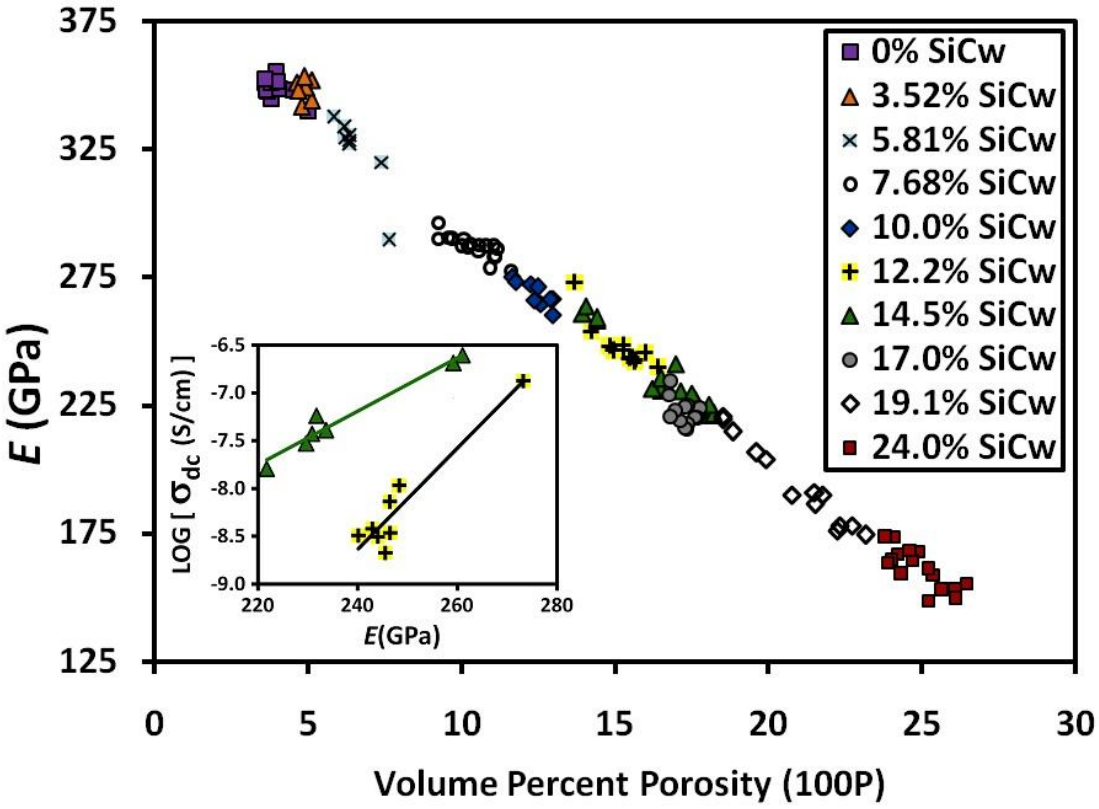

Figure 4.13. The effect of porosity (P=1- D) on the elastic modulus of full-length rods having varying SiC_w content. The inset shows electrical-mechanical correlations of the dc conductivity and the elastic modulus for the 12.2 and 14.5% SiC_w compositions.[20]

4.3.3.2. Limited Correlation to DC Conductivity

The inset of Figure 4.13 shows electrical-mechanical correlations between the dc conductivity and the elastic modulus for the 12.2 and 14.5 % SiC_w compositions. The fit lines correspond to $\log \sigma_{dc} = 0.0279E\text{-}13.89$ (R^2=0.959) and $\log \sigma_{dc} = 0.0529E\text{-}21.32$ (R^2=0.895), respectively. The existence of such relations could be useful for non-destructive testing compositions slightly above the percolation threshold. This correlation to conductivity is underpinned by the limited correlation between electrical behavior and density.

4.4. Conclusions

Three different methods were used to fabricate composites from the same batch of ball-milled dry-powder blends: hot pressing, dry pressing and pressureless sintering (PS), and extrusion followed by PS. From electrical, structural, and mechanical characterizations, it was found that the processing had a significant impact on the composite structure and behavior.

For the rods, whiskers were preferentially aligned with the extrusion direction and the microstructure exhibited significant porosity, which increased with the fraction of SiC_w in the powder. The elastic modulus of the rods decreased linearly with increasing porosity. The whisker alignment resulted in anisotropic shrinkage during sintering and increased electrical conductivity along the processing (extrusion) direction compared to dry-pressed and pressureless-sintered discs. These discs were comparable because they had similar porosities and were less conductive along the processing (pressing) direction because the whiskers were preferentially oriented perpendicular to this direction.

Compared to hot pressing, pressureless sintering resulted in significantly reduced dc conductivity. From this, it is inferred that the absence of a mechanical stress during densification resulted in reduced SiC_w-SiC_w connection quality in the final composites. Whisker percolation in the rods required greater SiC_w loading, took place over a wider range (i.e. 7.7-12.2 % SiC_w), and resulted in significantly decreased electrical conductivity compared to hot-pressed composites. The dc conductivity of percolated rods having composition near the percolation threshold was sensitive to small changes in porosity and was correlated to the elastic modulus.

The axisymmetric microstructure of percolated hot-pressed composites was characterized with a stereological method which measures the distribution of interfiller distances. The decrease of the mean average distance with filler volume fraction could be modeled as cubic or exponential. Also, this distance was longer along the microstructural symmetry axis (i.e. the hot-pressing direction, HPD) compared to the perpendicular direction. The relation between the orientation-based differences in average distance and dc conductivity (or resistivity) could also be modeled as cubic or exponential. With consideration of these parameters as measures of structural and electrical anisotropy, it was found that anisotropy was maximized near the percolation threshold and that isotropy increased with increasing SiC_w loading. Interestingly, the dc conductivity was smaller along the HPD compared to the perpendicular direction; this fact is considered further in Chapter 7.

CHAPTER 5

DEPENDENCE OF THE ELECTRICAL RESPONSE OF THE PERCOLATED CLUSTER ON LENGTH, TOPOLOGY, AND FILLER INTERFACES

5.1. Introduction

Applications of composites containing conductive fillers in insulating matrix materials include heating elements, discrete resistors, and sensors.[146] For these applications, a linear current-voltage characteristic is usually preferred. Yet, non-linear current-voltage behavior in such composites is common[146-149] and forms the basis for recent interest in using them as varistors in power applications. Thus, the physical basis for the non-linear behavior is a topic of considerable interest and is investigated in this Chapter.

Such behavior has been attributed to various attributes of the composite microstructure or the conduction process. The means by which the non-linearity arises is likely influenced by whether or not the sample contains a percolating cluster of conductive filler, i.e. a continuous interconnected pathway of filler particles spanning the sample between the electrodes. The increasing addition of filler to a matrix material leads to the formation of interconnected filler clusters whose size and number progressively increase.[20,83] At a critical volume fraction of filler, a sample-spanning percolating cluster of interconnected filler forms and provides a contiguous pathway for current flow across the sample. Additional filler further increases the composite conductivity.

In non-percolated composites, dielectric layers[146] between conductive particles have been reasonably assumed to be the main source of resistance and non-linear current-voltage behavior. Processes of dielectric breakdown[150] and tunneling[151] were proposed as mechanisms of current flow through such layers. For percolated composites, the non-linearity has sometimes been ascribed to Joule heating[146,151] or non-uniformity of the current path.[146] For the case of p-type Si filler particles in a SiO_2 matrix, the non-linearity was attributed to two different mechanisms, tunneling through the contacts between clustered filler particles, and the current being limited by space charge build-up at traps in layers of SiO_2 within the clusters of Si particles.[146] In composites of n-Si particles in polyethylene or polypropylene matrices which were likely percolated, the non-linear response was attributed to tunneling through barriers relating to the polymer interlayers.[151]

Since such composites are being considered for application as varistors and rely on conduction through semiconductor particles, it is interesting that the well-established non-linearity mechanism of conventional semiconductor varistors seems to have been overlooked as a possible source of the observed composite non-linearity. Varistors are typically made of polycrystalline semiconductor and their non-linear current-voltage behavior is believed to arise from symmetrical Schottky barriers at the interfaces of semiconducting grains[19] (Figure 1.21a) which depend on electronic trap states at these interfaces.[14,15] The resulting non-linear current (I) response to dc bias (V_{dc}) may be described by the empirical equation [14,15]

$$I_H / I_L = (V_H / V_L)^{\alpha_V} \qquad (5.1)$$

where subscripts H and L define the current and voltage at two different points H and L in the I-V_{dc} data, and $I_H > I_L$. The varistor coefficient of non-linearity is α_V, which describes the strength of the non-linearity, and ohmic behavior corresponds to $\alpha_V = 1$. Commercial varistors are often based on ZnO or SiC, which have typical α_V values of ~25-70 and ~5, respectively.[15,152] The electrical behavior of varistors is generally believed to be sensitive to the presence of electronic trap states.[14,15]

In one study of ZnO varistors, the dependence of the sample capacitance per unit area (C_s) was effectively modeled with an equation describing the bias dependence of the depletion-region capacitance associated with a symmetrical Schottky-like energy barrier at the thin intergranular layer between two semiconducting grains[19], i.e.

$$(1/C_s - 1/2C_0)^2 = 2(\Phi_i + V_i)(q\varepsilon_s N_d)^{-1} \qquad (5.2)$$

where $C_0 = C_s$ at zero bias, Φ_i is the barrier height (i.e., a potential) at the interface, V_i is the bias applicable to the interface, q is the fundamental charge, ε_s is the dielectric constant of the semiconductor, and N_d is the dopant concentration. This equation was also found to be effective in modeling the capacitance[103] of polycrystalline semiconductor $CaCu_3Ti_4O_{12}$ (CCTO), which is another candidate material for varistors exhibiting strongly non-linear current-voltage response.[153]

In Ref. 103, the effect of grain size on the bias dependence of the resistance and capacitance associated with the semiconductor-grain interfaces was studied by varying the sintering time of single-phase constant-thickness CCTO pellets. Long sintering time resulted in a large grain size, and the resistance and capacitance associated with the energy barriers at the interfaces were strongly bias-dependent in a manner agreeable with

Equations 5.1 and 5.2. Shorter sintering times resulted in smaller grain size and interfacial resistance and capacitance being relatively insensitive to dc bias. In the fine-grained material, it was reasoned that the current had to flow through ~20 times more interfaces in series (based on the grain-size change) and therefore the fraction of the total applied bias and the electric field across each interface was reduced.[103] As a result, the range of total applied bias effectively sampled smaller portions of the non-linear current-voltage response curves of the interfaces and thereby made them and the response of the aggregate appear more linear.

It seems that this is one means by which the *apparent* non-linearity (measured over a given bias range) of a series of non-linear interfaces can be reduced: by increasing the number of interfaces to decrease the fraction of total applied bias on each. If the series also includes a relatively linear resistance, the apparent non-linearity of the combination and the sensitivity of the non-linear interfaces to the total applied bias (V_{dc}) will be decreased if the fraction of V_{dc} dropping across the relatively linear resistance is increased. This was demonstrated for the Al_2O_3 composites of Batch #1 containing percolated silicon carbide whiskers (SiC_w) made by hot-pressing in Chapter 3. Some key results and insights from that Chapter and Chapter 4 are reviewed before building upon them in this one to understand more complicated behavior.

In Chapter 3, the complex impedance response showed two distinct and separable semicircles, thus indicating a series of two processes describable by parallel resistor-capacitor circuits. The higher-frequency semicircle was ascribed to the percolated SiC_w cluster of the bulk microstructure and was independent of the dc bias applied to the sample (V_{dc}), thereby indicating ohmic response. By contrast, the electrical response of

the electrodes was manifested by a separate semicircle at lower frequencies which was very sensitive to small dc biases ($V_{dc} \leq 6$ V). The bias dependence of the capacitance derived from the electrode semicircle was consistent with Equation 5.2, thereby affirming the applicability of the symmetrical-barrier model to the phenomenon occurring at separated Schottky barriers of opposite polarity, i.e. at the opposing electrodes of a metal-semiconductor-metal sandwich.[15] With increasing dc bias (V_{dc}), the through-thickness sample current (I) increased superlinearly and the dc resistance (R_c) of the contacts derived from the width of this semicircle decreased exponentially in magnitude,

$$R_c = R_{c0} \exp(\alpha_c V_{dc}) \tag{5.3}$$

where R_{c0} is the resistance of the electrode semicircle at zero bias and α_c is a constant having a negative value and a magnitude related to the strength of the bias dependence.[18] Values of R_{c0} were largest for samples having electrodes of conductive Ag paint and were smaller for sputtered electrodes due to improved metal-SiC interfacing. Sputtered Pt provided lower values of R_{c0} compared to sputtered Ag. Values of $|\alpha_c|$ increased with an estimate of the fraction κ_{c0} of the total applied bias dropping at the electrodes based on the relative contribution to the dc resistance at V_{dc}=0, i.e.,

$$\kappa_{c0} = R_{c0} /(R_{b0}+R_{c0}). \tag{5.4}$$

Here, R_{b0} is the ohmic resistance of the hot-pressed bulk and κ_{c0} was designated as κ_0 in the other paper.[18] Samples having high whisker content and Ag paint electrodes tended to have small values of R_{b0}, the largest values of R_{c0} and κ_{c0}, electrode semicircles exhibiting the strongest dependences on dc bias, and the largest values of $|\alpha_c|$.

Conversely, samples having low whisker content and sputtered electrodes tended to have large values of R_{b0} and small values of R_{c0}, κ_{c0}, and $|\alpha_c|$.

In some cases, the exponential dependence was very weak such that the electrode resistance appeared to decrease linearly with bias. This occurred when the fraction of the total applied dc bias dropping across the sample bulk (κ_{b0}) was large. When the bulk and electrode semicircles are separable, κ_{b0} can be estimated via

$$\kappa_{b0} = R_{b0}/(R_{b0}+R_{c0}) \approx 1-\kappa_{c0} \tag{5.5}$$

where the approximate equality results from the overlap of the semicircle widths in Nyquist plots. Equations 5.4 and 5.5 are based on partitioning of the total applied bias V_{dc} to the contact electrodes (V_c) and the sample bulk (V_b), i.e.

$$V_{dc} = V_c + V_b, \tag{5.6}$$

where $V_c \approx \kappa_{c0} V_{dc}$ and $V_b \approx \kappa_{b0} V_{dc}$ may be used as estimates.

In Chapter 4, it was shown that percolated composites of Al_2O_3-SiC_w were found to have much higher porosity and resistivity when made by pressureless-sintering[20] instead of hot-pressing the same powder blends.[21] It was proposed that the porosity contributed to the lower dc conductivity of the extruded and dry-pressed samples relative to fully-dense hot-pressed discs by disrupting and causing lower-quality SiC_w-SiC_w connections. This proposition was supported by the fact that the dc conductivity of the 12.2 and 14.5 % SiC_w extruded rods were sensitive to very small changes in porosity. Compared to 17.0-24.0 % SiC_w rods, these were more sensitive to porosity due to their relatively close proximity to the percolation threshold (p_c) at approximately 10.0 %

SiC_w,[20] where the connectivity of the percolating cluster was believed to be the most tenuous. It gains additional support from the results of this Chapter.

5.2. Experimental Methods

Long-rod remainders and thin slices of extruded and pressureless-sintered composite rods are focused on in this Chapter. Only SiC_w-percolated compositions are considered, i.e. 10.0, 12.2, 14.5, 17.0, 19.1, and 24.0 % SiC_w by volume in the starting powder blends. Dry-pressed and hot-pressed discs were measured for comparison. Conductive Ag paint was used for rods and Ag or Pt sputtering was used for slices and discs. Most electrical measurements were performed with the Solartron 1260-1296 combination using 1 V ac amplitude, and variable dc bias ($0 \leq V_{dc} \leq 40$ V). Some measurements employed the Keithley 2612A Sourcemeter from $-40 \leq V_{dc} \leq 40$ V. The electric field was applied parallel to the extrusion or pressing direction, i.e., across the *z* dimension of the samples. This is defined by the thicknesses (1.66 ± 0.29 mm for slices) or rod lengths (~23-26 cm). For hot- and dry-pressed discs, *z* was 2.6 and 7.4 mm, respectively. Determinations of static resistances, conductivities, and capacitances were based on fits of the associated semicircle in the complex impedance plane with Zview software by Scribner Associates, as described in Chapter 2.

5.3. Results and Discussion

5.3.1. Impedance Response of Long Extruded Rods

The character of the impedance response and the effect of dc bias thereon was different for long rods and thin slices and depended on the relative impedance contributions from the composite bulk and the electrodes. In Nyquist plots, the complex impedance of long rods was usually manifested as a single semicircle/arc and was independent or only very weakly dependent on $V_{dc} \leq 40$ V. This was the typical response of long rods, as shown by examples spanning the compositional range in Figure 5.1a. An additional example for the 14.5% SiC_w composition was shown in Chapter 4. For these rods, it is believed that the electrode impedance was much smaller than the impedance of the composite bulk, i.e. $R_{c0} << R_{b0}$, and therefore the former was concealed by the semicircle of the latter.

However, some of the more conductive rods (e.g. 19.1 and 24.0% SiC_w) displayed a different response, like that shown in Figure 5.1b. In Figure 5.1b, a second impedance semicircle appears at lower frequency, has a significant dependence on dc bias, and is attributed to Schottky blocking at the Ag-SiC interfaces at the electrodes, as in Chapter 3. Figure 3.3 is qualitatively similar to Figure 5.1b; in both cases, the application of dc bias shrinks the low-frequency semicircle and has no effect on the high-frequency semicircle. Thus, it can be inferred that the small low-frequency "tail" appearing in the $V_{dc} = 0$ V data of the 24.0% inset in Figure 5.1a resulted from the electrodes; for these samples, application of $V_{dc} \leq 20$ V was sufficient to eliminate these impedance tails, and $V_{dc} \leq 40$ V had no effect on the main semicircle. In Figure 5.1b, $V_{dc} \approx 20$ V was needed to eliminate the electrode feature and corresponds to $V_c \approx 6.7$ V dropping at the electrodes

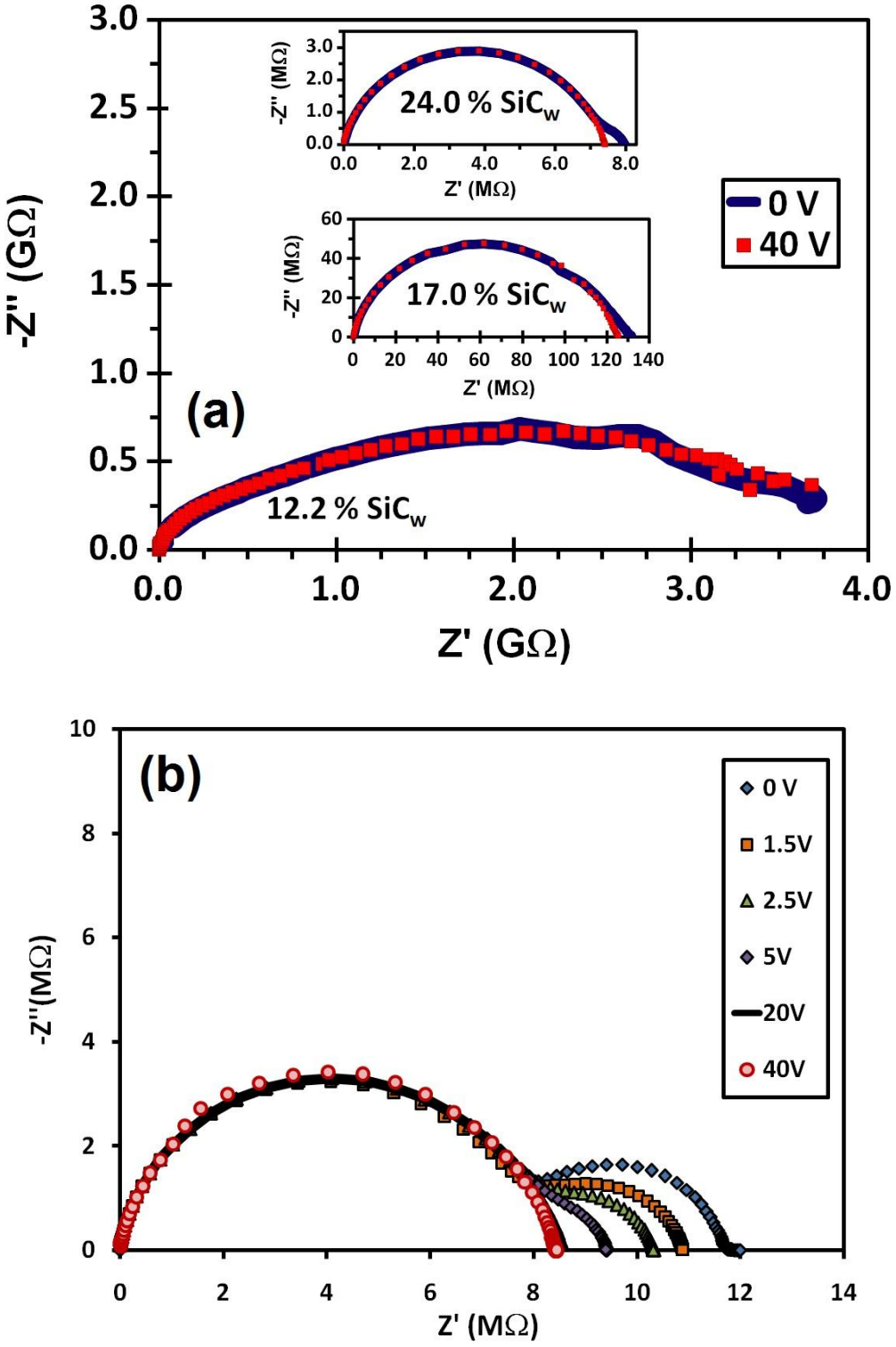

Figure 5.1. (a) Complex impedance response at V_{dc}=0 and 40 V for long rods ($z \approx 25$ cm) with Ag paint electrodes having 12.2 % SiC_w, 17.0 % SiC_w (middle inset), and 24.0 % SiC_w (top inset). Bias has minimal effect on the responses. (b) Effect of dc bias on a different 24.0 % SiC_w rod (z = 25.0 cm) having a larger electrode impedance.[22]

due to $\kappa_{c0} \approx \frac{1}{3}$. This V_c value has good correspondence to the low biases used in Chapter 3, e.g., see Figures 3.3 and 3.4.[18]

There[18], it was found that the electrode contributions to the impedance (R_{c0}) from Ag paint electrodes and sputtered electrodes vary significantly but may be distinguished due to order-of-magnitude differences. Here, the differences in impedance response observed among the more conductive long rods are attributed to such natural variability and the increased prominence of the electrode impedance when the bulk impedance is relatively low. Two-semicircle impedance response resulted when R_{b0} was relatively small, such that its magnitude was comparable to that of R_{c0}. This situation was more likely for samples containing a greater fraction of SiC_w, e.g. 24.0 % SiC_w rods with Ag-paint electrodes. One-semicircle impedance response resulted from larger values of R_{b0} such that the impedance from the electrodes was concealed by that from the composite bulk, i.e. $R_{c0} << R_{b0}$. This condition was often met for rods of higher composition (i.e., 19.1, 24.0 % SiC_w) and consistently met for the 12.2-17.0% SiC_w rods, which had larger resistivities. Samples having one semicircle and a small bias-dependent impedance tail are believed to be associated with an intermediate situation.

When there was a single impedance semicircle containing a concealed electrode contribution that was too small to manifest a tail, κ_{c0} must have been very small, which implies very small $|\alpha_c|$. Thus, the bias dependence of the electrode behavior was not manifested in the semicircle because most of the applied bias dropped across the relatively linear element of the bulk-electrode series equivalent circuit[18], i.e., the composite bulk. For all rods, the bulk impedance contribution was apparently independent of V_{dc} because the 0-40 V biases on the rods were partitioned across long

percolated clusters involving many SiC_w-SiC_w interfaces in series. Thus, the corresponding interfacial electric fields were relatively small and the aggregate rod response was apparently linear. This is an analogous result to that in Ref. 103, which was discussed earlier.

5.3.2. Impedance Response of Thin Slices of Rods

The above description of bias partitioning among the bulk and the electrodes is useful for understanding the different behavior of thin slices (z ~ 1.7 mm). For slices, it was important to use sputtered electrodes instead of Ag paint to minimize the electrode contribution (R_{c0}) to the impedance because the bulk contributions (R_{b0}) were ≥100 times smaller than those of long rods (z ~ 22-26 cm) of the same composition due to the different sample sizes. The use of Ag paint electrodes on thin slices resulted in bulk semicircle being partially or fully concealed by the superposition of the larger electrode semicircles (not shown); the data from such measurements is otherwise not discussed in this paper.

Figure 5.2a shows the complex impedance of a 24.0% SiC_w slice having Pt electrodes, which was found to result in the lowest contact resistances on Al_2O_3-SiC_w composites.[18] The figure shows a single semicircle which shrinks with increasing dc bias and is attributed to the percolated SiC_w cluster. For such slices, the contribution from the electrodes was believed to be negligible because the average σ_{dc} of slices ($2.12 \cdot 10^{-6}$ S/cm) was similar to that for long rods ($2.05 \cdot 10^{-6}$ S/cm). The significantly non-ohmic behavior which is evidenced by the bias-dependent dc resistance (R_b) differs from the mostly-

ohmic behavior of the bulk of long rods because the electric fields within thin slices were ≥100 times greater due to the smaller sample dimension (*z*).

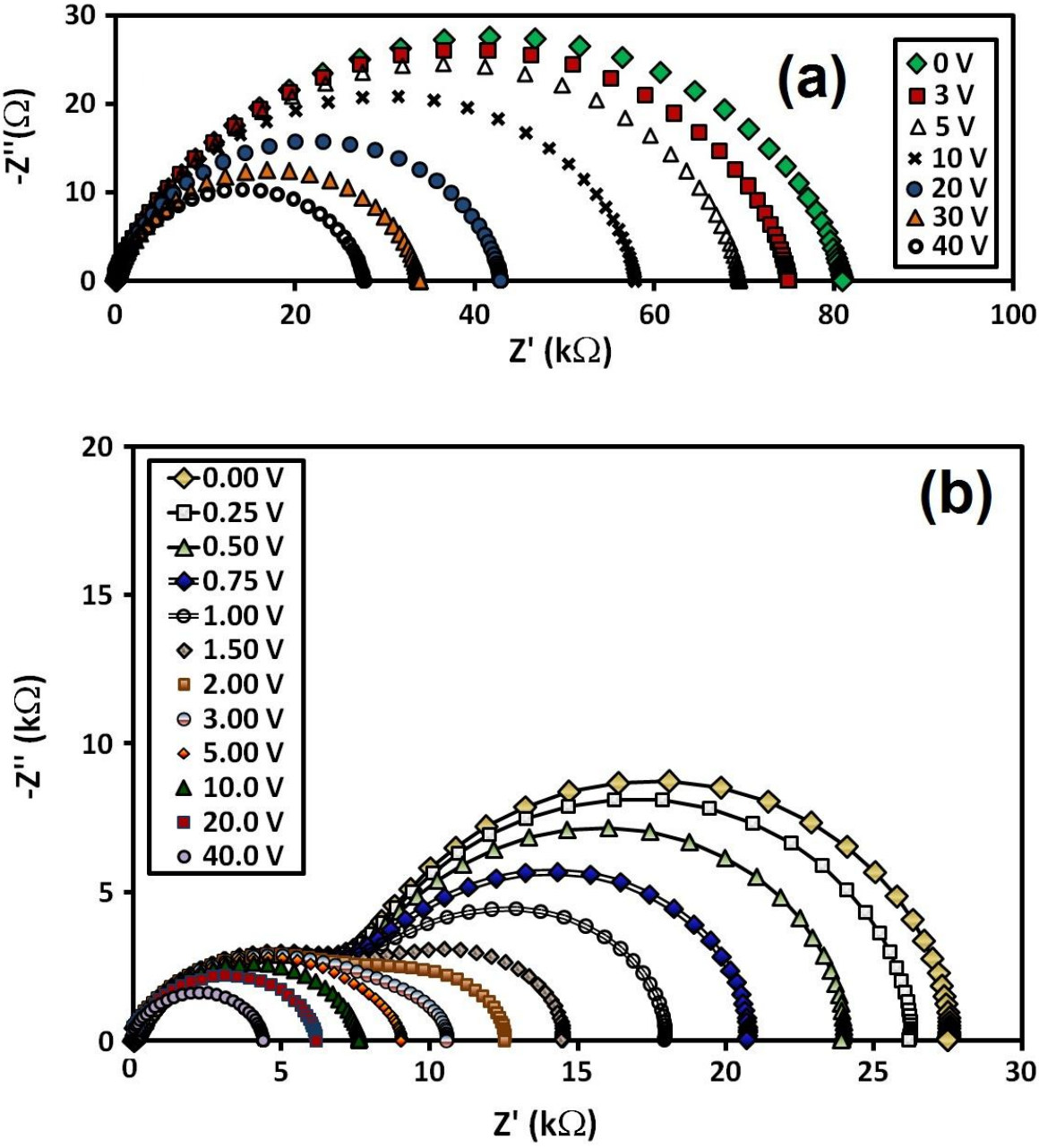

Figure 5.2. Effect of dc bias on the complex impedance of 24.0% SiC_w thin slices (*z* = 1.75 mm) with sputtered electrodes of different metals and comparatively different bulk-composite conductivities:[22] (a) Pt with low σ_{dc} , (b) Ag with high σ_{dc}.

For slices of 10.0-19.1% SiC_w rods, which had lower σ_{dc}, the use of sputtered Ag electrodes always resulted in a bias-dependent single-semicircle behavior which was qualitatively similar to that shown in Figure 5.2a. This implies that the electrode contribution to the complex impedance is concealed due to $R_{b0}>>R_{c0}$. For some 24.0% SiC_w slices, the use of sputtered Ag electrodes (having higher contact resistivity compared to Pt)[18] resulted in two distinct bias-dependent impedance semicircles due to R_{b0} and R_{c0} having comparable magnitudes. This happened when σ_{dc} of the slice was substantially higher than the composition average, e.g. in Figure 5.2b, for which the sample σ_{dc} was five times greater. The variability in the impedance response of 24.0% SiC_w slices is due to the same reasons as discussed above for long rods and is subject to the additional variability associated with a much smaller (≥100 times) sampling of the 24.0% composite mixture. It is suspected that the variable conductivity of slices is the result of variations in porosity and SiC_w alignment along the rod lengths, which may relate to the observed[20] non-uniform extrusion rate.

In Figure 5.2b, the application of a 5 V dc bias was sufficient to effectively eliminate the low-frequency electrode semicircle and had minimal impact on the bulk semicircle because most of V_{dc} applied at the electrodes. Using the bias partitioning approach (Equations 5.4-5.6), $\kappa_{c0} \approx 0.8 > \kappa_{b0}$, and $V_b \approx 1$ V and $V_c \approx 4$ V. For the long rod in Figure 5.1b, most of V_{dc} dropped across the rod length and it is estimated that $V_c \approx 6.7$ V was sufficient to eliminate the electrode semicircle. Thus, a bias on the order of $V_c \approx 5$ V was generally sufficient for overcoming blocking at the electrodes of both rods and slices. In Figure 5.2b, further increasing V_{dc} in the 5-40 V range resulted in shrinkage of

the high-frequency semicircle, i.e. decreasing R_b, and is attributed to non-linear response at SiC_w-SiC_w interfaces in the percolated SiC_w cluster.

5.3.3. Modeling the Capacitance-Bias Response for Slices

The bias-induced shrinkage of the impedance semicircles related to bulk composite material of thin slices with sputtered electrodes (e.g. Figure 5.2b) is first analyzed in terms of the effective capacitance which was obtained by fitting the semicircles, as in Chapter 3 and Ref. 18. For such fits, it was assumed that the electrode contribution to the impedance was negligible, i.e. $V_{dc} = V_b$. Figure 5.3 shows that the decrease in capacitance with total applied bias was well-modeled with Equation 5.2.

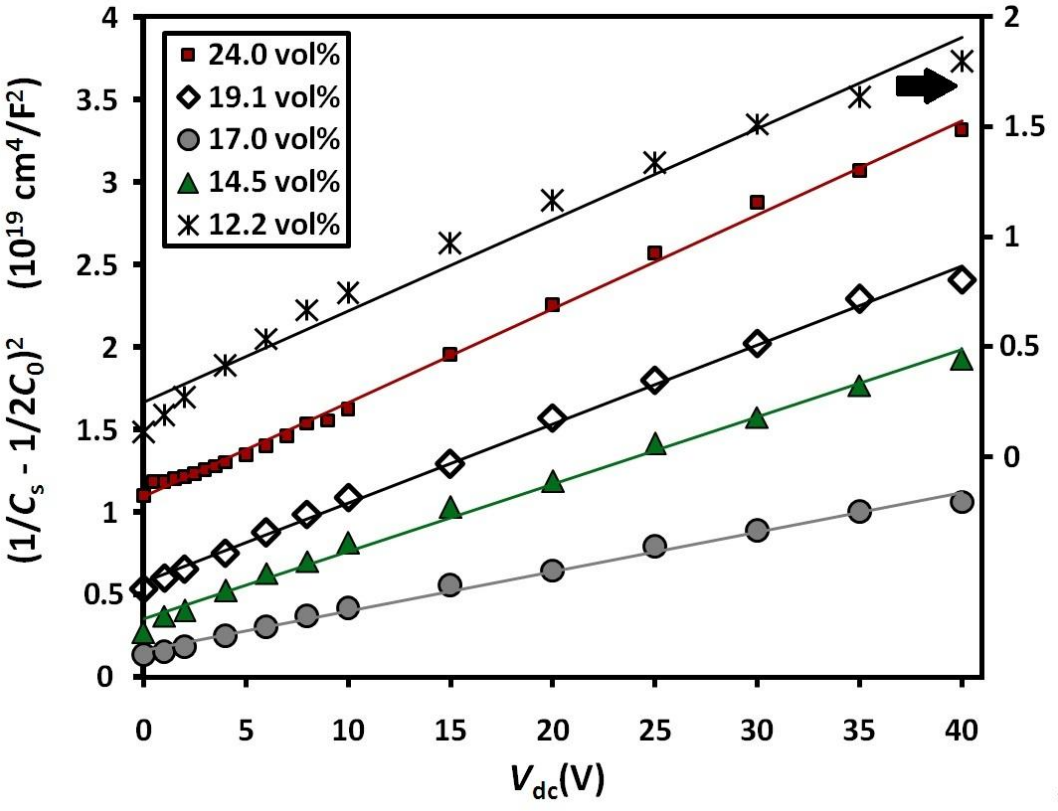

Figure 5.3. Capacitance-bias data plotted in terms of Equation 5.2 for thin slices. All data is plotted on the left axis, except for 12.2% SiC_w data, which is plotted on the right axis for clarity.[22]

Here, V_i=V_b is implicitly assumed and does not affect the goodness of the straight-line fits, which indicate agreement with the Mukae model[19] and that blocking at symmetrical Schottky-type barriers is the main source of the measured impedance. Therefore such barriers are believed to exist at interwhisker interfaces in the electrically-percolated cluster. As such, it is speculated that the Mukae model may be applicable over a range of interfacial thicknesses and that the bias distribution throughout a cluster is non-uniform and concentrated at these interfaces. Similar to grain boundaries in conventional polycrystalline varistors,[15,16] the electronic structure of these interfaces might be influenced by impurities from the sintering additives.[21]

Now, consider in more detail the use of Equation 5.2 for the analysis of systems containing symmetrical Schottky-like energy barriers at numerous interfaces. Estimation of the corresponding barrier height[19,103] generally assumes $V_i = \bar{\kappa}_i V_{dc}$. Here, $\bar{\kappa}_i$ is the fraction of the total applied bias relevant to each interface (a partitioning factor) and the overbar indicates averaging over the range of applied V_{dc} to account for the bias dependence of partitioning. If a straight-line is yielded from plotting the data in the form $(1/C_s\text{-}1/2C_0)^2$ vs. V_{dc}, then the model is applicable and the division of the line intercept ($2\Phi_i /q\varepsilon_s N_d$) at V_i=V_{dc}=0 by the slope ($2\kappa_i/q\varepsilon_s N_d$) yields $\Phi_i /\bar{\kappa}_i$. Similarly, the intercept/slope quotient yields an accurate Φ_i value for a linear plot of $(1/C_s\text{-}1/2C_0)^2$ vs. V_i, *if the assumed value of* $\bar{\kappa}_i$ *is accurate*. For both types of plots, the intercept has experimental correspondence to $1/4C_0^2$ and is unaffected by the estimated partitioning factor $\bar{\kappa}_i$, unlike the slope. In Mukae plots using V_i for the abscissa, the change (Δ) in $(1/C_s\text{-}1/2C_0)^2$ between two points on a line is independent of $\bar{\kappa}_i$, but the corresponding

change in V_i is not, i.e. $\Delta V_i = \bar{\kappa}_i \Delta V_{dc}$. Thus, such slopes and corresponding estimates of Φ_i depend significantly on assumptions about the bias distribution.

Therefore values of $\Phi_i / \bar{\kappa}_i$ were calculated from the division of the $1/4C_0^2$ intercepts by the slopes of fitting lines like those in Figure 5.3. In Section 5.3.8, the results are presented and explained in the context of model predictions for the bias distribution in a percolated cluster.

5.3.4. Modeling the Resistance-Bias Response for Slices

The dependence of the bulk composite dc resistance (R_b) on dc bias (V_{dc}) which is apparent in Figure 5.2a indicates a non-linear current-voltage response which may be modeled with an equation analogous to Equation 5.3,

$$R_b = R_{b0} \exp(\alpha_b V_{dc}). \qquad (5.7)$$

Here, $R_b = R_{b0}$ when $V_{dc}= 0$, $V_{dc}=V_b$ is assumed, α_b is negative and reflects non-linearity strength, and ohmic behavior corresponds to $\alpha_b=0$. In Figure 5.4a, R_b-V_{dc} data is presented from representative slices which have widely differing resistances due to SiC_w composition. The presentation is based on Equation 5.7 and considers the resistance normalized to the zero-bias value (R_b/R_{b0}) in order to assess the relative strength of the non-linearity in the I-V_{dc} response and the relative agreement with the model for the various compositions. With increasing SiC_w loading, the non-linearity of the I-V_{dc} response decreased and this is evidenced by the average slope of the data decreasing towards ohmic behavior, i.e., a flat horizontal line in Figure 5.4a described by $\ln(R_b/R_{b0})=0$ for all V_{dc}.

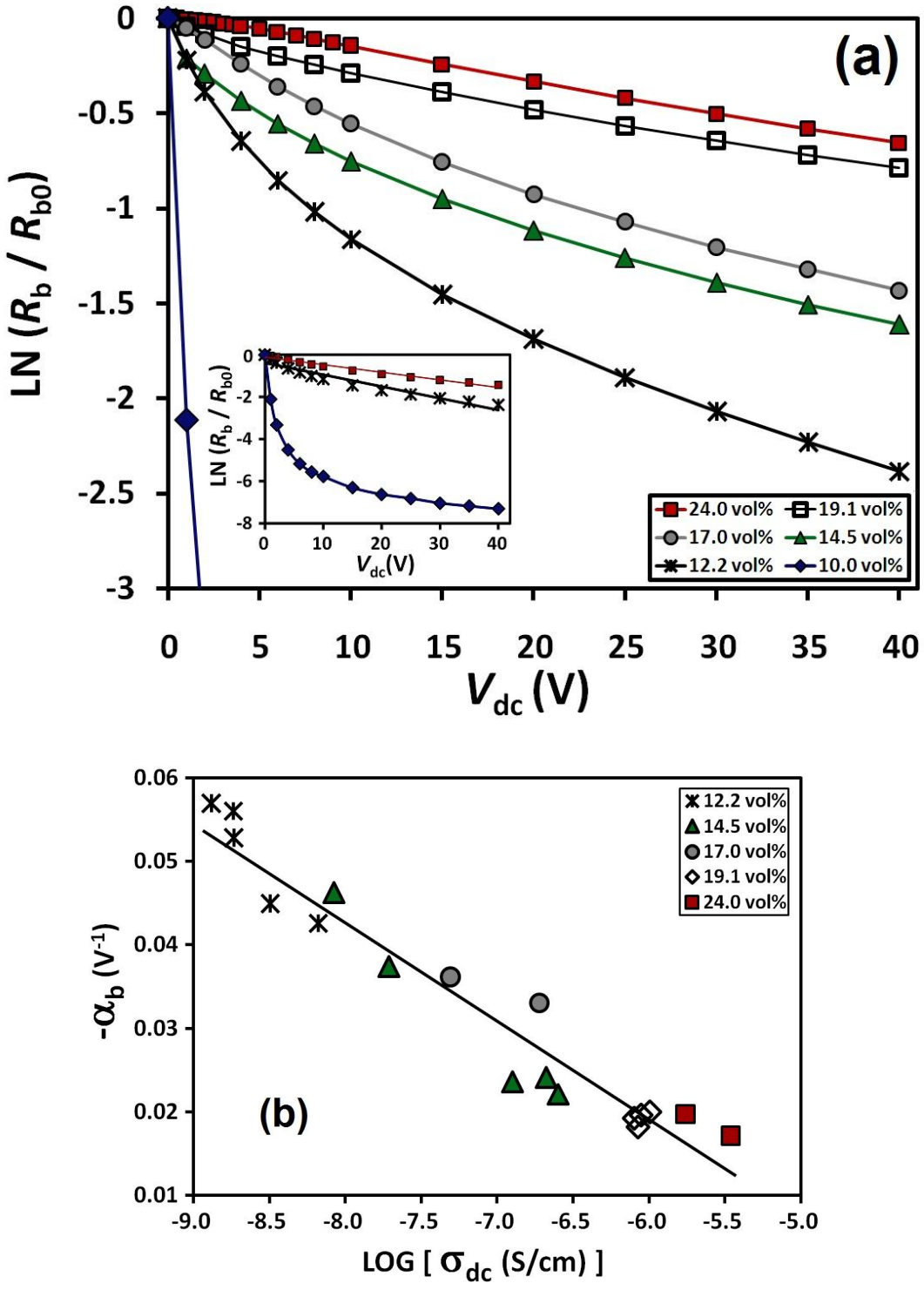

Figure 5.4. (a) Presentation of the effect of dc bias on the normalized resistance of thin slices having different SiC_w composition in accordance with Equation 5.7. The inset shows similar data for the 10.0% SiC_w sample and the linear fits for the 24.0% and 12.2% SiC_w samples. (b) The relationship between dc conductivity and α_b coefficient of non-linearity, as determined by linear fits of data like those shown in the inset of part (a).[22]

Figure 5.4b shows α_b values determined from different slices typically decreased with whisker content but had a more direct correlation with dc conductivity. The reason for this is elucidated throughout Sections 5.3.6, 5.3.7, and 5.3.8. In Figure 5.4a, the agreement of the data with Equation 5.7 is considered good if the data points (connected by curved lines for clarity of presentation) can be fit by a *straight* line. The inset of Figure 5.4a shows such linear fits for 12.0 and 24.0 % SiC_w data. The quality of such fits generally decreased with decreasing whisker content but remained acceptable for the 12.2-24.0% SiC_w range, for which R^2=0.94 and R^2=0.99 were typical for the respective compositional extremes. The inset of Figure 5.4a also demonstrates how the I-V_{dc} non-linearity of the 10.0% SiC_w samples, which correspond to the percolation threshold, was much greater than that of other compositions and could not be accounted for with Equation 5.7. By contrast, fitting 10.0% SiC_w data with Equation 5.1 yielded R^2=0.99 and α_V = 2.5.

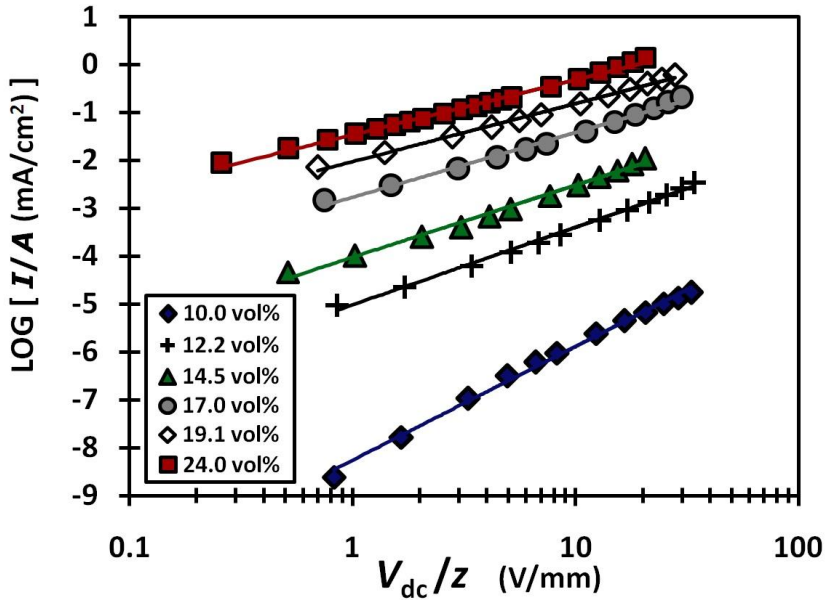

Figure 5.5. Geometrically-normalized I-V_{dc} data[22] from thin slices of various composition, plotted in accordance with Equation 5.1.

In Figure 5.5, data from all compositions is well-fit to straight lines on log-log scales, which indicates agreement with Equation 5.1; fitting quality and α_V values are not changed by the use of geometrically normalized values of current (I/A) and bias (V_{dc}/z). The good fitting for all the compositions means that Equation 5.1 is the most general description of the non-linear I-V_{dc} response of the SiC_w percolated cluster. The varistor non-linearity coefficient α_V scales with the magnitude of the α_b coefficient, as shown next.

5.3.5. Comparison of Resistance-Bias Response Models

Equations 5.1 and 5.7 adopt different approaches to modeling the non-linear I-V_{dc} behavior; in the latter equation, the constant of proportionality between the stimulus (V_{dc}) and the response (I) which is expected from Ohm's Law is modified to include an exponential dependence on dc bias, based on physics of semiconductor junctions.[18,118] The former equation states that the stimulus and response are related by a power law and is empirical. It may be alternatively stated[15] as

$$I = G\, V_{dc}^{\alpha_v} \tag{5.8}$$

where G is a conductance-like quantity whose units depend on α_V.

A relationship between the two approaches is developed as follows. The right-hand side of Equation 5.1 may be rewritten as the product $(V_H/V_L)^{\alpha_V - 1}\cdot(V_H/V_L)^1$ and rearranging the equation yields

$$(V_H/V_L)^{-\alpha_V + 1} = (V_H/I_H)\cdot(I_L/V_L). \tag{5.9}$$

The current-voltage ratios on the right-hand side may be considered to reflect the *bias-dependent* resistance R_b (determined from the low-frequency impedance) at the two points in the I-V_{dc} data which define the range over which fits were performed, i.e. 1 V and 40 V. Substitution of Equation 5.7 follows and results in

$$(V_H/V_L)^{-\alpha_V+1} = \exp(\alpha_b V_H) / \exp(\alpha_b V_L). \qquad (5.10)$$

Taking the natural logarithm of both sides and rearrangement yields

$$\alpha_V - 1 = \alpha_b(V_H - V_L) / \ln(V_H/V_L) \qquad (5.11)$$

and insertion of V_H = 40V and V_L = 1V provides the α_V-α_b relation expected to be observed, i.e.

$$\alpha_V - 1 = \alpha_b(39\text{V}) / \ln(40) \cong (10.57\text{V})\alpha_b \qquad (5.12)$$

This equation has good correspondence to the comparison of the results of fitting the experimental data to the alternative models shown in Figure 5.6. The linear regression trend which is apparent may be described by an equation which is very similar to Equation 5.12, i.e. $(\alpha_V - 1) = (10.722\text{V})\alpha_b$ with $R^2 = 0.988$. Therefore the values of α_V and α_b are related by the range of applied stimulus.

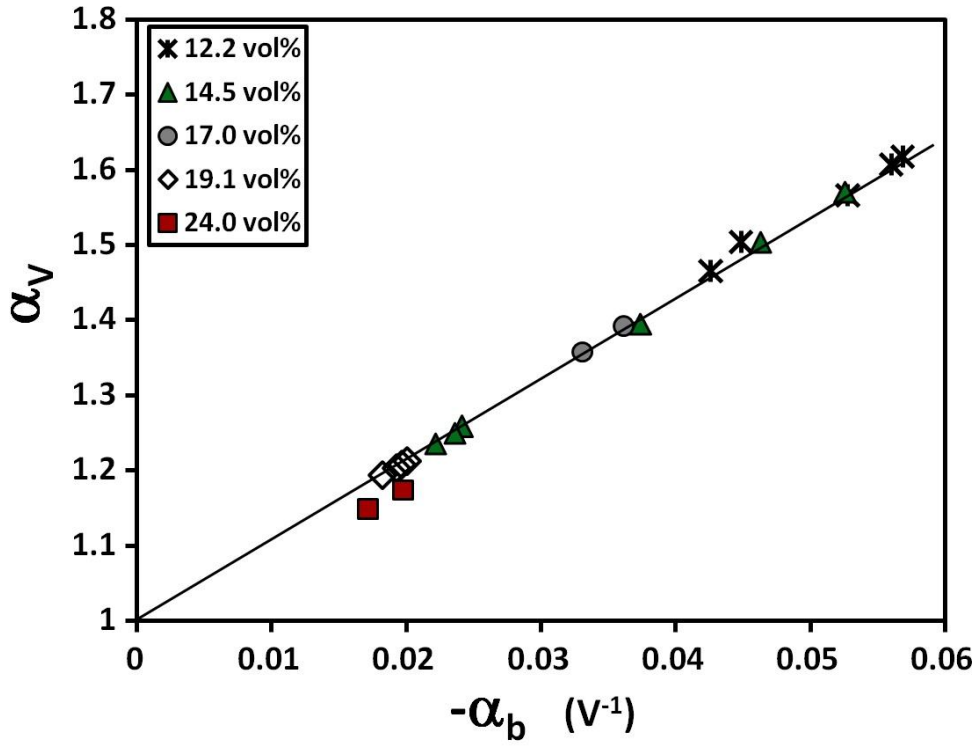

Figure 5.6. The relationship between the coefficients of non-linearity described by Equations 5.1 and 5.7, as determined from thin slices having variable SiC_w content. The solid line was calculated by linear regression.[22]

5.3.6. Effect of Composition on DC Conductivity and Non-Linearity Strength

The dc conductivity of the percolated samples increased with nominal whisker content (p), and the data was fit via the well-established power law, i.e.

$$\sigma_{dc} \propto (p - p_c)^t \tag{5.13}$$

using the average conductivity for each composition in the $12.2 \leq p \leq 24.0$ % SiC_w range and p_c = 9.96% SiC_w for the percolation threshold. The data and results are given in Table 5.1. For long rods, t =3.40 when $V_{dc} = 0$. For thin slices, t = 3.54 for $V_{dc} = 0$, and t = 2.95

when dc biases corresponding to ~20 V/mm homogeneous electric field were applied to the same set of samples.

Table 5.1. DC conductivities obtained from long rods and thin slices at V_{dc}= 0 V (σ_{dc}), and the same slices with a ~20 V/mm applied electric field ($\sigma_{dc,bias}$). Values are given in units of 10^{-8} S/cm ± one standard deviation. Exponents (*t*) and regression coefficients (R^2) from fits to Relation 5.13 using p_c = 9.96% SiC_w are also given.

***p* (%SiC_w)**	**12.21**	**14.45**	**17.0**	**19.1**	**24.0**	***t***	**R^2**
σ_{dc} (rods)	0.444 ± 0.305	9.05 ± 9.42	10.9 ± 4.3	132 ± 28	205 ± 49	3.40	0.933
σ_{dc} (slices)	0.280 ± 0.217	10.4 ± 10.9	11.9 ± 9.9	88.4 ± 9.1	212 ± 116	3.54	0.944
$\sigma_{dc,bias}$ (slices)	1.75 ± 0.67	28.1 ± 25.6	33.9 ± 26.2	174 ± 12	439 ± 192	2.95	0.957

With the dc electric field applied, the value of *t* was substantially reduced from 3.54 to 2.95. Thus, the conductivity increased with composition, and the extent to which it did so depended on dc bias. Similarly, Figures 5.4a and 5.4b indicate that conductivity increased with bias and that the extent to which it did so depended on composition. But in Figure 5.4b, the correlation of the non-linearity strength with σ_{dc} is stronger than that with the nominal whisker content and Table 5.1 shows that there was considerable variability in the dc conductivity for a given nominal whisker content. These facts suggest that the mechanism responsible for the increase of conductivity with increasing filler content could be coupled to the mechanism responsible for the decrease in the strength of the non-linearity. Such a possibility is now explored.

The conductivity of the samples should be considered in terms of conduction through the percolated whisker cluster. If the percolated filler cluster is viewed as a two-terminal network of resistors all having equal resistance, the only way to increase the corresponding composite conductivity is to increase the number of resistors in parallel or decrease the number of resistors in series.[8] Henceforth, these network characteristics will be referred to as conduction "parallelism" and "series character", respectively. When the fillers are aligned conductive sticks and the composite conductivity is limited by interfiller junctions rather than intrafiller conduction, the conductivity increase with filler loading reflects an increased preference to increase parallelism relative to decreasing series character, which tends to result in a smaller t value.[11] This result is manifested in Figure 1.14. Since the capacitance-bias trends in Section 5.3.3 indicate that the measured impedance was mainly due to interfacial barriers, and the $t \approx 3.5$ value is large, it is inferred that increasing whisker content increased the Al_2O_3-SiC_w composite conductivity primarily by increasing conduction parallelism in the percolated cluster.

But by itself, increasing parallelism cannot explain the trend of decreasing non-linearity. When a bias is applied across a set of equivalent linear or non-linear resistors in parallel, the voltage across each, current through each, and the effective non-linearity of the aggregate are the same regardless of how many elements exist in the set. Analytical work in random-resistor network (RRN) theory reveals a more striking generality. When non-linear resistors obeying Equation 5.8 with the same α_V are arranged in an arbitrary two-terminal RRN, the network also responds with the same α_V via Equation 5.8, even if the individual G values vary.[154,155] This implies that the strength of the non-linear response must vary within the percolated clusters of real materials, and the structural

evolution of such clusters which is associated with increasing filler content is, by itself, insufficient for explaining the composition dependence of the non-linearity.

When RRNs contain a mixture of two types of components, one linear and the other non-linear, the linearity of the aggregate typically increases with the fraction of linear components[13] (see Figure 1.20). However, the character of the relationship depends on the relative conductances of the different components. When the linear-component conductance is much greater than that of the non-linear component, the strength of the network non-linearity exhibits a divergence at equal-parts composition and decreases rapidly as the fraction of linear components increases.[13] The experimental trend of Figure 5.4b shows that the strength of the non-linearity decreased with σ_{dc} via a power law. This implies a similar divergence and suggests that, with increasing overall conductivity, the composite electrical response increasingly reflects contributions from relatively conductive and ohmic portions of the percolated cluster.

The trend of the non-linearity weakening with increasing filler content has been reported elsewhere,[146,149,151] and the last inference is consistent with the authors' interpretation in Ref. 149. They attributed the trend to an increased contribution to the electrical response from ohmic conduction within the graphite filler compared to tunneling through the epoxy matrix.[149] The interpretation of Ref. 151 was incomplete because there was no mention of the percolation concept, despite the fact that samples of that study used high levels of filler loading (10-50 vol%) and the composition dependence of the polyethylene-Si composite resistance at 10 V dc bias was suggestive of the percolation phenomenon. Those authors attributed the trend of weakening non-linearity to the thickness of the insulating matrix interlayers between Si particles

decreasing as particle loading increased.[151] For the present composites, the notion of significant spacings existing between percolated SiC_w does not agree with the mechanical rigidity of percolated-whisker networks which affects both sintering and the mechanical response.[20,50,56] Also, their interpretation[151] contradicts a previous work[18] in which it was deduced that, if the interfacial thickness is reduced, the interfacial electric fields strengthen more rapidly with increasing V_{dc} and thus amplify the observed non-linearity, all else being equal.

In that work,[18] the most basic type of equivalent circuit model having equal parts linear and non-linear components was used, i.e. a series of one of each. In the next section, a similar but expanded model is developed which follows logically from this discussion, and which correctly predicts the qualitative character and some quantitative aspects of the experimental results.

5.3.7. Model of the Electrically Percolated Cluster

Continuing from Section 5.3.6, I now propose an original model of the electrically-percolated cluster of discrete SiC_w. The model is based on the idea that this cluster consists of two components having different electrical behavior, whiskers and interfaces between whiskers, and is developed as follows. First, the topological structure and constituent features of single-component percolating clusters are examined. Then, based on the composition dependence of the topological structure, the experimental data, and results from the simulation of a similar system,[11] a structural simplification is employed and a composition-dependent equivalent circuit is developed. Next, characteristics about the nature of the current distribution in a real whisker cluster are inferred based on the electrical behavior and spatial distribution of the two components

within the context of the single-phase topology and the equivalent circuit. The properties of the whiskers and interfaces are accordingly assigned to the circuit elements based on these inferences. Finally, experimental data is compared to predictions of the model.

Consider the single-component approximation of the two-component electrically percolating cluster which ignores the interfaces between SiC_w, i.e., boundaries of "insignificant" small size such as tunneling gaps or grain boundaries. This allows one to consider the 'topology'[156] and the 'connectivity distribution'[157] in such a cluster. Connectivity (K) may be defined as the number of cuts that can be made through an object without dividing it into two disconnected parts.[133] The topological structure of a single-component cluster percolating between two terminals may be considered in terms of three distinct feature classes. In the literature,[157] these are known as (1) singly connected 'links' (2) 'blobs', and (3) 'dangling ends,' and are associated with colors. Links, or 'red' bonds, are bonds which divide the cluster into two separate non-percolating clusters when cut and do not contribute any connectivity. Dangling ends and blobs fully account for the non-zero K of percolating clusters. For a 'traveler' on a cluster starting at one of the terminals, a 'yellow' dangling end is a 'dead end'; upon entering a dangling end, it is impossible to reach either terminal without exiting through the original entrance point. Blobs define the remainder of the percolating cluster and are composed of multiply-connected 'blue' bonds. Percolation is maintained if a single blue bond is cut.

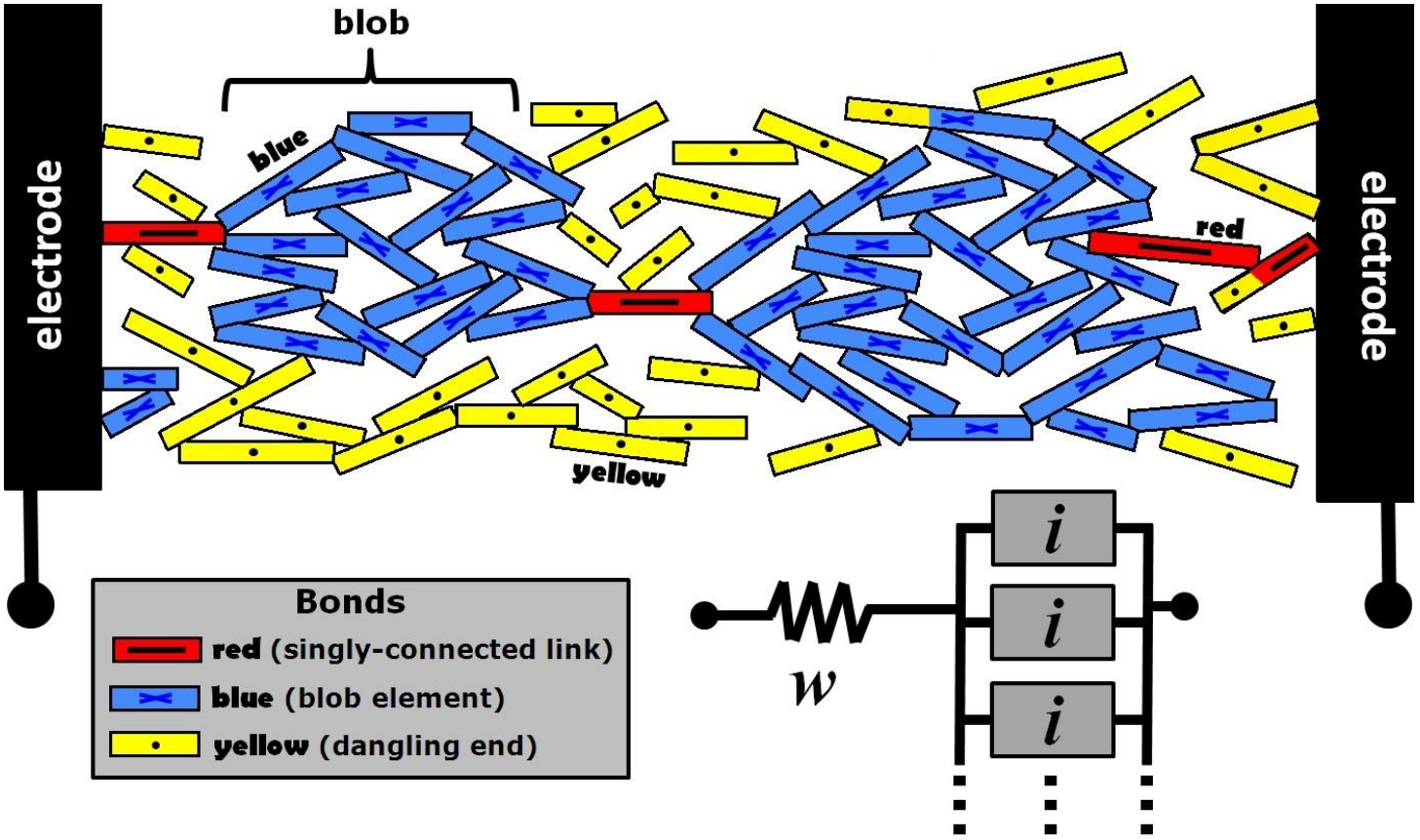

Figure 5.7. Whisker cluster percolating between two terminals. Whiskers are classified with colors (and symbols, for readers without color) to demonstrate the structural-topology approximation (which ignores whisker-whisker interfaces). Also, the two-terminal equivalent circuit model is shown.[22]

These topological concepts are demonstrated in the schematic diagram of an imagined percolating whisker cluster in Figure 5.7. In Figures 1.7b, 1.8b, and 1.13, it was seen that that red bonds do exist when the sticks are not aligned[6] along an axis and that preferred uniaxial alignment tends to reduce the connectivity of the ensemble,[8,158] thereby implying an increased probability of red bonds. This suggests that a significant number of red bonds exist in the extruded composites.

When a dc bias is applied across the opposing ends of a topological percolating cluster, red bonds carry the entire current, blobs divide the current amongst parallel branches, and dangling ends do not carry any current. Dangling ends may contribute to the cluster *K* but not to the cluster conductance, and one may imagine that the severance of a blue bond which has no potential difference across it affects *K* but not this conductance. Clearly, the correspondence between the *K* of a percolating cluster and the composite conductivity is convoluted.

Composite conductivity follows from the structure of the electrically-conducting "backbone," which is defined by the series combination of the red bonds and blobs and underpins the modeling approach. When all the red bonds have been cut, the blobs are all that remain of the backbone. The blobs account for all of the conduction parallelism whereas red bonds act as structural bottlenecks for current flow and necessarily act in series.

Based on these correspondences, the basic structure of an equivalent-circuit model (Figure 5.7) for a percolating cluster is proposed and its development is continued based on additional considerations. For now, the single '*w*' series resistor and the large set of parallel '*i*' elements in the model represent all of the red bonds and all of the blobs

in the corresponding whisker cluster, respectively. In the model, these two backbone elements are defined to have effective total conductances G_{Tw} and G_{Ti}, respectively. Subscript "*T*" denotes an effective total, whereas the '*w*' and '*i*' labels are based on insights realized later. The effective total conductance G_T of a sample containing a percolated cluster is given by $G_T = (1/G_{Tw} + 1/G_{Ti})^{-1}$ since the red bonds and blobs are in series. This cluster is imagined to exist inside an imaginary sample of fixed geometry and therefore the dc conductivity of this sample goes as $\sigma_{dc,m} \propto G_T$. For clarity, subscript '*m*' is used to specify some parameters and results of the model which are analogous to already-defined experimental variables.

Now, consider how G_{Tw} and G_{Ti} change with filler content (p_m) above the percolation threshold ($p_{c,m}$). The conductances of the red bonds in a percolating cluster add in series, i.e. $G_{Tw} = G_w / N_{red}$, when N_{red} individual red bonds exist and each has conductance G_w. It has been exactly proven[159,160] that $N_{red} \propto (p_m - p_{c,m})^{-1}$ and thus

$$G_{Tw} \propto G_w (p_m - p_{c,m})^{+1}. \tag{5.14}$$

If the red bonds controlled the total conductance, then $G_{Tw} << G_{Ti}$ and $\sigma_{dc,m} \propto (p_m - p_{c,m})^{+1}$, but the experimental results indicate a much larger exponent, i.e., $t \approx 3.5$ from Relation 5.13. Since the attrition of red bonds with increasing p_m does not sufficiently account for the rate of increase of σ_{dc} with p, it is assumed that the evolution of the blobs does. Thus, $G_{Tw} >> G_{Ti}$ and that G_{Ti} increases dramatically with increasing p_m in order to account for Relation 5.13. In the equivalent circuit, the blob-based structure contains N_i parallel elements each having conductance G_i. Therefore the effective conductance of the blob is $G_{Ti} = N_i G_i$ and it is assumed that $N_i \propto (p_m - p_{c,m})^{\gamma}$ with $\gamma = 3.5 \approx t$ so that

$$G_{Ti} \propto G_i (p_m - p_{c,m})^{\gamma}. \quad (5.15)$$

In this approach, the effect of composition on the series character of the blobs is neglected based on the experimental and simulation results which suggest preferential expansion of parallelism relative to a diminishment of series character; this was discussed in Section 5.3.6. Certainly, such a reduction could reasonably be expected from Relation 5.13, but the attrition of red bonds via $N_{red} \propto (p_m - p_{c,m})^{-1}$ implies some degree of blob extension and an increase in blob series character. Such contradictory expectations also help to justify the simplification, which facilitates the circuit analysis of the model and its correlation to experimental results.

When a dc bias $V_{dc,m}$ is applied to the circuit model of Figure 5.7, it is partitioned between the parallel '*i*' block and the '*w*' series element, i.e. $V_{dc,m}=V_{i,m} + V_w$. The effective total current (I_m) through the parallel block equals that through the series element. Thus, following Relations 5.13-5.15, the model states

$$X^{\gamma} G_i V_{i,m}^{\alpha_i} = X^{+1} G_w V_w^{\alpha_w} \quad (5.16)$$

where the left and right sides of the equation describe the current for the '*i*' block and the '*w*' series element, respectively, in the form of Equation 5.8. Here, $X = (p_m - p_{c,m})/4$, and the non-linearity coefficients for the parallel '*i*' elements and the '*w*' series element are α_i and α_w, respectively. Using the load-line method,[118] Equation 5.16 was solved for I_m and $V_{i,m}$ at $V_{dc,m}$ =1,2,4,6,8, and 10. This was done for six ($p_m - p_{c,m}$) compositions which were chosen to roughly follow the experimental ($p - p_c$). The model parameters describing the electrical behavior of the components warrant discussion.

Relatively high conductances and low non-linearity coefficients were assigned to the '*w*' element compared to '*i*' elements in the model, which preferentially represent

conduction through the whiskers and through interwhisker interfaces, respectively. Specifically, $G_w = 10^3 G_i$ and $\alpha_w = 1.1 < \alpha_i = 3.0$. These assignments are consistent with the notion that interfiller interfaces are the main source of composite resistance,[8,149] the previous discussion of mixed RRNs, and structural considerations for stick-like filler. Hypothetically, a single (red-bond) whisker could electrically percolate a sample and thus completely avoid whisker-whisker interfaces, whereas the occurrence of current branching (e.g., within blobs) *necessarily requires* conduction through interfaces. Interfaces *may* but *need not* be involved in red bonds.

Such assignments are also consistent with the likely effects of the interfaces on the current distribution within the electrically percolating whisker cluster; it is the purpose of the equivalent circuit to model this current distribution with preference over modeling the topology. The capacitance-bias data presented earlier suggests that the interfaces between fillers are the main source of composite impedance, and relevant simulations[11] indicate a preference for conduction parallelism when this is the case. The current is expected to branch out when there is no path having resistance much lower than all parallel alternatives, and concentrate in such paths when they are available. In the equivalent circuit model of Figure 5.7, these situations have clear correspondence to the parallel '*i*' block and the '*w*' series element, respectively. They are also likely to have preferential correspondence to conduction through interfaces and through whisker bulks, respectively. Figure 5.8 demonstrates this by depicting the current distribution in an imagined percolating cluster for which the conductance of the whiskers is much greater than that of the interfaces. In analogy to a single-component topological approximation, the presentation uses colors in order to elucidate possible differences between the current

distribution that might be assumed from said topology and those which could actually occur when the interfaces control the composite conductivity. As the topological abstraction ignores ‘small’ interparticle gaps, this approximation of the current distribution ignores ‘negligible’ current flows and thus involves a degree of relativism. A current is considered negligible if it and all other parallel currents having the same magnitude may be subtracted from the total current without significantly affecting that total. For conceptual clarity, the effects discussed are exaggerated in the figure and new terminology adapted from river geography is proposed. In Figure 5.8, the percolating cluster contains ‘red channels’, ‘yellow billabongs,’ and a ‘normal delta,’ which is primarily composed of ‘blue tributaries.’ Current passes through these structures exactly as indicated by the previous descriptions for the similarly-colored bonds in the single-component topology, e.g., the total cluster current passes through every red channel. However, the percolating cluster also contains ‘shorted deltas’ and ‘incited deltas’ which likely have preferential correspondence to ohmic and non-linear conduction, respectively. A shorted delta is a topological blob for which the current is highly concentrated along a single pathway (i.e., a ‘maroon channel’) due to much larger interfacial resistances along all alternative pathways (i.e., ‘green tributaries’). Thus, the electrical behavior of maroon channels is similar to that of red bonds in a single-component topology. Maroon channels imply exceptionally high interfacial conductances, and conduction along the lengths of whiskers that are much longer and more favorably connected compared to their neighbors. Green tributaries carry negligible or zero current and may possibly exist in normal deltas, e.g., when there is a non-uniform current distribution in the delta or there is no potential difference across a blue bond. Blue tributaries carry significant current.

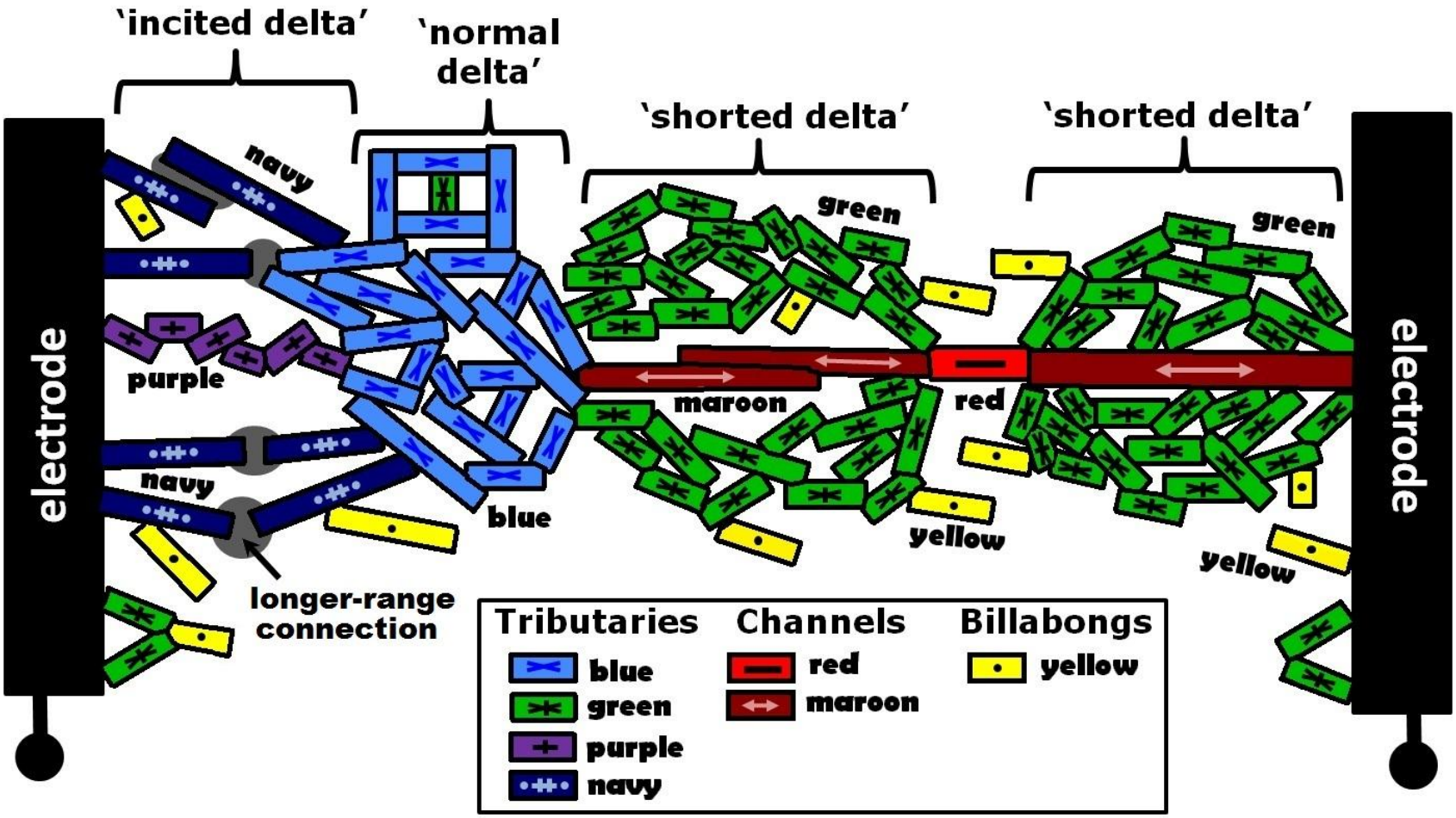

Figure 5.8. Whisker cluster percolating between two terminals. Conduction is limited by these interfaces and the cluster has exaggerated features to show how this affects the electrical-current distribution, which is described using the classifications based on river terminology which are introduced in the text.[22] The figure is a two-dimensional projection of a three-dimensional cluster.

An ‘incited delta’ is a structure which contains a red bond and narrowly misses being defined as a blob in the single-component topological approximation. This bond acts as a ‘purple tributary’ because it has high enough (interfacial) resistance such that there is sufficient impetus for longer-range connections between favorably positioned dangling ends called ‘navy tributaries.’ Such behavior for navy tributaries is agreeable with the idea of tunneling in dynamic RRN theory.[161] Dangling ends having insufficient impetus and/or proximity for such connections are named ‘billabongs.’ Purple and navy tributaries require each other to exist and contribute to conduction parallelism.

In this view of the percolating cluster, maroon and red channels conduct in series and have preferential physical correspondence to the high-conductance components and ohmic conduction through the crystal lattices of SiC_w. Purple, navy, and blue tributaries have preferential correspondence to current branching, the low-conductance non-linear components, and conduction across whisker interfaces. The dependence of the non-linearity strength on composition suggests that incited- and shorted-delta activity would be most prevalent slightly above and far above the percolation threshold, respectively. By these arguments, the equivalent circuit model and the assigned electrical properties of the components are justified.

5.3.8. Comparison of Model Predictions to Experimental Results

The current (I_{1m}) through the equivalent-circuit at $V_{dc,m} = 1$ is proportional to the effective dc conductivity of the model (i.e., $I_{1m} \propto \sigma_{dc,m}$) and exhibited a composition dependence similar to Relation 5.13, i.e. $I_{1m} \propto (p_m - p_{m,c})^{t_m}$ where $t_m = 3.39 \approx t \approx \gamma$ with correlation coefficient R^2=0.999, thereby giving confidence to the model. For larger bias, the goodness of fits decreased slightly and t_m decreased significantly, e.g., to R^2=0.991

and t_m = 2.15 for I_{10m} at $V_{dc,m}$ = 10. The $V_{dc,m}$ -t_m trend is apparent in Table 5.2 and is qualitatively consistent with the bias-dependence of t in Table 5.1. It reflects the fact that, at higher biases, the relatively composition- and bias-insensitive series conductors in the percolating cluster (i.e., the maroon and red channels) provided a greater relative contribution to the electrical response compared to those associated with conduction parallelism (i.e., navy, purple, and 'true' blue tributaries). This can be understood in terms of a shift in the bias distribution from the tributaries onto the channels, i.e., from the '*i*' block onto the '*w*' series resistor.

Table 5.2. Model parameters (composition, bias) for Equation 5.16 and results ($\alpha_{V,m}$, $\bar{\kappa}_{i,m}$, κ_i, t_m). Values of t_m were obtained via Relation 5.13. Results for κ_i are given in the box having a thick outline. Other parameters were $\gamma = 3.5$, $\alpha_w = 1.1$, $\alpha_i = 3.0$, $G_w = 1$, and $G_i = 10^{-3}$.

Composition		$\alpha_{V,m}$	$\bar{\kappa}_{i,m}$	**Bias ($V_{dc,m}$),** Conductivity Exponent (t_m)					
X	***$p_m/p_{c,m}$***			**1**, 3.39	**2**, 3.16	**4**, 2.80	**6**, 2.54	**8**, 2.35	**10**, 2.15
1	**1.25**	2.953	0.9643	0.9982	0.9939	0.9805	0.9617	0.9414	0.9100
2	**1.50**	2.682	0.8864	0.9912	0.9718	0.9198	0.8637	0.8106	0.7614
3	**1.75**	2.448	0.8053	0.9780	0.9345	0.8408	0.7583	0.6908	0.6292
4	**2.00**	2.268	0.7358	0.9602	0.8920	0.7618	0.6637	0.5970	0.5400
5	**2.25**	2.116	0.6772	0.9376	0.8445	0.6945	0.5927	0.5256	0.4684
6	**2.50**	1.999	0.6280	0.9130	0.7985	0.6372	0.5363	0.4684	0.4148

In the model, the bias $V_{i,m}$ across each parallel '*i*' element is the same. The fraction of the total bias $V_{dc,m}$ that was partitioned to the parallel block ($\kappa_i = V_{i,m}/V_{dc,m}$) was calculated for each X-$V_{dc,m}$ combination and given in Table 5.2. Of course, $\kappa_w = 1-\kappa_i$. It was found that κ_i decreased with increasing $V_{dc,m}$, and the strength of this trend

increased with increasing X. Also, κ_i decreased with increasing X and the strength of *this* trend increased with increasing $V_{dc,m}$. These trends reflect the decrease of the quantity (G_{Tw} - G_{Ti}) and the corresponding increase in the fraction of the total bias being applied to the '*w*' series element, which accounts for red and maroon channels.

For each composition, the I_m-$V_{dc,m}$ curves of the model were constructed and the effective non-linearity coefficients $\alpha_{V,m}$ were determined by fitting to Equation 5.8. In Figure 5.9a, the model results are plotted alongside experimental results from slices (α_V) which were obtained by similar fits. In this plot, the model and experimental results use $\log(I_{1m})$ and $\log(\sigma_{dc})$ for the abscissa, respectively, because $I_{1m} \propto \sigma_{dc,m}$. The experimental data shows how Al_2O_3-SiC_w composites exhibit varistor-like I-V_{dc} response which is generally weak compared to commercial varistors. The values of the non-linearity coefficient α_V decreased with increasing SiC_w content and composite conductivity. The similar straight-line behavior of the model trend resulted from a shift in the bias distribution from the '*i*' block to the '*w*' series element, which implies a greater relative contribution to the electrical response from ohmic conduction through the whiskers (channels) compared to non-linear interfaces (tributaries). The experimental trend can be described by $\alpha_V=0.6773(\sigma_{dc}\ [S/cm]\ )^{-0.04165}$ or $\sigma_{dc}=(11.90\ S/cm)\cdot\exp(-13.94\alpha_V)$ with $R^2=0.986$ and $R^2=0.981$, respectively. The trend of the model has approximately the same type of mathematical form, as evidenced by the similar straight-line fitting on a linear vs. log plot. This semi-quantitative agreement speaks to the model's validity.

The effective non-linearity coefficient of a series circuit containing elements of different non-linearity depends on the bias partitioning to the different elements, and the bias partitioning itself depends on the magnitude of the bias, as noted earlier.

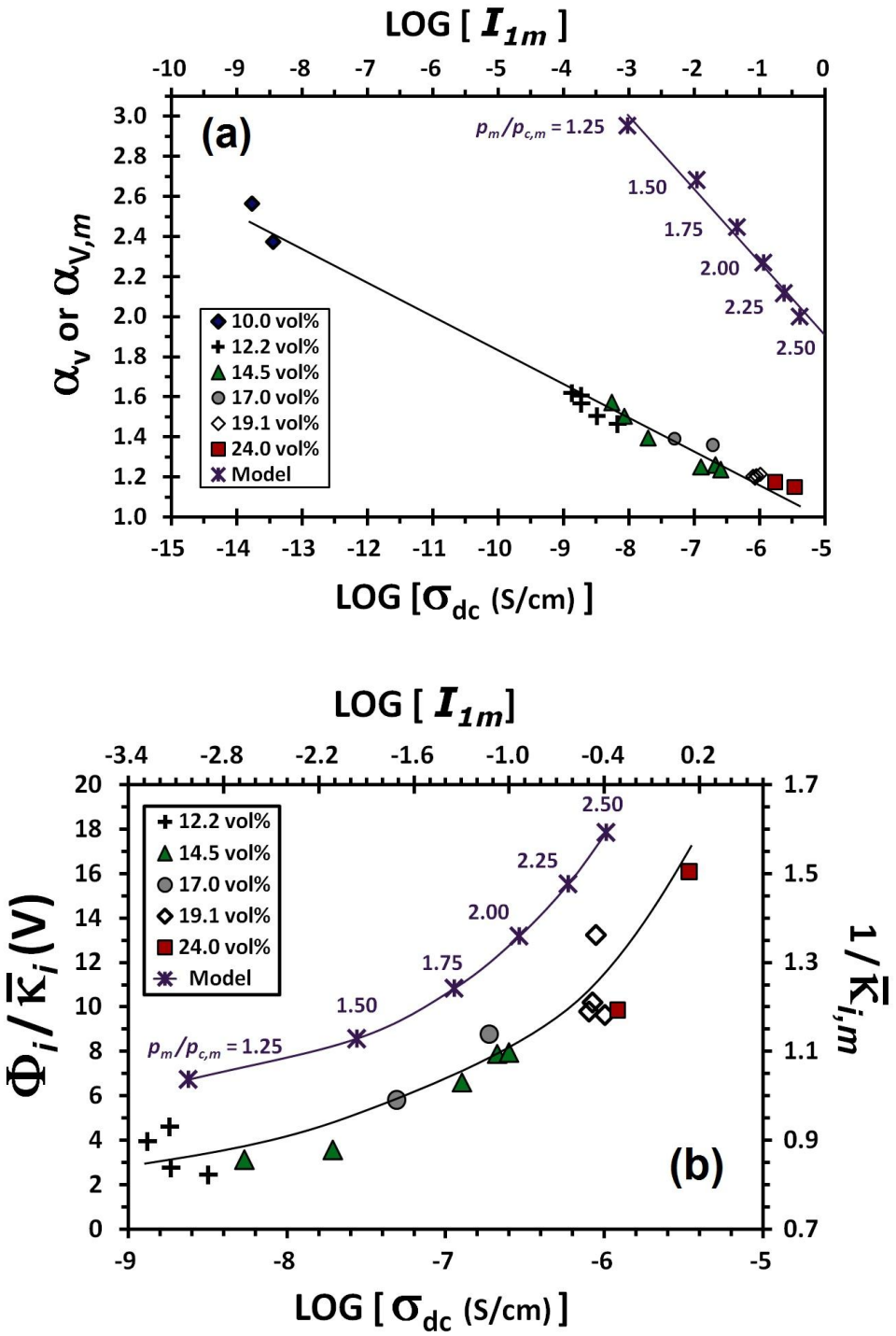

Figure 5.9. (a) The varistor coefficient of non-linearity strength from thin slices of various SiC_w composition plotted as a function of dc conductivity (on the bottom axis) alongside analogous model results (using the top axis). (b) Experimental results for the $\Phi_i/\bar{\kappa}_i$ parameter as a function of dc conductivity (using the left and bottom axes). Analogous model results are plotted against the top and right axes.[22]

In the model, $\alpha_{V,m}$ increased with κ_i calculated at the lowest bias ($V_{dc,m}$ =1), and the rate at which it did so increased with that κ_i, as apparent in Table 5.2. Such a trend is consistent with the experimental dependence[18] of the non-linearity coefficient on the fraction of the bias partitioned to the non-linear circuit element at low bias, i.e., the departure from $\alpha_c \propto \kappa_{c0}^{1.0}$ linearity in Figure 3.6b in Chapter 3. The *bias-averaged* κ_i was found to increase linearly (R^2=0.996) with $\alpha_{V,m}$ and will henceforth be referred to as $\bar{\kappa}_{i,m}$ in analogy to $\bar{\kappa}_i$ from the experimental capacitance-bias data. The $\alpha_{V,m} \propto \bar{\kappa}_{i,m}^{1.0}$ linear trend makes sense because $\alpha_{V,m}$ is calculated over a range of bias.

Figure 5.9b shows values of $\Phi_i / \bar{\kappa}_i$ from fitting the experimental capacitance-bias data plotted as a function of $\log(\sigma_{dc})$ alongside model results of $1/\bar{\kappa}_{i,m}$ plotted as a function of $\log(I_{1m})$. Based on its relation to the models, the experimental data primarily reflects blocking at the symmetrical Schottky barriers of thin interwhisker interfaces along tributaries, i.e., the main source of bias-dependent capacitance. With this view, each parallel element in the '*i*' block of the equivalent circuit is regarded as a parallel combination of a bias-dependent resistor and capacitor. The channels likely had minimal capacitive character and the billabongs could have provided a relatively bias-independent capacitance contribution.

The value of Φ_i is expected to depend on the electronic structure of the energy bands at the SiC_w-SiC_w interfaces and be relatively insensitive to whisker loading fraction and percolated-cluster connectivity. Therefore, Φ_i is considered a constant. This is in contrast to $\bar{\kappa}_i$, which depends on how the bias is distributed to the barriers and is expected to strongly depend on whisker loading and percolated-cluster connectivity. When the barriers occur at the grain-boundary interfaces in polycrystalline

semiconductors, estimation of $\bar{\kappa}_i$ follows straightforwardly from the grain and sample sizes.[19,103] For the Al_2O_3-SiC_w composites, the equivalent circuit model suggests that $\bar{\kappa}_i$ decreased as whisker content and composite σ_{dc} increased due to the relative shift of the bias onto the channels (whiskers) and away from the tributaries (interfaces). Figure 5.9b shows the experimental data trending similarly to the model, thereby lending credence to the model and this interpretation.

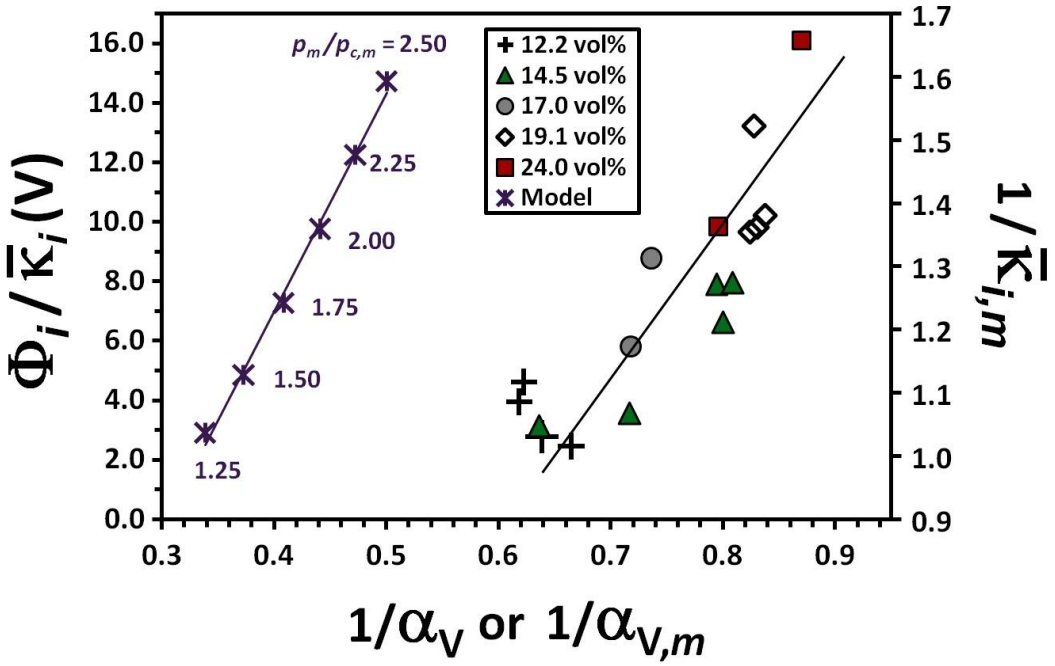

Figure 5.10. Combined plot which shows the direct correlation between the parameters describing the resistance-bias and capacitance-bias responses. Experimental and model results are plotted against the left and right axes, respectively.[22]

Figure 5.10 shows the relationship between the parameters $1/\alpha_V$ and $\Phi_i/\bar{\kappa}_i$ which were separately extracted from the experimental dependencies of the capacitance and resistance on dc bias, respectively. In this figure, the data of Figures 5.9a and 5.9b are effectively combined by directly associating the ordinates of the points plotted within

based on their common association with composition and dc conductivity. The scatter in the experimental data is increased as a result of this combination. Still, the similarity of the experimental trend with the model trend ($\alpha_{V,m} \propto \bar{\kappa}_{i,m}$, noted earlier) validates the conceptual foundation of the model. Thus, the dc-bias sensitivities of the resistance and capacitance of percolated composites are intrinsically linked and provide information about the current and voltage distribution in the percolated cluster and the contrast between interfiller and intrafiller conduction processes.

In Figures 5.9a-b and 5.10, analogous results from the experiment and model are plotted in reference to the dual-abscissa and/or dual-ordinate axes, and the analogous log scales span the same number of decades so that the *strengths* of the experimental trends can be compared to those of the model. Although there is qualitative and some semi-quantitative agreement between the data and the model, the magnitudes of the values and the strength of the trends are in disagreement. The former discrepancy is expected because the model was not constructed to match the actual experimental values, but rather explain the composition/conductivity dependence of α_V and $\Phi_i/\bar{\kappa}_i$ and the effect of large bias on *t*. The model seems to over-predict the decrease in *t* with bias, and in Figure 5.9a, the steeper slope of the model indicates that it over-predicts the strength of the trend. In Figure 5.9b, the contracted scale for the $1/\bar{\kappa}_{i,m}$ values relative to those of $\Phi_i/\bar{\kappa}_i$ suggests the model under-predicts the strength of the trend. This was confirmed by multiplying the $1/\bar{\kappa}_{i,m}$ values by a scaling-factor voltage $\Phi_{i,m}$ in an attempt to make the model results coincide with the experimental trend. If achieved, $\Phi_{i,m}$ would act as an estimate of composition-averaged barrier height, but reasonable values ($\Phi_{i,m} < 10$ V) did not match and under-predicted the curvature of the experimental trend. These

discrepancies may be attributed to the assumed values of experimentally unknown model parameters (e.g., G_w, G_i) and/or the relative simplicity of the model compared to the experimental system.

5.3.9. Comparison to the Behavior of Pressed Composites

Figure 5.11a shows the geometrically-normalized static current-voltage response of a hot-pressed disc with 14.5% SiC_w and sputtered Ag contacts from Keithley measurements. The resistance associated with the slope (661 Ω) is in good agreement with complex impedance data which was obtained separately at $V_{dc} = 0$ and shown in the inset. From the latter, R_{b0}= 657 Ω was extrapolated and the total dc resistance was 706 Ω.

Explanations for the ohmic behavior of hot-pressed samples which assume that interwhisker interfaces behave the same as in extruded material fall short. For example, it may be pointed out that extrapolating the experimental trend in Figure 5.9a to the higher conductivity (connectivity) eventually results in α_V=1. This implies that the apparently-linear response is the result of higher topological connectivity leading to a greater fraction of the bias falling across whiskers rather than interfaces. Such is doubtful in light of results in Chapter 7 showing percolated-composite conductivity being controlled by the behavior of the oxide matrix. An alternative explanation for the linearity based on bias partitioning over a greater number of barriers in series (as previously discussed for long-rods and fine-grained polycrystalline varistors) is at odds with the observed higher dc conductivity of the hot-pressed composites.

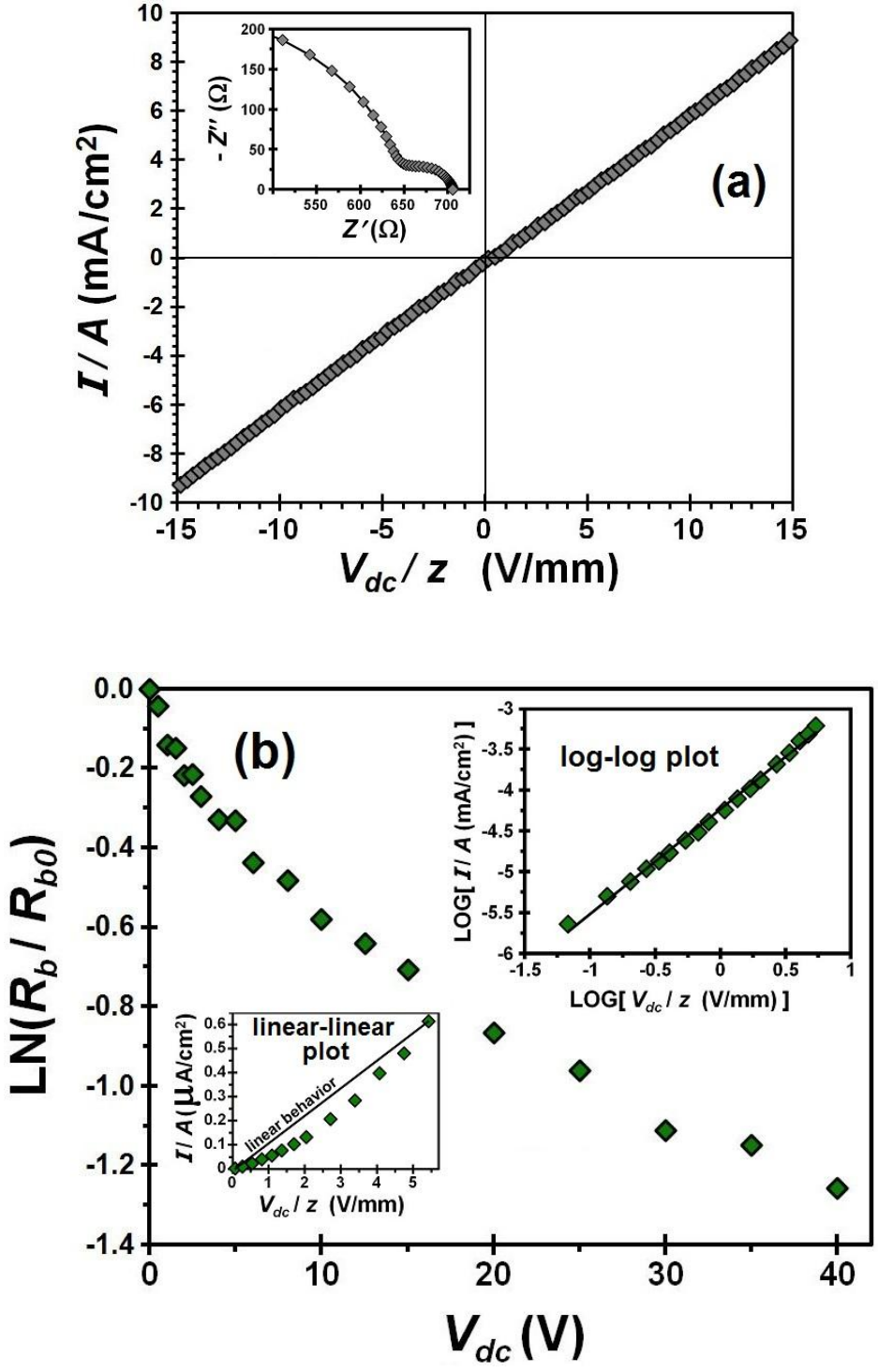

Figure 5.11. (a) Geometrically-normalized static current-voltage data for a hot-pressed 14.5% SiC_w sample with A=6.6 cm^2 and -40 ≤ V_{dc} ≤40 V. The inset shows complex impedance data. (b) Bias-dependent resistance of a dry-pressed and pressureless sintered disc containing 24.0% SiC_w. The big and small insets show geometrically-normalized current-voltage data on log-log and linear-linear scales, respectively.

The notion that pressureless sintering results in fundamentally different interwhisker interfacial behavior compared to hot-pressing is in agreement with the non-linear response of dry-pressed discs shown in Figure 5.11b, whose scales relate to Equation 5.7. The agreement with Equation 5.1 and the deviation from linearity are demonstrated in the insets. The coefficient $\alpha_V = 1.28$ for this data, which is somewhat higher than $\alpha_V = 1.16$ for slices of 24.0% SiC_w extruded rods. In context of a mixed RRN,[13] the difference might reflect greater involvement of non-linear and resistive components (interfaces) compared to conductive and linear components (whiskers). The fact that the divergence exponent t is far greater for pressureless-sintered extruded composites ($t = 3.54$) than hot-pressed composites (see Section 4.3.2.2, $t = 2.61$ or 2.22 for the HPD and perpendicular direction, respectively) also suggests a stronger influence from the interfaces in the extruded type. The greater exponent for the HPD relative to the perpendicular direction is consistent with the idea that increased network parallelism reduces the influence of the interfaces.

The increased non-linearity of the interfaces in the pressureless-sintered composites is attributed to changes in the electronic structure associated with porosity, which is virtually absent in the hot-pressed materials. The Schottky barriers at the interfaces of semiconductor grains which underlie varistor behavior depend on traps at these interfaces, i.e., electronic states in the forbidden gap far away from the edges of the conduction and valence bands.[14] Extensive porosity (e.g., from pressureless sintering) implies a large surface area within the microstructure volume and a large volume density of electronic surface states which exist approximately in the middle of the gap.[104] In some varistors, it has been found that a large degree of porosity is needed to obtain strong non-

linearity.[162] Therefore it is inferred that the varistor response of the pressureless-sintered composites is related to trapping phenomena at the surface states associated with the pores. The character of these surface states might be different from those at grain boundaries of densified ceramics in which the close spatial proximity of the parallel crystal surfaces defining the boundaries may affect the energy levels of or trapping by the states. Evidence for the dependence of interfacial (interwhisker) conduction on trapping phenomena is shown in Chapter 7.

5.4. Conclusions

For the extruded composites, the observed impedance response was different for long rods and thin slices due to the relative size of the contributions to the impedance from the electrodes and the SiC_w-percolated cluster of the bulk composite. When the latter greatly exceeded the former, a single semicircle which primarily corresponds to the bulk appeared in the complex impedance. A second lower-frequency semicircle corresponding to the electrodes was distinguishable when the impedance from the electrodes was comparable to that from the bulk. Single-semicircle response was more likely for long rods compared to thin slices and for samples having relatively low SiC_w loading due to the relatively large impedances of the percolated cluster under such conditions. Such differences reflect the number of SiC_w-SiC_w interfaces in series and extent of current branching in the cluster, respectively.

These two cluster characteristics affect the sensitivity of the bulk impedance to applied dc bias because they affect the bias distribution in the percolated cluster. Due to the former characteristic, 0-40 V bias translated to interfacial electric fields which were

insignificantly small to induce non-linearity in long rods, unlike in thin slices. The dc capacitance and resistance associated with the bulk impedance semicircle mainly resulted from blocking at symmetrical Schottky-barriers at SiC_w-SiC_w interfaces in the percolated cluster and decreased with increasing bias in accordance with models for varistor behavior. The Mukae model for the capacitance-voltage behavior was used to establish this mechanism and outputted a parameter (Φ_i /$\bar{\kappa}_i$) which reflects both the bias partitioning to and the height of the energy barriers. The non-linear current-voltage behavior was well-modeled for most percolated compositions by a resistance which exponentially decreased with dc bias. At the percolation threshold, the strength of the non-linearity was greatest and required use of a more general model, i.e., the varistor equation. The non-linearity coefficients of the different models are related by the range of the measurement and indicated weak varistor behavior (i.e. $1.15 < \alpha_V < 2.57$).

With increasing whisker loading and composite conductivity, Φ_i /$\bar{\kappa}_i$ increased and α_V decreased. For large dc bias, the percolation conductivity exponent *t* decreased. To explain these key observations, an original model of a percolated cluster was developed which correctly predicted the qualitative as well as some quantitative character of the trends. This agreement affirms the conceptual foundation of the model, which is based on expectations for the effects of topological structure and contrast between intrafiller and interfiller conduction processes on the current distribution in the percolated cluster. The model states that these processes have preferential correspondence to the bottlenecking and parallel branching of the current in what are named ‘channels’ and ‘tributaries’, respectively. Increasing the whisker loading and/or dc bias results in the relatively composition- and bias-insensitive ‘channels’ taking on a greater fraction of the applied

bias and providing a greater relative contribution to the composite electrical response. This interpretation is consistent with the observations noted above.

Non-linear behavior similar to that of the extruded slices was observed for the similarly-porous dry-pressed discs. In contrast, the bulk response of fully-dense hot-pressed discs was ohmic. The increased non-linearity of the pressureless sintered composites is attributed to the surface states associated with porosity affecting electronic-trapping phenomena.

CHAPTER 6

BROADBAND DIELECTRIC RESPONSE

6.1. Introduction

Ceramic composites of alumina (Al_2O_3) filled with silicon carbide whiskers (SiC_w) have a commercialized application in grills and flat stones for microwave heating and cooking.[35,78] Furthermore, it has been deduced that some characteristic of the SiC whiskers produced by Advanced Composite Materials results in faster heating rates compared to other forms of SiC when subjected to a microwave electric field.[82] The microwave-frequency dielectric properties of the composites are the basis of the heating application but so far we have only considered the impedance-based response at frequencies ≤ 10 MHz.

Some work has been done on the dielectric properties of similar composites which use mullite in place of alumina for the matrix.[17,48,163] These studies show snapshots of particular high frequencies and do not show the complete spectrum transitioning to the microwave range from lower frequencies. Regardless of matrix material, the electrical and dielectric properties of SiC_w-containing composites have been found to depend on the orientation of the electrical measurement relative to the preferred orientation of the whiskers[9,17,90] and the axisymmetric microstructure which results from hot-pressing.[87-89] In such structures, the orientation of a typical whisker tends to be perpendicular to the hot-pressing direction (HPD) and random within planes which are perpendicular to the HPD. The dielectric constant has been found to be greater when measured perpendicular rather than parallel to the hot-pressing direction.[17]

The effective dielectric constant (ε_e) of a slab of material of thickness (z_s) and area (A_{cs}) is a (geometrically normalized) property describing its capacitance (C) when metal electrodes are applied to each side and a bias is applied across these electrodes, i.e.,

$$\varepsilon_e = C z_s / A_{cs} . \tag{6.1}$$

Estimates of the effective dielectric constant (ε_e) of composites depend on the morphology of the different phases. For composites made by sandwiching parallel slabs of two different materials having dielectric constants ε_1 and ε_2 and constituting fractions of the volume V_1 and V_2 where $V_1 + V_2 = 1$,

$$\varepsilon_e = V_1\varepsilon_1 + V_2\varepsilon_2 \tag{6.2}$$

when the electric field is applied parallel to the interface between the slabs. When the field is applied perpendicular to this interface,

$$1/\varepsilon_e = V_1/\varepsilon_1 + V_2/\varepsilon_2 \tag{6.3}$$

Equations 6.2 and 6.3 are known as the parallel and series rules of mixture (ROM) and are analogous to circuit rules for adding capacitors in parallel and in series, respectively.

When the filler is not continuous and is dispersed, ε_e is commonly estimated via effective medium theory (EMT). In EMT, it is assumed that the polarizabilities of the different constituent phases sum to zero and the dielectric constant is calculated from the (static) dielectric constants of the these phases.[7,10] For a volume fraction p of fibers of length $2A$, diameter $2B$, and dielectric constant ε_f embedded with random three-dimensional orientation in a matrix of dielectric constant ε_d,

$$p\,(\varepsilon_f - \varepsilon_e) / [\varepsilon_e + N_f\,(\varepsilon_f - \varepsilon_e)\,] + 3(1-p)(\varepsilon_d-\varepsilon_e) / [\varepsilon_e + N_d\,(\varepsilon_d - \varepsilon_e)\,] = 0. \tag{6.4}$$

The depolarization factors are $N_d = 1/3$ and $N_f \approx (B/A)^2 \ln(A/B)$, assuming that the regions of the matrix are approximately spherical and that the fibers may be approximated as ellipsoids due to $A >> B$. This approach is based on the Bruggeman symmetric equation,[10] accounts for the filler aspect ratio, and may be rewritten to calculate the dielectric constant of the fiber:

$$\varepsilon_f = \varepsilon_e (1 + \psi - N_f \psi) / (1 - N_f \psi) \tag{6.5}$$

where

$$\psi = (-3/p)(1 - p)(\varepsilon_d - \varepsilon_e) / [\varepsilon_e + N_d (\varepsilon_d - \varepsilon_e)]. \tag{6.6}$$

In general, the frequency-dependent complex relative permittivity $\varepsilon_r^*(\omega)$ is composed of a real part $\varepsilon_r'(\omega)$ and an imaginary part $j\varepsilon_r''$ and is often written as[76,108]

$$\varepsilon_r^*(\omega) = \varepsilon_r'(\omega) - j\,\varepsilon_r''(\omega) \tag{6.7}$$

where ε_r' and ε_r'' are respectively called the dielectric constant and the dielectric loss, $j = \sqrt{-1}$, and the subscript "r" indicates relation to the vacuum permittivity ε_0, i.e., the complex permittivity of a general medium is $\varepsilon^*(\omega) = \varepsilon_0\varepsilon_r^*(\omega)$. The volumetric microwave-heating rate $\left(\frac{dT}{dt}\right)_V$ of a material at a particular frequency depends on the imaginary part in Equation 6.7 and is given by the equation [76]

$$\left(\frac{dT}{dt}\right)_V = \frac{2\pi f E^2 \left(\varepsilon_r''\right)\varepsilon_0}{DC_p} \tag{6.8}$$

where f is the frequency, E is the magnitude of electric field, C_p is the heat capacity at constant pressure, and D is the material density. Thus, ε_r'' is the material property that determines the power delivered per unit volume (i.e. the numerator in Equation 6.8) and

generally includes loss contributions from all forms of frequency-dependent polarization or resonance and the dc conductivity σ_{dc} of the material (see Figures 1.22 and 1.23), i.e.

$$\varepsilon_r'' = (\varepsilon_r'')^{di} + (\varepsilon_r'')^{ion} + (\varepsilon_r'')^{el} + (\varepsilon_r'')^{MW} + \frac{\sigma_{dc}}{2\pi f \varepsilon_0} \qquad (6.9)$$

Here, the superscripts refer to dipolar (di), ionic (ion), electronic (el) and Maxwell-Wagner (MW) polarizations and the last term in the sum follows from the Maxwell-Wagner theory of a two-layer condenser.[109] In this theory, interfacial space-charge polarization occurs at the interface of two contacting slabs of frequency-independent materials with significantly different conductivities (σ_1, σ_2) and static dielectric constants (ε_1, ε_2). The relaxation time constant τ of such a polarization can be written as

$$\tau = \varepsilon_0 \frac{\varepsilon_1 V_2 + \varepsilon_2 V_1}{\sigma_1 V_2 + \sigma_2 V_1} \qquad (6.10)$$

where V_2 and V_1 are the effective volume fractions of the two different materials. The complex dielectric constant resulting from a Maxwell-Wagner interfacial space-charge polarization $(\varepsilon_r^*)^{MW}$ can be written as

$$(\varepsilon_r^*)^{MW} = \varepsilon_\infty' + \frac{\varepsilon_s' - \varepsilon_\infty'}{1 + (j\omega\tau)^{1-\alpha_\tau}} - j\frac{\sigma_{dc}}{\omega\varepsilon_0} \qquad (6.11)$$

where ε_∞' and ε_s' are the real parts of the complex relative dielectric constant at the high- and low-frequency extremes, $\omega = 2\pi f$, and $(1-\alpha_\tau)$ is an empirical fitting exponent which accounts for a distribution of relaxation times. For an ideal Maxwell-Wagner polarization

with a single relaxation time, $\alpha_\tau = 0$ and the right-hand side of the equation is indistinguishable from the Debye form (Equation 1.11) if the imaginary term containing σ_{dc} is excluded. Cole and Cole[108] first introduced such an exponent and analytically determined the explicit effects of α_τ on the real and imaginary parts of ε_r^* (see Equation 1.12). The σ_{dc} term makes a contribution to the loss which increases and decreases with dc conductivity and frequency, respectively, and will be called the dc-conductivity "tail".

Runyan, Gerhardt and Ruh employed such an exponent to account for a distribution of relaxation times and fit the real (ε_r') part of data for a Maxwell-Wagner polarization in another composite system based on SiC conductivity.[164] For Maxwell-Wagner polarizations, the loss function ε_r'' is characterized by a peak,[109,165] and if dc conductivity is significant, a "tail" which increases with decreasing frequency. This dc-conductivity tail follows from the rightmost term in Equation 6.11 and superimposes on top of and can fully or partially obscure the presence of the loss peak.[76] It also follows from the general relation of the dielectric loss with the quantities of the complex impedance ($Z^* = Z' - jZ''$)

$$\varepsilon_r'' = \frac{Z'}{\omega C_0[(Z')^2 + (Z'')^2]} \tag{6.12}$$

at the limit of $Z'' \rightarrow 0$, where C_0 is the empty-cell capacitance associated with the parallel-plate sample geometry, i.e. $C_0 = \varepsilon_0 A/z$ where A and z are the cross-sectional area and thickness of the sample, respectively.

Additionally, the existence of common power-law relations have been noted for the frequency dispersions of the ac conductivity $\sigma(\omega)$ and $\varepsilon_r'(\omega)$ for a "general" material (e.g. one which can be modeled by a parallel RC circuit[125]), i.e.

$$\sigma(\omega) \propto \omega^{x} \tag{6.13}$$

$$\varepsilon_r'(\omega) \propto \omega^{-y} \tag{6.14}$$

where $x + y = 1$. The ac conductivity is the geometrically-normalized magnitude of the complex admittance function.[166,167]

6.2. Experimental Methods

Hot-pressed composites of both orientation types and thin slices of extruded rods were electroded via sputtering measured over a wide frequency range (10 mHz-1.8 GHz) using the parallel plate method with the Solartron 1260 and Agilent 4291B, as described previously. Pieces of different wafers of nominally pure and n-type doped α-polytype SiC were also measured with the Agilent 4291B at room temperature for comparison. There were four different wafer pieces (labeled 1-4) and an example is shown in Figure 6.1.

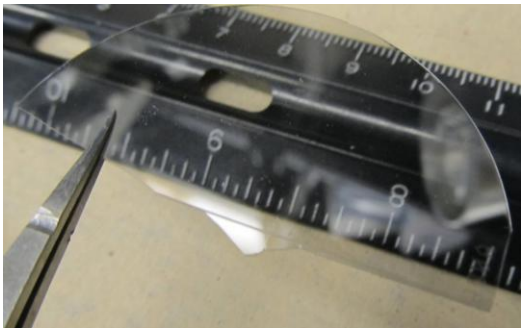

Figure 6.1. Image of optically-transparent SiC wafer #4 held with tweezers.

Also, small donuts of the 0, 3.5, 5.8, 7.7, 10.0, 14.5, 19.1, and 28.2 compositions were machined by Mindrum Precision, Inc. in Rancho Cucamonga, CA from thin hot-pressed discs to have inner and outer diameters (IDs and ODs) of 0.120 and 0.275 inches (3.05 and 6.99 mm), respectively. These were made to fit inside a 10 cm long coaxial airline (Model 2653S10, Maury Microwave Corporation, Cucamonga, CA) with minimal airgaps (Figure 6.2a). The samples were then measured with an Agilent 8363C PNA Network Analyzer (Figure 6.2b) from 1-18 GHz and the calculation of the permittivity accounted for the air gaps at the walls of the inner and outer conductors with a frequency-independent model treating the gaps as capacitors in series with the sample.[168] Specifically,

$$\varepsilon_{gc}' = \varepsilon_{meas}'[\, L_b / (L_c - L_a\, \varepsilon_{meas}') \,] \tag{6.15}$$

$$\varepsilon_{gc}'' = \varepsilon_{gc}' \,[\, (\tan\delta)_{meas}\, (1 + \varepsilon_{gc}' L_a / L_b) \,] \tag{6.16}$$

$$L_a = \ln(\, r_2 / r_1) + \ln(\, r_4 / r_3) \tag{6.17}$$

$$L_b = \ln(\, r_3 / r_2) \tag{6.18}$$

$$L_c = \ln(\, r_4 / r_1) \tag{6.19}$$

where subscripts 1,2,3, and 4 designate radii (r) of the concentric circles associated with the inner conductor, sample ID, sample OD, and outer conductor, respectively. Relative-permittivity quantities are designated as real and imaginary by single and double dashes, respectively, and as being measured or gap-corrected by subscripts '*meas*' and '*gc*', respectively. The gap-corrected loss tangent $(\tan\delta)_{gc} = \varepsilon_{gc}''/\varepsilon_{gc}'$ is given by the term in brackets in Equation 6.16. Equation 6.15 breaks down when $\varepsilon_{meas}' \geq L_c/L_a$, and from the experimental data, it was found that $L_c/L_a \approx 47.5$ and $\varepsilon_{meas}' \leq 32$.

(a)  (b) 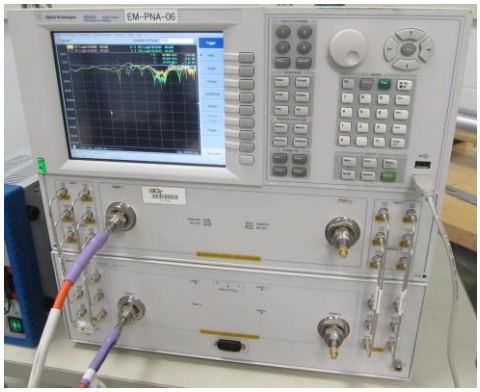

Figure 6.2. (a) Coaxial airline with inner conductor removed, and donut samples cut from a thin hot-pressed disc. (b) Agilent 8363C PNA network analyzer.

The airgaps were estimated by imaging the donut samples with a stereomicroscope and using software to measure the diameter of the inner conductor and fit the circumferences associated with the ID and OD (Figure 6.3). The average inner and outer airgaps were 0.045 ± 0.029 mm and 0.029 ± 0.013 mm, respectively. The average thickness of the donuts was 2.55± 0.08 mm. The experimental method was tested for accuracy with a Rexolite standard having 12.68 mm thickness and airgaps of 0.146 mm (inner) and 0.06 mm (outer).

(a) 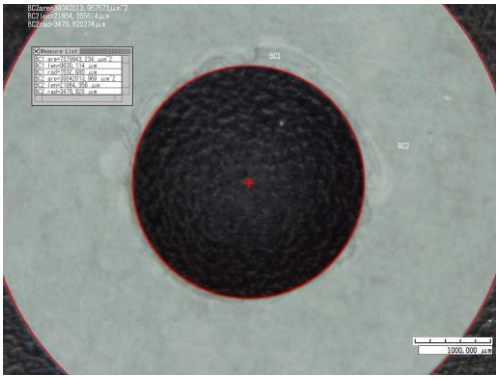 (b) 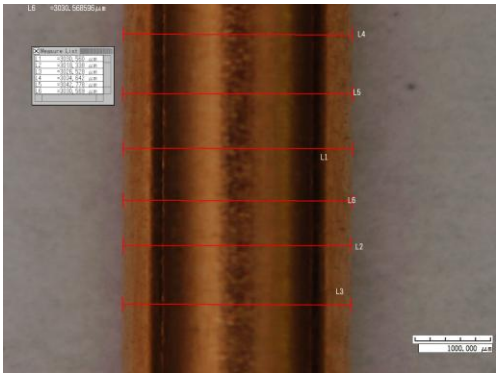

Figure 6.3. (a) Optical-microscope image of a donut sample of hot-pressed material showing software-measurement of the ID and OD by thin red curves. (b) Similar image of the inner conductor of the coaxial airline, showing software measurement of the diameter by thin red lines.

6.3. Results and Discussion

6.3.1. Manifestation of the Insulator-Conductor Transition in the Complex Permittivity

In Figures 6.4a and 6.4b**,** the effects of whisker content and percolation on the dielectric response of representative thin slices of extruded rods are demonstrated.

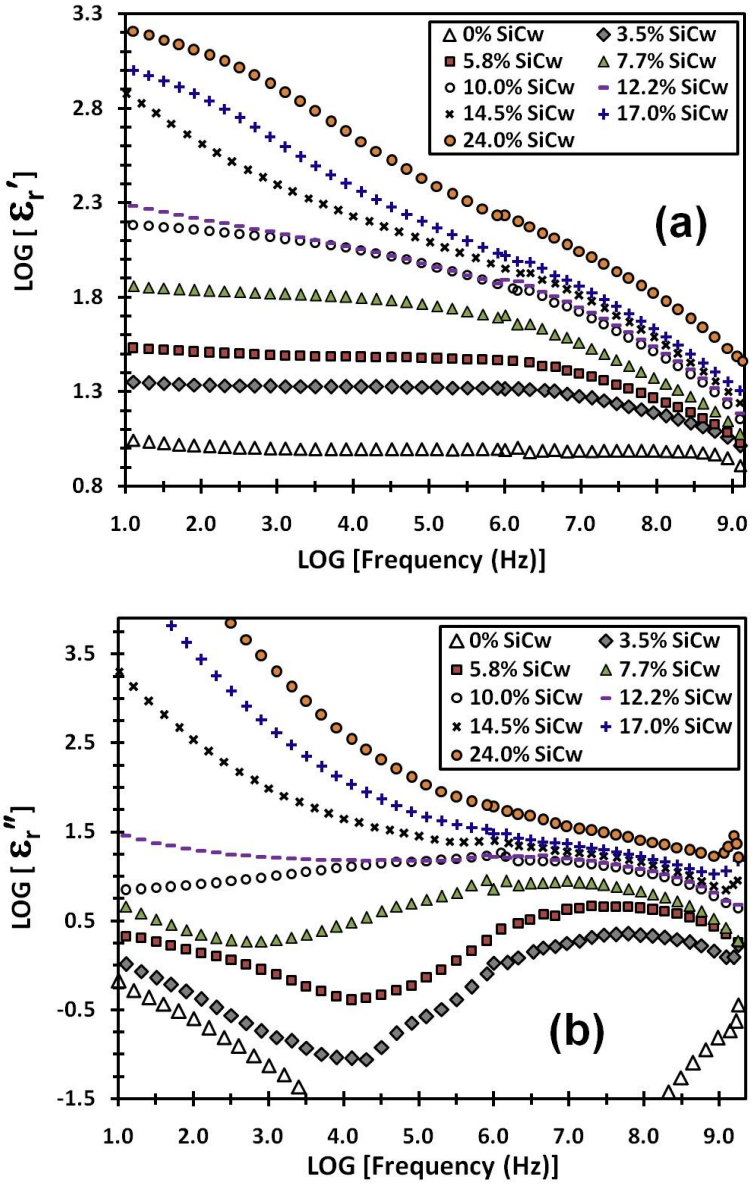

Figure 6.4. The dependence of the frequency dispersions of the dielectric constant (a) and dielectric loss (b) on whisker content for representative thin slices of extruded rods. The electric field was applied along the extrusion direction.[20]

Such slices were used because the high-frequency analyzer is restricted to thin samples. Figure 6.4a shows the dielectric constant ε_r' and Figure 6.4b shows the dielectric loss, ε_r''. For the matrix material (0% SiC_w), the dielectric constant was mostly flat ($\varepsilon_r' \approx 10$) and the loss was lower than that of whisker-filled composites at all frequencies, consistent with previous work.[21] For the 3.5-10.0 % SiC_w extruded material, the high-frequency portions of the spectra are characterized by broad loss peaks and dispersions in ε_r', whereas the low-frequency portions of the spectra are characterized by dc-conductivity tails in $\varepsilon_r''$and mostly-flat plateaus in ε_r'. The flat-to-dispersive transitions in ε_r' and peaks in ε_r'' indicate a dielectric relaxation. Above 10% SiC_w, both ε_r' and ε_r'' continue to rise in value with increasing SiC_w content.

Figure 6.5a shows frequency dispersions of the dielectric constant ε_r' measured parallel to the hot-pressing direction for varying whisker content. Figure 6.5b shows the corresponding dielectric loss, ε_r''. For 0–5.8 vol% samples, the low-frequency ε_r' dispersion shifts upward with SiC_w content and is flat up until 0.1-1 MHz. For the 3.5 and 5.8 vol% compositions, close examination of the dispersion shapes reveals that a broad dielectric relaxation occurs between this approximate frequency and ~1 GHz. In these, the ε_r'' function peaks broadly between 50–120 MHz and 7–45 MHz for the 3.5 and 5.8 vol% samples, respectively. Above 7.7% SiC_w, both ε_r' and ε_r'' continue to rise with increasing SiC_w content, with the noted exception relating to the crossover of the ε_r' spectra of the 7.7% and 10% SiC_w samples at ~2 kHz. This is believed to be an effect of the electrodes; the height of the low-frequency ε_r' plateaus were strongly dependent on the electrode material based on results with conductive Ag paint electrodes (not shown)

and seemed to be correlated with the low-frequency (electrode) semicircle in corresponding Nyquist plots of the impedance.

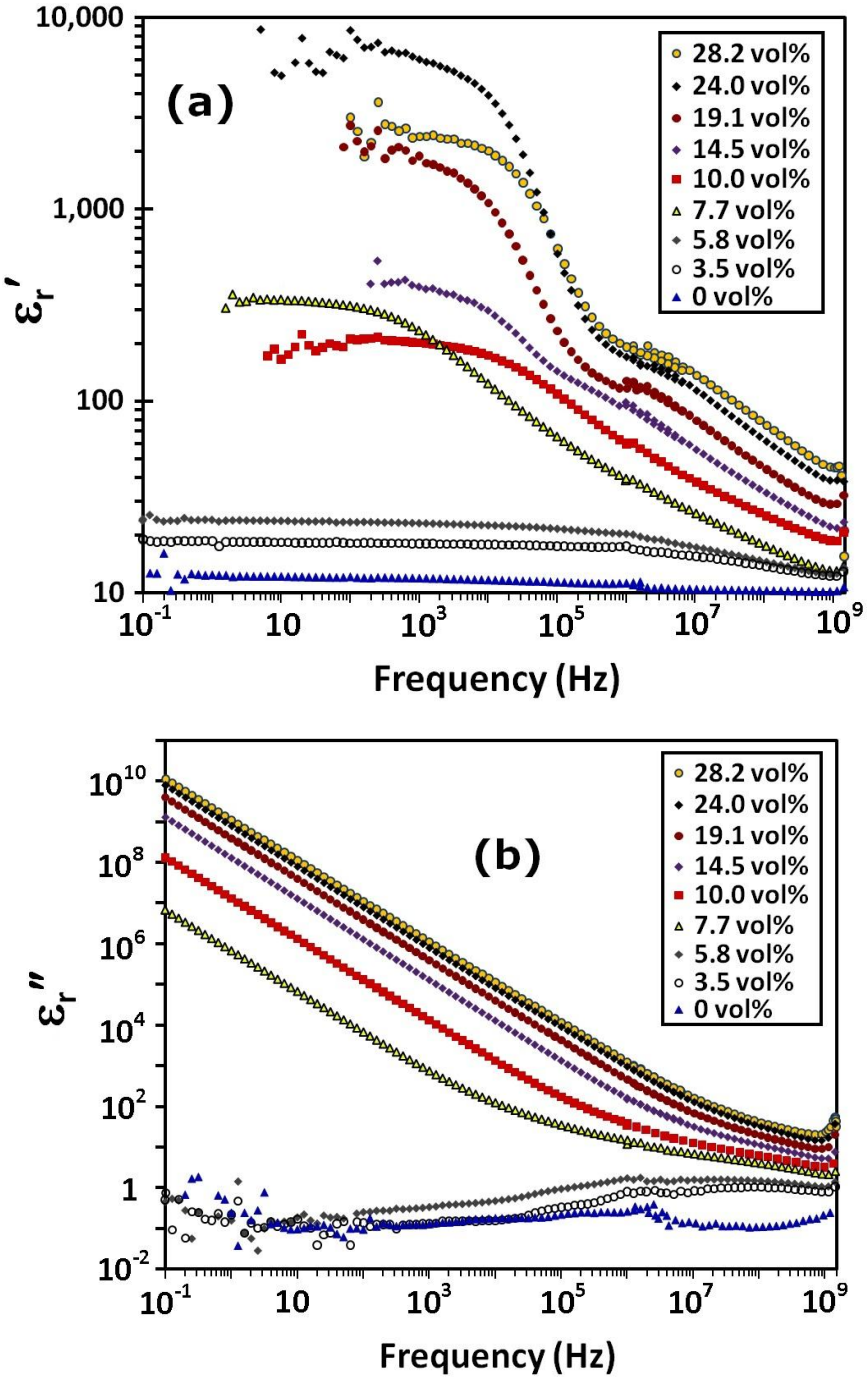

Figure 6.5. The dependence of the frequency dispersion of the relative dielectric constant ε_r' (a) and the dielectric loss ε_r'' (b) on whisker content in thin hot-pressed composite discs. The electric field was applied parallel to the hot-pressing direction.[21]

The evolution of the dielectric spectra with increasing SiC_w content was qualitatively similar for the hot-pressed and extruded composites in terms of the high-frequency dielectric relaxation and rising magnitudes of the ε_r' and ε_r'' spectra. For the hot-pressed material, an abrupt change in the character of the spectra occurred between the 5.8 and 7.7 vol% SiC_w compositions, especially for ε_r'', which decreased with increasing frequency and increased with the continued addition of SiC_w. The loss trending as such in the context of the abrupt change and the concurrence with dc-conductivity percolation establish this feature as the dc-conductivity tail.

For the extruded material, the changes in dispersion behavior took place more gradually between the 7.7 and 12.2 % SiC_w compositions across which percolation happened. This shift and softening of the transition between insulating- and conducting-type dielectric spectra is correlated to the reduced magnitude, shift, and wider compositional range of the percolation transition of dc conductivity (Figure 4.10a) for extruded material compared to hot-pressed material. For compositions which are well-percolated (i.e. 12.2-24.0 % SiC_w), the tail superimposes on the high-frequency loss peak and increasingly conceals it as whisker content and dc conductivity increase. This is particularly noticeable for the 14.5-24.0 % SiC_w compositions. The low-frequency upturn of the tail of the 12.2 % SiC_w spectrum is perceptible from 10-1000 Hz. For the 10.0 %SiC_w composition, which corresponds to the approximate center of the percolation transition, this upturn occurred between 0.1-1.0 Hz (not shown) and the loss peak is so broad that the overall ε_r'' frequency dispersion is relatively flat. For the non-percolated compositions, it appears that the minimum in dielectric loss which occurs at the changeover between the tail and the high-frequency loss peak shifts to lower frequency as

whisker content increases toward percolation due to the increasing broadness of the loss peak.

6.3.2. Interpretation and Modeling of the Relaxation and DC-Conductivity Tail

The absence of a loss peak in the 0 vol% dispersions confirms the whisker involvement in the relaxation. The relaxations are believed to reflect interfacial polarizations (see Figure 1.22) at the interfaces of SiC inclusions and are modeled via the modified Maxwell-Wagner model for interfacial polarization, i.e. Equation 6.11. The tailing-off behavior of the dielectric loss at relatively low frequencies and the dependence of this on whisker content are suggestive of the dc-conductivity term which follows directly from the original Maxwell-Wagner model[76,109] but which can also be seen to follow from the definition of the loss (Equation 6.12) at the limit of $Z'' \rightarrow 0$.

The frequency $f_p = (2\pi\tau)^{-1}$ of the peaks in the ε_r'' function can be evaluated in terms of Equation 6.10 in order to verify model applicability on a basic level, i.e., whether or not interfacial polarizations are related to the observed relaxation. Considering phases 1 and 2 to be the SiC_w and mostly-Al_2O_3 matrix, respectively, the variables can be roughly estimated as $\sigma_2 \approx 10^{-12}$ S/cm, $\varepsilon_2 \approx 10$, $\sigma_1 \geq 10^{-3}$ S/cm, and $\varepsilon_1 \approx 200$. This value of ε_1 is based on results of effective medium theory (i.e., applying Equations 6.5-6.6) at 18 GHz, as shown in Section 6.3.4. It is also agreeable with values of $200 < \varepsilon_1 < 600$ determined by using the series ROM (Equation 6.3) to generate the effective permittivity values on the low-frequency side of the relaxation for the hot-pressed material. The latter approach should be most applicable for data taken parallel to the HPD, since the whiskers are believed to form interconnected but non-percolated nets on planes perpendicular to the HPD, as discussed more later. Estimates of ε_1 based on other mixing-rule equations,[24]

(e.g., Maxwell-Sphere, parallel ROM, Lichtenecker logarithmic) resulted in completely unreasonable values, e.g., $\varepsilon_1 < 0$ and $\varepsilon_1 > 10^6$. In Equation 6.4, inputs of ε_1=200, $\sigma_1=10^{-3}$ S/cm, and V_1 =0.035-0.058 yield τ = 18 ns and f_p = 9 MHz, which have fair (order-of-magnitude) agreement with the experimental results. This suggests that interfacial polarizations contribute to the relaxation. Also, τ and f_p are predicted by Equation 6.4 to increase and decrease with increasing composition, respectively, in qualitative but not quantitative agreement with the experimental data. The modesty of the agreement is partially attributed to the difference between the simple parallel-slab structure of the underlying model[109] and the disordered composite microstructure, and suggests that describing the relaxation simply as "interfacial" is an oversimplification.

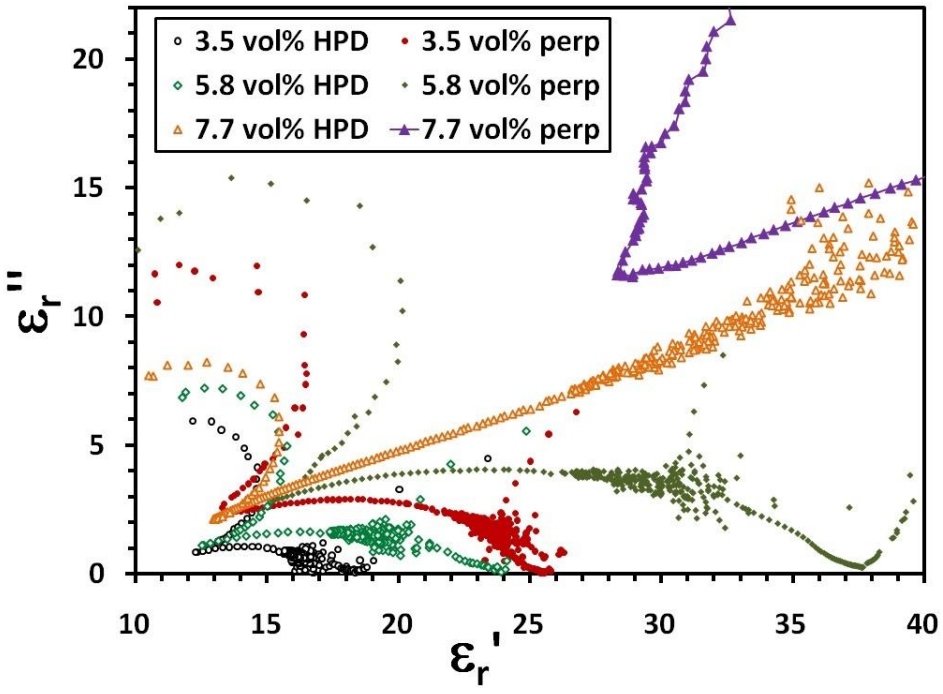

Figure 6.6. Cole-Cole plot of the complex dielectric constant measured along different directions of the hot-pressed samples.[21]

Figure 6.6 shows a Cole-Cole plot of $\varepsilon_r^*(\omega)$ for an additional perspective on relaxations from non-percolated hot-pressed samples measured in different microstructural directions. The plot shows semicircles which relate to the space-charge relaxations and whose depressed shapes suggest a distribution of relaxation times. On the right side of the Figure, the dc conductivity tail is apparent for the 5.8 vol% SiC_w sample measured in the perpendicular direction. On the left side, there is evidence of damped resonances which are discussed in Section 6.3.4.

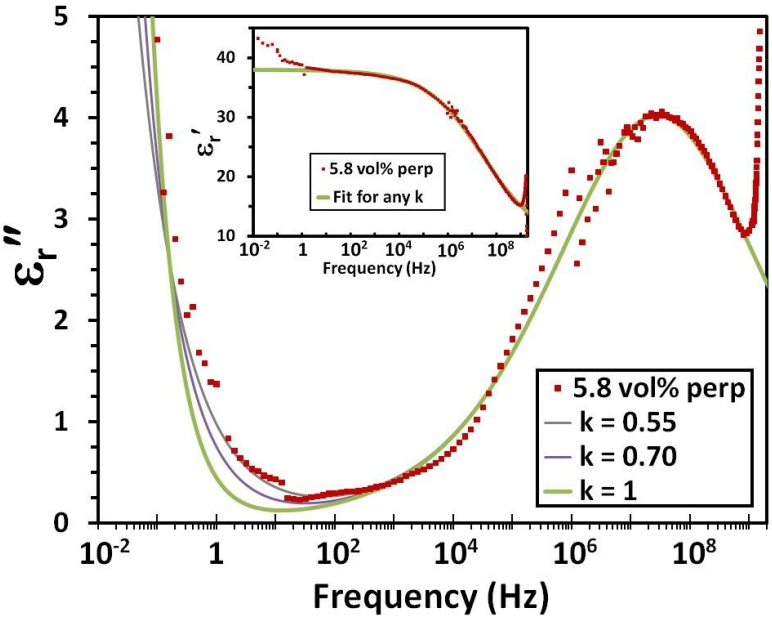

Figure 6.7. Dielectric loss ε_r'' of a 5.8 vol% sample fit with $\alpha_\tau = 0.655$, τ=5.66 ns, ε_s'=38, ε_∞'=9, σ_{dc}= 2.26 x 10^{-11} S/m, and varied *k*. These parameters relate to Equation 6.11 and the *k*-modification discussed in the text. The quality of fit to the loss peak seen here represents the highest-quality fit of Table 6.1. Using $0.55 < k < 0.70$ improved the quality of fit around the minimum at $1 < f < 100$ Hz compared to $k = 1$ but was detrimental at lower frequencies. The inset shows the fit to the real part ε_r'. From Ref. 21.

Concurrent curve fitting of Bode plots of $\varepsilon_r'(\omega)$ and $\varepsilon_r''(\omega)$ and Cole-Cole plots of $\varepsilon_r^*(\omega)$ was performed with the modified Maxwell-Wagner equation (Equation 6.11) for

each composition-orientation combination below the percolation threshold. These fits used the related σ_{dc} values from Chapter 4. It was not appropriate to use a "β" exponent in the style of Davidson-Cole[169] or Havriliak-Negami[170] because much of the high-frequency data is obscured by the superimposed resonance. The best fitting was achieved with data from perpendicular measurements on a 5.8 vol% sample (Figure 6.7).

The dc-conductivity tail was less prominent in the other non-percolated composition-orientation combinations due to their reduced conductivities. Modifying the dc-conductivity term of Equation 6.11 with an empirical exponent *k* and units-consistency factor k_0 such that it becomes $jk_0\sigma_{dc}/\omega^k\varepsilon_0$ provided a marginal improvement to the fitting of some of the σ_{dc} tails, as shown by the example of Figure 6.7. A similar empirical modification was made by van Beek.[171]

Values for *k* and other parameters of the fits are listed in Table 6.1. Values for ε_∞' ranged from 9 to 11 and seem to coincide with ε_r' values for the unfilled matrix. The values of τ, ε_s' and α_τ increase with SiC_w content. Values of τ and α_τ are larger for the HPD, whereas values ε_s' are larger for the perpendicular direction.

Table 6.1. Parameters for Fitting Data from Hot-Pressed Samples to Equation 6.10 (reprinted from Ref. 21, Copyright 2010 by The American Ceramic Society).

SiC_w vol%	**Orientation**	**τ (ns)**	**ε_s'**	**ε_∞'**	**α_τ**	***k***
0.0352	HPD	2.31	17.5-18.2	11.0-10.3	0.60-0.67	0.40-0.70
0.0352	perpendicular	2.12	25.6	9.5-10.3	0.565-0.542	N/U
0.0581	HPD	9.36	23.5-23.6	10.0-10.1	0.695	N/U
0.0581	perpendicular	5.66	38.0	9.0	0.655	0.55-0.70

The dielectric relaxations for the non-percolated extruded samples were similarly fit with Equation 6.11 using $\varepsilon_\infty'=10$ for all compositions, and examples are shown in Figure 6.8. With increasing whisker content, the central frequency of the peak shifted to lower frequency and the relaxation spread out over a wider frequency range and increased in strength. The results given in Table 6.2 quantify these trends by showing that, as for hot-pressed samples, τ, ε_s', and α_τ all increased with whisker content. Also, the relaxation (semicircle) was increasingly concealed by the σ_{dc} tail as SiC_w loading increased. For the tails, the departure of the data from the fitting lines occurs because the slight dispersion of ε_r' on the low-frequency side of the relaxation is not accounted for in Equation 6.11.

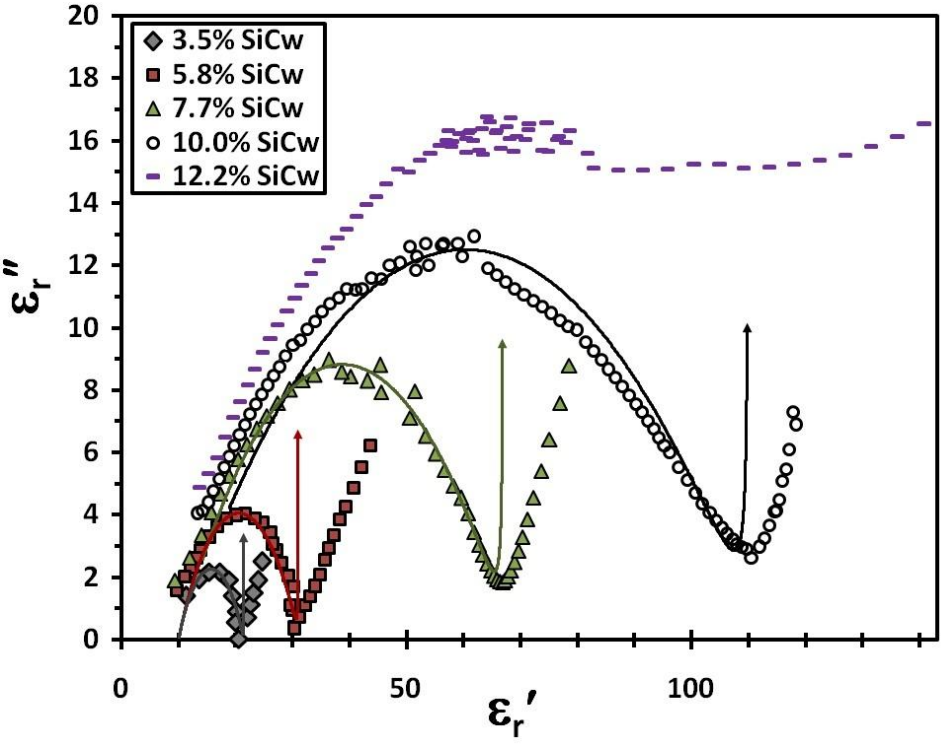

Figure 6.8. Data for extruded Al_2O_3-SiC_w samples plotted in the complex plane and representative fits (solid lines) using parameters consistent with Table 6.2, which relate to Equation 6.11 and the *k*-modification discussed in the text. For clarity, some data and fitting line pertaining to the σ_{dc} tail is not shown.[20]

Table 6.2. Parameters for Fitting Data from Extruded-Rod Slices to Equation 6.10. (reprinted from Ref. 20, Copyright 2011 by The American Ceramic Society).

SiC_w %	τ (ns)	ε_s'	α_τ	*k*
3.5	2.2-2.4	19.4-20.5	0.48-0.50	0.35-0.42
5.8	3.6-4.0	22.8-33.3	0.53-0.58	0.23-0.36
7.7	25-30	65-72	0.60-0.62	0.29-0.40
10.0	80-220	110-160	0.68-0.74	0.25-0.44

$^{\epsilon}$ Note: ε_∞'=10 was used for all fits. The empirical factor *k* is described in the text.

With increasing whisker content, the increase in relaxation strength (ε_s'- ε_∞') can be attributed to an increased density of polarization sites. However, this view does not help interpret the trends of the other fitting parameters, which are believed to provide insight into the nature of the underlying polarizations and the role played by the interfaces in these. Some alternative interpretation schemes are now considered for this purpose.

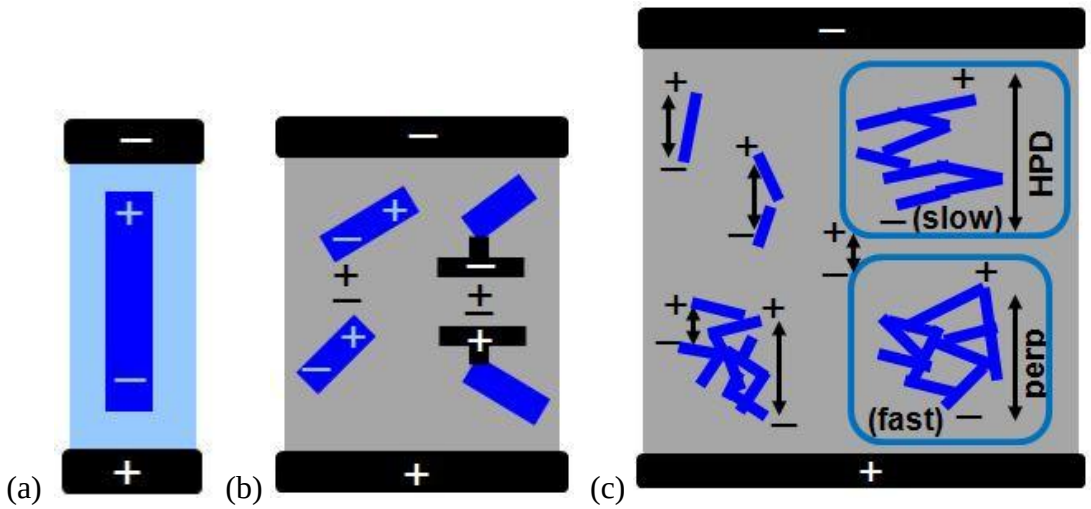

Figure 6.9. Illustrations of (a) a single polarized whisker, (b) a pair of polarized whiskers and the microcapacitor concept, and (c) the transition from the former two into the cluster polarization concept.

The scale-dependent effective medium theory (SDEMT) for conductive-stick composites predicts dielectric relaxations both above and below the percolation threshold.[85] In this theory, the relaxations are the result of polarizations of conductive sticks (e.g., Figure 6.9a), having metal-like conductivity and is not related to the interfaces between the sticks or the formation of conducting clusters of sticks. The relaxation strength is predicted to increase linearly with composition, whereas the values in Table 6.2 are more suggestive of a superlinear dependence. More importantly, the explicit description of the relaxation time does not contain a filler-concentration term, although the authors comment that the relaxation time *decreases* somewhat with increasing composition above percolation; in the experimental data of Table 6.1 and 6.2, the central relaxation time *increases* with increasing composition. This contradiction suggests that the observed relaxation is unlikely to be accounted for by this theory, in which the relaxation time is explicitly described to increase and decrease with increasing stick aspect ratio and conductivity, respectively.

In the second interpretation scheme, the interfacial polarization associated with the space-charge double layer at the interface of two materials is recast in terms of the polarization of the matrix material between two SiC whiskers (i.e., the interface) interacting by capacitive coupling. This idea is illustrated in Figure 6.9b and is similar to the micro-capacitor theory of Ref. 172; in this view, the microstructure is regarded in terms of SiC_w-Al_2O_3-SiC_w microcapacitors. With decreasing whisker content, the reduction in relaxation strength ($\varepsilon_s' - \varepsilon_\infty'$) and sample effective capacitance can be attributed to the increased average distance between SiC inclusions giving rise to smaller coupling capacitances. The shift of the loss peak to higher frequency might be similarly

explained by the increase in the average distance between whiskers in the context of the "frequency shorting" concept,[6,21] which is now described. The corresponding average microcapacitor has an impedance which is directly proportional to this SiC_w distance and inversely proportional to the frequency. To maintain a given level of impedance, an increase in distance (e.g., from decreased SiC_w loading) could be compensated for by an increase in frequency. A similar result of the loss peak shifting to higher frequency as the amount of conductive filler decreases is available in the literature.[93] The substantial values of α_τ might be related to the distribution of interparticle distances; unfortunately, it was not possible to measure these distances since the samples were very insulating and thus unsuitable for SEM.

In the third scheme of interpretation, the observed relaxation is attributed to polarizations of non-percolated clusters of electrically-connected but physically-discrete SiC_w and SiC-matrix-SiC interfaces within and between these clusters, whose overall conductivity is controlled by the interfaces. Since a sample-spanning electrically-connected cluster exists at percolation, it stands to reason that smaller, separated clusters exist at compositions slightly below percolation and have topologically similar character to the percolating cluster which follows from a small addition of filler. This qualitative model draws on ideas from single-stick polarization, the microcapacitor concept, and connectivity from Chapters 4 and 5.

Polarizations (and thus relaxations) occur within pairs of whiskers via the microcapacitor concept, within individual whiskers, and more importantly, within and between clusters of whiskers. This is shown qualitatively in Figure 6.9c. The composition variation of the fitting parameters is the result of an increase in SiC_w clustering, and

presumably, average cluster size, as filler content increases towards percolation. The relaxations of the polarized clusters or cluster pairs could be expected to be associated with slower relaxations and thus larger relaxation times compared to individual SiC_w and SiC_w-matrix-SiC_w due to the greater number of interfaces through which charges must travel in the larger structures. Also, increasing whisker content corresponds to increasing cluster size and thereby suggests increased low-frequency permittivity. The large values of τ and ε_s' for the 7.7-10.0 % SiC_w compositions seem to support these ideas, which do not preclude the occurrence of faster relaxations of smaller SiC_w-based structures encompassed by or outside of such clusters. The increase of α_τ with increasing SiC_w content is attributed to SiC_w clustering and relaxations from polarizations happening on an increasingly large range of size scales (and thus, time scales and frequencies) within and possibly between such clusters. This scaling concept is similar to that which underlies the broadband reception of fractal antennas.[173]

The anisotropy of the fitting exponents for hot-pressed materials (which have the same connection quality) seem to contradict the SDEMT, which states that the relaxation (associated with individual sticks) is slowed in time for longer sticks and for sticks having reduced width and/or conductivity. It is inferred that the first dependency reflects greater distances of charge displacement and the latter two reflect an increased resistance to the homogenization of charges by current flow. For the application of an electric field to the composites along the HPD, the perpendicular alignment of whiskers suggests that individual whiskers would relax relatively quickly and give rise to smaller relaxation times compared to when the field was applied perpendicularly. This contradicts the experimental data, which show τ is smaller when the field is applied perpendicularly.

These data can be understood by considering how these factors which determine individual-stick relaxation times would apply to non-percolated clusters.

Like percolated clusters, non-percolated clusters are expected to exhibit interface controlled conductivity and greater intracluster-conduction parallelism in the perpendicular direction. The latter is tantamount to the polarizing object having an increased conductivity and thereby suggests a faster relaxation and smaller τ, in agreement with the experimental results. The anisotropy of τ may also be explained by the microcapacitor and frequency-shorting concepts, for which shorter distances between SiC_w along the HPD (shown in Chapter 4) suggest larger τ. However, the shorter distances also suggest larger effective sample capacitances, which contradicts the smaller values of ε_s' for the HPD compared to the perpendicular direction. This anisotropy can also be explained by increased conduction parallelism along the perpendicular direction, as illustrated for fully percolated clusters in the next section. The anisotropy of α_τ could plausibly be attributed to the random orientations of SiC_w within planes perpendicular to the HPD allowing for a wider variety of interactions. Alternatively, it might be explained by an increased variability in the SiC_w-volume-fraction-dependent interwhisker distances: from stereology, one expects to observe more variation in the SiC volume fraction when viewing the structure along the symmetry axis (i.e., the HPD) compared to the perpendicular direction.[141]

To summarize, the trends of the fitting parameters are better explained by polarizations of non-percolated clusters having interface-controlled conductances rather than those of microcapacitors defined by whisker pairs, individual conductive sticks, or simple interfaces between parallel slabs of material. The non-ideal frequency dependence

of the dc-conductivity tail is not easy to explain and deserves additional remarks. Since ideal tails ($k = 1$) and the high-frequency sides of ideal (Debye-relaxation, $\alpha_\tau = 0$) loss peaks have indistinguishable frequency dependencies, perhaps these non-ideal ($k \neq 1$) tails are associated with the high-frequency side of non-ideal ($\alpha_\tau \neq 0$) loss peaks of relaxations centered at frequencies so low that they are not practical for measurements. In principle, the electromagnetic spectrum is infinite.

6.3.3. Anisotropic Permittivity and Power-Law Behavior

Figures 6.10a and 6.10b show the frequency dispersions of ε_r' and ε_r'' from measurements conducted in the two principal microstructural directions, i.e., the hot-pressing direction (HPD) and the perpendicular direction ("perp"). The specific compositions (5.8, 7.7, 24.0 vol%) were selected to highlight the orientation effect for representative barely-percolated and well-percolated samples, and show data from an non-percolated sample for comparison. As for the σ_{dc} of percolated samples presented in Chapter 4, the $\varepsilon_r'(\omega)$ and $\varepsilon_r''(\omega)$ data are significantly greater when the electric field is applied perpendicular to the hot-pressing direction. This result is consistent with previous studies[48,49] and complements them by extending the result with continuity into the GHz range.

In Figure 6.10b, significant orientation-based differences between ε_r'' dispersions of the 7.7 and 24.0 vol% samples are maintained for all frequencies. For f < ~0.1-1 MHz (i.e. for the frequencies unaffected by the loss peak), these differences are attributed to dc conductivity anisotropy, i.e., the effect of $\Delta_o\sigma_{dc}$ (in Chapter 4) on the rightmost term in Equation 6.11. The difference at higher frequencies is considered in Section 6.3.5.

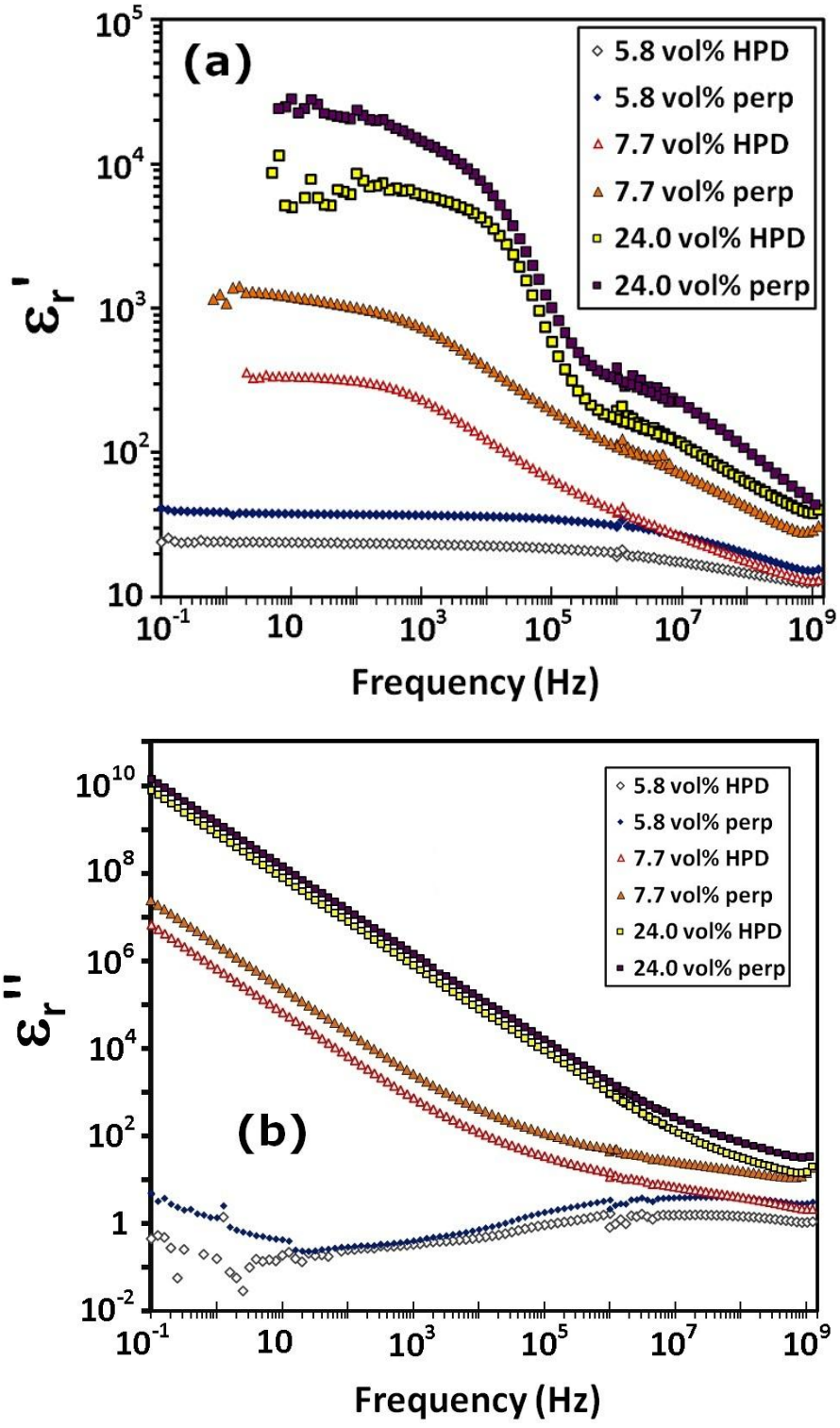

Figure 6.10. The dependence of ε_r' (a) and the loss ε_r'' (b) on the direction of the applied electric field in hot-pressed samples. Three compositions were chosen to represent non-percolated (5.8%), barely percolated (7.7%), and well-percolated (24.0%) samples.[21]

The noisy character of the 5.8 vol% low-frequency data is attributed to poor propagation of the signal through the high-impedance sample compared to samples with greater SiC_w loading. As shown in Equation 6.12, the loss may be linked through Z' to the sample dc conductivity and the associated current.

The anisotropy of the dielectric constant is also believed to arise mutually with that of σ_{dc} and ε_r'', and is explained with a new qualitative model which follows from Chapter 4. There, the large σ_{dc} perpendicular to the HPD was attributed to the increased connectivity and conductivity associated with random orientations of whiskers within planes perpendicular to the HPD, i.e., "perpendicular planes," like that shown in Figure 4.11b on the right. The small σ_{dc} along the HPD was attributed to the stick alignment perpendicular to the HPD, which suggests that connections between perpendicular planes are relatively unlikely and that conduction across a given distance parallel to the applied field necessarily involves a greater number of stick-stick interfaces. This concept is also shown in Figure 4.11b, and is translated into the equivalent circuit model of current flow along the HPD in Figure 6.11a.

In Figure 6.11a, the perpendicular planes having high intraplane connectivity are represented by rows of resistors through which the current flows perpendicular to the HPD. These are separated by rows of capacitors which are sparsely interrupted by resistors through which current flows parallel to the HPD; these latter rows represent the low degree of connectivity in between the well-connected 'perpendicular planes.' As a result, the current flow has a high degree of series character and the effective capacitance of the rows of capacitors is reduced by their combination in series. This is exacerbated by

the increased density of circuit elements along the HPD, which reflects the impact of preferred SiC_w orientations on the density of interfaces involved in conduction.

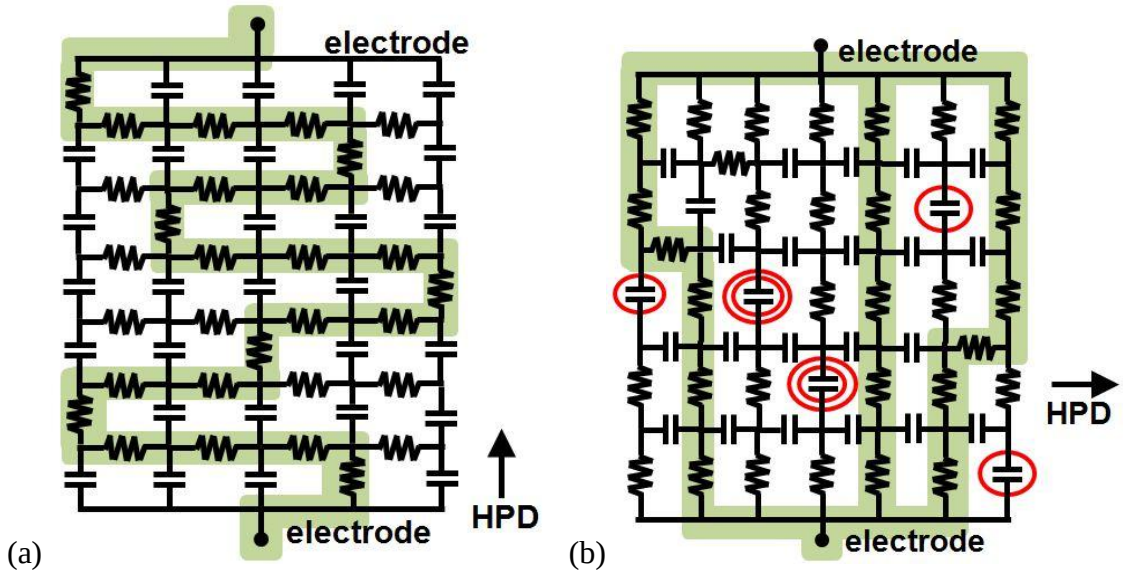

Figure 6.11. Qualitative circuit models showing the increased series character of conduction and capacitance along the HPD (a) and the increased parallelism of conduction and capacitance when the field is applied perpendicular to the HPD (b). The green paths are viable pathways for direct-current flow. The red-circled capacitors represent rare interruptions in the connectivity within planes perpendicular to the HPD.

In Figure 6.11b, the HPD is rotated by 90° and "the tables have turned." The rows of resistors corresponding to the well-connected 'perpendicular planes' are now aligned with the applied electric field (along the perpendicular direction) and are sparsely interrupted by (red-circled) capacitors. These capacitances add in parallel regardless of whether or not the current is able to find a (relatively rare) interplane connection to circumvent singly-circled interruptions, i.e., a resistors aligned along the HPD. When the current cannot find such a path, the entire bias applied to the network is applied to the (double-circled) interrupting capacitor, which corresponds to a thin interface in the microstructure. This, in addition to the parallel combination of all of the other interplane

capacitors which polarize along the hot-pressing direction, results in the network and thus the sample having a large effective capacitance. To summarize, the increased dc conductivity and effective permittivity along the perpendicular direction is the result of increased conduction and capacitance parallelism and decreased series character compared to along the HPD. These effects are exaggerated for qualitative clarity in Figures 6.11a and 6.11b, which are also consistent with the result of Figure 1.24b.

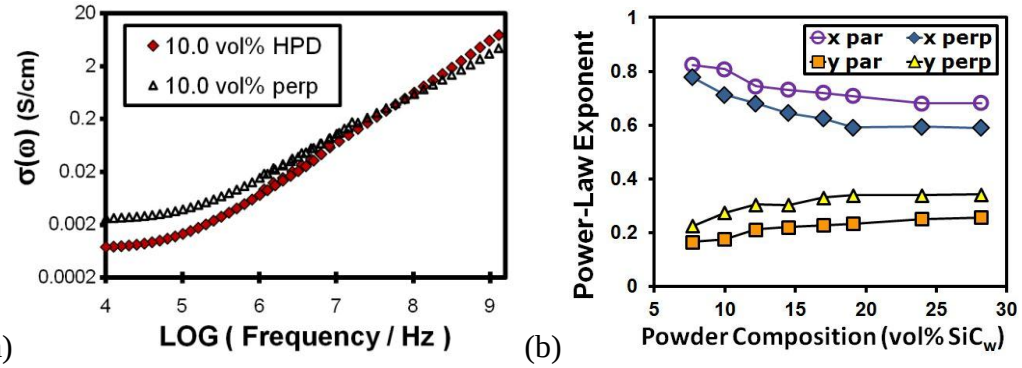

Figure 6.12. (a) The ac conductivity dispersions for hot-pressed samples containing 10 vol% SiC_w measured parallel and perpendicular to the HPD.[21] (b) The power-law exponents relating to Equations 6.12 and 6.13 for different measurement directions and SiC_w loading.

Figure 6.12a shows the effect of orientation on the ac-conductivity dispersion of 10 vol% SiC_w hot-pressed samples. It is apparent that the power law of Equation 6.13 is applicable to both datasets in the high-frequency regime and that the *x*-values (the slopes) depend on sample orientation. For percolated-sample responses, fitting the data with Equations 6.13-6.14 in the linear region (e.g., approximately 2 – 800 MHz) resulted in the *x*- and *y*-values plotted in Figure 6.12b. Clearly, *x* and *y* depend on sample orientation, and reasonable agreement is found with the theoretically[94] expected result of

$x + y = 1$, i.e., 0.956 ± 0.021 and 0.960 ± 0.029 for the HPD and perpendicular directions, respectively.

The power-law behavior for the percolated samples occurs in the same approximate frequency range as the dielectric relaxation for non-percolated samples. This suggests that x and y are also related to the electrically-connected clusters of SiC_w, whose effective conductivities are controlled by the SiC_w-matrix-SiC_w interfaces. In the next Chapter, this idea is explored further.

6.3.4. High-Frequency Dielectric Response

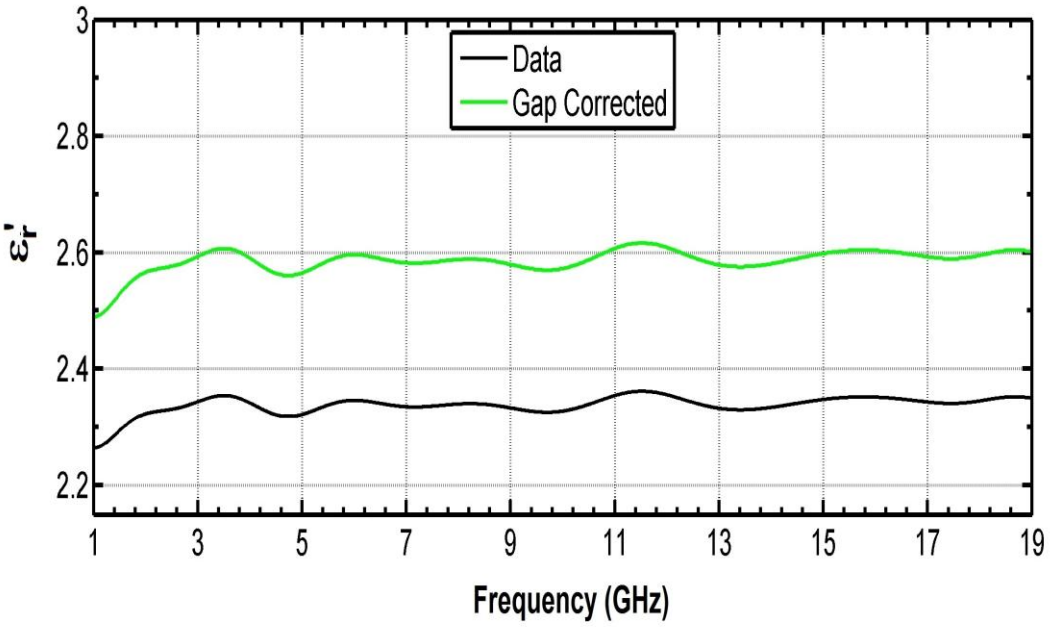

Figure 6.13. Raw data and gap-corrected values of the dielectric constant of the rexolite standard measured by the coaxial airline method.

The results of the coaxial-airline measurement of the rexolite standard are shown in Figure 6.13. The gap-corrected values are relatively close to the expected frequency-

independent value of 2.53, but oscillations exist throughout the data and an anomalous dispersion exists at the low-frequency extreme of the data; these are believed to be experimental artifacts.

Figure 6.14 shows the gap-corrected frequency dispersions of the dielectric constant of the hot-pressed composites. Oscillations in the data are apparent, and it is not clear to what extent these are genuine features of the spectra (e.g., related to relaxations or resonances, as predicted by the SDEMT[85] in the GHz range) or experimental artifacts (e.g., pertaining to higher order modes on coaxial lines).[174] In Figure 6.14, the shift of the minima occurring at $\log(f / \text{Hz}) \approx 10.12$ for the 0% sample to $\log(f / \text{Hz}) \approx 9.88$ for the 28.2% SiC_w sample seems agreeable with expectations for the cut-off wavelength to increase with the refractive index of the sample and thus the (square root of the) dielectric constant. The straight black lines are power-law fits which assume that the oscillations are artifacts and effectively average them out to get an overall sense of the strength of the dispersion in this frequency range. In Figure 6.15, the dispersion exponents from these fits of the coaxial-airline 1-18 GHz data are plotted alongside those from the parallel plate method in the ~2-800 MHz range. The coaxial values are much lower than the parallel-plate values measured in the perpendicular direction, which they should be compared against, and are also lower than the values extracted from measurements along the HPD. This result indicates that as frequency increases, the composite dielectric constant becomes increasingly independent of frequency. It also suggests that the behavior is becoming more capacitor-like (i.e., $y = 0$) and approaching predictions of classic effective medium theory (EMT).

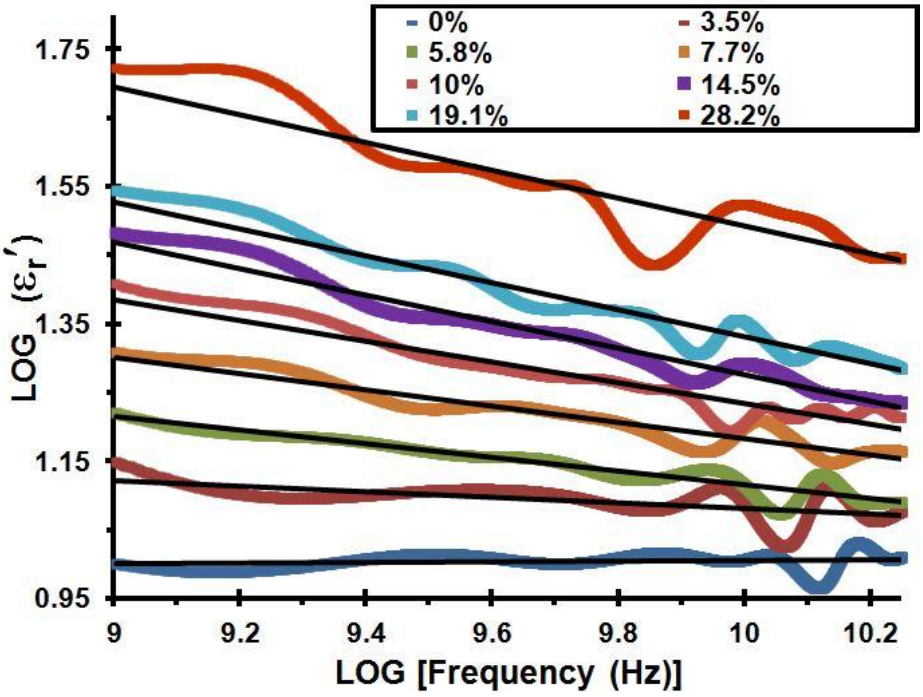

Figure 6.14. Gap-corrected values of the dielectric constant perpendicular to the hot-pressing direction obtained by the coaxial airline method. The black straight lines are power-law fits to the data.

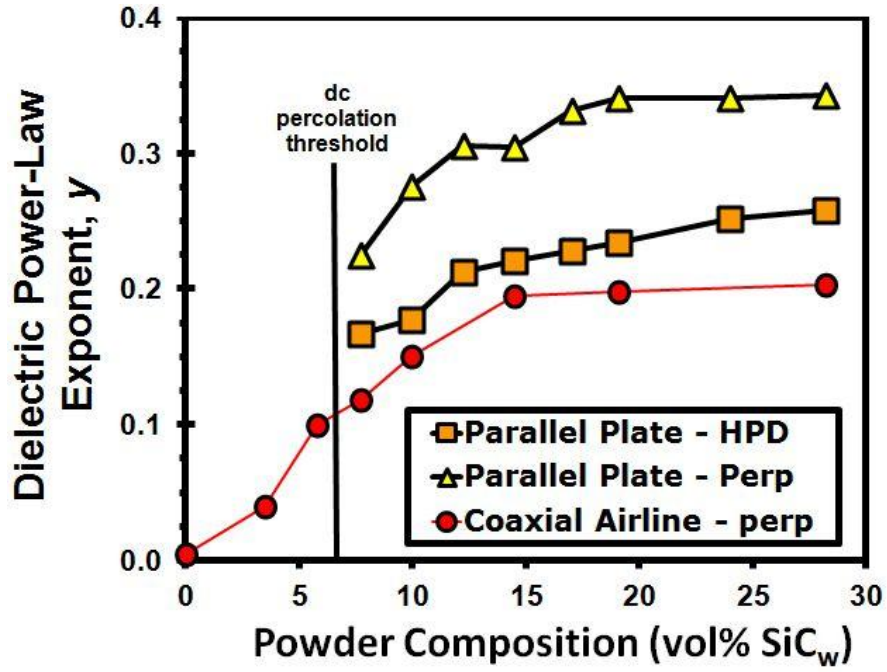

Figure 6.15. Values of the dielectric power-law exponent as a function of loading. These were extracted from parallel-plate measurements between ~2-800 MHz and from coaxial-airline data in Figure 6.14.

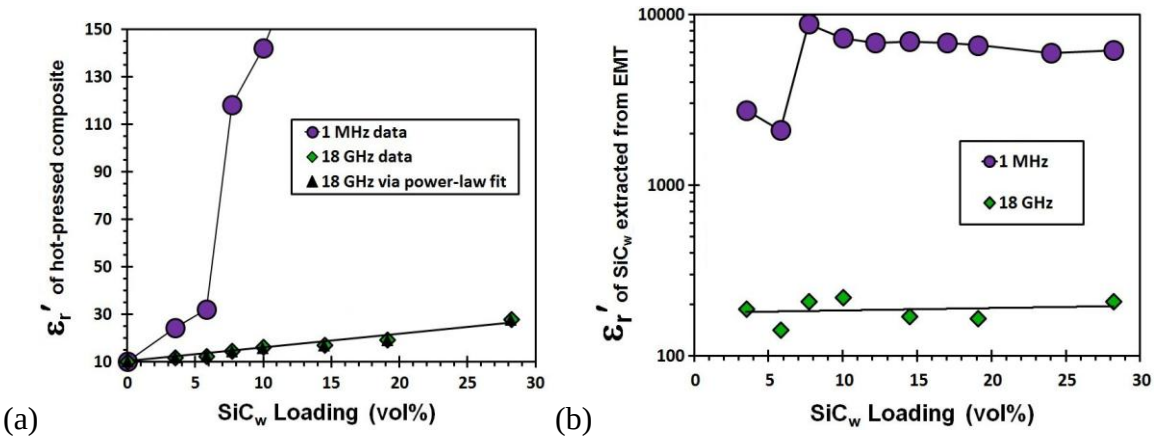

Figure 6.16. Dielectric constant as a function of loading, at low and high frequency, for (a) the hot-pressed composites and (b) the SiC filler. The latter was extracted via the EMT of Equations 6.5-6.6.

At 1 MHz, Figure 6.16a shows that the dielectric constant (measured perpendicularly to the HPD) increased sharply at percolation. This indicates a large contribution of cluster polarizations to the composite permittivity and the inapplicability of the EMT, which ignores the electrical connections through interfaces between the fillers which define clusters. At 18 GHz, where the influence of interfaces should be minimal, the dielectric constant of the composites increased approximately linearly with SiC_w loading. The differences between the data and the values from the power-law fits were insignificantly small. Interpreting this linear trend in the context of the parallel ROM (Equation 6.2) implies that the SiC may be estimated to have a dielectric constant of 66.5, assuming that its capacitance may be regarded to add in parallel with that of the matrix, e.g., as a set of parallel planes which are perpendicular to the HPD. This assumption implies the SiC phase is continuous, which implies that interfacial polarization is negligible. A similar result of the dielectric constant trending

approximately linearly with whisker content was found for hot-pressed mullite-SiC_w composites at 2 GHz via coaxial-airline measurement[49] and was similarly interpreted.[17]

In Figure 6.16b, the dielectric constant of the SiC extracted from the EMT (Equations 6.5-6.6) at 1 MHz and 18 GHz is plotted as a function of whisker loading based on typical whisker lengths and diameters of 10 and 0.5 μm, respectively. At the lower frequency, the dielectric constant changes significantly at the dc-percolation transition, thereby corroborating the inapplicability of the EMT since the dielectric constant of the SiC whiskers should not depend on the formation of an electrically percolated cluster. At 18 GHz, cluster polarizations are too slow to keep up with the oscillations in the applied field, the application of the EMT is more appropriate, and the compositionally-averaged dielectric constant of 190 ± 30 for the SiC is relatively independent of the percolation transition. Changing the assumed whisker length to 5 μm on the basis of whiskers having apparent lengths ≤10 μm in SEM micrographs resulted in a dielectric constant of 220±40 for the SiC, which is not significantly different. Therefore, the dielectric constant of the SiC whiskers is roughly estimated to be ~200.

At 1 GHz frequency, the data from coaxial airline and the Agilent 4291B are near their limits of reliability due to the proximity to the frequency extremes of the different methods. Figures 6.17a and 6.17b show data from the latter instrument scaled to highlight the damped dielectric resonance which was observed in the composites and centered between 1.4-1.7 GHz. The resonance grows in prominence and shifts to lower frequency as SiC_w content increases, and when loading is high, it resulted in a dielectric constant close to zero at 1.7 GHz. In the coaxial data of Figure 6.14, the dielectric constant at these frequencies (which correspond to 9.15 and 9.23 on the log frequency scale) shows

no indication of a resonance, increases with whisker content, and greatly exceeds zero when whisker loading is high.

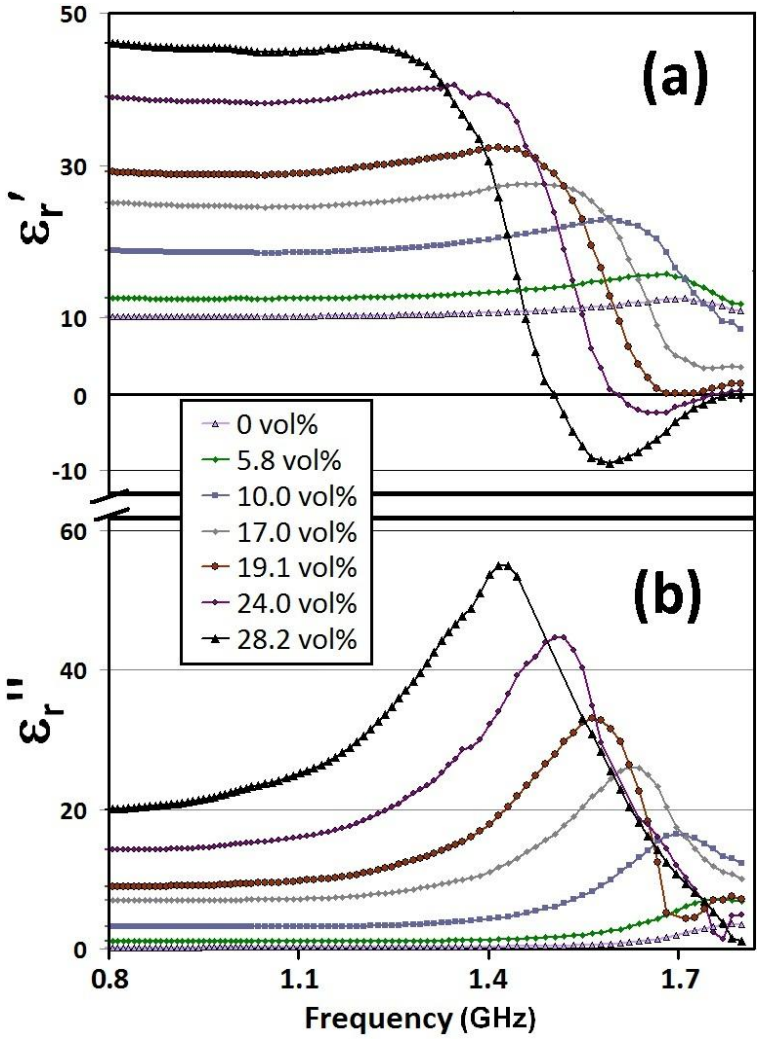

Figure 6.17. Real (a) and imaginary (b) parts of the complex dielectric constant measured by the Agilent 4291B, showing a damped resonance near the high-frequency extreme of the instrument.[21]

However, if the entirety of the resonance is assumed to be an artifact, the coaxial data also seems to contradict the loading-insensitive (extrapolated) values of ε_∞' in Table 6.1 which were derived from data from the Agilent 4291B and suggest that the dielectric

constant of non-percolated samples is unaffected by SiC inclusions. The portion of the resonance in which the dielectric constant increases with frequency or the anomalous low-frequency dispersion and artifacts in the coaxial data (demonstrated by Figures 6.13 and 6.14) might account for the discrepancies.

The resonance might be an anomalous result of parasitic equipment inductance taking on a significant role when sample conductance was high, i.e., when SiC loading was high. Partial qualitative agreement was found between the experimental data in the ε_r^* and Z^* planes and a circuit model[175] for the resonance. Since the agreement was not extremely strong, some other explanations for this resonance are considered.

First, the SDEMT for conductive-stick composites[85] predicts dielectric resonance from interactions between the sticks and such resonances have been confirmed by experiment[7] in the low-GHz range. The theory also predicts a similar type of magnetic response (even when the composite does not contain magnetic components) which, interestingly enough, is expected to grow in prominence and shift to lower frequency as the stick concentration increases. However, the theory also predicts that (A) the dielectric resonance requires the skin effect to occur in the metallic sticks, and that (B) the resonant frequency depends mainly on the stick length, and is (C) independent of the stick conductivity. Although the SiC is a semiconductor with non-metallic conductivity, Point A might be applicable because as-fabricated SiC_w are sometimes characterized by a carbon-rich surface layer[176] or free carbon and high-frequency currents might concentrate in this layer. Point (C) seems questionable because the skin effect itself depends on conductivity and might be the result of one of the assumptions applied by the authors in developing the theory. Also, the theory predicts the first order resonance to occur at

$f_{res} = c\varepsilon_d^{-1/2}/2L_s$ where c is the speed of light, ε_d is the dielectric constant of the matrix, and L_s is the stick length. For this work, L_s ~10 μm, ε_d ~10, and thus f_{res} ~ 5 THz, which disagrees with the observed resonant frequency by three orders of magnitude.

Interfacial compounds between connected SiC_w are another possible source of the observed resonance and offer better agreement in terms of the resonance frequency.[135] Dielectric resonance in liquid-phase-sintered ZnO varistors at ~3 MHz was attributed to the material possessing an inductive component related to charge (de)trapping at the interfacial reaction products of sintering additives between ZnO grains. The resonant frequency was found to shift to 1 GHz for a lower concentration of additives (3 mol%). In the present work, small x-ray diffraction peaks were observed with 0 vol% samples and seemed to match compounds consistent with the sintering-additive chemistries. However, these peaks were not resolvable in 24.0 and 28.2 vol% samples (for which the resonance was clearly observed).

The resonance might also result from the properties of the SiC_w. Similar measurements were performed on four α-polytype SiC wafers: #1. undoped, nominally "pure" 6H, #2. n-type 6H, #3. n-type 6H, #4. n-type 4H. The ε_r' dispersion for the nominally-pure Wafer 1 was entirely flat (ε_r' ~9.5) and did not exhibit a resonance. Resonances were observed for Wafers 2-4 at frequencies of ~1.3 GHz, 0.94, and 0.91 GHz, respectively, and are shown in Figure 6.18. The $\varepsilon_r'(\omega)$ dispersions were flat at lower frequencies with $60 < \varepsilon_r' < 80$, in agreement with the extrapolated result of ε_r'=66.5 from the parallel ROM at 18 GHz . These results on bulk single-crystals of SiC suggest that the resonance in Figure 6.17a-b relates to impurities in the SiC_w.

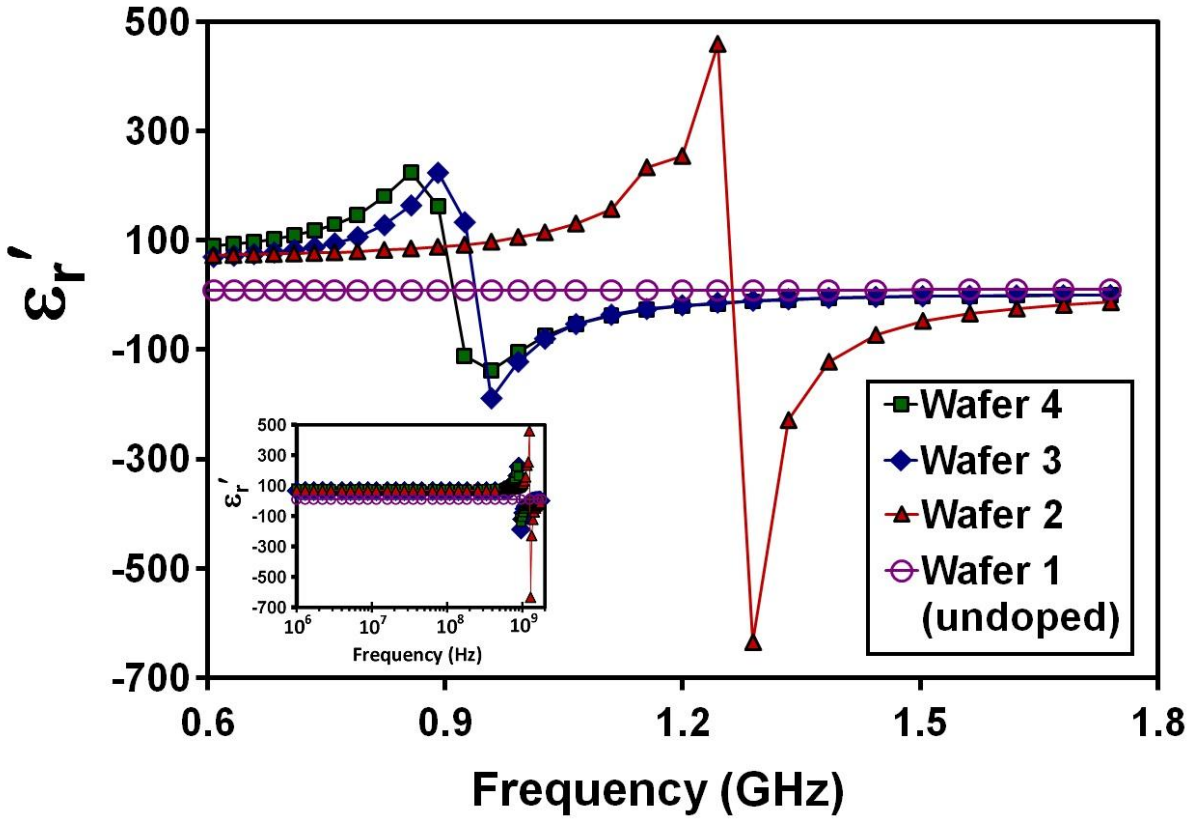

Figure 6.18. The dielectric constant of four α-polytype SiC wafers. The inset shows that there was no dispersion at frequencies beneath the resonance.

6.3.5. Application Perspective

The microwave-heating application depends on the microwave-heating rate (Equation 6.8), which in turn depends on the dielectric loss (Equation 6.9). The dielectric loss measured along the processing direction tended to be greater for extruded material compared to hot-pressed material when frequency was high and SiC_w content was low. For example, the maxima of the loss peaks attributed to interfacial polarizations in non-percolated 3.5 and 5.8 % SiC_w samples were two times larger for extruded material. At the application-relevant frequency of 915 MHz, the dielectric loss of extruded material

was comparable and in most cases somewhat larger than that of hot-pressed material. This can be seen in Figure 6.19.

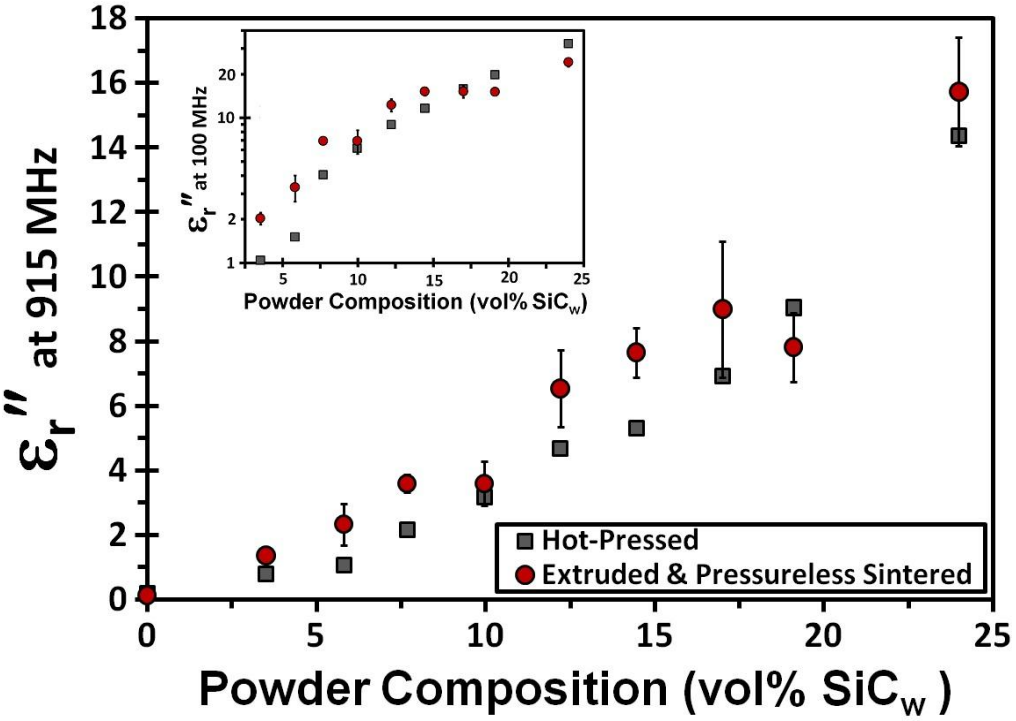

Figure 6.19. Dielectric loss at 915 MHz for hot-pressed and extruded and sintered composites as a function of SiC loading. The inset shows the loss at 100 MHz on a log scale. Error bars on extruded data points give one standard deviation on each side of sample averages. Hot-pressed data had minimal variation.

It is speculated that the increased whisker alignment with the electric field for extruded material provides for the increased values via greater charge displacements and thus larger displacement currents. The inset of Figure 6.19 shows that the loss at 100 MHz was greater for hot-pressed material only for the 19.1-24.0 % SiC_w compositions. This reflects the fact that the dielectric loss tended to be greater for the hot-pressed material when SiC_w loading was high and frequency was low due to the much stronger dc

conductivity tail. At 10 MHz, the crossover occurred between 7.7 and 10.0 % SiC_w (not shown).

In Figure 6.20a, the loss at the application-relevant frequencies of 915 and 2450 MHz is plotted as a function of whisker content. At 915 MHz for 3.5 – 5.8 vol% SiC_w, the primary source of this loss is the ε_r'' peak of the relaxations of electrically-connected SiC_w clusters with interface-controlled conductivity. Due to percolation and the accompanying growth of the dc-conductivity tail, this loss increases much more rapidly for samples having ≥7.7 vol% SiC_w. The 24.0 and 28.2 vol% data points are not included on the trend line with the other compositions because they reflect additional contributions from the damped-resonance loss peaks. At 2450 MHz, the apparent trending of the data (not shown) appeared to be less affected by percolation.

For percolated compositions in Figure 6.20a, it is also apparent that the loss tends to be higher for perpendicular measurements at 915 MHz compared to those at 2450 MHz and those along the HPD at 915 MHz. One might guess that these differences could be fully accounted for by the (imaginary) σ_{dc} term in Equation 6.11. To this effect, Figure 6.20b plots the loss at the relevant frequencies as a function of (σ_{dc} / $\omega\varepsilon_0$). For all three data sets, it can be seen that dc conductivity starts to play a significant role at 10% SiC_w.

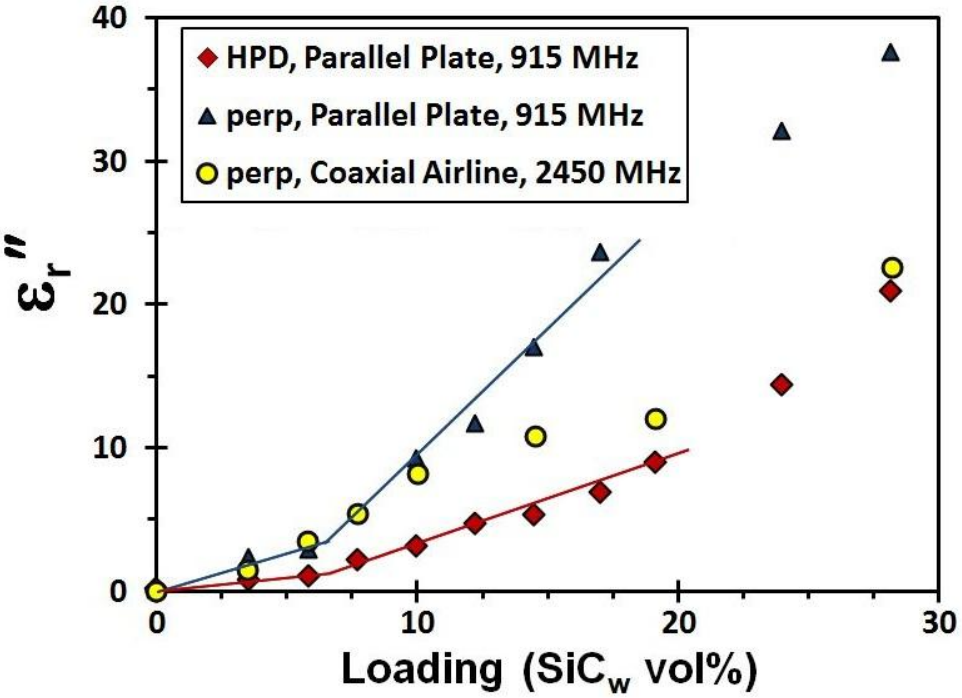

(a)

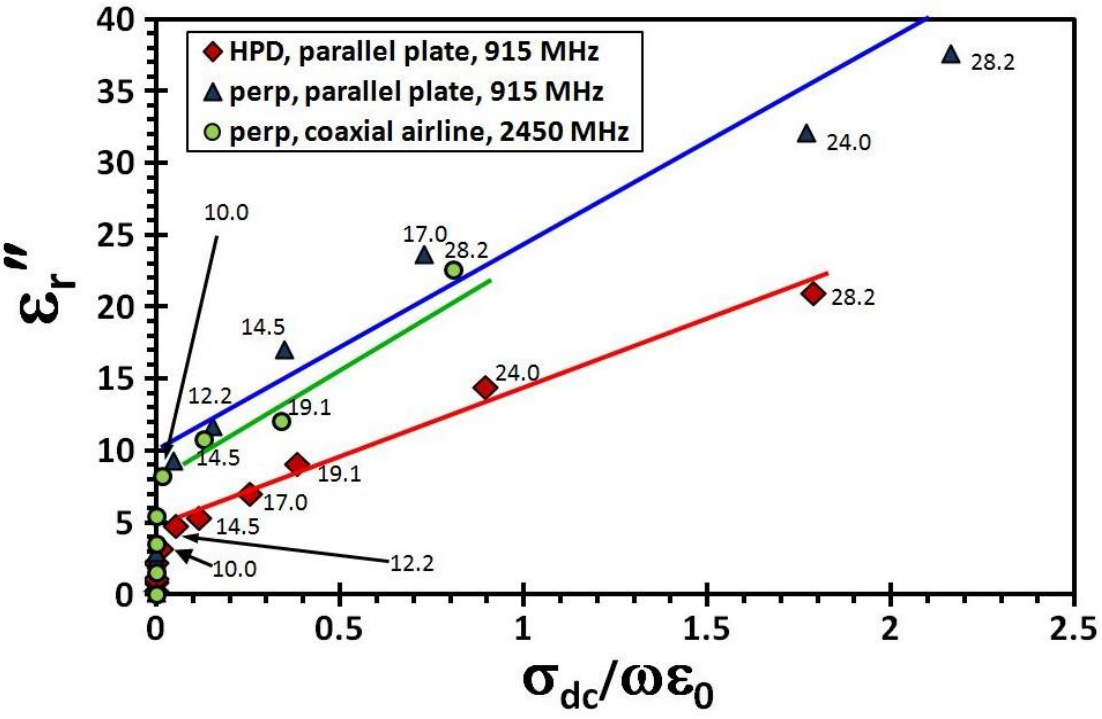

(b)

Figure 6.20. Dielectric loss of hot-pressed samples for different frequencies and measurement types as a function of (a) whisker loading and (b) the dc-conductivity term in Equation 6.11. The numbers at each data point designate the whisker loading in volume percent; arrows are used to specify points in crowded areas of the plot.

For the perpendicular orientation, the two frequencies are similar in terms of the trending of the data and the proximity of most data points at or above 10% SiC_w, e.g., 17% and 28.2% SiC_w at 915 and 2450 MHz, respectively. This seems suggestive of dielectric loss controlled by dc conductivity, but comparison of the values on the different axes (which have the same units) shows that the measured loss is much higher than that predicted by dc conductivity alone.

Near $\sigma_{dc} = 0$, the difference likely reflects one or more buried dielectric relaxations, e.g., those corresponding to defect complexes[106] in SiC, intrawhisker polarization, and non-percolated-cluster relaxations. For both orientations, the loss at 915 MHz increases with dc-conductivity, but a substantial separation between the two trend lines remains in Figure 6.20b. Therefore dc conductivity does not fully explain the orientation dependence of the loss because data from the two measurement directions cannot be fitted by a single line. Some portion of the additional difference might be accounted for by a buried loss peak that is concealed by the σ_{dc} tail and corresponds to a large and broad dielectric relaxation which cannot be explained by intrinsic SiC loss,[106] e.g., a relaxation relating to the percolating cluster. In Figure 6.10, such a buried relaxation might also contribute to the orientation-based differences in $\varepsilon_r'(\omega)$ and $\varepsilon_r''(\omega)$ dispersions noted for percolated samples. Indeed, it is apparent in Figure 6.6 that the loss peak is larger for the perpendicular direction and calculations revealed that it is 2.76 and 2.47 times larger for the 3.5 and 5.8 vol% compositions, respectively. These values are agreeable with the approximate factor-of-two orientation difference in the trend lines for ε_r'' at 915 MHz in Figure 6.20b.

Figure 6.21 shows experimental dielectric loss data from a 7.7 vol% sample after subtracting out the σ_{dc} term of Equation 6.10 with the *k*-modification discussed in the text. The applied field was perpendicular to the HPD. Using $0.72 \leq k \leq 0.83$ recovered a broad ε_r'' peak suggestive of the relaxation term in Equation 6.10. The low-bound of 0.72 is close to the high-bound of 0.70 reported in Table 6.1 for fits of 5.8 vol% data. This suggests continuity in the material system. Using more ideal values of $0.93 \leq k \leq 0.99$ recovered a similar peak for the more conductive 24.0 vol% composition. Using $k = 1$ failed to recover a Cole-Cole peak for all attempts. It is not surprising that $k \neq 1$ seems to be required to recover these high-frequency relaxation loss peaks because Figure 6.7 and results of others[177] show that the use of $k = 1$ is better-suited to fitting low-frequency data.

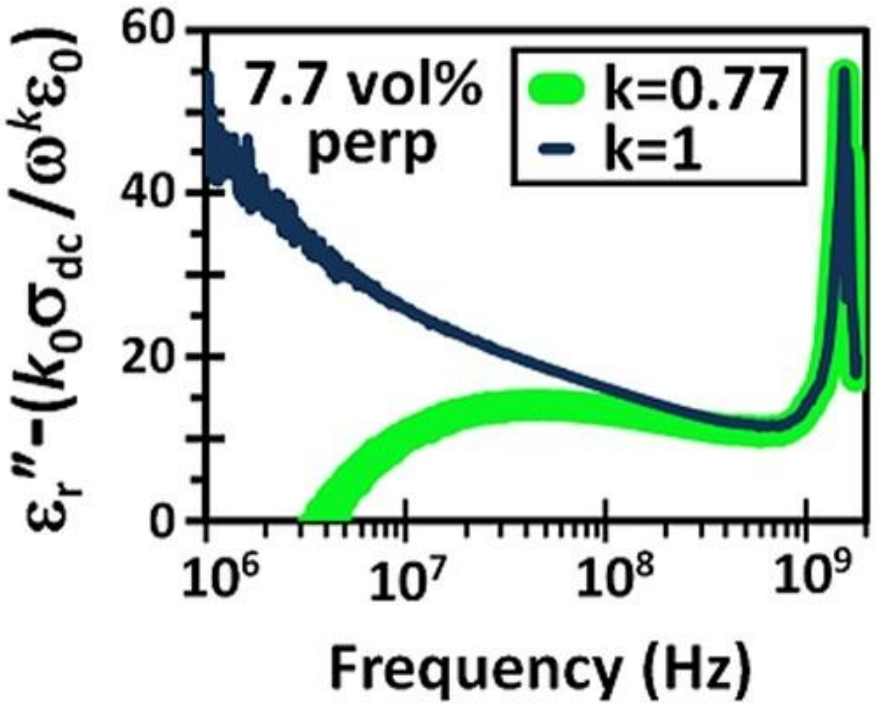

Figure 6.21. The results of attempts to subtract out the σ_{dc} tail from the loss spectrum of a 7.7 vol% SiC_w sample with and without the empirical factor *k* discussed in the text.

6.4. Conclusions

Together, the hot-pressed and extruded data provide considerable insight into the insulator-conductor transition for general composites. They show that the introduction and continued addition of relatively conductive (SiC_w) filler to an insulator having a frequency-independent dielectric constant results in a small relaxation which grows in strength, slows down in time, spreads over a wider frequency range, and evolves into a dispersion strongly dependent on frequency and in accordance with the common $\varepsilon_r' \propto \omega^{-y}$ power law.[125] Meanwhile, the loss peak associated with the relaxation grows in magnitude but is eventually concealed by the superimposing loss "tail" associated with dc conductivity, which also grows in magnitude with increasing SiC_w. The abruptness and magnitude of the dc-conductivity percolation transition determines the speed of the compositional evolution of the complex relative permittivity. For this system, the percolation transition and permittivity evolution were slower for the extruded material.

The relaxation is best explained in terms of polarizations within and between non-percolating whisker clusters whose conductances are controlled by the interfaces between electrically-connected whiskers. This can explain the aforementioned dependencies of the relaxation on loading as well as those on the measurement orientation relative to the microstructural texture. The prominent role of the interfaces in this idea is agreeable with the modeling approach, which was based on Maxwell-Wagner interfacial polarizations and used to quantify trends in the relaxation appearance. At high frequencies, the influence of the interfaces on the dielectric constant and its frequency dispersion wane and the composite behavior approaches that predicted by effective medium theory for elongated inclusions.

The frequency-dependent dielectric constant and loss were generally smaller along the HPD compared to the perpendicular direction. This is because macroscopic conduction along the HPD requires a relatively circuitous conduction pathway with an extensive series character. Conduction and capacitance along the perpendicular direction is characterized by greater parallelism due to the random orientation of whiskers within planes which are perpendicular to the HPD. For percolated samples, modeling the ac conductivity and dielectric constant with frequency power laws revealed that the power-law exponents are also orientation-dependent. Also, a damped resonance was observed between 1.4 - 1.7 GHz. Various plausible sources for this phenomenon are discussed. Generally speaking, the commercial application of these composite materials in microwave heating is influenced by the relaxation, the dc-conductivity tail, and possibly the resonance. The role of the dc-conductivity is increased for higher whisker loading and lower frequencies, and is substantial for the application frequencies of 915 and 2450 MHz and whisker loadings $\geq$ 10 vol% in the hot-pressed material. There is reason to believe that the loss peak from the relaxation attributed to cluster polarization is concealed by the dc-conductivity tail and makes a large contribution to the loss of percolated samples at the application frequencies.

CHAPTER 7

INVESTIGATION OF THE INTERFACIAL CONDUCTION MECHANISM VIA THE TEMPERATURE DEPENDENCE

7.1. Introduction

The literature of disordered insulator-conductor composite materials suggests that the mechanism controlling electrical conduction may be conclusively determined from the temperature-dependence of dc conductivity.[94] To our knowledge, all previous investigations based on this principle considered composites having insulating polymer matrices and highly-conductive carbon-black fillers.[94,178,179] It is of interest to know if and how the conduction mechanism would be affected by the replacement of these with an oxide matrix and wide-bandgap semiconductor filler. Some authors have predicted that the inclusion of semiconductor phases should allow for a greater diversity of phenomena compared to metal-insulator systems.[180] In this Chapter, we examine the temperature dependence of the electrical response of composites of such an oxide-semiconductor composite system, i.e., alumina (Al_2O_3) and SiC whiskers (SiC_w). Being entirely made of ceramics, this system allows the exploration of the fundamental physical processes to higher temperatures than is possible with composites having polymer matrices and thus reduced thermal stability.

The widely-observed phenomenon of dc-conductivity percolation in disordered insulator-conductor composite materials implies that electrical current in such percolated materials is guided through the discrete conductive-filler particles. Since the interfaces

between these particles generally have finite widths, a fundamental question arises: how do the charge carriers traverse these gaps between the conductive particles? In attempts to answer this question, theories of conduction by carrier hopping[181] and fluctuation-induced tunneling[178] (FITC) have been met with some apparent success.[94,179] These models will now be briefly introduced.

Nearest-neighbor hopping (NNH) of carriers between randomly distributed localized electronic states in disordered systems is a thermally activated process.[181] The associated dc conductivity (σ_{dc}) follows an Arrhenius law, i.e., it depends on absolute temperature (T) via

$$\sigma_{dc} = \sigma_0 \exp(-Q / kT). \qquad (7.1)$$

Here, k is the Boltzmann constant, Q is the activation energy, and σ_0 is a temperature-independent constant assuming the implicitly-contained temperature dependencies of the mobility and density of states cancel out.[181] It is believed that the NNH mechanism is more likely to control the conductivity when the temperature and spatial distances between traps are relatively large.[182]

When temperature is relatively low, it is believed that carriers need not hop only to nearest neighbors and the variable-range hopping (VRH) occurs.[181,183] This process exhibits a characteristic temperature dependence, i.e.,

$$\sigma_{dc} \propto \exp[- (T_H / T)^h] \qquad (7.2)$$

Here, T is the absolute temperature in degrees K, T_H is a fitting parameter which depends on the density of states at the Fermi level and wave function decay, and h has a constant value which follows from theoretical considerations. For three dimensional systems[182,184]

h = 1/4 is the characteristic value, and h = 1/2 when Coulomb interactions are significant.[185] Some theory for VRH predicts $1 > h > 1/2$ for higher temperatures,[185] and h = 1 corresponds to the limit of NNH and Arrhenius behavior.[182,186]

The fluctuation-induced tunneling model[178] for conduction (FITC) states that conductivity results from quantum mechanical tunneling through barriers which exist between conductor particles and whose heights decrease with increasing temperature due to thermal fluctuations. According to the FITC model, the conductivity depends on temperature via

$$\sigma_{dc} \propto \exp[\, -T_1 / (\, T + T_0 \,) \,] \qquad (7.3)$$

where T_1 and T_0 are fitting parameters which are said to be related to the energy required for electrons to cross the insulating tunneling gaps and the low-temperature temperature-independent resistivity, respectively.[187] Given these interpretations, which seem to imply $T_1 > T_0$, the values used for composites of carbon black (CB) and polyvinylchloride in the original proposal of the theory[178] seem quite reasonable, i.e., $1.2 \leq T_0 \leq 5$ K, $22 \leq T_1 \leq 135$ K, and $T_1 >> T_0$. However, in a later of expansion of the theory using composites of CB and polyethylene terephthalate,[94] the employed values of T_0 and T_1 were of similar magnitudes (i.e., 109-216 K), and for composites having greater CB loading, $T_0 > T_1$. These dramatically different values of T_1 and T_0 were not thoroughly explained, and were attributed to differences in the nature of the polymer, the structure and loading of the conductive filler, and the percolation threshold. Unfortunately, neither T_0 nor T_1 can be uniquely related to the physical quantities involved in the derivation of the theory,[178] such as the barrier width (w), which may be expected to scale with the filler volume fraction (p) via $w \propto p^{-1/3}$ when filler dispersion is homogeneous.[94] According to the FITC model,

the conductivity is expected to decrease exponentially with *w*, and it follows that $-\log(\sigma_{dc}) \propto p^{-1/3}$ and $(T_1 / T_0) \propto p^{-1/3}$; notably, agreement with these proportionalities has been used as a sort of verification for the applicability of the FITC model.[94]

For composites of alumina and silicon carbide (SiC) whiskers, the dependence of the electrical response on temperature is of practical as well as scientific interest. These composites are effective electromagnetic absorbers,[82] and their commercial application in microwave heating and cooking[78] requires them to perform over a range of temperatures, and depends on dielectric loss from dc conductivity.[21] There is apparently only one other study[114] on the effects of temperature on Al_2O_3-SiC_w composite electrical response. In that work, the composite dc resistance decreased linearly with increasing temperature, and this was attributed to semiconductor behavior in the SiC whiskers; the data was not interpreted by modeling. For the related AlN-SiC composite system, the increase of the conductivity at 30 GHz with increasing temperature between -180° and 200°C was modeled via two Arrhenius processes with different activation energies.[188]

7.2. Experimental Methods

The hot-pressed Al_2O_3-SiC_w composites were cut with a diamond saw into different shapes appropriate for two different experimental setups. These setups were used to separately measure the effects of temperature on the high-frequency and low-frequency alternating-current electrical response of the composite bulk in parallel-plate configurations. For the former, small samples were cut from thin hot-pressed discs which spanned the compositional range in order to fit inside the relatively small sample cell. Rectangular bars of ~4.5 mm width were cut from the middle of these discs and

subsequently sliced to yield a few rectangular-prism samples (~2.4-2.6 mm thicknesses, ~4.5 mm widths) for each whisker composition. For low-frequency measurements, samples were made by quartering thick hot-pressed discs which were electrically percolated (i.e., 7.7 - 28.2 vol% SiC_w) via slicing. This was done to increase the sample impedance via geometry so that it remained sufficiently large for measurement after temperature-induced decreases. Images of samples of electroded samples are shown in Figure 7.1.

(a)

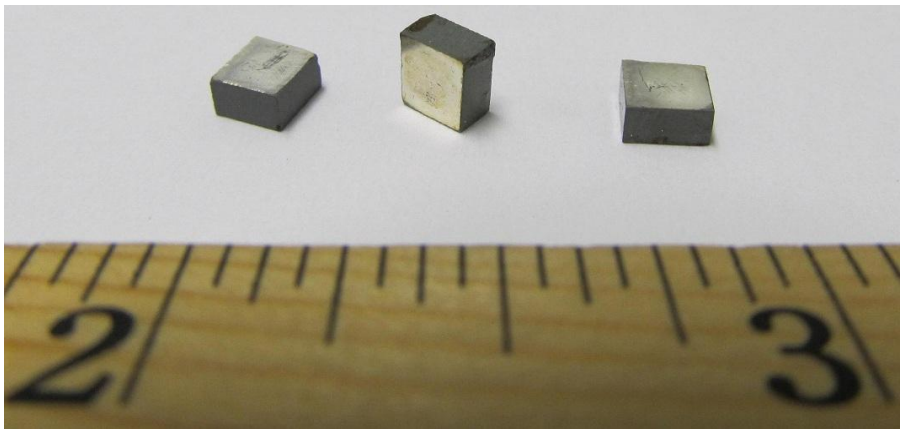

(b)

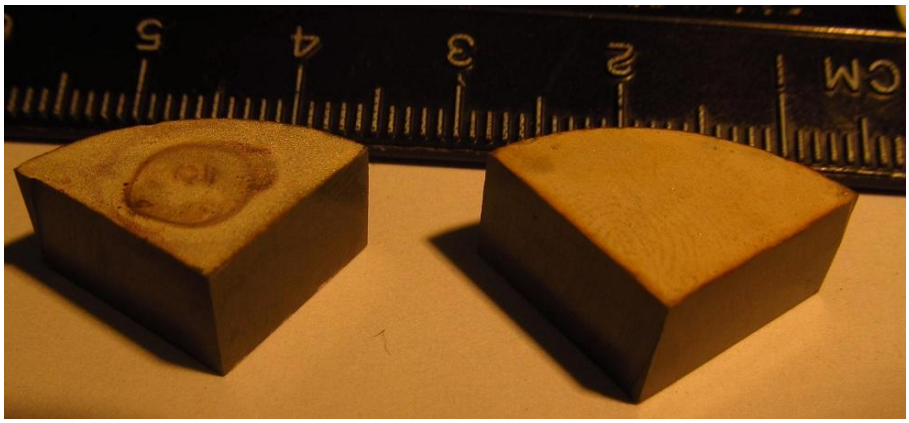

Figure 7.1. (a) Samples used in Novocontrol measurements next to the inch side of a ruler. (b) Samples used in Solartron measurements next to the centimeter side of a ruler. The appearance of the electrodes was significantly different before (right) and after (left) high temperature measurements, but the separable bulk conductivity was not. The lighting conditions for the two images were different.

Sputtered Ag electrodes were applied to all samples. For the low-frequency measurements, robust Ag coatings were applied on top of the sputtered Ag films which were relatively fragile and otherwise prone to mechanical damage during use with the custom fixture. Coatings consisted of conductive Ag paint which was allowed to dry for ~60 hours, and then hardened by heating in air first at 200°C for 2.5 hours and then at 350°C for 40 minutes. Such coatings were unnecessary for and were not applied to samples used in high-frequency measurements. These employed the Agilent 4291B dielectric analyzer (1 MHz – 1.8 GHz) in conjunction with a Novocontrol temperature-control system and a computer with WinDETA software (Novocontrol Technologies GmbH & Co., Frankfurt/Main, Germany). With this setup (Figure 7.2a), the temperature (T) was controllably varied in the $-160 \leq T \leq 300$°C range with flowing nitrogen gas. Samples were tightly clamped during measurement by means of a spring-loaded screw-locked sample cell (Figure 7.2b) and the addition of maximum manual force. The data was interpreted in terms of permittivity.

For low frequencies (0.1 Hz – 32 MHz), variable-temperature impedance measurements were performed with the Solartron 1260/1296 impedance analyzer/interface and a custom-built fixture between ambient temperature (~20°C) and 700°C, typically in 50°C increments. The overall setup and the fixture are shown in Figures 7.3a and 7.3b, respectively; the latter was originally designed by Ming Dong[189] in the late 1990s. The top half of the fixture was made of glass and had inlets for gas flow, the positive and negative electrical terminals (i.e., steel rods functionalized with a spring-loaded sample holder), and a K-type thermocouple, which was placed next to the sample. The sample holder was located in the bottom half, which was quartz and was inserted into

a Lindberg furnace. Air-tight seals were made with polymeric o-rings. For $T \geq 250°C$, measurements were conducted under flowing Ar gas after evacuating the tube with a

(a)

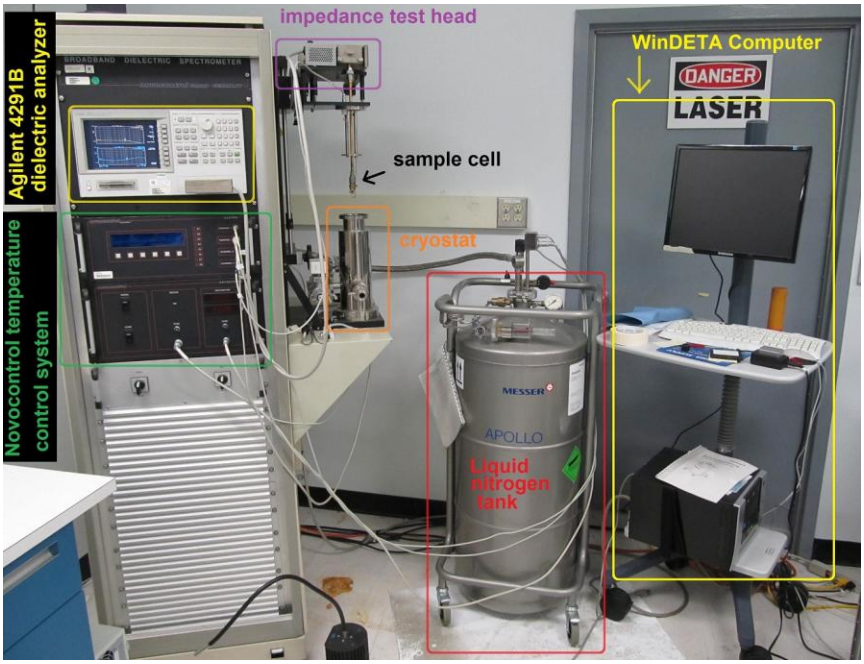

(b)

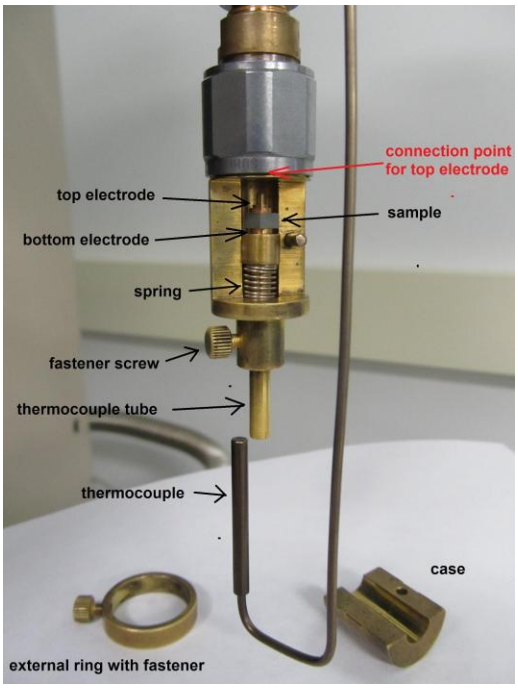

Figure 7.2.(a) Experimental setup for Novocontrol measurements. (b) Novocontrol sample cell taken apart to show various components.

(a)

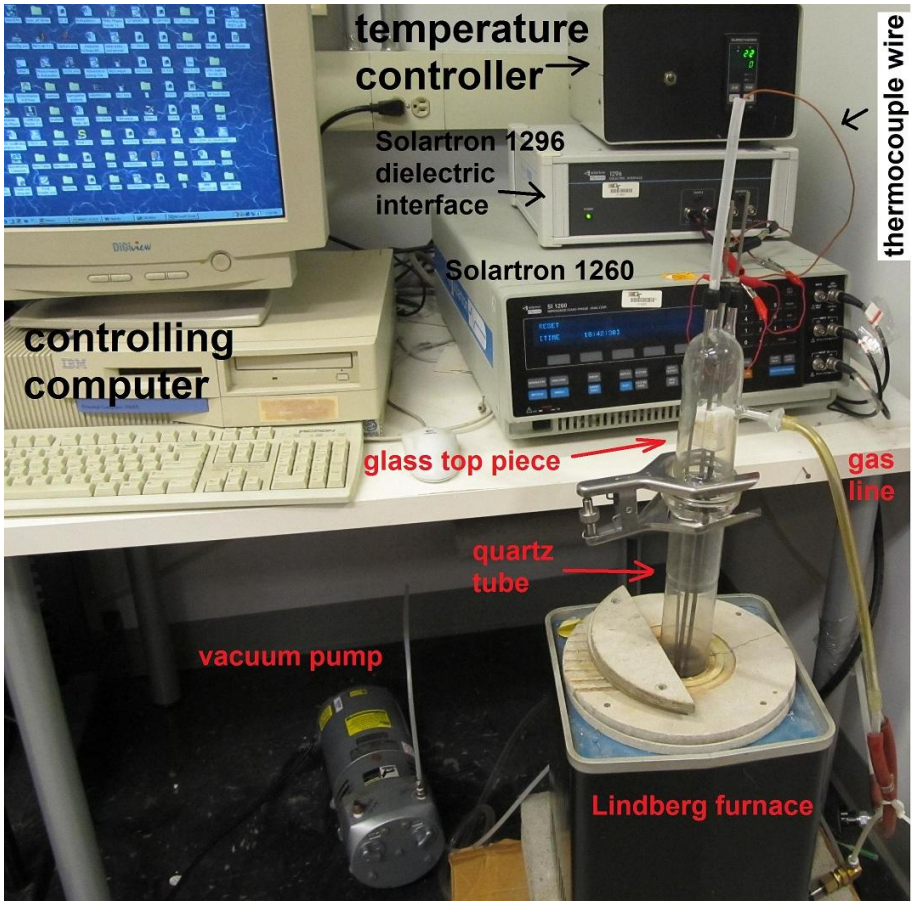

(b)

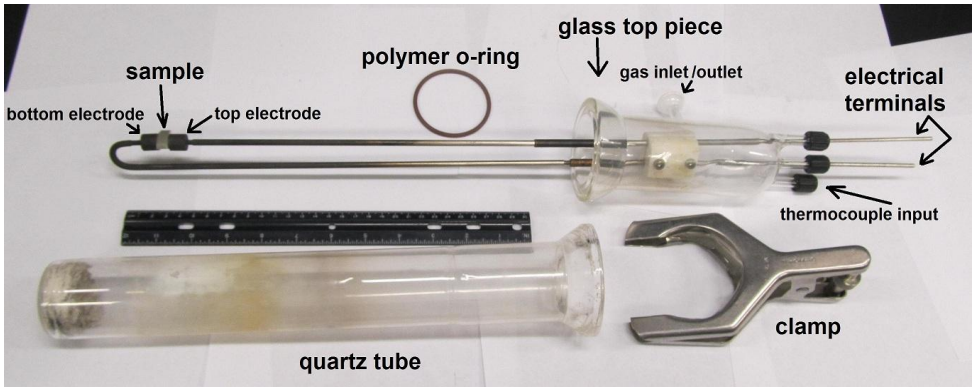

Figure 7.3.(a) Experimental setup for Solartron measurements. (b) High-temperature fixture taken apart to show various components (designed by Min Dong).[189]

vacuum pump and back-filling it with Ar gas in order to prevent oxidative changes to the sample. After high-temperature runs, the hot-pressed samples were re-measured to verify

that the room-temperature dc conductivity (σ_{dc}) was not significantly altered, as such would indicate irreversible changes to the sample induced by high temperature. As in Chapter 3, the electrically-percolating SiC_w network of the hot-pressed composite bulk was associated with a separable complex-impedance semicircle and this was used to calculate σ_{dc} (see Figure 3.2a). For SiC_w-percolated samples, the microstructure was imaged with a LEO 1530 SEM and the distributions of distances between the SiC inclusions were measured by the stereological method (see Sections 2.4.1 and 2.4.2).

Some σ_{dc}–T data was also obtained for pressureless-sintered samples to which robust Ag electrodes were similarly applied. This is presented for comparison to the hot-pressed data at the end of this Chapter. The comparison is limited because these samples were not as well-behaved at variable temperatures due to the different microstructures and variable porosity. The electrode semicircle was sometimes but not always separable in the raw data and therefore σ_{dc} was calculated from data taken with large dc bias (V_{dc}) in order to minimize its influence on σ_{dc}.

7.3. Results and Discussion

7.3.1. Consideration of the Hopping and FITC Models

Generally, the experimental temperature dependence of conductivity can be said to agree with one of the aforementioned models (Equations 7.1-7.2) if fitting data points to $\ln(\sigma_{dc}) \propto f(T)$ yields a straight line, where $f(T)$ is a function of temperature. For hopping conductivity, $f(T) \propto T^{-h}$, where $1 > h \geq ¼$ for variable-range hopping and $h = 1$ for nearest-neighbor hopping, as described above. For the FITC model, $f(T) = T_1/(T + T_0)$. In Figure 7.4a, fits of the experimental data from 10% and 28.2% SiC_w samples to

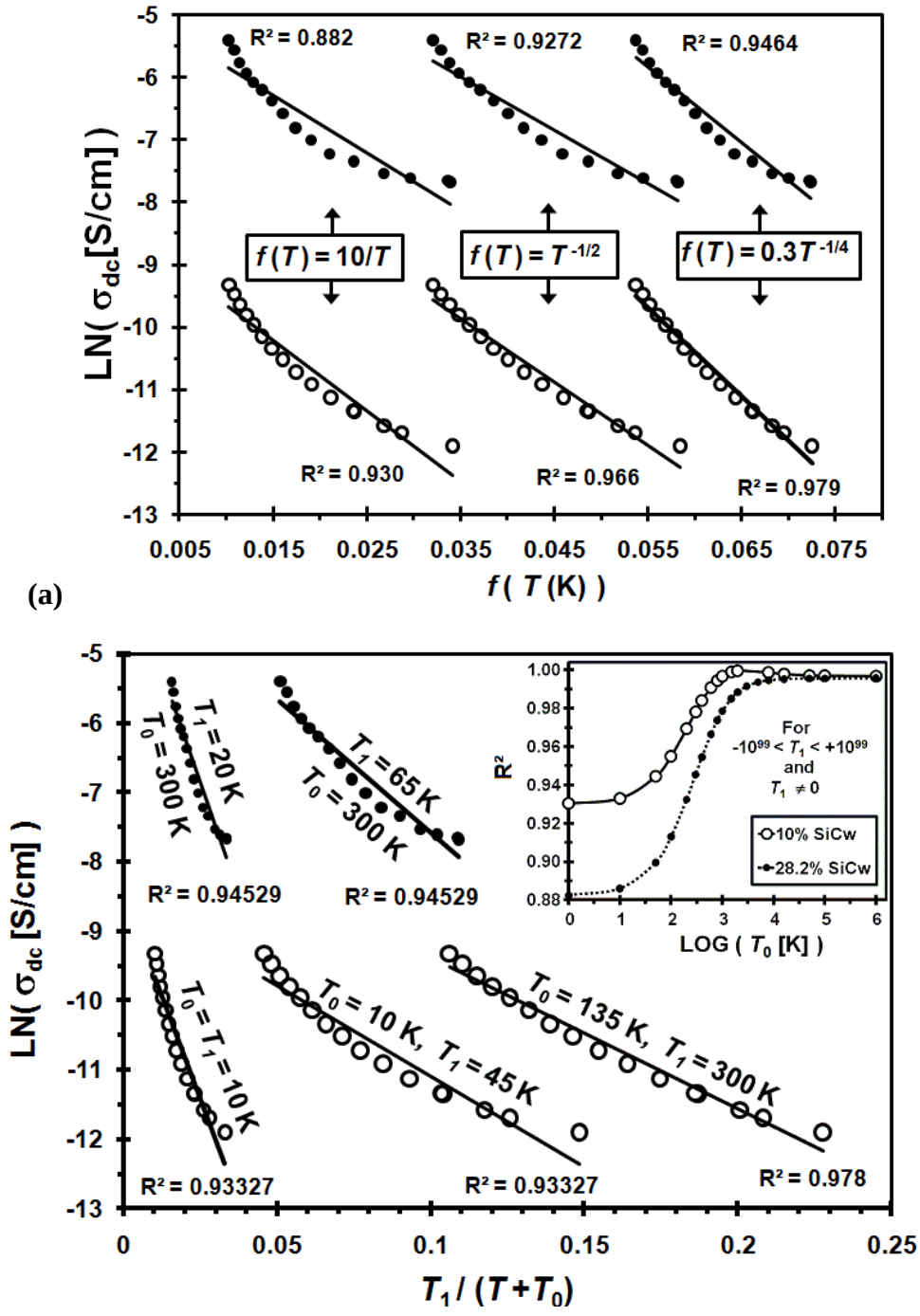

Figure 7.4. Fitting of various models to the temperature dependence of σ_{dc} for the same two data sets, i.e., for 10% SiC_w and 28.2% SiC_w samples. These data are represented by open and filled circles, respectively. Lines are the linear regressions, and the quality of fit (R^2) is given next to each line.[23] In part (a), fits to hopping models are shown. The scaling factors of 10 and 0.3 were used for plotting convenience and did not affect R^2. In part (b), fits to the FITC model are shown for different values of T_0 and T_1, which are written alongside the fitting lines. The inset shows the effect of T_0 on R^2 for arbitrary $T_1 \neq 0$.

the hopping models for $h = 1$, ½, and ¼ are shown.

As h decreases, the quality of fit (i.e., the coefficient of determination from linear regression, R^2) increases. Since the 20-700°C range constitutes relatively high temperature, this result contradicts the prediction of larger values of h (i.e., $1 > h > ½$) for high-temperature VRH[185] and Mott's effective prediction of $h = 1$ for thermally activated NNH.[182] The fit of our data with the more commonly employed $h = 1/4$, which is expected to hold for low temperatures, results in the highest R^2 value, and the deviation from linearity is relatively great for the 28.2 % SiC_w sample compared to the 10.0% sample. In both cases, the failure to eliminate the concave-up curvature of the whole range of experimental data with respect to the straight line is not qualitatively different from the results of fitting with $h = 1$ and $h = 1/2$. Such misfit is regarded as failure of the models to predict the experimentally-observed functional form of the σ_{dc} versus T relationship, and thus, an indication that the models do not provide an appropriate description of the underlying physical situation. The associated non-random distributions of residual errors for these fits, which span limited ranges of conductivity (i.e., approximately one order of magnitude), are in sharp contrast to the tight fits of the VRH model to data from other systems spanning 3-4 orders of magnitude in conductivity and having apparently randomly-distributed residual errors.[181,187] Therefore the hopping models are regarded as inapplicable to this system and the fluctuation-induced tunneling model for conduction (FITC), which is more well-established in its application to insulator-conductor composites,[92,94,178,187,190,191] is considered.

The $1/d_{avg} \propto p^{1/3}$ trends noted in Section 4.3.1.2.2 suggest that FITC theory might be applicable. The data is in reasonably good agreement with $-\log(\sigma_{dc}) \propto p^{-1/3}$; R^2 was

0.954 (0.996) and 0.934 (0.972) for the conduction along the HPD and perpendicular directions (if the 7.7 vol% data is excluded), respectively. Notably, the difference in the average interwhisker distance along the two principal directions of the axisymmetric microstructure was exponentially related to the difference in dc conductivity (Section 4.3.2.2). This is a correlation between the *magnitudes* of structural and electrical anisotropy and, at first glance, may seem to be agreeable with the FITC theory. However, the notion of tunneling controlling the conductivity seems to contradict the finding that the average dc conductivity and average interwhisker distance were both smaller along the hot-pressing direction compared to the perpendicular direction. In other words, the sign of the orientation-based difference in distance was the opposite of what one would expect if FITC was the operable mechanism.

In regards to the temperature dependence, which is the key prediction of FITC, it is appropriate to ask: what are the constraints on the fitting parameters T_0 and T_1 for the model to be meaningful? Considering Relation 7.3, it is clear that in the limit of $T_0 \rightarrow 0$ K the functional form is not meaningfully different from Arrhenius thermal activation, i.e., where $T_1 = Q/k$. When fitting the data while holding T_0 at an arbitrary fixed value greater than zero, it was found that the value of T_1 had *absolutely no bearing* on the quality of $\ln(\sigma_{dc})$ versus $T_1/(T + T_0)$ fits; in other words, T_1 could be varied from negative to positive infinity without any effect on R^2. Two examples of this are demonstrated in Figure 7.4b, which shows fits of the same σ_{dc}-T experimental data plotted in Figure 7.4a to the FITC model; it can be seen that the use of different values of T_1 with $T_0 = 10$ K and T_0=300 K for the data from 10% and 28.2% SiC_w samples (respectively) does not affect R^2. This indicates that, at least in the context of our system, T_1 is not a physically

significant fitting parameter; clearly, the interpretation of T_1 in terms of the energy required to cross the insulating gaps does not hold true here.

The inset of Figure 7.4b shows the effect of T_0, the other FITC fitting parameter, on the goodness of fits for arbitrarily-valued $T_1 \neq 0$ K. After starting with $T_0 = 1$ K and increasing its value until the fit to Relation 7.3 became "good," e.g., at an arbitrarily-defined value of R^2 such as R^2=0.99, it was found that good fitting was maintained even if the increase of T_0 was continued up to enormous (e.g., $T_0 = 10^6$ K) values. This lack of uniqueness means that T_0 is not a meaningful physical parameter for the conduction process in this composite system.

Based on the observed lack of uniqueness for the T_0 and T_1 fitting parameters, the FITC model is deemed inapplicable to the Al_2O_3-SiC_w system and other investigators are encouraged to perform and report the results of similar T_0 and T_1 uniqueness analyses when applying the FITC model to their data. In particular, caution is urged to those using relatively large values of T_0. Some authors, including the leading developer of the FITC model,[178] recently noted and worked towards correcting its deficiency in terms of the seemingly-unphysical predicted values for energy-barrier widths and heights.[190] Similar uniqueness findings from other investigators would create the need for an address of this issue as well, or a new modeling approach.

Altogether, it is not really surprising that the temperature dependencies of the hopping and FITC models do not describe conduction in this system because these are rooted in the idea of quantum mechanical tunneling. In consideration of tunneling, the crystalline lattices of discrete SiC whiskers may be regarded as potential wells which are filled with relatively free carriers and separated by finite energy barriers corresponding to

insulating gaps of the matrix. Tunneling between two such wells implies an electron wave function continuously bridging the gap between them, and the wave function within the gap is expected to decay exponentially with distance just outside the wells. Experimentally, the maximum distance for which tunneling produces a measurable current has been observed to be a few nanometers.[192,193]

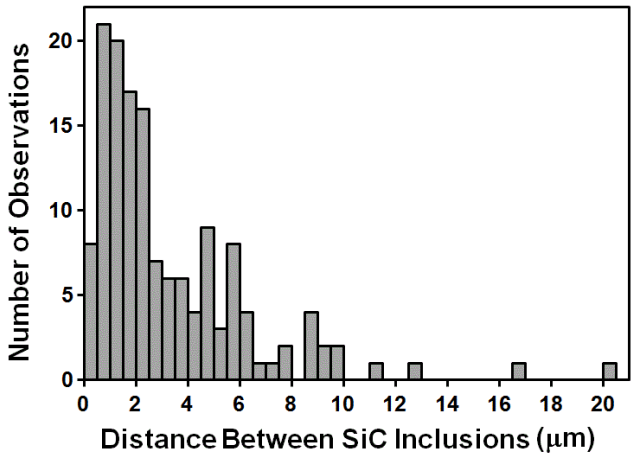

Figure 7.5. The stereologically-measured distribution of distances between SiC inclusions along the hot-pressing direction of a 10.0% SiC_w sample.[23] The bin width is 0.5 μm.

In contrast, the mean-average distances between the SiC inclusions along the two principal directions of this material were measured by stereology to be >1 μm (see Figure 4.9) which suggests that the average whisker-to-whisker nearest neighbor distance is not much less than ~1 μm. The measured distribution of distances along the hot-pressing direction for a 10% SiC_w sample is shown in Figure 7.5; the lognormal shape was typical for all compositions. In this distribution, the minimum observed distance was 0.3 μm, and only 5.5% of observed distances were ≤ 0.5 μm. For a 28.2% SiC_w sample, the minimum observed distance was 0.1 μm, and only 3.2% of observed distances were ≤ 0.2 μm. The transmission coefficient for tunneling across such distances should be

negligibly small, especially since the barrier height relates to the wide bandgap of alumina. Moreover, correlations to dc conductivity were found with the average distances (not the minimum distances) in the inset of Figure 4.11a.

7.3.2. Temperature Dependencies and Relation of Conduction and Switching

Since the FITC and hopping models are incongruent with the observed temperature dependence of conductivity and the relatively large distances between conductive particles in these composites, we now consider relatively long-range electrical transport through oxide-insulator films by the phenomena known as dielectric breakdown and thermal switching.[194] For these, different types of relationships between temperature and conductivity have been observed experimentally. For example, they may depend on temperature by way of an Arrhenius law or by

$$\sigma_{dc} \propto \exp(aT) \qquad (7.4)$$

where a is a positively-valued constant.[26,194]

Figure 7.6 shows the temperature dependence of all eight percolated compositions, and the good straight-line fits indicate agreement with Relation 7.4. For this set of fits, the average quality of fit was $R^2 = 0.995 \pm 0.004$, which is significantly better than that yielded by modeling based on hopping or FITC with "reasonable" values of T_0. The slope did not vary much with whisker loading and $a = (3.68 \pm 0.25) \times 10^{-3}$ K^{-1} on average. Such good fitting to Relation 7.4 means that $\ln(\sigma_{dc})$ is a linear function of T, and this explains why fits to the FITC model were good when T_0 was very large. As T_0 increases, the function $f(T) = -T_1/(T+T_0)$ appears increasingly linear *for a given range of*

T, and it follows that plots of $\ln(\sigma_{dc})$ versus $T_1/(T+T_0)$ appear increasingly linear as well. Therefore, in this system, the minimum value of T_0 required to achieve a given value of R^2 for fitting to Relation 7.3 is actually a function of the measured temperature range.

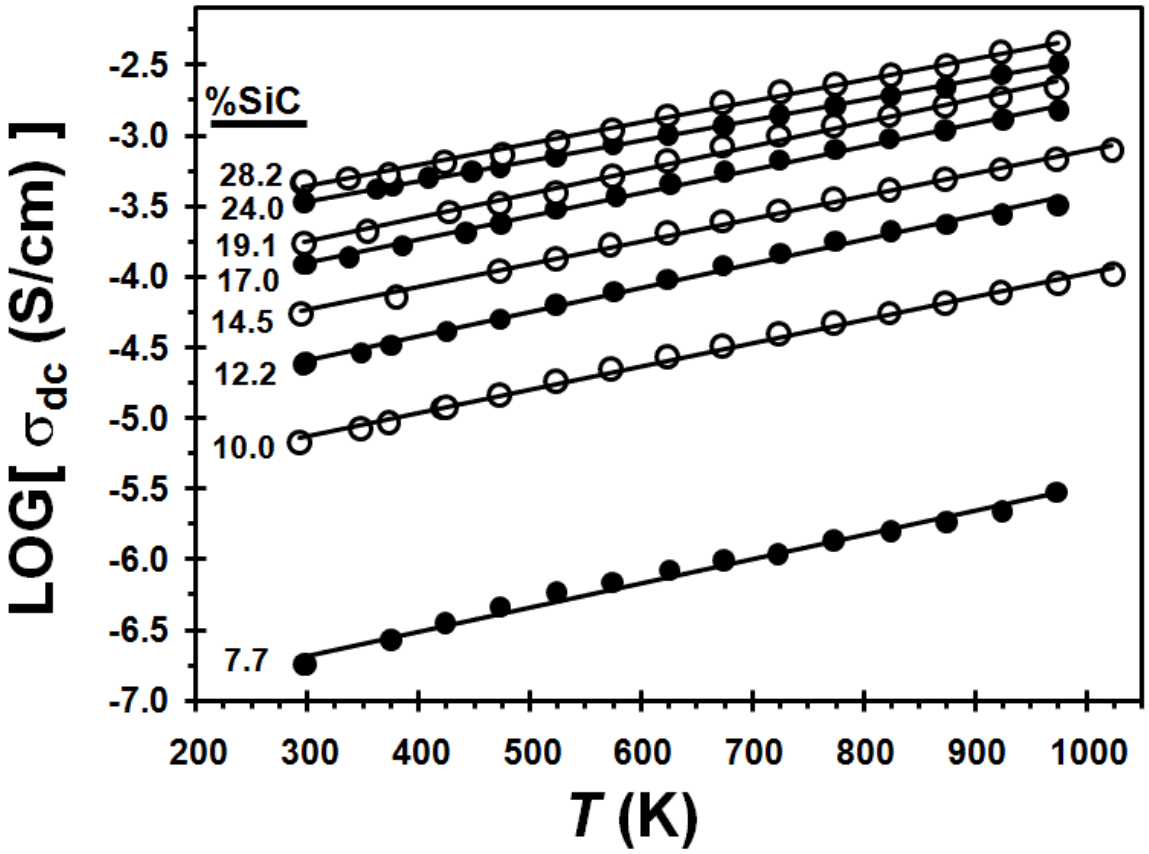

Figure 7.6. Dependence of dc conductivity on temperature for SiC_w-percolated composites.[23] The SiC_w loading associated with each data set is written on the left in terms of volume percent. The straight lines represent fits to Relation 7.4.

To my knowledge, dielectric breakdown is the only process associated with the temperature dependence of conductivity described in Relation 7.4, which was used to describe electrical conduction in thin SiO_2 films[26] having a relative dielectric constant (ε_r') ranging from 3 to 7. The latter value is rather high compared to the expected value[102] of 3.9 for SiO_2, and suggests additional polarization from microstructural features which

are not intrinsic to SiO_2. Similarly, ε_r' for the Al_2O_3 –based matrix material was ~10.6 at room temperature and significantly exceeded the expected value[102] of ~8.5 for pure Al_2O_3, even at low temperature; this is apparent in Figure 7.7. Therefore the possibility that electrical transport in the composites is controlled by a process in the oxide matrix which is in some way similar to dielectric breakdown is now considered.

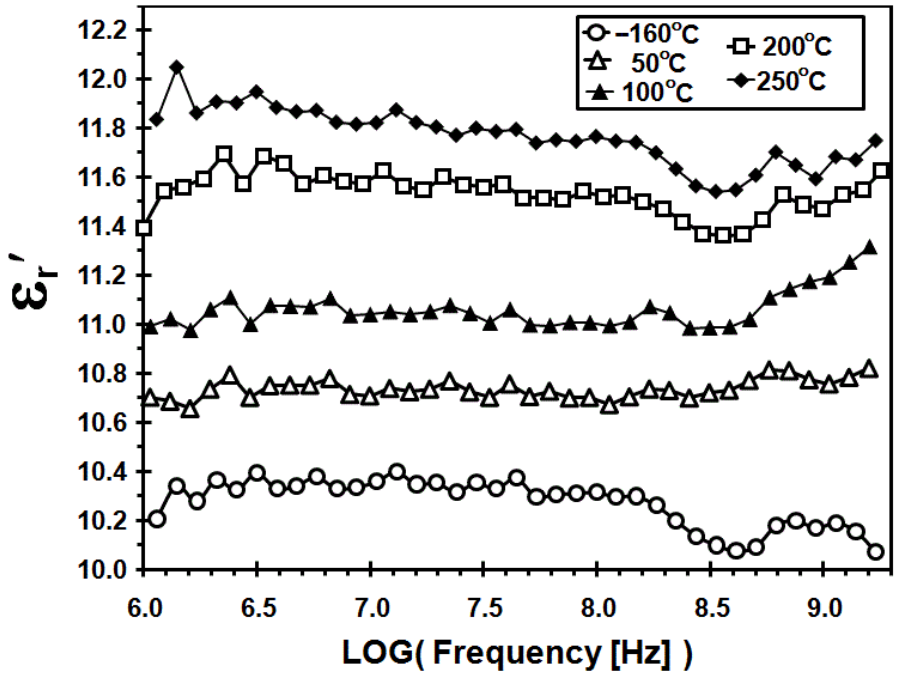

Figure 7.7. Effect of temperature on the frequency dispersion of the dielectric constant for a 0% sample, i.e., a sample of the matrix without any SiC inclusions.[23]

In the conventional description, dielectric breakdown is the passage of a measurable current through an insulator which occurs upon the application of a sufficiently strong critical electric field, i.e., the dielectric strength. This field is regarded as being intrinsic to a given insulator material and the breakdown process itself is thought to significantly and irreversibly damage the material and change the electrical response.

This viewpoint is contradictory to our experimental results which exhibited a high degree of reversibility. The σ_{dc} of samples at fixed temperature was very reproducible and was not significantly altered by heating runs up to 700°C; after such runs, σ_{dc} at room temperature was typically increased by ≤ 5%.

However, there is a growing body of evidence supporting an alternative view of breakdown. In this view, breakdown is a reversible switching process from a low-conductivity state to a high-conductivity state[195-197] and conduction occurs via traps at defects in the insulator.[25] The irreversible thermal damage which is commonly associated with breakdown is the result of the very large currents resulting from the conductivity increase and can be decoupled from the switching process by externally limiting the current.[195] The general tendency of the breakdown field to decrease with increasing ambient temperature[198] suggests that the breakdown process may be thermally induced and has been called thermal switching.[194] The notion of conduction through the composite occurring by such a mechanism, i.e., by a trap- and thermally-assisted switching process, gains support from high-frequency permittivity data.

Figure 7.8 shows the increase of the frequency-dependent dielectric constant (ε_r') and dielectric loss (ε_r'') with temperature for a 10% SiC_w sample; the behavior of other compositions was qualitatively similar. Sometimes, resonances or relaxations were observed, but these are not shown or considered until Section 7.3.4. In Figure 7.8, the increase of the magnitude of the loss spectra with increasing temperature is attributed to dc conductivity. This interpretation is consistent with the fact that the rate of loss increase with temperature (i.e., $d\varepsilon_r''/dT$) increased with whisker content and decreased with increasing frequency, as shown in Figure 7.9; the contribution of dc conductivity to the

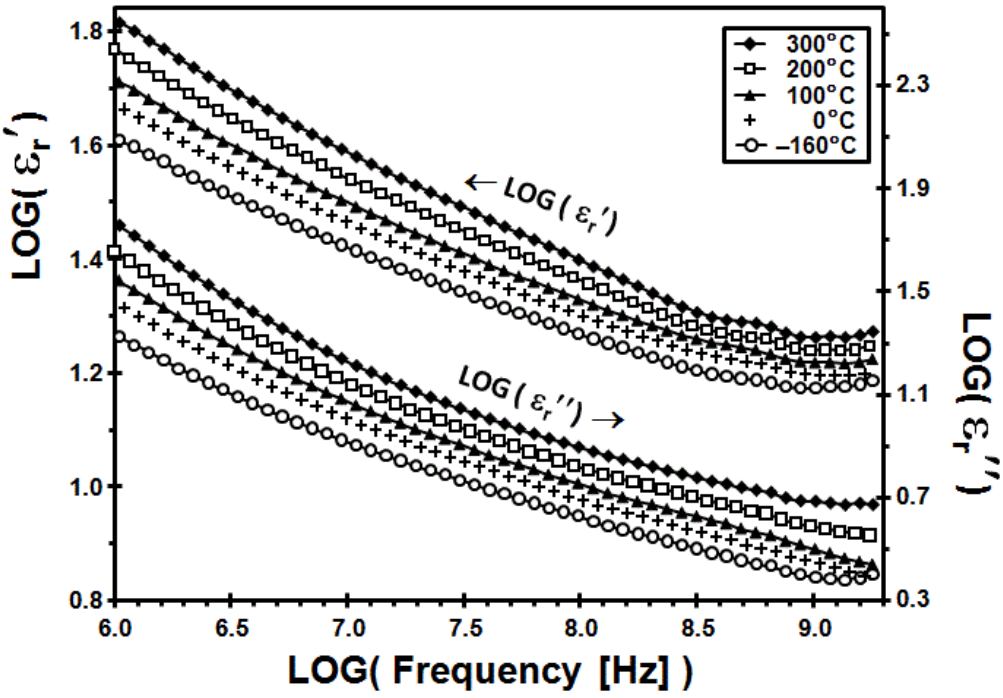

Figure 7.8. The effect of temperature on the frequency dispersion of the complex dielectric constant for a 10.0% SiC_w sample. The real and imaginary parts relate to the left and right axes, respectively.[23]

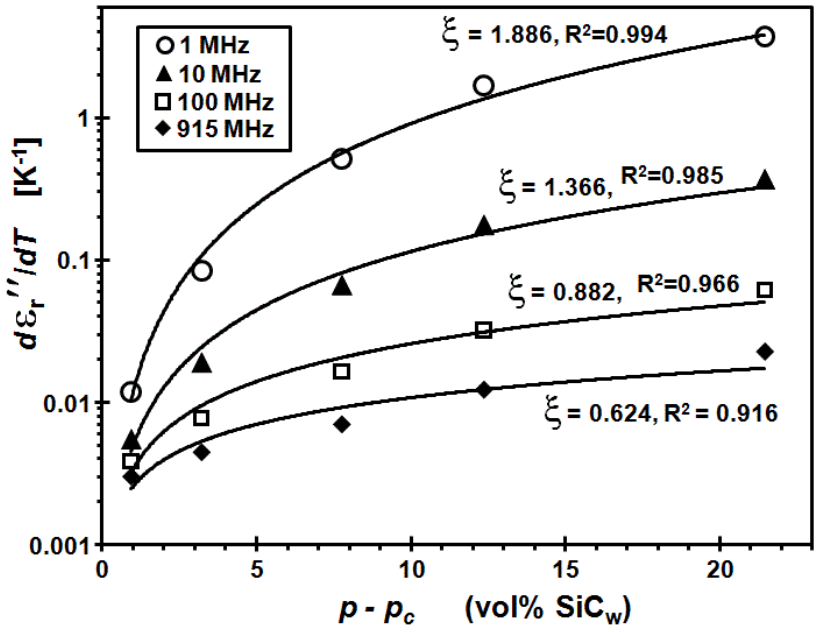

Figure 7.9. Effects of composition on the linearly-approximated temperature-rate-of-change of the dielectric loss at fixed frequency. The curved lines represent fits to the power law $(d\varepsilon_r''/dT) \propto (p\text{-}p_c)^{\xi}$, and the exponent and R^2 value are given next to each curve.[23]

loss spectra is expected to vary inversely with frequency (see Chapter 6). At low frequencies (e.g., 1 Hz), ε_r'' increased exponentially with temperature (not shown), as expected from Relation 7.4. At frequencies ≥ 1 MHz, linear fitting approximations to $\varepsilon_r'' \propto T$ were acceptable ($R^2 \geq 0.94$), and R^2 increased with increasing frequency. The slopes of these fits were then found to be well-described by power laws of the form $(d\varepsilon_r''/dT) \propto (p-p_c)^{\xi}$, where ξ is a constant. Since dc conductivity similarly scales with composition[94] as $\sigma_{dc} \propto (p-p_c)^{t}$, this affirms the close relation of $d\varepsilon_r''/dT$ to the dc conductivity and is a consequence of the relatively composition-independent temperature dependence of dc conductivity, i.e., the value of *a* in Relation 7.4.

In Figure 7.8, the trend of the dielectric constant increasing with temperature is likely related to the matrix having a positive temperature coefficient of permittivity (Γ), as demonstrated in Figure 7.7. From such data, it was found that $\Gamma = 310$ ppm K^{-1} for the matrix, where $\Gamma = (d\varepsilon_r'/dT)/\varepsilon_{r0}'$ and ε_{r0}' is the dielectric constant at 0°C. In Figure 7.8, the linear character of the $\log(\varepsilon_r') \propto \log(f)$ data between 1-250 MHz is suggestive of the universality[125] relation commonly observed for heterogeneous materials,[125]

$$\varepsilon_r' \propto f^{-y}, \tag{7.5}$$

where *y* is a constant between 0 and 1, and f is the frequency. It can be seen that the gaps between the curves are greater at low frequency compared to at high frequency, thereby indicating that *y*, the slope, increased with temperature. The value of *y* and its dependence on temperature in the $-160 \leq T \leq 300$°C range was measured for multiple samples of the SiC_w-percolated compositions in the power-law regimes. It was found that the $y \propto T$

relationship was linear with $0.96 \leq R^2 \leq 0.999$ for the various samples, and the averaged results are summarized in Table 7.1 in the form of

$$y = m_L T + y_0 \tag{7.6}$$

where $m_L = dy/dT$ and y_0 is the value of y at 0°C. In Table 7.1, it can be seen that y increased with both composition and temperature for all of the percolated samples. This is shown another way in Figure 7.10, which allows comparison of the relationship between dc conductivity and y which results from increasing composition and the σ_{dc}-y relationships which result from increasing temperature. It can be seen that the trending in the data is similar for both compositional and temperature changes. This suggests that we may regard y as primarily a function of dc conductivity, and σ_{dc} as a function of composition and temperature. To interpret this result, the physical significance of y and the power law of Relation 7.5 are considered.

Relation 7.5 can be reproduced with and interpreted in terms of a modeling approach based on electrical networks of resistors of resistance (R) and capacitors of capacitance (C) in random configurations (Figure 1.18).[12,91] For such networks, the so-called "emergent" frequency range where this power law holds (Figures 1.19a and 1.19b) was found to coincide with the range where the ac conductance of the individual capacitors ($2\pi f C$) is approximately equal to that of the individual resistors ($1/R$). At this condition, the network response is relatively independent of the network configuration.[12] The composite results of large numbers of random configurations suggest that y represents the fraction of resistors and (1-y) represents the fraction of capacitors.[12,91]

Table 7.1. Results of fitting the temperature dependence of the power-law exponent y from Relation 7.5 associated with the given frequency ranges to Equation 7.6 and to $y \propto \exp(m_E T)$.

p (%)	m_L (10^{-5} K^{-1})	y_0	m_E (10^{-4} K^{-1})	Frequency Range (MHz)
7.68	4.86 ± 0.84	0.124 ± 0.003	3.82 ± 0.66	1 - 250
9.96	8.56 ± 0.23	0.180 ± 0.004	4.60 ± 0.22	1 - 250
14.5	6.44 ± 0.04	0.206 ± 0.002	3.071 ± 0.005	1 - 250
14.5	9.05 ± 0.08	0.199 ± 0.002	4.41 ± 0.08	2.5 - 250
19.1	3.93 ± 0.83	0.230 ± 0.005	1.73 ± 0.40	2.5 - 250
19.1	8.88 ± 0.97	0.223 ± 0.007	3.88 ± 0.52	7.76 - 250
28.2	5.79 ± 1.99	0.232 ± 0.002	2.45 ± 0.85	7.76 - 250

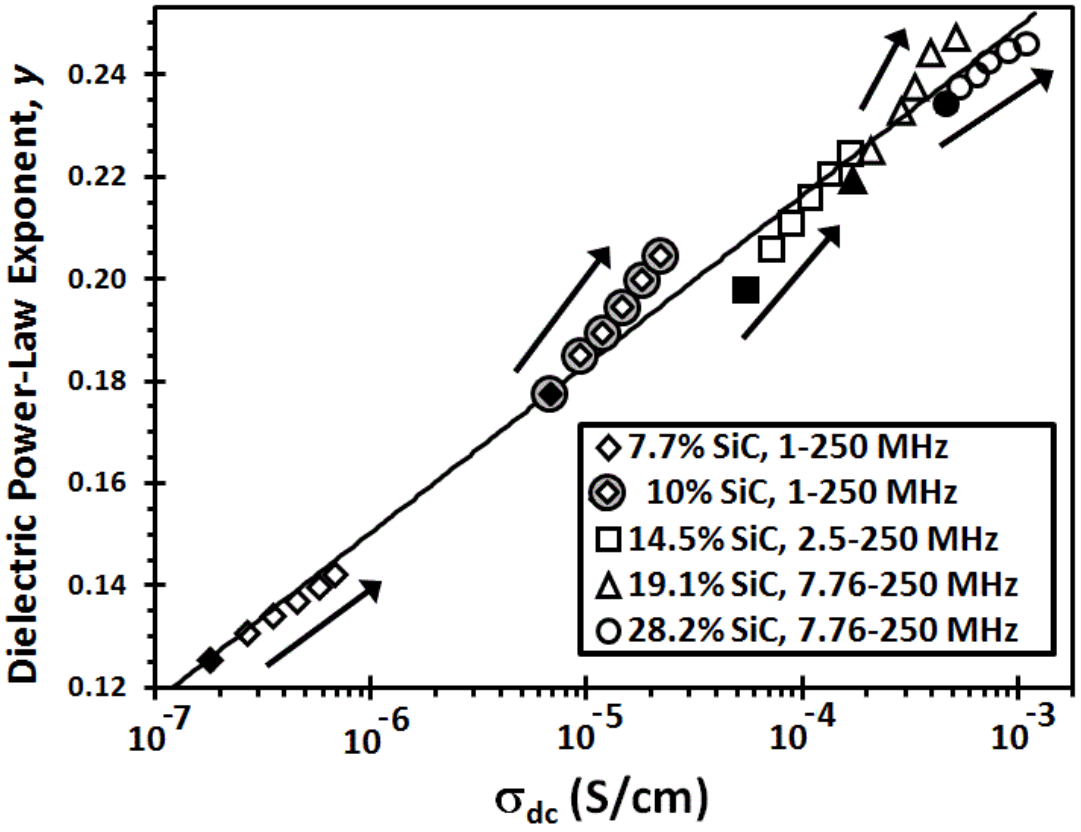

Figure 7.10. The relationship between the dc conductivity and the power-law exponent y for different amounts of SiC loading in the 20-300°C temperature range.[23] For each composition, the single filled symbol designates 20°C data, the arrow gives the direction of increasing temperature, and the legend gives the frequency range associated with y.

In interpreting our experimental data in the context of this model, one might take a phase-based view of the resistors and capacitors corresponding to SiC whiskers and regions of the matrix, respectively. Alternatively, one could view the network elements as relating to interwhisker junctions; like other material interfaces, these are likely to have mixed resistor-capacitor character, but they will be regarded as being primarily resistor-like (i.e., conductive) or capacitor-like (i.e., insulating) for the purpose of obtaining basic insight into a complex situation. In either viewpoint, for current to flow at dc, the resistors must percolate through the network. Then, the only ways of increasing the effective dc conductivity of the resistor-percolated network are by increasing the parallelism and decreasing the series character of the resistors forming the percolating cluster. For a network which is already resistor-percolated, both of these acts require replacing capacitors with resistors, and therefore they are tantamount to increasing *y*. By this line of logic, increasing dc conductivity is qualitatively linked to increasing *y*. The quantitative relationship will be considered later.

The experimental result of both *y* and σ_{dc} increasing with SiC_w loading seems agreeable with both the phase-based and the junction-based view of the network elements in the randomly configured resistor-capacitor network model. For the junction-based view, it is reasonable to imagine that the proportion of relatively conductive junctions increases with increasing SiC_w loading.[110] By contrast, the experimental result of *y* and σ_{dc} increasing with temperature does not make sense in terms of the phase-based view; increasing temperature simply does not increase the quantity of SiC. Similarly, regarding intrawhisker conduction in terms of resistors and interwhisker interfaces as capacitors makes dc-conductivity percolation impossible. Given this, and the aforementioned

description of dielectric breakdown of oxides in terms of thermal switching between two states of different conductivity, the experimental result of y and σ_{dc} increasing with temperature is interpreted to mean that such a switching process occurred in the alumina-based matrix at the interwhisker junctions. In this interpretation, the low-conductivity and high-conductivity states related to dielectric breakdown are associated with capacitors and resistors in the randomly-configured RC network model. The lower-bound frequency of the power-law regime (given in Table 7.1) increased with SiC loading because the percolation of resistor-like junctions caused an increasing amount of departure from the power-law trend on the low-frequency side.[12]

7.3.3. Analysis of the Mathematical Forms Describing Conduction and Switching

The similarity of composition and temperature-related trending in Figure 7.10 is interpreted to mean that y is a function of dc conductivity, σ_{dc} depends on temperature and composition, and the effects of these variables on y are isolated within σ_{dc}. One mathematical form which fit the data while maintaining consistency with this interpretation was

$$\exp(y) = C(\sigma_{dc})^{\eta} \qquad (7.7)$$

where C and η are constants and σ_{dc} is entered in units of S/cm; specifically, C=1.416, η=0.014325, and R^2=0.987. This equation does not compute at the limit of σ_{dc}=0, but may be used to solve for the conductivity of a material having a frequency-independent dielectric constant, i.e., with $y = 0$. With our data, this yields $\sigma_{dc} = 2.8 \times 10^{-11}$ S/cm, in approximate agreement with the small but finite conductivity of the unfilled matrix.[20,21] An alternative relation was also considered,

$$y \propto (\sigma_{dc})^{\chi} \tag{7.8}$$

where χ is a constant. This implies that the conductivity must be zero to have a dielectric constant that is truly flat with frequency, and fitting the data in Figure 7.10 (not shown) yielded $\chi = 0.0782$ with a slightly lower quality of fit, $R^2 = 0.977$.

While Relation 7.8 may be appealing from a theoretical standpoint, Equation 7.7 seems to be more experimentally useful and offer slightly better empirical performance. Separate fits to Equation 7.7 based on the composition dependencies at six fixed temperatures in the $20 \leq T \leq 300$°C range yielded $\eta = (1.42 \pm 0.04) \times 10^{-2}$ with $R^2 = 0.990 \pm 0.010$ on average; Relation 7.8 yielded $\chi = (7.77 \pm 0.10) \times 10^{-2}$ with $R^2 = 0.978 \pm 0.010$ on average. Separate fits to Equation 7.7 based on the temperature dependencies at the five percolated compositions (i.e., 7.7, 10.0, 14.5, 19.1, and 28.2 % SiC_w) yielded $\eta = (1.98 \pm 0.64) \times 10^{-2}$ with $R^2 = 0.988 \pm 0.013$ on average; Relation 7.8 yielded $\chi = (9.95 \pm 2.64) \times 10^{-2}$ with $R^2 = 0.987 \pm 0.014$ on average.

Since $\sigma_{dc} \propto \exp(aT)$ was shown earlier and $\sigma_{dc} \propto (p\text{-}p_c)^t$ is well-known (Relation 1.10), Equation 7.7 implies

$$\exp(y) \propto [\,(p - p_c)^t \exp(aT)\,]^{\eta} \tag{7.9}$$

where p is the volume fraction of filler, p_c is the percolation threshold, and t is a constant, whereas Relation 7.8 implies

$$y \propto [\,(p - p_c)^t \exp(aT)\,]^{\chi} \tag{7.10}$$

if η and χ are independent of composition and temperature. Relation 7.9 may be rewritten as

$$y \propto \eta[\, t \ln(p - p_c) + aT \,] \qquad (7.11)$$

which suggests that plots of $y \propto \ln(p - p_c)$ and $y \propto T$ should be linear and yield slopes of ηt and ηa, respectively. At the six temperatures, separate linear fits to $y \propto \ln(p - p_c)$ yielded $\eta t = (3.44 \pm 0.03) \times 10^{-2}$ with $R^2 = 0.97 \pm 0.02$ on average, and the variation of ηt with temperature was random, as predicted by Relation 7.10. The value of $\eta = 0.014325$ from the mixed composition-temperature fit of Figure 7.10 then implies $t = 2.405$, which agrees well with fits of conductivity data to $\sigma_{dc} \propto (p - p_c)^{t}$; with $p_c = 0.06745$, these yielded $t = 2.44 \pm 0.05$ with $R^2 = 0.991 \pm 0.001$ on average and indicated that t did not change systematically with temperature. Alternatively fitting the data to $\ln(y) \propto \ln(p-p_c)$ based on the expectation of

$$\ln(y) \propto \chi[\, t \ln(p-p_c) + aT \,] \qquad (7.12)$$

which follows from Relations 7.10 and 7.8 yielded a slope $\chi t = 0.187 \pm 0.007$ with $R^2 = 0.94 \pm 0.02$ on average. Significantly, the value of χt resulting from these fits decreased monotonically by 10.4% as temperature increased from 20 to 300°C. As this contradicts the expectation from Relation 7.12 of a temperature-independent slope, it may be that χ as defined is *not* temperature independent, and that Relations 7.7, 7.9, and 7.11 give a slightly better description of the data compared to Relations 7.8, 7.10, and 7.12.

At the five percolated compositions, linear fits to $y \propto T$ yielded the slopes (m_L) given in Table 7.1, which have an average value of $(6.79 \pm 2.07) \times 10^{-5}\ K^{-1}$. This has good

correspondence to the result of $\eta a = 5.27 \times 10^{-5}\ K^{-1}$, which is based on Relation 7.11, $a = (3.68 \pm 0.25) \times 10^{-3}\ K^{-1}$ from fits of conductivity data to $\sigma_{dc} \propto \exp(aT)$ at the different compositions, and η=0.014325 from the fit of Figure 7.10. Fits of the data from the various samples to $y \propto \exp(m_E T)$ based on Relation 7.12 yielded the values of m_E in Table 7.1 and $m_E = (3.42 \pm 1.05) \times 10^{-4}\ K^{-1}$ on average. This agrees with the result of $\chi a = 2.88 \times 10^{-4}\ K^{-1}$ calculated from the values of a and χ determined via fitting the data in Figures 7.6 and 7.10, respectively.

Table 7.2 gives a summary of the aforementioned analyses of the experimental data. These indicate that Relations 7.7, 7.9, and 7.11 accurately describe the effects of filler loading and temperature on the frequency dependence of the electrical response in the power law regime in a manner which is self-consistent with various perspectives on the multi-parameter dataset. This means that the initial assumption holds up under scrutiny, i.e., that the frequency dependence in the power-law regime depends directly on the dc conductivity and only indirectly on composition and temperature. The parameter η is a temperature- and composition-independent property of the matrix/percolated-filler composite system. According to the random-network interpretation of Relation 7.5, the value of $1/\eta$ gives a measure of how much the switching character of the interfiller junctions throughout the entire composite affects the structure of the percolated cluster and its dc response. Relations 7.8, 7.10, and 7.12 perform similarly, but it should be noted that the fits tend to be slightly worse and χ seems to have the undesirable quality of being (weakly) dependent on temperature. However, in this functional form, one may view the high-conductivity junctions as a population which grows exponentially with temperature;

Table 7.2. Summary of fitting results pertaining to the discussion of Section 7.3.3.

Relation {Number}	**Type of Fit**	**Results**	**R^2**
$\sigma \propto (p - p_c)^t$ {1.10)	varying p at separate fixed T	$t = 2.44 \pm 0.05$	0.995 ± 0.004
$\sigma_{dc} \propto \exp(aT)$ {7.4)	varying T at separate fixed p	$a = (3.68 \pm 0.25)\, x10^{-3}\ K^{-1}$	0.991 ± 0.001
$\exp(y) = C(\sigma_{dc})^{\eta}$ {7.7)	varying T, varying p	$\eta = 0.014325$, $C = 1.416$ with S/cm units for σ_{dc}	0.987
{7.7)	varying p at separate fixed T	$\eta = (1.42 \pm 0.04)\, x10^{-2}$	0.990 ± 0.010
{7.7)	varying T at separate fixed p	$\eta = (1.98 \pm 0.64)\, x10^{-2}$	0.988 ± 0.013
$y \propto (\sigma_{dc})^{\chi}$ {7.8}	varying T, varying p	$\chi = 0.0782$	0.977
{7.8}	varying p at separate fixed T	$\chi = (7.77 \pm 0.10)\, x10^{-2}$	0.978 ± 0.010
{7.8}	varying T at separate fixed p	$\chi = (9.95 \pm 2.64)\, x10^{-2}$	0.987 ± 0.014
$y \propto \eta[\, t \ln(p - p_c) + aT\,]$ {7.11}	$y \propto \ln(p - p_c)$, at separate fixed T	$\eta t = 3.44 \pm 0.03 \rightarrow t = 2.405$; $\eta t - 0.034 = 6.7\ x\ 10^{-7}\ T/°C$	0.97 ± 0.02 ; 0.04
{7.11}	$y = m_L T + y_0$ at separate fixed p	$m_L = 6.79 \pm 2.07\ x10^{-5}\ K^{-1} \approx$ $\eta a = (0.0142)\ (0.00368\ K^{-1})$	N/A
$\ln(y) \propto \chi[\, t \ln(p - p_c) + aT\,]$ {7.12}	$\ln(y) \propto \ln(p - p_c)$, at separate fixed T	$\chi t = 0.187 \pm 0.007$; $\chi t - 0.198 = -6.3x10^{-5}\ T/°C$	0.94 ± 0.02 ; 0.94
{7.12}	$y \propto \exp(m_E T)$, at separate fixed p	$m_E = 3.42 \pm 1.05\ x10^{-4}\ K^{-1} \approx$ $\chi a = (0.0782)\ (0.00368\ K^{-1})$	N/A

the notion of the widely-observed phenomenon of exponential population growth as being the source of the unusual temperature dependence of dc conductivity makes Relation 7.4 more palatable. Indeed, this form may break down at the limit of $T \rightarrow 0$, where it implies $\sigma_{dc} \neq 0$.

In attempting to rationalize this form, another conjecture which involves several assumptions is considered. The energy for the conduction should be entirely thermal in origin, and the Stefan-Boltzmann law for blackbody radiation, which states that the power flux emitted from the surface of a material increases proportionally with T^4, is invoked. Small partitions of the volume within the bulk of the sample can also be expected to radiate thermally when $T > 0$, and since the composite is an excellent absorber with a high degree of dielectric loss from dc conductivity, it is assumed that some of the electromagnetic waves emitted internally are reabsorbed and converted into electrical currents in various branches of the percolated network before reaching the surface. It is additionally assumed that the volumetric power density of the resulting currents is proportional to the power flux of the thermal radiation, and therefore, to T^4. Further assuming that the current *densities* in the *power-dissipating* branches of the network remain temperature-independent implies that the electric fields (E) associated with the currents scales with T^4. *Having fixed current densities in the active branches implies that the only way to increase the total current through a sample (and thus, its conductivity) is by making more of them, i.e., by 'switching open' branches which were formerly closed and did not pass any current.* The idea of internal fields rapidly increasing with temperature and switching open new current paths seems agreeable with a breakdown-like process for the switching mechanism. Additionally, it is assumed that the composites behave according to the Poole-Frenkel model for trap-assisted conductivity,[199] $\sigma_{dc} \propto \exp(\nu E^{1/2}/kT)$ where ν is a constant, and the electric field E corresponds to the thermally-stimulated internal fields. Finally, insertion of $E \propto T^4$ into this model yields the empirically observed result of $\sigma_{dc} \propto \exp(aT)$.

7.3.4. Evidence of Charge Trapping and Detrapping

Observations suggestive of charge trapping and detrapping in the of Al_2O_3-SiC_w composites were made during high-frequency electrical measurements and scanning electron microscopy, and are agreeable with a breakdown-like trap-assisted switching mechanism of conductivity. Recent studies suggest that breakdown depends on the trapping and release of charges at defects in the insulator and the energetics of the mechanically strained host lattice accommodating the charges.[25,195] Such a dependence on defects suggests that breakdown is a stochastic process dependent on the probability of finding a defect in a given volume of the material. This notion seems agreeable with observations of the critical breakdown field of insulators generally decreasing with increasing sample thickness[198] and the finding that the room-temperature conductivity of Al_2O_3-SiC_w composites was greater along the microstructural direction having greater interparticle distances (see Figures 4.9 and 4.11a). Unfortunately, the specific nature of the trapping defects controlling the conduction process and the considerations which determine the relative significance of different types of traps is not yet clear for general insulators.

For the breakdown of polycrystalline alumina, the results of one study indicated that impurities give rise to the traps of primary importance.[101] Adding a small amount of impurities (e.g., 0.0675% MgO or 0.1% SiO_2) to pure samples or increasing the level of sintering additives caused significant decreases in the critical breakdown field,[101] which is tantamount to facilitating breakdown conduction. Also, the behavior of the commercial sintering-aided sample having a greater impurity concentration was suggestive of a

greater quantity of trapped charges and premature breakdown.[101] Thus, increasing the level of impurity traps in alumina increased the propensity for breakdown-like switching.

In the same study, increases in alumina grain size (i.e., reductions in the grain-boundary density) were associated with a decreasing or statistically-unchanged critical field[101] for relatively impure and pure samples, respectively. This result suggests that breakdown conductivity and the relevant trap activity depends on the distribution of impurities to alumina surfaces but not the surface states associated with pure alumina-grain boundaries. However, it does not conclusively elucidate the microstructural location of the relevant impurity-related traps, i.e., whether they reside within the bulk of grains or are segregated along the grain boundaries. In polycrystalline ceramics, injected electrons may be trapped at both locations.[25] The preeminence of the former type is agreeable with the reasonable proposition that the propensity for breakdown processes increases with the probability of finding a defect in a grain because this increases with grain size for a fixed volume concentration of defects. The latter type implies conduction along the grain boundaries, and in consideration of this, it is reasonable to assume that a given amount of impurity would result in an increased concentration of traps at the alumina grain-boundary surfaces when the grain-boundary density is small. This could increase the propensity for breakdown due to the relevant concentration of traps being large. The notion of the relevant trap activity depending on the chemical environment of the matrix-grain surfaces seems agreeable with the coincidence of very different internal surfaces and behavior for the pressureless-sintered composites. For these, the response is non-linear and pore surfaces within the bulk have interfaces with ambient gas rather than adjacent solid surfaces.

In the experiments of this Chapter, charging and discharging of traps in the insulating and mostly-alumina matrix material are believed to have given rise to dielectric resonances and relaxations which were observed for many samples. Insulators which can store a surplus of electric charges for an extended period of time are known as electrets,[198,200] electrets of alumina have been observed,[201] and electrets of polymer insulators containing charged traps have exhibited dielectric resonances and piezoelectric behavior.[200,202] In insulators, charge detrapping and breakdown have been correlated to dielectric relaxation.[24,203] In the hot-pressed Al_2O_3-SiC_w samples, the traps are suspected to relate to impurities from the oxide sintering additives,[21] and resonances and relaxations were commonly but not always observed. The likelihood of observing resonances and their prominence in the spectra seemed to be greater for measurements done at low temperatures (i.e., $-160 \leq T \leq -50$ °C), especially when these immediately followed measurements at relatively high temperature. Dielectric relaxations were observed only at higher temperatures, i.e., $225 \leq T \leq 300$ °C. Figures 7.11 and 7.12 show examples of this and suggest that charges may be "frozen" inside or thermally released from the composite matrix by trapping and detrapping, respectively. Thus, it seems that the composites behave as thermoelectrets, i.e., electrets which have increased charging and discharging rates when temperature is high[198,204] and therefore depend on the thermal-electrical history of the sample.

The larger part of Figure 7.11 shows permittivity spectra from a sample of the unfilled matrix material at three sequential temperatures. After measuring at 275°C (not shown) and then immediately cooling to -160°C, measurement revealed a strong resonance, and subsequent heating to -50°C weakened the resonance observed upon re-

measurement due to the "freeze in" effect. At room temperature, no resonance was observed and this is attributed to thermally-facilitated discharging.

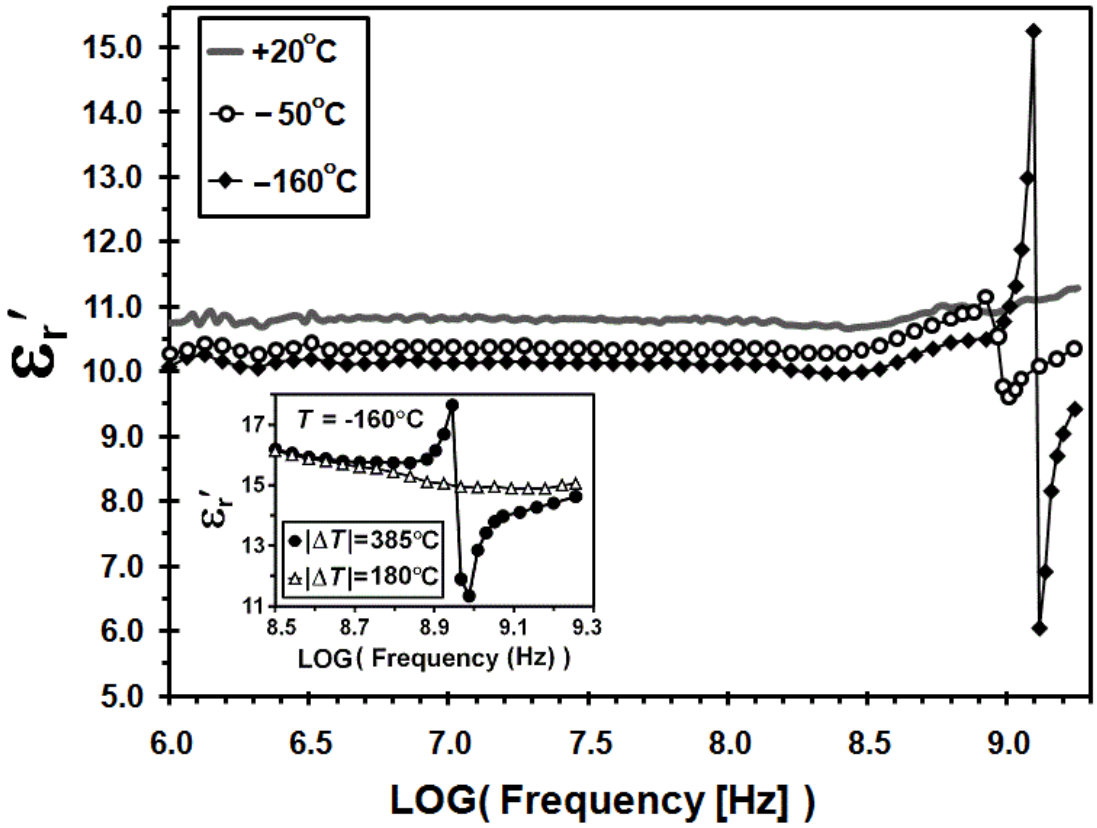

Figure 7.11. The effect of temperature on the dielectric resonance of a 0% sample, i.e., a sample of unloaded matrix. The data were taken after measuring at and cooling from 275°C (not shown) to -160°C, and sequentially heating to -50°C and 20°C. The inset shows dielectric-constant spectra of a 10.0% SiC_w sample measured at T = -160°C after measuring at and cooling from temperatures given by (-160°C+ΔT), where ΔT is given in the legend.[23]

The inset of Figure 7.11 shows data from a 10% SiC_w sample which was measured at 225°C (not shown) and then immediately cooled to -160°C, where subsequent measurement revealed a resonance. During the same automated-Novocontrol experiment schedule, measuring at room temperature (not shown) and then subsequently

re-measuring after cooling to -160°C did not produce a detectable resonance. This is attributed to the extent of trap charging being greater at 225°C compared to 22°C and the resulting concentration of "frozen in" excess charge upon cooling to -160°C being greater as well.

Figures 7.12a and 7.12b give examples of dielectric relaxations which are attributed to charge detrapping in the insulating matrix. In the former, the data is from a 0% sample at 300°C and shows the dielectric constant decreasing from ~12.6 to ~7.6. This is attributed to thermally-facilitated trap discharging, and the similarity of the latter value to the expected[102] value of ~8.5 for pure Al_2O_3 suggests that the source of the increased dielectric constant may be related to that of the trapping behavior. Figure 7.12b shows the occurrence of a similar relaxation for a sample containing 10% SiC_w, but it is not as prominent in the spectra because it is superimposed with the previously discussed dc-conductivity tail and power-law behavior of Relation 7.5.

The increased prominences of the resonance and relaxation for 0% SiC_w samples compared to the whiskered samples might be related to other factors as well. For example, the increased volume fraction of matrix material and the somewhat-higher charging temperature for the 0% samples imply a higher concentration of charged traps. Also, the grains of these samples are expected to have grown to larger sizes during hot pressing compared to samples containing SiC whiskers, which inhibit alumina grain growth.[59] As discussed above, increased alumina grain size seems to be associated with increased trap activity when impurities are involved, and combination of these two factors might explain the decrease in conductivity with increasing whisker content below the percolation threshold.[21] The lattices of the grains in the 0% sample are not

encumbered by mechanical stress from whisker-matrix thermal-expansion mismatch and may be able to accommodate additional stress from an increased density of trapped charges. However, clamping pressure on the sample during measurement might affect this.

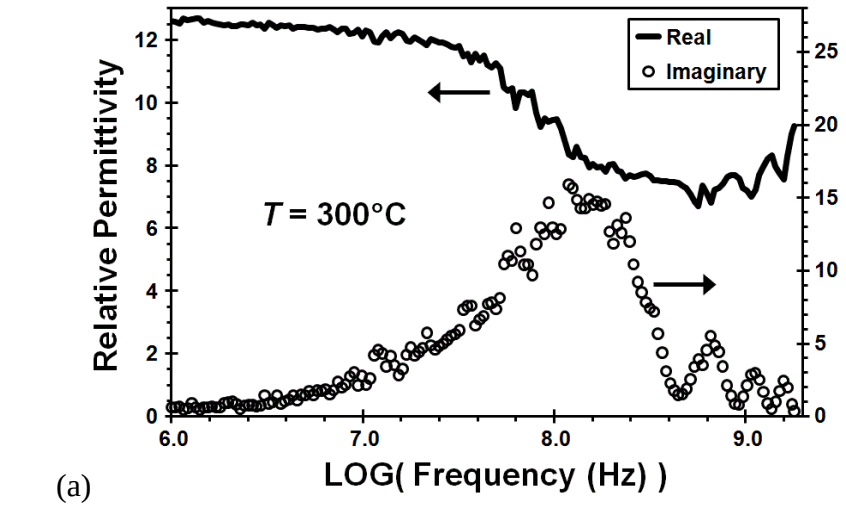

(a)

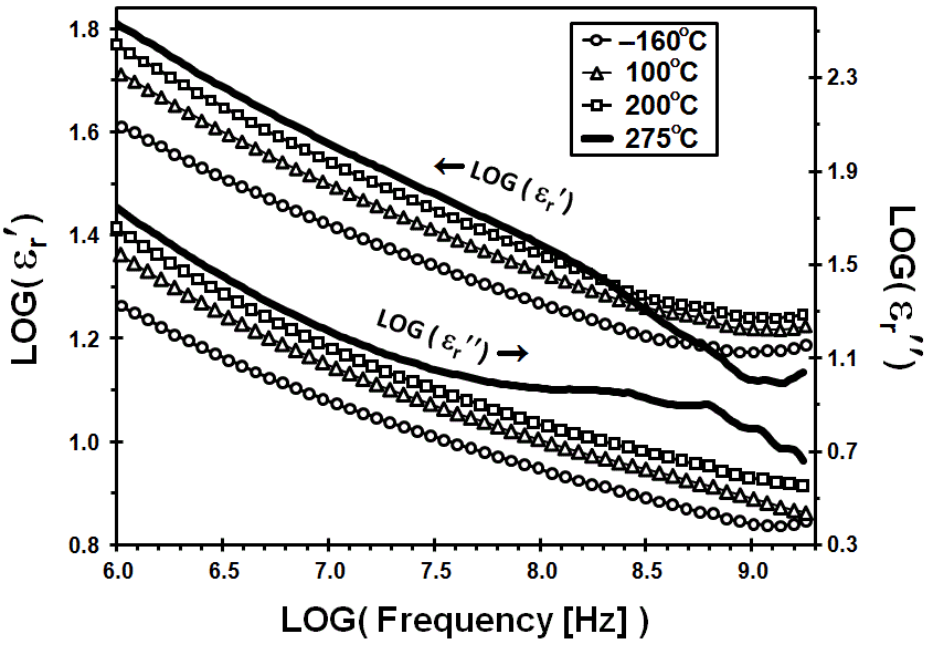

(b)

Figure 7.12. Relaxations in the complex relative permittivity observed for (a) a 0% (matrix) sample at 300°C, and for (b) a 10.0% SiC_w sample at 275°C with lower-temperature spectra shown for comparison. The real and imaginary parts relate to the left and right axes, respectively.[23]

Images from scanning electron microscopy (SEM) were also suggestive of charge trapping and detrapping occurring in conjunction with electron injection from the SEM beam. Figures 7.13a-d show how charging patterns on the sample surface evolved with an increasing fraction of SiC inclusions, which are colored black. A 10% SiC_w sample is pictured in Figure 7.13a, and the bright-white color which is characteristic of most of the matrix material is believed to be an indication of trapping via electron injection. In this image, small, grey, and blob-shaped regions of the matrix can be seen and tend to be located between black SiC inclusions. Throughout Figures 7.13a-d, these grey-colored regions/spots encompass a greater fraction of the total matrix area as whisker content increases (and some are marked with red arrows for clarity). Therefore, these grey regions are interpreted as indications of interwhisker conduction by charge detrapping in the matrix. In Figure 7.13d, the bright-white color of the matrix in the whisker-dilute upper-left portion of the image corroborates the interpretation.

Figures 7.14a and 7.14b are SEM images of 7.7% and 28.2% SiC samples showing a plethora of dark spots which do not appear to be whiskers, and which appear smaller in the 28.2% SiC_w sample. These spots look similar to those described as thermally-etched pits resulting from surface outgassing caused by charge detrapping in a wide-bandgap insulator[28,41] (Figure 7.15a).[24,25] They also appear somewhat similar to those caused by the self-healing dielectric breakdown of the aforementioned SiO_2 films[26] (Figure 7.15b). The seeming arrangement of the spots with roughly equal spacing in linear arrays in Figure 7.14a (aligned with the arrows) might be related to the grinding and polishing of the samples. These processes sometimes left linear scratches on the composite surfaces, and machining has been known to affect trapping in oxides.[25]

(a)

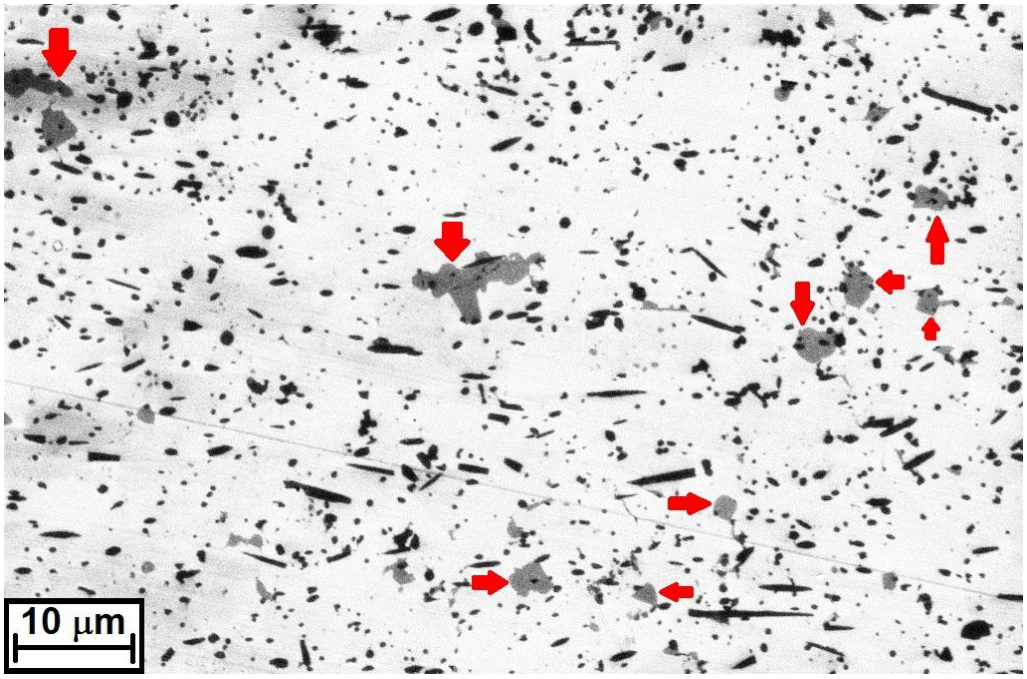

(b)

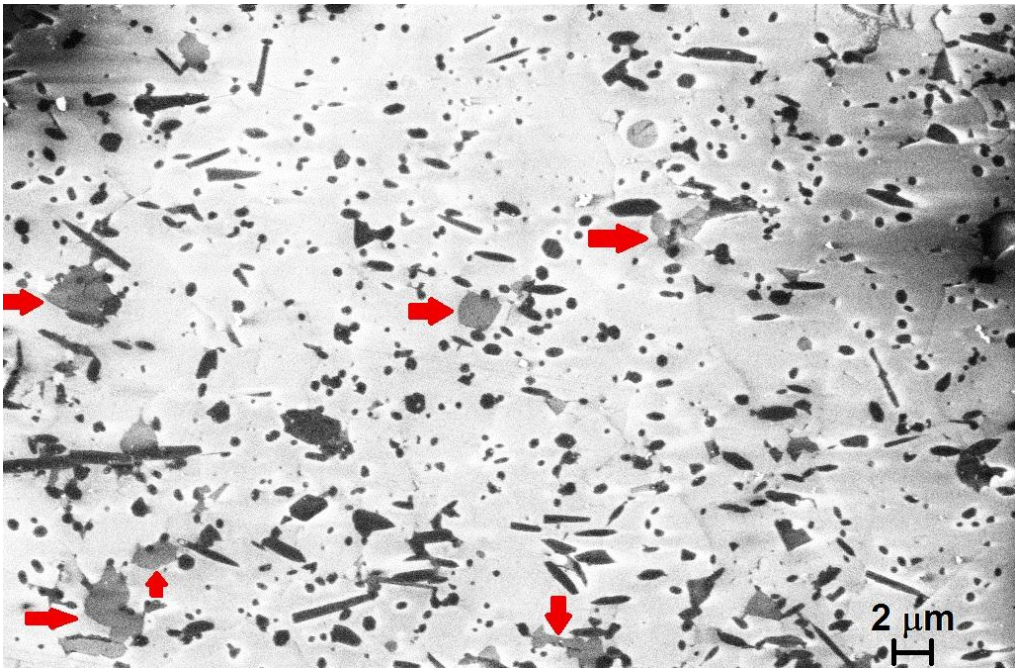

Figure 7.13. Scanning-electron micrographs of the microstructures of (a) 10.0%, (b) 14.5%, (c) 19.1%, and (d) 24.0% SiC_w samples. The accelerating voltages were 5, 5, 8, and 10 kV, respectively. For parts (a),(b), and (d), the red arrows mark particularly prominent grey blob-shaped regions discussed in the text.[23] (see next page)

(c) 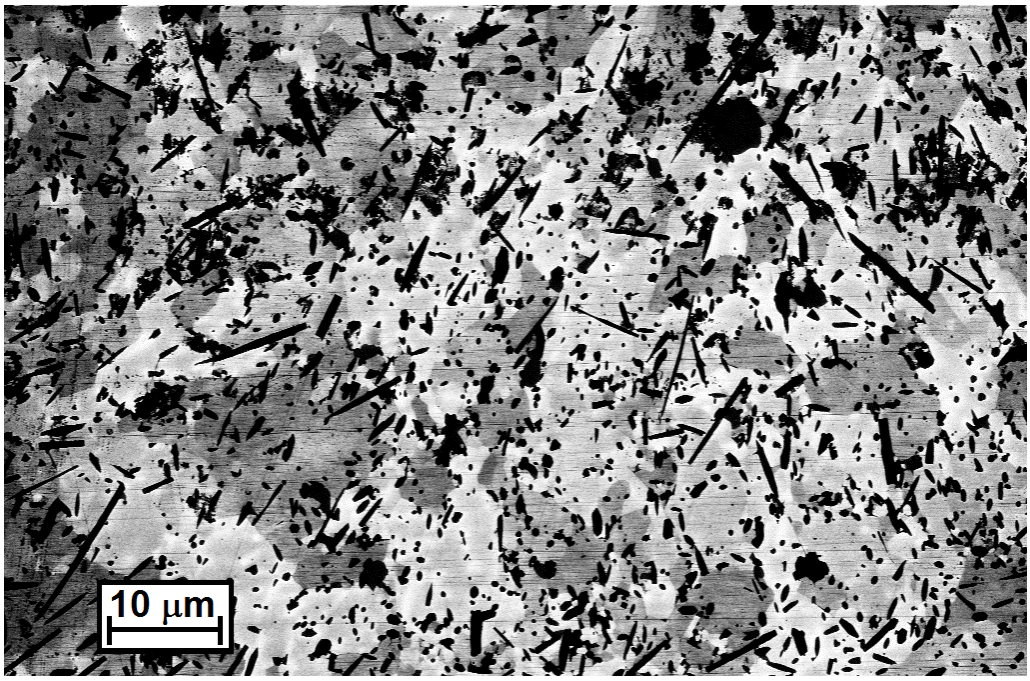

(d) 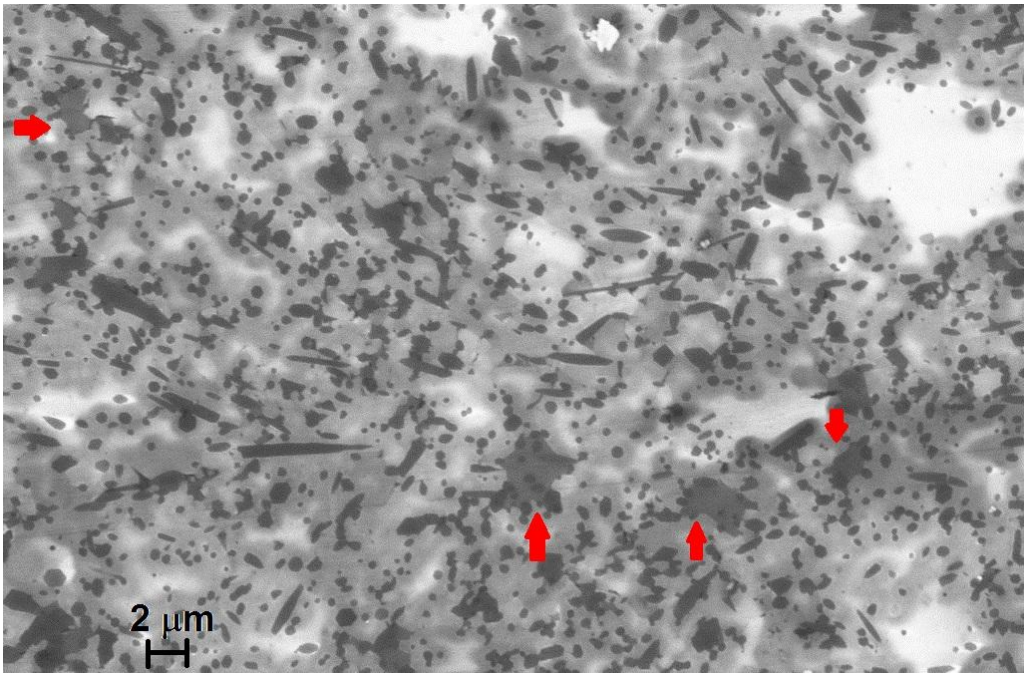

(see last page for caption)

(a)

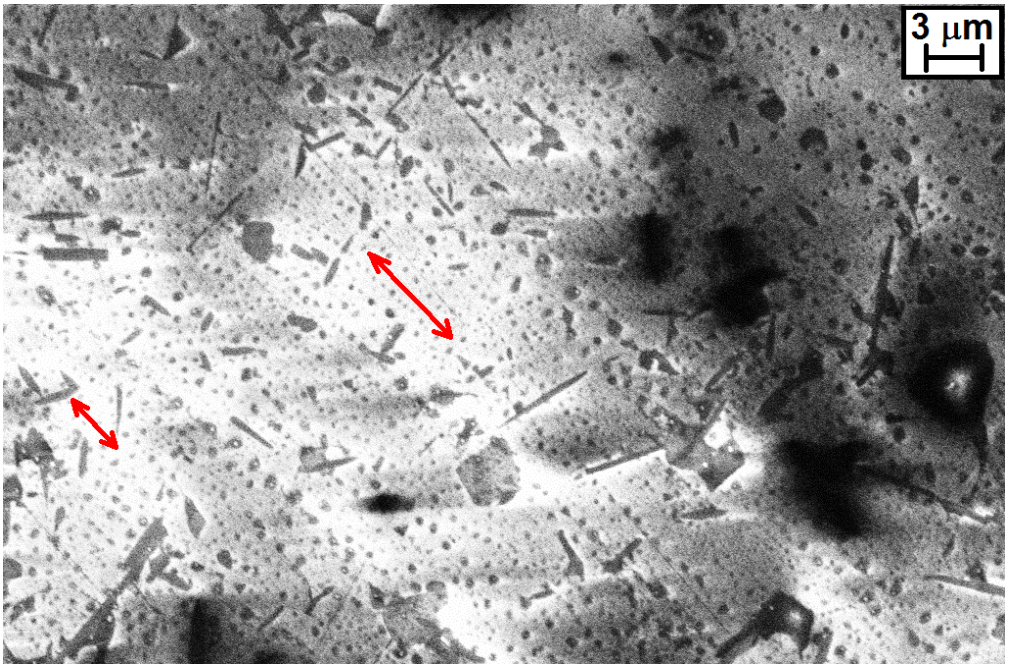

(b)

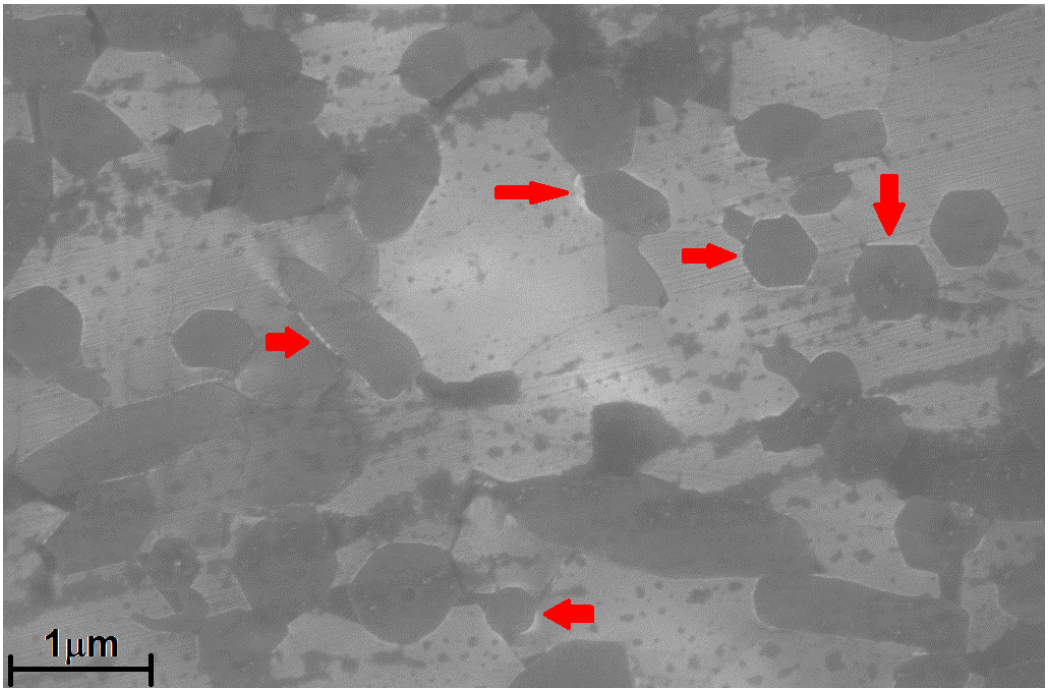

Figure 7.14. Scanning electron micrographs of composites containing (a) 7.7% SiC_w and (b) 28.2% SiC_w. In part (a), the double-headed arrows point in the direction of the linear arrays of spots discussed in the text. In part (b), the spots appear smaller, and arrows mark SiC fillers with relatively prominent interface charging.[23]

(a)

(b)

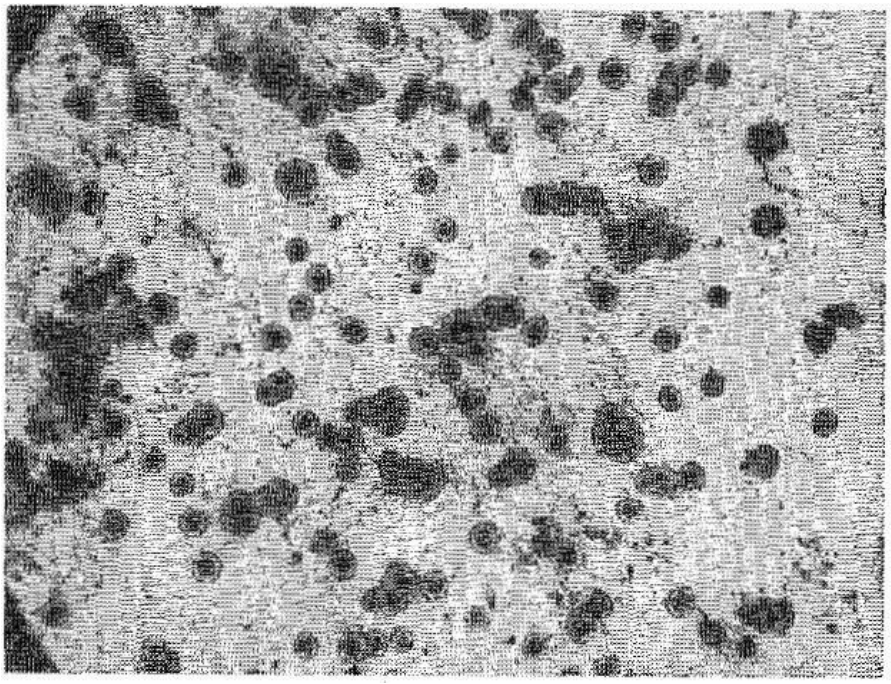

Figure 7.15. Microscope images of damage spots resulting from dielectric breakdown of wide-bandgap insulators from (a) Refs. 24,25 and (b) Ref. 26.

Such similarities in the appearance and the temperature-dependence of conductivity for Al_2O_3-SiC_w composites and dielectrically broken-down single-phase oxides are interesting because breakdown is classically associated with large applied electric fields. Relatively small ac voltages were applied without external bias to the composites, and it seems questionable that these could have caused breakdown in the conventional sense, even with the externally-applied field being concentrated at the whisker-whisker junctions. However, it has been pointed out that space charge in a material (like that associated with traps) can give rise to internal electric fields which can raise the total field above the breakdown value by superimposing on the applied field.[25] For example, the charge density of trapping at semiconductor-insulator interfaces is close to that associated with fields of breakdown magnitude, i.e., 10^{10}-10^{11} V/m.[25] In our samples, it is possible that charge trapping at the SiC-matrix interfaces contributes to significant internal electric fields. Figure 7.14b shows white outlines appearing around the faceted black SiC inclusions of a macroscopically conductive 28.2% sample, which indicates charging at these interfaces. Also, injection-charging of traps in the present composites might have occurred during previous electrical measurements.

The observed resemblances to dielectric breakdown in insulators also compel us to consider another commonly observed aspect of this phenomenon: the associated current-treeing process. This produces a self-similar fractal structure when the growth probability is proportional to the local electric field,[205] which seems agreeable with the aforementioned idea of switching open formerly closed current branches in the presence of a strong electric field. Furthermore, electrically-percolating networks in composites have been independently described as having fractal structures.[94] Therefore, conduction

in the present composites should be considered on a scale greater than that of the individual SiC-matrix-SiC junctions. On the scale of the macroscopic electrically percolating network, the whiskers may be regarded as defects in the matrix, and the presumably-fractal network of the whiskers might serve as a growth template for a breakdown-like self-similar current-branching process across the sample, i.e., a growing but not-highly destructive Lichtenberg figure. In Figure 7.16, the growth of a point-sourced destructive current tree is captured in a camera image.[27]

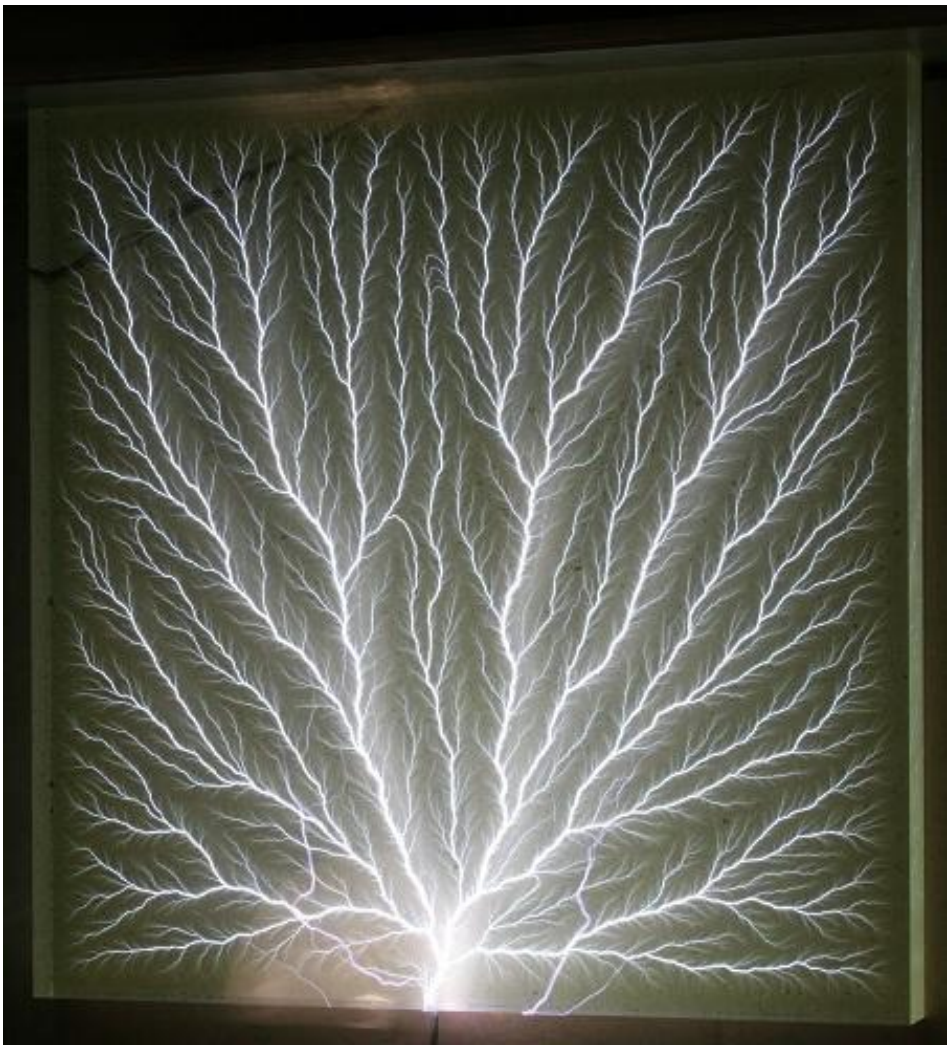

Figure 7.16. Creation of a Lichtenberg figure in acrylic, from Ref. 27. The estimated charge-plane potential and peak current were 2.2 MV and 3.5 kA, respectively.

7.3.5. Effect of Pressureless Sintering on the Temperature Dependence of Conduction

Figure 7.17 shows the temperature dependence of a thin slice of a 24.0% SiC_w extruded rod. The straight black lines are fits to Relation 7.4 at V_{dc} = 10, 20, and 40 V and have slopes corresponding to a = 5.599, 5.306, and 4.976 x10^{-3} K^{-1} with R^2 = 0.992, 0.996, and 0.997, respectively. Assuming that the macroscopic temperature dependence of composite σ_{dc} is the same as that for individual interfiller junctions,[178] the good fits indicate that the interfacial conduction mechanism for the extruded and pressureless-sintered sample is fundamentally the same as that described for the hot-pressed composites in Sections 7.3.2–7.3.4. Scatter in the data is attributed to the influence of the electrode impedance.

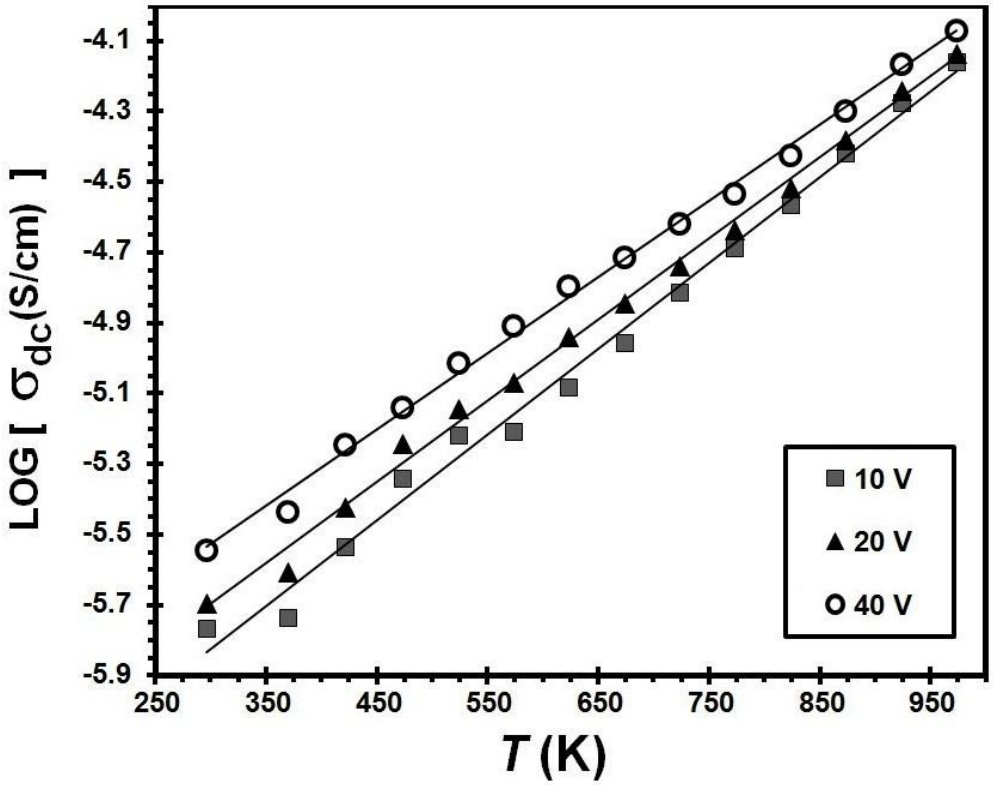

Figure 7.17. The temperature dependence of the bulk conductivity of a slice of an extruded rod containing 24.0% SiC_w. The straight lines are fits to Relation 7.4.

The *a* values are significantly greater than the value of 3.282 x10^{-3} K^{-1} obtained from hot-pressed 24.0% SiC_w data and indicate a stronger temperature dependence and perhaps larger energy barriers at interwhisker interfaces. Given the non-linear current-voltage response of these samples described in Chapter 5, this would not be surprising. For the pressureless sintered composites, it is suspected that the surface states associated with the pores affect the interfacial conduction process. The decrease of *a* with increasing V_{dc} may indicate that temperature and V_{dc} may have superimposing effects on carriers attempting to surmount the barriers in a manner which is qualitatively similar to the process for single Schottky barriers. This is described by Equation 3.3 in Section 3.1.

7.3.6. Considerations of Thermal Expansion Mismatch and Residual Stress

It is reasonable to suppose that the trapping-based conduction mechanism may be affected by residual thermal stresses which result from the mismatch between the coefficients of thermal expansion[4] (CTE) of alumina (~8 ppm/°C) and silicon carbide (~4.5 ppm/°C). During hot-pressing, nearly-full density was achieved and the mismatch implies that subsequent cooling to lower temperatures results in the matrix shrinking more than the whiskers which it encompasses and thereby results in the whiskers being in a compressive state of stress. The presence of the whiskers prevents the matrix from shrinking as much as it otherwise would and therefore the residual-stress state of the matrix is tensile. For the pressureless sintered samples, CTE mismatch likely had less (if any) impact on the response because the existence of free volume within the bulk of the composite could help accommodate the mismatch. For all samples, the residual stress is supposed to be similarly alleviated by heating the solidified samples above room temperature (and closer to the processing temperature).

7.4. Conclusions

The temperature dependence of dc conductivity (σ_{dc}) of SiC whisker-percolated alumina composites made by hot-pressing was measured over a wide temperature range and compared to well-known theories for disordered and relatively conductive materials. These include models for fluctuation-induced tunneling conduction (FITC), nearest-neighbor hopping, and variable-range hopping. Scrutiny of fits to the hopping models revealed them to be inappropriate for these composites, even though fairly large R^2 values resulted in some cases. Analysis of the FITC model indicated that the "T_1" fitting parameter had no bearing on the quality of fits and that deceptively good fits result when the "T_0" fitting parameter is very large compared to the measured temperature range. This is because the empirically-observed temperature dependence of dc conductivity was $\ln(\sigma_{dc}) \propto T$, i.e., the same as that observed for an insulating oxide having undergone dielectric breakdown. The failure of the hopping and FITC models to explain the data are not surprising because the distances between the SiC inclusions are relatively large compared to those associated with the quantum-mechanical tunneling phenomenon which underlies them.

From permittivity measurements spanning 1-1800 MHz and an overlapping range of temperatures, it was found that the variation of the dielectric loss spectra with temperature had a straightforward dependence on the dc conductivity. In the same frequency range, the dielectric constant scaled inversely with frequency via universal power-law behavior. The exponent giving the strength of this power law appeared to be directly related to σ_{dc} and vary with temperature and SiC loading via the temperature dependence of σ_{dc} and the composition dependence of σ_{dc}, respectively. This trend was

analyzed quantitatively and interpreted qualitatively in terms of a model for randomly-configured resistor-capacitor networks and a newly-emerging description of reversible dielectric breakdown of insulating oxide systems in the literature. Altogether, these suggest that increasing temperature causes switching of the matrix-material behavior at the whisker-whisker junctions from a low- to a high-conductivity state such that the fraction of junctions in the high-conductivity state increases with temperature. This results in the growth of *y*, the percolated cluster, and its dc conductance. The extruded and pressureless sintered sample also behaved via $\sigma_{dc} \propto \exp(aT)$, which implies that the same interfacial conduction mechanism controlling the hot-pressed-composite response was operable. However, *a* was smaller for the hot-pressed composites.

The conduction and switching processes are believed to involve charge trapping and detrapping at defects in the oxide matrix based on some key observations and the new view of breakdown in the literature. Low-temperature dielectric resonances and charging in select regions of the matrix during scanning electron microscopy (SEM) were suggestive of charge trapping. High-temperature dielectric relaxations and SEM observation of grey blotches in between SiC whiskers and breakdown-like spot damage in the matrix are attributed to charge detrapping. For the hot-pressed and pressureless-sintered samples, the relevant traps are most likely associated with the oxide sintering additives and the pore surfaces, respectively.

The present understanding of breakdown and trapping phenomena is limited, even within its usual context of insulators *without* electrically-percolated semiconductor inclusions. In a pertinent review,[25] the authors stated that "not only do we not understand breakdown, but also we do not understand for sure the nature of an electron trap."

Therefore, a deeper understanding of the Al_2O_3-SiC_w conduction mechanism will likely require advances in this field and additional studies carefully controlling or varying the electrical-thermal history, grain size, additives, machining process, and mechanical strain of the composites.

CHAPTER 8

CONCLUSIONS, BROADER PERSPECTIVE, AND SUGGESTED FUTURE WORK

8.1. Conclusions

In regards to the electrical response of Al_2O_3-SiC_w composites, this work has provided significant insight into the effects of interfaces and preferred SiC_w orientation. It was instructive to study the easy-to-control interfaces at the electrodes first. The impedance contribution from the electrodes was separable from the linear response of the hot-pressed composite bulk. For percolated samples, the electrodes are manifested in the complex impedance plane by a semicircle whose properties are rooted in symmetrical Schottky-barrier blocking at opposing metal contacts to surface whiskers participating in percolated linkages. This process can be modeled with a parallel resistor-capacitor equivalent circuit, and the interpretation was corroborated by microscopic AFM observations and agreement with a model for symmetrical Schottky barriers. The electrode impedance was also exponentially dependent on applied dc bias (V_{dc}), and this translated to samples exhibiting current-bias responses which became more non-linear as the fraction of V_{dc} partitioned to the electrodes relative to the linear bulk increased. The interfaces between the whiskers in the bulk of hot-pressed composites did not give rise to discernibly non-linear response.

The bias partitioning concept and symmetrical-Schottky-barrier model used to understand the electrode response were also combined with basic percolation topology to help understand the response of the electrically-percolated cluster inside the composite bulk in more detail. In pressureless sintered composites, the whisker-whisker interfaces

within the cluster exhibited non-linear behavior similar to that previously described for the electrodes. For thin slices of extruded rods, it was possible to distinguish between the non-linear responses of the electrodes and the whisker-whisker interfaces when the associated impedances were comparable in magnitude. Also, the whisker-whisker interfaces could be regarded as distinct electrical components compared to the whiskers comprising the electrically-percolated cluster. The distribution of the applied bias between the relatively conductive and linear whisker components vs. the resistive and non-linear interface components was manifested in the bias dependencies of the dc resistance and static capacitance. The cluster may be viewed as a network of these with a mostly random configuration, but the former and latter components have preferential correspondence to current bottlenecking and branching, respectively. The non-linearity strength was decreased when filler loading was greater because the greater conduction parallelism of the conducting cluster resulted in a shift of the bias distribution onto the linear whiskers from the non-linear interfaces. This is similar to the increasing linearity of sample behavior which resulted from the reduction of the non-linear electrode impedance compared to the linear bulk impedance for hot-pressed composites.

The divergence exponent *t* characterizing the loading dependence of composite conductivity above the percolation threshold increased with the influence of the whisker-whisker interfaces and the extent to which they limited that conductivity. It was reduced when the bias distribution was shifted from the interfaces onto the whiskers themselves. For extruded slices, this occurred when a large bias was applied. For hot-pressed discs, this occurred when the connectivity and conduction parallelism of the percolated cluster was increased via whisker-orientation randomness.

The processing method significantly affected the composite structure in terms of whisker orientation, whisker interfaces, and porosity. The composite conductivity was greater when the whiskers were preferentially aligned parallel rather than perpendicular to the applied field, i.e., for extruded compared to dry-pressed composites. For the hot-pressed material, the preferred whisker orientation resulted in conduction and polarization anisotropy which may be explained by the enhanced connectivity and conduction parallelism associated with networks of randomly aligned sticks. Such connectivity was present within planes perpendicular to the hot-pressing direction.

The whiskers inhibited densification during pressureless sintering and thereby induced porosity which was essentially absent in hot-pressed materials. The influence of surface states at the pores on the interfacial conduction process is likely responsible for the non-linear response of pressureless sintered samples. Yet, there was some evidence that the fundamental nature of this process was the same in both pressureless-sintered and hot-pressed composites.

For the hot-pressed specimens, interfacial conduction was modeled in terms of a switching mechanism within a randomly-configured network of resistors and capacitors, which represented the relative extremes of interfacial behavior. This idea was based on an observed coupling between the temperature dependencies of the dc conductivity and the radio-frequency dielectric-constant dispersions. The conduction process bore considerable resemblance to reversible dielectric breakdown and apparently involved charge trapping and detrapping. These processes were evidenced in electron micrographs by microstructural features suggestive of dielectric breakdown and local charging phenomena. In the electrical response, trapping and detrapping manifested as

temperature-dependent dielectric resonances and relaxations, respectively. Furthermore, the dc conductivity and average interwhisker distance were smaller parallel rather than perpendicular to the hot-pressing direction. Such a structure-property correlation is relatively agreeable with a breakdown-like process but not other mechanisms previously proposed for insulator-conductor composites, e.g., hopping and fluctuation-induced tunneling. It is hypothesized that composite conduction occurs through the defective and whisker-studded insulator via a current treeing process which depends on the local internal electric fields between neighboring whiskers.

The percolation transition for hot-pressed composites was comparatively sharp compared to that for extruded materials. The frequency dispersions of the complex permittivity of non-percolated extruded and hot-pressed non-percolated samples were characterized by a relaxation having a broad distribution of relaxation times. These also exhibited a dc-conductivity tail which was more prominent for samples nearer to the percolation threshold. As SiC_w content was increased, the tail grew in magnitude and the relaxation grew in strength, shifted to lower frequency, and spread out over a wider frequency range. These changes were quantified with a Cole-Cole-modified version of the Maxwell-Wagner model for interfacial polarization. For the extruded material, the dielectric relaxation can be seen to slowly evolve as whisker loading is increased through and beyond the percolation threshold into ‘universal’ power-law behavior for the dielectric constant and dc-conductivity behavior for the dielectric loss, which conceals the relaxation loss peak. For the hot-pressed composites, the evolution of the permittivity was qualitatively similar but much more abrupt due to the sharper percolation transition.

The dielectric relaxation occurred at similar frequencies to the power law behavior which was associated with the interfaces. It is best interpreted in terms of multiscale polarizations of electrically-connected but non-percolated whisker clusters having interface-controlled conductivity because this can explain both its compositional and orientation dependencies. At higher frequencies (> ~1 GHz), the behavior becomes more agreeable with effective medium theory because the influence of the interfaces wanes and faster processes are more important. These probably include those related to charge displacement across whisker lengths and intrinsic crystalline defects in the SiC.

At the microwave-application frequencies, the composites may exhibit significant dielectric loss without any significant dc conductivity. Yet, the dielectric loss of well-percolated composites scales with dc conductivity more strongly than expected, and the anisotropy of this loss cannot be accounted for with intrinsic-defect polarization. This suggests that, in addition to dc conductivity, polarizations of clusters, whisker lengths, and intrinsic defects all significantly contribute to the microwave heating application.

8.2. Broader Perspective

Besides the specific conclusions outlined above, it is important to take a broader perspective on the implications of the present work. This dissertation provides several contributions to the field of insulator-(semi)conductor composites and is the first comprehensive study in the field to focus on a ceramic system and the electrical behavior of the interfaces of the conductive fillers. Most work in the field is on polymeric systems. It is also the first to provide the specific connections (described within) between the effects of loading, frequency, bias, temperature, and anisotropic structure.

Means for clearly identifying and a relatively detailed description of the effects of the electrode-sample interfaces on composite behavior (which are often ignored) were established. Visual schematics showing how the preferred orientation of the conductive fillers affects the composite response were provided and should be more broadly applicable to other systems containing stick-like fillers. The electrical behavior of interfaces between fillers was shown to depend upon porosity and have a dramatic effect on direct-current percolation, i.e., the insulator-conductor transition, which was clearly related to the evolution of the wide-band frequency response. A new physical description of the dielectric relaxation which occurs for filler-loaded but non-percolated samples (in this and other[93] systems) was provided, i.e., polarizations of electrically-connected but non-percolated filler clusters. For percolated samples, straightforward approaches for thinking about both the real and imaginary parts of the permittivity dispersion were put forward. The applicability of models for randomly configured electrical networks to the filler interfaces in real-world disordered insulator-conductor composites was elucidated. Significantly, a model for electrically-percolated clusters which combines the effects of these interfaces and knowledge of topology, *and which can be directly related to experimentally measured parameters*, was developed and shown to have merit. More importantly, this work provides evidence that the interfacial conduction mechanism in ceramic insulator-conductor composites is related to dielectric breakdown and depends upon electronic trap states when the fillers are separated by micron-scale distances. This mechanism is different from the proposed mechanisms for insulator-conductor composites having polymeric matrices, e.g., fluctuation-induced tunneling. Possible flaws in the model for this process were exposed.

8.3. Suggested Future Work

Although this thesis amounts to a great deal of progress, there are many more experiments which could be performed. A significant amount of leftover powders from the original blends currently remains in the care of the advisor of this dissertation and would be suitable for some new experiments. Anyone who works with these powders or other loose whiskers should take care and make safety a personal priority (see Section 1.1.3). Other experiments would require newly fabricated powder blends. Generally, it is suggested that the entire compositional range need not be tested. It should be generally sufficient to analyze one composition on each side of the percolation threshold, which may be controllably altered via the aspect ratio (Figure 1.8).

In the present thesis, the same powder blends were used for the samples processed by all methods and the distributions of whisker aspect ratios were held constant in order to investigate the effects of preferred orientation and interfaces. Incrementally varying the aspect ratios could provide additional insight into matters of geometrical connectivity and could be done by variable-time ball milling. Aspect ratios in the leftover powders could be reduced by additional ball milling.

Besides the aspect ratios, another important feature of the whisker distribution is the number density of whiskers per unit volume. A given volume fraction of whiskers having a fixed aspect ratio can correspond to different number densities if the whisker diameters or lengths are varied. Although it may be presumed that higher number density gives rise to increased connectivity, conductivity, and interfacial area, this matter deserves systematic study. Varying the diameters might be difficult since it would require

modification and good control of the whisker growth process, which likely depends on the details of the starting organic waste.

Although the effects of widely differing preferred orientations were determined, it is desirable to observe the effects of incrementally varying the orientation to test the simulation results of Ref. 8. This could possibly be done by extrusion of a single composition through variable-diameter dies.[46] Also, fully dense samples with three-dimensionally random orientations could be made by hot isostatically pressing in order to further verify the randomness-connectivity association.

A better understanding of the trapping phenomena and matters of electronic structure are also desired. This could be explored by systematically varying one of several parameters while keeping whisker loading, orientation, and the rest of the parameters (if applicable) constant. The parameters are: sintering-additive chemistry, porosity, matrix-grain size, matrix material type, intrawhisker doping/chemistry, and sample electrical-thermal history. It is suggested that a study of the matrix-grain size (and its distribution) should be done by varying the size of the starting (unmilled) alumina powder while keeping the whisker loading and milling parameters fixed due to the effects of the whiskers on matrix-grain growth.

Also, a more-reliable electrical characterization method is needed to span the 1–2 GHz range. Measuring materials in this range can be challenging because it corresponds to the frequency extremes and thus the reduced reliability of the associated electrical characterization equipment.

REFERENCES

1. S. R. Nutt, "Defects in silicon carbide whiskers," *Journal of the American Ceramics Society*, **67**[6] 428-31 (1984).

2. S. R. Nutt, "Microstructure and growth model for rice-hull-derived SiC whiskers," *Journal of the American Ceramics Society,* **71**[3] 149-56 (1988).

3. J. Runyan, R. A. Gerhardt, and R. Ruh, "Electrical properties of boron nitride matrix composites: I, analysis of McLachlan equation and modeling of the conductivity of boron nitride-boron carbide and boron nitride-silicon carbide composites," *Journal of the American Ceramics Society,* **84**[7] 1490-96 (2001).

4. C. B. Carter and M. G. Norton, "Ceramic Materials Science and Engineering.″ Springer: New York, (2007).

5. R. W. Rice, "Ceramic Fabrication Technology.″ Marcel Dekker, Inc.: New York, (2003).

6. D. S. Mebane and R. A. Gerhardt, "Interpreting impedance response of silicon carbide whisker/alumina composites through microstructural simulation," *Journal of the American Ceramics Society*, **89**[2] 538-43 (2006).

7. A. N. Lagarkov, S. M. Matytsin, K. N. Rozanov, and A. K. Sarychev, "Dielectric properties of fiber-filled composites," *Journal of Applied Physics,* **84**[7] 3806-14 (1998).

8. S. I. White, B. A. DiDonna, M. Mu, T. C. Lubensky, and K. I. Winey, "Simulations and electrical conductivity of percolated networks of finite rods with various degrees of axial alignment," *Physical Review B,* **79**[2] 024301 (2009).

9. D. S. Mebane and R. A. Gerhardt, "Orientation dependence of resistivity in anisotropic ceramic composites," *Ceramic Transactions*, **150,** pg. 265-72 (2004).

10. M. Taya, "Electronic Composites.″ Cambridge University Press: Cambridge, (2005).

11. Y. Hazama, N. Ainoya, J. Nakamura, and A. Natori, "Conductivity and dielectric constant of nanotube/polymer composites," *Physical Review B,* **82**[4] 045204 (2010).

12. S. Panteny, R. Stevens, and C. R. Bowen, "The frequency dependent permittivity and ac conductivity of random electrical networks," *Ferroelectrics,* **319**[1] 199-208 (2005).

13. C. S. Yang and P. M. Hui, "Effective nonlinear response in random nonlinear resistor networks - numerical studies," *Physical Review B,* **44**[22] 12559-61 (1991).

14. L. M. Levinson, "ZnO Varistor Technology." in Ceramic Materials for Electronics**.** Edited by R. C. Buchanan. Marcel Dekker, Inc., New York, 2004.

15. A. J. Moulson and J. M. Herbert, "Electroceramics.*"* Wiley: Chichester, (2003).

16. R. C. Buchanan, "Ceramic Materials for Electronics" Marcel Dekker, Inc., New York, 2004.

17. R. A. Gerhardt and R. Ruh, "Volume fraction and whisker orientation dependence of the electrical properties of SiC-whisker-reinforced mullite composites," *Journal of the American Ceramics Society,* **84**[10] 2328-34 (2001).

18. B. D. Bertram and R. A. Gerhardt, "Room temperature properties of electrical contacts to alumina composites containing silicon carbide whiskers," *Journal of Applied Physics,* **105** 074902 (2009).

19. K. Mukae, K. Tsuda, and I. Nagasawa, "Capacitance-vs-voltage characteristics of ZnO varistors," *Journal of Applied Physics*, **50**[6] 4475-76 (1979).

20. B. D. Bertram, R. A. Gerhardt, and J. W. Schultz, "Extruded and pressureless-sintered Al_2O_3-SiC_w composite rods: fabrication, structure, electrical behavior, and elastic modulus," *Journal of the American Ceramics Society,* DOI: 10.1111/j.1551-2916.2011.04745.x (2011).

21. B. D. Bertram and R. A. Gerhardt, "Effects of frequency, percolation, and axisymmetric microstructure on the electrical response of hot-pressed alumina-silicon carbide whisker composites," *Journal of the American Ceramics Society,* **94**[4] 1125-32 (2011).

22. B. D. Bertram, R. A. Gerhardt, and J. W. Schultz, "Impedance response and modeling of composite varistors containing aligned semiconductor whiskers: effects of dc-bias partitioning and percolated-cluster length, topology, and filler interfaces," *Journal of Applied Physics* submitted (2011).

23. B. D. Bertram, R. A. Gerhardt, and J. W. Schultz, "Temperature-dependent conduction and switching involving traps in electrically-percolated alumina-SiC composites and incongruence with other models," *Physical Review B (in preparation)* (2011).

24. C. Legressus and G. Blaise, "Breakdown Phenomena related to trapping/detrapping processes in wide band-gap insulators," *IEEE Transactions on Electrical Insulation,* **27**[3] 472-81 (1992).

25. G. Damamme, C. LeGressus, and A. S. DeReggi, "Space charge characterization for the 21st century," *IEEE Transactions on Dielectrics and Electrical Insulation,* **4**[5] 558-84 (1997).

26. N. Klein and H. Gafni, "The maximum dielectric strength of thin silicon oxide films," *Electron Devices, IEEE Transactions on,* **13**[2] 281-89 (1966).

27. Image courtesy of Bert Hickman, www.capturedlightning.com.

28. C. B. Raju and S. Verma, "SiC whiskers from rice hulls: formation, purification, and characterisation," *British Ceramic Transactions,* **96**[3] 112-15 (1997).

29. F. Ye, T. C. Lei, and Y. Zhou, "Interface structure and mechanical properties of Al_2O_3-20vol% SiC_w ceramic matrix composite," *Materials Science and Engineering A-Structural Materials Properties Microstructure and Processing,* **281**[1-2] 305-09 (2000).

30. K. W. Lee and S. W. Sheargold, "Particulate matters in silicon-carbide whiskers," *American Ceramics Society Bulletin,* **65**[11] 1477-77 (1986).

31. P. Singh, A. Selvam, and N. G. Nair, "Synthesis of SiC whiskers from a mixture of rice husks and coconut shells," *Advances in Powder Metallurgy & Particulate Materials,* **1** 3-53 - 3-64 (1998).

32. R. S. Wagner and W. C. Ellis, "Vapor-liquid-solid mechanism of single crystal growth," *Applied Physics Letters,* **4**[5] 89-90 (1964).

33. L. M. Porter and R. F. Davis, "A critical review of ohmic and rectifying contacts for silicon carbide," *Materials Science and Engineering: B,* **34**[2-3] 83-105 (1995).

34. Image courtesy of the Greenleaf Corporation, Saegertown, PA.

35. Advanced Composite Materials LLC website, www.acm-usa.com.

36. S. Karunanithy, "Chemical processes that degrade composites of alumina with SiC whiskers," *Materials Science and Engineering A-Structural Materials Properties Microstructure and Processing,* **112** 225-31 (1989).

37. K. Roedelsperger and B. Brueckel, "The Carcinogenicity of WHO fibers of silicon carbide: SiC whiskers compared to cleavage fragments of granular SiC," *Inhalation Toxicology,* **18**[9] 623-31 (2006).

38. G. L. Vaughan and S. A. Trently, "The toxicity of silicon carbide whiskers, a review," *Journal of Environmental Science and Health Part a-Environmental Science and Engineering & Toxic and Hazardous Substance Control,* **31**[8] 2033-54 (1996).

39. W. S. Johnson and M. J. Birt, "Comparison of some micromechanics models for discontinuously reinforced metal matrix composites,"*Journal of Composites Techonology Research,* **13**[3] 161-67 (1991).

40. R. M. Jones, "Mechanics of Composite Materials,*"* 2nd ed. Taylor & Francis: Philadelphia, PA, (1999).

41. J. J. Zeng, B. Saltysiak, W. S. Johnson, D. A. Schiraldi, and S. Kumar, "Processing and properties of poly(methyl methacrylate)/carbon nano fiber composites," *Compos. Pt. B-Eng.*, **35**[2] 173-78 (2004).

42. C. J. Capozzi and R. A. Gerhardt, "Novel percolation mechanism in PMMA matrix composites containing segregated ITO nanowire networks," *Advanced Functional Materials,* **17**[14] 2515-21 (2007).

43. P. F. Becher and G. C. Wei, "Toughening behavior in SiC-whisker-reinforced alumina," *Journal of the American Ceramics Society*, **67**[12] C267-C69 (1984).

44. P. F. Becher, C. H. Hsueh, P. Angelini, and T. N. Tiegs, "Theoretical and experimental analysis of the toughening behavior of whisker reinforcement in ceramic matrix composites," *Materials Science and Engineering A-Structural Materials Properties Microstructure and Processing*, **107** 257-59 (1989).

45. W. D. Kingery, "Introduction to Ceramics.*"* John Wiley & Sons, Inc.: New York, (1960).

46. M. Farkash and D. G. Brandon, "Whisker alignment by slip extrusion," *Materials Science and Engineering A-Structural Materials Properties Microstructure and Processing*, **177**[1-2] 269-75 (1994).

47. M. King, "Review of Ball Milling" (2004) obtained online at: www.dur.ac.uk/superconductivity.durham/ballmilling.ppt

48. R. Ruh and H. M. Chizever, "Permittivity and permeability of mullite-SiC-whisker and spinel-SiC-whisker composites (vol 81, pg 1069, 1998)," *Journal of the American Ceramics Society*, **81**[6] 1699-99 (1998).

49. R. Ruh and H. M. Chizever, "Permittivity and permeability of mullite-SiC-whisker and spinel-SiC-whisker composites," *Journal of the American Ceramics Society*, **81**[4] 1069-70 (1998).

50. E. A. Holm and M. J. Cima, "Two-dimensional whisker percolation in ceramic matrix ceramic whisker composites," *Journal of the American Ceramics Society*, **72**[2] 303-05 (1989).

51. M. Sinott, "Ceramic Technology for Advanced Heat Engines." in**.** Edited by N. R. C. N. M. A. Board, Washington D.C., 1987.

52. J. Carter, "Proposed Energy Policy for United States." (televised speech) 1977.

53. G. Ford, "Address on the State of the Union before a Joint Session of the 94th Congress." in Washington, D.C., 1975.

54. R. T. DeHoff, "Thermodynamics in materials science.″ McGraw-Hill, Inc.: New York, (1993).

55. A. R. de Arellano-Lopez, F. L. Cumbrera, A. Dominguez-Rodriguez, K. C. Goretta, and J. L. Routbort, "Compressive Creep of SiC-whisker-reinforced Al_2O_3," *Journal of the American Ceramics Society,* **73**[5] 1297-300 (1990).

56. A. R. De Arellano-Lopez, A. Dominguez-Rodriguez, and J. L. Routbort, "Microstructural constraints for creep in SiC-whisker-reinforced Al_2O_3," *Acta Materialia,* **46**[18] 6361-73 (1998).

57. A. R. de Arellano-Lopez, J. J. Melendez-Martinez, A. Dominguez-Rodriguez, and J. L. Routbort, "Creep of Al_2O_3 containing a small volume fraction of SiC-whiskers," *Scr. Mater.,* **42**[10] 987-91 (2000).

58. A. R. de Arellano-Lopez, J. J. Melendez-Martinez, A. Dominguez-Rodriguez, J. L. Routbort, H. T. Lin, and P. F. Becher, "Grain-size effect on compressive creep of silicon-carbide-whisker-reinforced aluminum oxide," *Journal of the American Ceramics Society,* **84**[7] 1645-47 (2001).

59. H. T. Lin, K. B. Alexander, and P. F. Becher, "Grain size effect on creep deformation of alumina-silicon carbide composites," *Journal of the American Ceramics Society,* **79**[6] 1530-36 (1996).

60. H. T. Lin and P. F. Becher, "Creep behavior of a SiC-whisker reinforced alumina," *Journal of the American Ceramics Society,* **73**[5] 1378-81 (1990).

61. H. T. Lin and P. F. Becher, "High-temperature creep deformation of alumina SiC-whisker composites," *Journal of the American Ceramics Society,* **74**[8] 1886-93 (1991).

62. P. Lipetzky, S. R. Nutt, D. A. Koester, and R. F. Davis, "Atmospheric effects on compressive creep of SiC-whisker-reinforced alumina," *Journal of the American Ceramics Society,* **74**[6] 1240-47 (1991).

63. S. R. Nutt, P. Lipetzky, and P. F. Becher, "Creep deformation of alumina-SiC composites," *Materials Science and Engineering A-Structural Materials Properties Microstructure and Processing,* **126** 165-72 (1990).

64. C. O'Meara, T. Suihkonen, T. Hansson, and R. Warren, "A microstructural investigation of the mechanisms of tensile creep deformation in an Al_2O_3/SiC_w composite," *Materials Science and Engineering a-Structural Materials Properties Microstructure and Processing,* **209**[1-2] 251-59 (1996).

65. G. C. Quan, K. T. Conlon, and D. S. Wilkinson, "Investigation of anelastic creep recovery in SiC whisker-reinforced alumina composites," *Journal of the American Ceramics Society,* **88**[11] 3104-09 (2005).

66. R. Raj and M. F. Ashby, "Grain boundary sliding and diffusional creep," *Metallurgical Transactions,* **2**[4] 1113-& (1971).

67. Q. Tai and A. Mocellin, "Review: High temperature deformation of Al2O3-based ceramic particle or whisker composites," *Ceramics International,* **25**[5] 395-408 (1999).

68. M. I. K. Collin and D. J. Rowcliffe, "Influence of thermal conductivity and fracture toughness on the thermal shock resistance of alumina-silicon-carbide-whisker composites," *Journal of the American Ceramics Society,* **84**[6] 1334-40 (2001).

69. A. R. Thangaraj and K. J. Weinmann, "On the wear mechanisms and cutting performance of silicon-carbide whisker-reinforced alumina," *Journal of Engineering for Industry-Transactions of the Asme,* **114**[3] 301-08 (1992).

70. X. Li, "Ceramic Cutting Tools - An Introduction," *Key Engineering Materials,* **96** 1-18 (1994).

71. P. Mehrotra, "Applications of ceramic cutting tools," *Advanced Ceramic Tools for Machining Application - Iii,* **138**[1] 1-24 (1998).

72. E. Billman, P. Mehrotra, A. Shuster, and C. Beeghly, "Machining with Al_2O_3-SiC-whisker cutting tools,"*American Ceramics Society Bulletin,* **67**[6] 1016-19. (1988).

73. C. Dogan and J. Hawk, "Influence of whisker toughening and microstructure on the wear behavior of Si_3N_4- and Al_2O_3-matrix composites reinforced with SiC," *Journal of Materials Science,* **35**[23] 5793-807 (2000).

74. M. Amateau, B. Stutzman, J. Conway, and J. Halloran, "Performance of laminated ceramic composite cutting tools," *Ceramics International,* **21**[5] 317-23 (1995).

75. T. Quantrille, private communications.

76. A. C. Metaxas and R. J. Meredith, "Industrial Microwave Heating.″ Peter Peregrinus Ltd. on behalf of the Institution of Electrical Engineers: London, UK, (1983).

77. T. Basak and A. S. Priya, "Role of ceramic supports on microwave heating of materials," *Journal of Applied Physics,* **97**[8] (2005).

78. T. E. Quantrille, "Ceramic Composites for Microwave Grilling and Speed Cooking." in 42nd Annual Microwave Symposium**.** International Microwave Power Institute, New Orleans, LA, 2008.

79. P. E. Parris and V. M. Kenkre, "Thermal runaway in ceramics arising from the temperature dependence of the thermal conductivity," *Physica Status Solidi B-Basic Research,* **200**[1] 39-47 (1997).

80. P. H. McCluskey, R. K. Williams, R. S. Graves, and T. N. Tiegs, "Thermal diffusivity/conductivity of alumina-silicon carbide composites," *Journal of the American Ceramics Society,* **73**[2] 461-64 (1990).

81. W. J. Lee and E. D. Case, "Cyclic thermal shock in SiC-whisker-reinforced alumina composites," *Materials Science and Engineering A-Structural Materials Properties Microstructure and Processing,* **119** 113-26 (1989).

82. T. E. Quantrille, "Novel Composite Structures for Microwave Heating and Cooking." in 41st Annual Microwave Symposium**.** International Microwave Power Institute, Vancouver, BC, 2007.

83. G. H. Weiss, "Contemporary Problems in Statistical Physics.″ Society of Industrial and Applied Mathematics: Philadelphia, (1994).

84. B. D. Bertram and R. A. Gerhardt, "Properties and Applications of Ceramic Composites Containing Silicon Carbide Whiskers." in Properties and Applications of Silicon Carbide**.** Edited by R. A. Gerhardt. In Tech, 2011.

85. A. N. Lagarkov and A. K. Sarychev, "Electromagnetic properties of composites containing elongated conducting inclusions," *Physical Review B,* **53**[10] 6318-36 (1996).

86. I. Balberg, C. H. Anderson, S. Alexander, and N. Wagner, "Excluded volume and its relation to the onset of percolation," *Physical Review B,* **30**[7] 3933-43 (1984).

87. H. J. Park, H. E. Kim, and D. Y. Kim, "Evaluation of whisker alignment in axisymmetrical SiC_w-reinforced Al_2O_3 composite materials," *Journal of the American Ceramics Society,* **77**[11] 2828-32 (1994).

88. M. S. Sandlin, E. J. Lee, and K. J. Bowman, "Simple geometric model for assessing whisker orientation in axisymmetrical SiC-whisker-reinforced composites," *Journal of the American Ceramics Society,* **75**[6] 1522-28 (1992).

89. D. S. Mebane, A. M. Gokhale, and R. A. Gerhardt, "Trivariate, stereological length-radius-orientation unfolding derived and applied to alumina-silicon carbide whisker composites," *Journal of the American Ceramics Society,* **89**[2] 620-26 (2006).

90. C. A. Wang, Y. Huang, Y. Li, Z. T. Zhang, Z. P. Xie, and J. B. Li, "Resistivity controlled by SiC whisker orientation in Si_3N_4 matrix composites," *Journal of Materials Science Letters,* **17**[10] 829-31 (1998).

91. K. D. Murphy, G. W. Hunt, and D. P. Almond, "Evidence of emergent scaling in mechanical systems," *Philosophical Magazine,* **86**[21-22] 3325-38 (2006).

92. E. K. Sichel, "Carbon-Black Polymer Composites: The Physics of Electrically Conducting Composites." in Plastics Engineering**.** Edited by D. E. Hudgin. Marcel Dekker, Inc., New York, 1982.

93. G. M. Tsangaris, N. Kouloumbi, and S. Kyvelidis, "Interfacial relaxation phenomena in particulate composites of epoxy resin with copper or iron particles," *Materials Chemistry and Physics,* **44**[3] 245-50 (1996).

94. M. T. Connor, S. Roy, T. A. Ezquerra, and F. J. Baltá Calleja, "Broadband ac conductivity of conductor-polymer composites," *Physical Review B,* **57**[4] 2286 (1998).

95. A. A. Kiejna and K. F. Wojciechowski, "Metal Surface Electron Physics.″ Elsevier Science Ltd.: Tarrytown, (1996).

96. C. D. Geddes and J. R. Lakowicz, "Radiative Decay Engineering.″ Springer Science + Business Media, Inc.: New York, (2005).

97. R. Bindi, P. Iacconi, D. Lapraz, and F. Petel, "The effective electron affinity estimation from the simultaneous detection of thermally stimulated luminescence and exoelectronic emission. Application to an alpha-alumina single crystal," *Journal of Physics D-Applied Physics,* **30**[1] 137-43 (1997).

98. K. Irmscher, "Electrical properties of SiC: characterisation of bulk crystals and epilayers," *Materials Science and Engineering B-Solid State Materials for Advanced Technology,* **91** 358-66 (2002).

99. D. W. Peters, L. Feinstein, and C. Peltzer, "On the High-Temperature Electrical Conductivity of Alumina,″ *Journal of Chemical Physics,* pp. 2345-46 (1965).

100. Y. Zhou, M. Ogawa, X. H. Han, and K. L. Wang, "Alleviation of Fermi-level pinning effect on metal/germanium interface by insertion of an ultrathin aluminum oxide," *Applied Physics Letters,* **93**[20] 3 (2008).

101. J. Liebault, J. Vallayer, D. Goeuriot, D. Treheux, and F. Thevenot, "How the trapping of charges can explain the dielectric breakdown performance of alumina ceramics," *Journal of the European Ceramic Society,* **21**[3] 389-97 (2001).

102. S. O. Kasap, "Principles of Electronic Materials and Devices,″ 2nd ed. McGraw-Hill: New York, (2002).

103. T. B. Adams, D. C. Sinclair, and A. R. West, "Characterization of grain boundary impedances in fine- and coarse-grained $CaCu_3Ti_4O_{12}$ ceramics," *Physical Review B,* **73**[9] (2006).

104. C. A. Mead and W. G. Spitzer, "Fermi Level Position at Metal-Semiconductor Interfaces," *Physical Review,* **134**[3A] A713 (1964).

105. F. Klaus, "Jump relaxation in solid ionic conductors," *Solid State Ionics,* **28-30, Part 1**[0] 100-07 (1988).

106. B. Zhang, J. B. Li, J. J. Sun, S. X. Zhang, H. Z. Zhai, and Z. W. Du, "Nanometer silicon carbide powder synthesis and its dielectric behavior in the GHz range," *Journal of the European Ceramic Society,* **22**[1] 93-99 (2002).

107. P. Debye, "Polar Molecules.″ Chemical Catalog Company: New York, (1929).

108. K. S. Cole and R. H. Cole, "Dispersion and absorption in dielectrics I. Alternating current characteristics," *Journal of Chemical Physics,* **9**[4] 341-51 (1941).

109. A. R. von Hippel, "Dielectrics and Waves.″ Wiley: New York, (1954).

110. D. S. Mebane, "Impedance Response of Alumina-Silicon Carbide Whisker Composites." Master of Science Thesis in Materials Science & Engineering, Georgia Institute of Technology, Atlanta, GA, 2004.

111. T. N. Tiegs and D. M. Dillard, "Effect of Aspect Ratio and Liquid-Phase Content on Densification of Alumina Silicon-Carbide Whisker Composites," *Journal of the American Ceramics Society,* **73**[5] 1440-42 (1990).

112. S. J. Barclay, J. R. Fox, and H. K. Bowen, "Processing of Pressureless-Sintered SiC Whisker-Reinforced Al_2O_3 Composites," *Journal of Materials Science,* **22**[12] 4403-06 (1987).

113. D. S. Mebane, S. I. Lieberman, A. M. Gokhale, and R. A. Gerhardt, "Bivariate stereological unfolding procedure for randomly oriented chopped fibers or whiskers," *Acta Materialia,* **53**[18] 4943-53 (2005).

114. J. S. Zhang, H. Huang, L. H. Cao, F. Xia, and G. Q. Li, " Semiconductive property and impedance spectra of alumina silicon-carbide whisker composites," *Journal of the American Ceramics Society,* **75**[8] 2286-88 (1992).

115. C. Virojanadara, P. Glans, T. Balasubramanian, L. Johansson, E. Macak, Q. Wahab, and L. Madsen, "Schottky barrier height studies of Au/4H-SiC(0001) using photoemission and synchrotron radiation," *Journal of Electronic Materials,* **31**[12] 1353-56 (2002).

116. S. H. Hagen, "Surface-Barrier Diodes on Silicon Carbide," *Journal of Applied Physics,* **39**[3] 1458-61 (1968).

117. M. Bhatnagar, P. K. McLarty, and B. J. Baliga, "Silicon-carbide high-voltage (400 V) Schottky barrier diodes," *IEEE Electron Device Letters,* **13**[10] 501-03 (1992).

118. B. G. Streetman and S. Banerjee, "Solid State Electronic Devices," 5th ed. Prentice Hall, Inc.: Upper Saddle River, NJ, (2000).

119. J. R. Waldrop, R. W. Grant, Y. C. Wang, and R. F. Davis, "Metal Schottky barrier contacts to alpha 6H-SiC," *Journal of Applied Physics,* **72**[10] 4757-60 (1992).

120. Z. T. Zhang, H. B. Shan, Y. Huang, and Z. Z. Jiang, "Characterisation of interfacial bonding in Al_2O_3 coated SiC whisker reinforced TZP composites," *British Ceramic Transactions,* **95**[3] 125-28 (1996).

121. R. Ou, H. Qin, R. A. Gerhardt, and R. Ruh, "Electrical properties of SiC-AlN composites," pp. 349-54. in 27th International Cocoa Beach Conference on Advanced Ceramics and Composites: B, **Vol. 24.** *Ceramic Engineering and Science Proceedings.* Edited by W. M. Kriven and H. T. Lin, 2003.

122. M. Ben Farah, F. Lapicque, and M. Matlosz, "Electrical characterization of the semiconducting properties of n-TiO_2," *Journal of the Electrochemical Society,* **145**[10] 3550-56 (1998).

123. Y. Y. Proskuryakov, K. Durose, B. M. Taele, and S. Oelting, "Impedance spectroscopy of unetched CdTe/CdS solar cells-equivalent circuit analysis," *Journal of Applied Physics,* **102**[2] (2007).

124. J. Scherbel, P. H. Nguyen, G. Paasch, W. Brutting, and M. Schwoerer, "Temperature dependent broadband impedance spectroscopy on poly-(p-phenylene-vinylene) light-emitting diodes," *Journal of Applied Physics,* **83**[10] 5045-55 (1998).

125. A. K. Jonscher, "Dielectric Relaxation in Solids." Chelsea Dielectrics Press Ltd.: London, (1983).

126. I. Balberg, D. Azulay, D. Toker, and O. Millo, "Percolation and tunneling in composite materials," *International Journal of Modern Physics B,* **18**[15] 2091-121 (2004).

127. R. A. Gerhardt, J. Runyan, C. Sana, D. S. McLachlan, and R. Ruh, "Electrical properties of boron nitride matrix composites: III, observations near the percolation threshold in BN-B_4C composites," *Journal of the American Ceramics Society,* **84**[10] 2335-42 (2001).

128. E. S. Yang, "Fundamentals of Semiconductor Devices." McGraw-Hill: New York, (1978).

129. E. L. Murphy and R. H. Good, "Thermionic emission, field emission, and the transition region," *Physical Review,* **102**[6] 1464-73 (1956).

130. L. Patrick and W. J. Choyke, "Static Dielectric Constant of SiC," *Physical Review B,* **2**[6] 2255 (1970).

131. SPI Website. http://www.2spi.com/catalog/spec_prep/silver-paint.shtml, (01/06/09).

132. R. Barbucci, "Integrated Biomaterials Science." Springer: New York, (2002).

133. J. C. Russ and R. T. DeHoff, "Practical Stereology." Springer, (2000).

134. B. D. Bertram, "The phenomenon of negative capacitance." unpublished paper for MSE 7140 Course at Georgia Tech, Atlanta, GA, 2009.

135. S. Ezhilvalavan and T. R. N. Kutty, "High-frequency capacitance resonance of ZnO-based varistor ceramics," *Applied Physics Letters,* **69**[23] 3540-42 (1996).

136. X. Wu, E. S. Yang, and H. L. Evans, "Negative capacitance at metal-semiconductor interfaces," *Journal of Applied Physics,* **68**[6] 2845-48 (1990).

137. W. W. Gerberich and M. J. Cordill, "Physics of adhesion," *Rep. Prog. Phys.,* **69**[7] 2157-203 (2006).

138. B. Budiansky and R. J. Oconnell, "Elastic moduli of a cracked solid," *International Journal of Solids and Structures,* **12**[2] 81-97 (1976).

139. R. L. Salganik, "Mechanics of bodies with many cracks," *Mechanics of Solids,* **8**[4] (1973).

140. D. W. Richerson, "Modern Ceramic Engineering," 2nd ed. Marcel Dekker: New York, NY, (1992).

141. Prof. Arun Gokhale, Graduate Stereology Lectures. Atlanta, GA, 2009.

142. J. Zhang, "A study of compaction of composite particles by multi-particle finite element method," *Composites Science and Technology*, **69**[13] 2048-53 (2009).

143. R. W. Rice, "Porosity of Ceramics." Marcel Dekker, Inc.: New York, (1998).

144. M. Asmani, C. Kermel, A. Leriche, and M. Ourak, "Influence of porosity on Young's modulus and Poisson's ratio in alumina ceramics," *Journal of the European Ceramic Society*, **21**[8] 1081-86 (2001).

145. D. Munz and T. Fett, "Ceramics: Mechanical Properties, Failure Behaviour, Materials Selection." Springer: Berlin, (1999).

146. N. A. Poklonskii, N. I. Gorbachuk, I. V. Pototskii, and D. A. Trofimchuk, "Electrical conductivity of composite materials based on fine-particle silicon near the metal-insulator transition," *Inorganic Materials*, **40**[11] 1133-37 (2004).

147. R. K. Chakrabarty, K. K. Bardhan, and A. Basu, "Nonlinear I-V characteristics near the percolation threshold," *Physical Review B*, **44**[13] 6773 (1991).

148. A. Celzard, G. Furdin, J. Mareche, and E. McRae, "Non-linear current-voltage characteristics in anisotropic epoxy resin-graphite flake composites," *Journal of Materials Science*, **32**[7] 1849-53 (1997).

149. V. Panwar, V. K. Sachdev, and R. M. Mehra, "Insulator conductor transition in low-density polyethylene-graphite composites," *European Polymer Journal*, **43**[2] 573-85 (2007).

150. S. S. Manna and B. K. Chakrabarti, "Dielectric breakdown in the presence of random conductors," *Physical Review B*, **36**[7] 4078 (1987).

151. M. K. Kerimov, M. A. Kurbanov, I. S. Sultanahmedova, I. A. Faradzhzade, F. N. Tatardar, H. S. Aliyev, F. F. Yahyaev, and U. V. Yusifova, "Varistor Effect in Polymer-Semiconductor Composites," *Semiconductors*, **44**[7] 904-11 (2010).

152. T. Masuyama and M. Matsuoka, "Current Dependence of Voltage Nonlinearity in SiC Varistors," *Japanese Journal of Applied Physics*, **7**[10] 1294-& (1968).

153. M. Guo, T. Wu, T. Liu, S.-X. Wang, and X.-Z. Zhao, "Characterization of $CaCu_3Ti_4O_{12}$ varistor-capacitor ceramics by impedance spectroscopy," *Journal of Applied Physics*, **99**[12] 124113 (2006).

154. S. W. Kenkel and J. P. Straley, "Percolation Theory of Nonlinear Circuit Elements," *Physical Review Letters*, **49**[11] 767 (1982).

155. J. P. Straley and S. W. Kenkel, "Percolation theory for nonlinear conductors," *Physical Review B,* **29**[11] 6299 (1984).

156. R. Haggenmueller, C. Guthy, J. R. Lukes, J. E. Fischer, and K. I. Winey, "Single Wall Carbon Nanotube/Polyethylene Nanocomposites: Thermal and Electrical Conductivity," *Macromolecules,* **40**[7] 2417-21 (2007).

157. R. Pike and H. E. Stanley, "Order propagation near the percolation-threshold," *J. Phys. A-Math. Gen.,* **14**[5] L169-L77 (1981).

158. F. Du, J. E. Fischer, and K. I. Winey, "Effect of nanotube alignment on percolation conductivity in carbon nanotube/polymer composites," *Physical Review B,* **72**[12] 121404 (2005).

159. A. Coniglio, "Thermal Phase Transition of the Dilute s-State Potts and n-Vector Models at the Percolation Threshold," *Physical Review Letters,* **46**[4] 250 (1981).

160. A. Coniglio, "Cluster Structure Near the Percolation Threshold," *J. Phys. A-Math. Gen.,* **15**[12] 3829-44 (1982).

161. Y. Gefen, W. H. Shih, R. B. Laibowitz, and J. M. Viggiano, "Nonlinear Behavior near the Percolation Metal-Insulator Transition," *Physical Review Letters,* **57**[24] 3097 (1986).

162. H. Ochi, A. Igari, and M. Toyoda, "Varistor material and method of producing same from zinc oxide and manganese oxide: controlled porosity and high non-linear coefficient " United States Patent 5116542. Somar Corporation (JP),1992.

163. R. A. Gerhardt and R. Ruh, "Electrical Properties of SiC Reinforced Mullite Composites." in 92nd Annual Meeting of the American Ceramic Society**.** Edited by K. M. Nair. American Ceramic Society, Dallas, TX, 1990.

164. J. Runyan, R. A. Gerhardt, and R. Ruh, "Electrical properties of boron nitride matrix composites: II, dielectric relaxations in boron nitride-silicon carbide composites," *Journal of the American Ceramics Society,* **84**[7] 1497-503 (2001).

165. R. W. Sillars, "The Properties of a Dielectric Containing Semiconducting Particles of Various Shapes," *J. Inst. Elect. Engrs.,* **80** 378-94 (1937).

166. C. Peng, "Electrostatic layer-by-layer assembly of hybrid thin flims using polyelectrolytes and inorganic nanoparticles" Ph.D. Thesis in Materials Science & Engineering, Georgia Institute of Technology, Atlanta, GA U.S.A., 2011.

167. C. J. Capozzi, "Controlled Self Assembly of ITO nanoparticles into Aggregate Wire Structures in PMMA-ITO Composites" Ph.D. Thesis in Materials Science & Engineering, Georgia Institute of Technology, Atlanta, GA, 2009.

168. J. Baker-Jarvis, "Transmission / Reflection and Short-Circuit Line Permittivity Measurements" National Institute of Standards and Technology, Department of Commerce, Boulder, Colorado, 1990.

169. D. W. Davidson and R. H. Cole, "Dielectric Relaxation in Glycerol, Propylene Glycol, and n-Propanol," *The Journal of Chemical Physics,* **19**[12] 1484-90 (1951).

170. S. Havriliak and S. Negami, "A Complex Plane Representation of Dielectric and Mechanical Relaxation Processes in Some Polymers," *Polymer,* **8**[4] 161-& (1967).

171. L. K. H. van Beek, "Dielectric behaviour of heterogeneous systems," *Prog. Dielectrics,* **7** 69 (1967).

172. Z. H. Chen, J. Q. Huang, Q. Chen, C. L. Song, G. R. Han, W. J. Weng, and P. Y. Du, "A percolative ferroelectric-metal composite with hybrid dielectric dependence," *Scr. Mater.,* **57**[10] 921-24 (2007).

173. K. J. Falconer, "Fractal geometry: mathematical foundations and applications.*"* John Wiley & Sons, Ltd: West Sussex (2003).

174. S. Ramo, J.R. Whinnery, and T. Van Duzer, "Fields and Waves in Communication Electronics." John Wiley & Sons, Inc.: New York (1984).

175. J. W. Schultz, "Anomalous dispersion in the dielectric spectra of conductive materials," *IEEE Transactions on Instrumentation and Measurement,* **47**[3] 766-68 (1998).

176. J. J. Brennan and S. R. Nutt, "SiC-Whisker-Reinforced Glass-Ceramic Composites - Interfaces and Properties," *Journal of the American Ceramics Society,* **75**[5] 1205-16 (1992).

177. B. V. Hamon, "Maxwell-Wagner loss and absorption currents in dielectrics," *Aust. J. Phys.,* **6** 304 (1953).

178. P. Sheng, E. K. Sichel, and J. I. Gittleman, "Fluctuation-induced tunneling conduction in carbon-polyvinylchloride composites," *Physical Review Letters,* **40**[18] 1197-200 (1978).

179. P. Mandal, A. Neumann, A. G. M. Jansen, P. Wyder, and R. Deltour, "Temperature and magnetic-field dependence of the resistivity of carbon-black polymer composites," *Physical Review B,* **55**[1] 452-56 (1997).

180. D. Azulay, O. Millo, E. Savir, J. P. Conde, and I. Balberg, "Microscopic and macroscopic manifestations of percolation transitions in a semiconductor composite," *Physical Review B,* **80**[24] (2009).

181. N. F. Mott, "Conduction in Non-Crystalline Materials, 3. Localized States in a Pseuogap and Near Extremities of Conduction and Valence Bands," *Philosophical Magazine,* **19**[160] 835-& (1969).

182. N. F. Mott and E. A. Davis, "Electronic Processes in Non-Crystalline Materials.″ Oxford: Clarendon, (1979).

183. V. Ambegaokar, B. I. Halperin, and J. S. Langer, "Hopping Conductivity in Disordered Systems," *Physical Review B,* **4**[8] 2612 (1971).

184. O. Chauvet, T. Stoto, and L. Zuppiroli, "Hopping conduction in a nanometer-size crystalline system - A SiC fiber," *Physical Review B,* **46**[13] 8139-46 (1992).

185. P. Sheng and J. Klafter, "Hopping conductivity in granular disordered systems," *Physical Review B,* **27**[4] 2583-86 (1983).

186. L. Zhang and Z.-J. Tang, "Polaron relaxation and variable-range-hopping conductivity in the giant-dielectric-constant material $CaCu_3Ti_4O_{12}$," *Physical Review B,* **70**[17] 174306 (2004).

187. E. K. Sichel, J. I. Gittleman, and P. Sheng, "Transport properties of the composite material carbon-poly(vinyl chloride)," *Physical Review B,* **18**[10] 5712 (1978).

188. J. P. Calame, D. K. Abe, B. Levush, and B. G. Danly, "Variable temperature measurements of the complex dielectric permittivity of lossy AlN-SiC composites from 26.5-40 GHz," *Journal of Applied Physics,* **89**[10] 5618-21 (2001).

189. M. Dong and R. A. Gerhardt, "Electrical Characterization of Sol-gel Derived $Pb(Zr,Ti)O_3$ Ceramics," pp. 367-76. in *Ceramic Transactions*., vol. 100: Dielectric Ceramic Materials. Edited by K. M. N. a. A. S. Bhalla, 1999.

190. H. Xie and P. Sheng, "Fluctuation-induced tunneling conduction through nanoconstrictions," *Physical Review B,* **79**[16] 165419 (2009).

191. S. Paschen, M. N. Bussac, L. Zuppiroli, E. Minder, and B. Hilti, "Tunnel junctions in a polymer composite," *Journal of Applied Physics,* **78**[5] 3230-37 (1995).

192. A. V. Ferris-Prabhu, "Maximum tunnelling distance in MNOS devices theory," *physica status solidi (a),* **11**[1] 81-86 (1972).

193. D. H. Woo, E. M. Choi, Y. H. Yoon, K. J. Kim, I. C. Jeon, and H. Kang, "Current-distance-voltage characteristics of electron tunneling through an electrochemical STM junction," *Surface Science,* **601**[6] 1554-59 (2007).

194. L. Altcheh and N. Klein, "Influence of the law of electrical conductivity on thermal switching and breakdown," *Electron Devices, IEEE Transactions on,* **20**[9] 801-11 (1973).

195. M. Nafría, J. Suné, and X. Aymerich, "Exploratory observations of post-breakdown conduction in polycrystalline-silicon and metal-gated thin-oxide metal-oxide-semiconductor capacitors," *Journal of Applied Physics,* **73**[1] 205-15 (1993).

196. S. K. Srivastava and R. Bhattacharyya, "Post-breakdown conduction in thin film Al-(Al_2O_3)-CdS-Al switching element," *Thin Solid Films,* **9**[3] 357-61 (1972).

197. M. Shatzkes, M. Av-Ron, and R. M. Anderson, "On the nature of conduction and switching in SiO_2," *Journal of Applied Physics* **45** pp. 2065-77 (1974).

198. I. Bunget and M. Popescu, "Physics of Solid Dielectrics." Elsevier: Amsterdam, (1984).

199. J. G. Simmons, "Poole-Frenkel Effect and Schottky Effect in Metal-Insulator-Metal Systems," *Physical Review,* **155**[3] 657 (1967).

200. A. Mellinger, "Charge Storage in Electret Polymers: Mechanisms, Characterization, and Applications." Doctoral Thesis, Potsdam, 2004.

201. L. W. Davies and R. E. Collins, "Anodic Oxide Electrets," *Electron. Lett.,* **5**[19] 462-& (1969).

202. A. Mellinger, "Dielectric resonance spectroscopy: a versatile tool in the quest for better piezoelectric polymers," *IEEE Transactions on Dielectrics and Electrical Insulation,* **10**[5] 842-61 (2003).

203. G. Blaise, "Charge detrapping induced dielectric relaxation. Application to breakdown in insulating films," *Microelectronic Engineering,* **28**[1-4] 55-62 (1995).

204. B. Gross and L. F. Denard, "On Permanent Charges in Solid Dielectrics I. Dielectric Absorption and Temperature Effects in Carnauba Wax," *Physical Review,* **67**[7-8] 253 (1945).

205. L. Niemeyer, L. Pietronero, and H. J. Wiesmann, "Fractal Dimension of Dielectric Breakdown," *Physical Review Letters,* **52**[12] 1033 (1984).